

Exploring NASICON and Garnet Structured Lithium ion Conductors and their Composites with Ionic Liquids as Electrolytes for Energy Storage Devices

THESIS

Submitted in partial fulfilment
of the requirements for the degree of

DOCTOR OF PHILOSOPHY

by

Gurpreet Kaur

ID: 2018PHXF0010P

Under the supervision of

Prof. S. C. Sivasubramanian and Prof. Anshuman Dalvi

Department of Chemistry and Department of Physics



BIRLA INSTITUTE OF TECHNOLOGY AND SCIENCE, PILANI

2024

**BIRLA INSTITUTE OF TECHNOLOGY AND SCIENCE,
PILANI**

CERTIFICATE

This is to certify that the thesis titled “**Exploring NASICON and Garnet Structured Lithium ion Conductors and their Composites with Ionic Liquids as Electrolytes for Energy Storage Devices**” submitted by **Gurpreet Kaur** ID No. **2018PHXF0010P** for award of Ph.D. of the Institute embodies original work done by her under my supervision.

(Dr. S. C. Sivasubramanian)

Professor, Department of Chemistry

BITS Pilani, Pilani campus, Rajasthan, India

(Dr. Anshuman Dalvi)

Professor, Department of Physics

BITS Pilani, Pilani campus, Rajasthan, India

Date:

Acknowledgements

First and foremost, I would like to thank my PhD supervisors, Prof. S. C. Sivasubramanian and Prof. Anshuman Dalvi. Their constant support, guidance and encouragement have been invaluable throughout the entire process. From the initial stages of refining my research proposal to the final submission of my thesis, their unwavering presence and wealth of wisdom have been instrumental in shaping my academic growth. I am profoundly grateful for the immeasurable contributions they made towards my professional development.

I am extremely thankful to Prof. V. Ramgopal Rao, Vice Chancellor, BITS-Pilani and Prof. Sudhirkumar Barai, Director, BITS-Pilani for providing me necessary facilities and financial support to pursue my doctoral research. I am also grateful to Prof. A. P. Singh (Dean) and Prof. Shamik Chakraborty (Associate Dean), Academic Graduate Studies and Research Division, BITS-Pilani for the administrative and official support. I thank Prof. Bharti Khungar, Convener, Departmental Research Committee (DRC), Department of Chemistry, BITS Pilani, Pilani Campus for her official support and encouragement and members of DRC, Department of Chemistry, BITS Pilani, Pilani Campus for their cooperation and constant guidance during each of the past few years.

I wish to thank the present head of the Department of Chemistry, BITS-Pilani, Prof. Indresh Kumar and all the previous heads of the department for their constant support. It gives me immense pleasure to express my sincere gratitude to my Doctoral Advisory Committee (DAC) members, Prof. Bharti Khungar and Prof. A. K. Sah for their valuable suggestions and support during the thesis review and overall progress review in PhD. At the same time, I am also thankful to all the faculty member of the Chemistry Department and Physics Department for their kind support. I humbly extend my thanks to all the research scholars and office staff of the department. I would like to thank Prof. K. S. Nalwa and Dr. M. D. Singh from IIT Kanpur for their help and inputs in battery fabrication.

I am indebted to my lab mates, whose support has been a constant source of motivation. I am thankful to Dr. Rajinder Kaswan, Dr. Neelakshi Sharma, Dr. Dinachandra Singh, Ms. Shrishti Sharma, Ms. Neha, Mr. Bhargab, and Mr. Hardeep. I am filled with deep gratitude towards the

divine for blessing me with remarkable friends Neha, Mahesh, Kavya, and Sumit. I would also like to thank my school and college teachers and friends. I want to extend my heartfelt thanks to Dalvi, Bhanot, and Sharma family for making me feel at home during my time at BITS.

Finally, I would like to extend my heartfelt gratitude to my wonderful extended family, both near and far, for their unwavering support, encouragement, and understanding throughout my doctoral journey. Your love and encouragement provided the motivation and strength I needed to complete this journey. Mumy and Papa, you made immense sacrifices and worked tirelessly to provide a better life for your daughters. Look how far we have come! Your dedication and resilience continue to inspire me as I look on my journey.

Lastly, I offer my sincere gratitude to the Divine for its unwavering presence, guiding me and providing the fortitude needed during challenging moments. Thankyou Baba ji for everything and this life. Wherever you are, keep showering your blessings! You will always be remembered and missed!

(Gurpreet Kaur)

Abstract

The world's growing energy demands and the imperative shift towards sustainable energy sources have propelled the rapid development of energy storage devices. To overcome the issues related to current energy storage devices, the shift towards solid-state energy storage devices has led to the emergence of fast ionic solid electrolytes. Among these fast ionic systems Li^+ ion conductors such as NASICONs (LTP, LATP) and garnets (LLZO, LALZO) have been considered promising for future solid ionic devices. However, high grain boundary impedance restricts its applications as total conductivity falls drastically. Also, electrode-electrolyte interface is another major issue which needed to be resolved before their direct application in devices. In order to tailor these issues, the present thesis deals with synthesis and characterization of Li^+ -NASICON and garnet based composites with ionic liquid. These ceramics have been synthesized by sol-gel route and small amount of ionic liquid (IL) dispersed to get composites. Further, thesis explores the thermal stability and electrochemical stability of these composites.

Present thesis has been divided into seven chapters. Chapter 1 contains the brief literature review about various fast ionic solid systems, their synthesis routes, development, and issues in solid electrolytes. Chapter 2 discusses the synthesis routes, experimental techniques, and preparation/fabrication of solid-state batteries and supercapacitors. Chapter 3 describes about the effect of ionic liquid dispersion NASICON structured Li^+ ion system $\text{LiTi}_2(\text{PO}_4)_3$ (LTP) and $\text{Li}_{1.3}\text{Al}_{0.3}\text{Ti}_{1.7}(\text{PO}_4)_3$ (LATP). It has been observed that addition of small IL content can enhance the conductivity by suppressing the grain boundary effects. The composites have been explored as a potential electrolyte for the lithium batteries. Chapter 4 explores the conductivity of LTP/LATP with different ILs and thorough characterization of solid-state supercapacitors developed using these composites. The role of IL ions and Li^+ ions from the NASICON framework in the device performance has been assessed in detail. Chapter 5 emphasizes on wide thermal stability of the developed solid-state supercapacitors and demonstrates the potential of these composites to adopt various geometries. As per literature reports, no supercapacitor specific to low and high temperature requirement exist in the market. Chapter 6 describes the effect of IL dispersion on LALZO ($\text{Li}_{16.75}\text{Al}_{0.25}\text{La}_3\text{Zr}_2\text{O}_{12}$) and further explores these composites as electrolytes for solid-state

batteries and supercapacitors. Chapter 7 summarizes the conclusions of the overall thesis and suggest the future scope of the research work.

	Page
List of Figures	xi
List of Tables	xx
Abbreviations	xxiii
Notations	xxv

Chapter 1 Introduction

1.1	General background	1
1.2	Solid state ionics	2
1.3	Fast ionic solids	5
1.4	Inorganic solid-state electrolytes	7
	1.4.1 NASICONs and NASICON structured Li ⁺ ion system	7
	1.4.2 Garnets	11
	1.4.3 Perovskites	14
	1.4.4 LISICON-type	15
	1.4.5 Li ⁺ ion-based glass ceramics	16
	1.4.6 Shortcomings of Li ⁺ ion-based inorganic solid and glass-ceramic electrolytes	17
1.5	Organic solid-state electrolytes	18
	1.5.1 Polymers and their composites	19
	1.5.2 Gel Polymers	20
	1.5.3 Shortcomings of Li ⁺ ion based organic solid-state electrolytes: polymers, gel polymers	21
1.6	Ionogel	22

1.7	Ionic liquid and fast ionic solids dispersed with ionic liquids	23
1.8	Energy storage: Batteries and Supercapacitor	25
1.9	Gaps in the existing research	28
1.10	Statement of problem and objective	29

Chapter 2 Experimental Procedures

2.1	Ionic liquid dispersed Li ⁺ NASICON and garnet preparation	54
2.2	Device fabrication	55
2.3	Characterization techniques	58
2.3.1	X-ray diffraction	58
2.3.2	Field emission scanning electron microscopy	60
2.3.3	Fourier Transform Infrared Spectroscopy	62
2.3.4	Raman Spectroscopy	63
2.3.5	Differential Scanning Calorimetry (DSC)	64
2.3.6	Thermo-gravimetric Analysis (TGA)	65
2.3.7	BET surface area analysis	66
2.3.8	Electrical characterization: Impedance spectroscopy	67
2.3.9	Electrochemical cell characterization	73

Chapter 3 Ionic Liquid Dispersed Sol-Gel Derived LiTi₂(PO₄)₃ composites

3.1	Structural studies	82
3.1.1	X-ray diffraction	82
3.1.2	Field emission scanning electron microscopy	83
3.2	Thermogravimetric analysis	84
3.3	Electrical conductivity	85
3.4	The hybrid electrolyte under battery conditions	90
3.5	Replacing LTP by its superior version LATP	91
3.6	A possible mechanism for ionic transport	92

Chapter 4 Li⁺-NASICONs-IL Composites as Electrolyte for Solid- State Super Capacitors

4.1 Li ⁺ -NASICONs-IL solid composite electrolyte characterization	99
4.2 Activated charcoal (electrode) characterization	100
4.3 SSC characterization	102
4.4 Summary	114

Chapter 5 Li_{1.3}Al_{0.3}Ti_{1.7}(PO₄)₃-EMIMBF₄ electrolyte with wide thermal stability for SSCs

5.1 Activated Charcoal (electrode) characterization	118
5.2 Description of three geometries	118
5.3 Important results for different geometries	119
5.4 Summary	133

Chapter 6 Ionic Liquid-garnet composites for Solid State Batteries (SSBs) and Solid State Supercapacitors (SSCs)

6.1 FESEM	137
6.2 Electrical Transport	137
6.3 Thermal stability investigations	140
6.4 Conductivity- structure correlation	145
6.5 Electrochemical characterization in battery configuration	148
6.6 Electrochemical characterization in supercapacitor configuration	150
6.7 Summary	159

Chapter 7 Conclusions and future scope

7.1 Conclusion 163

7.2 Future scope 170

List of publications xxvii

List of conferences/workshops xxix

Brief biography of the supervisors xxx

Brief biography of the candidate xxxii

List of Figures

Chapter 1

- Fig. 1.1(a)** Crystal structure of Na- β -Al₂O₃. The mobile sodium ions, oxygen, and aluminum atoms are represented by blue, red, and yellow colors, respectively, **(b)** Li⁺ ion transport in Li₂SO₄ depicted by paddle wheel mechanism. 4
- Fig. 1.2** Classification of fast ionic solids based on their structure. 6
- Fig. 1.3** Temperature dependence of electrical conductivity for various fast ionic solids. 7
- Fig. 1.4** Rhombohedral structure of Li⁺ NASICON, Li_{1.5}Al_{0.5}Ti_{1.5}(PO₄)₃. The oxygen at red and blue octahedral sites represent (Al/Ti)O₆ while the one at purple tetrahedral sites shows PO₄ sites. The Li⁺ ions at M1 sites are shown in green colour with Wyckoff position 6b. Additional Li⁺ ions in the top half occupy the M2 site in 18e position while the bottom half are at M3 site at 36f position. 9
- Fig. 1.5** A schematic diagram based on the Brick layer model showing grains and grain boundaries in a solid-state electrolyte placed between two symmetric electrodes. 10
- Fig. 1.6** Crystal structures of Li₇La₃Zr₂O₁₂ with **(a)** cubic and **(b)** tetragonal phases. 13
- Fig. 1.7** Crystal structures (a) cubic and (b) tetragonal perovskite. 14
- Fig. 1.8** Li⁺ ion battery. 26
- Fig. 1.9** Classification of supercapacitors. 26
- Fig. 1.10.** EDL models, (a) Helmholtz model, (b) Gouy-Chapman model, (c) Stern model. 27

Chapter 2

- Fig. 2.1(a)** A picture of the composite pellet with electrodes, **(b)** A picture of Swagelok cell used for battery testing, **(c)** Glove box (MTI) filled with Argon for fabrication. 57
- Fig. 2.2** Fabrication process steps for SSC having electrodes as activated charcoal coated copper foil, and IL dispersed ceramic composite as electrolyte. **(a)** Composite preparation: IL mixing with

LATP in a ball mill, **(b)** Sprinkling composite powder on the activated charcoal electrode (coated on Cu foil) of diameter $\sim 14\text{mm}$, **(c)** Sandwich to press with $\sim 3\text{ tons/cm}^2$ in a hydraulic press (room temperature) for 10 minutes, **(d)** The SSC Cu|AC|LATP-IL|AC|Cu as obtained from the press in step (c). For casing the supercapacitor, the following geometries were chosen: **(e)** 2032 cell assembly, **(f)** Swagelok assembly, **(g)** Hot roll lamination. 57

Fig. 2.3 **(a)** Geometrical representation of Bragg's law, **(b)** Block diagram of XRD setup. 60

Fig. 2.4 Block diagram for experimental setup for FESEM. 61

Fig. 2.5 Schematic diagram for sample analysis in FTIR Spectrophotometer in **(a)** ATR mode and **(b)** Transmission mode. 62

Fig. 2.6 Schematic diagram of a typical Raman spectrometer. 64

Fig. 2.7 Block diagram of DSC setup. 64

Fig. 2.8 Schematic diagram of TGA instrument. 66

Fig. 2.9 Schematic diagram of BET surface area analyzer. 67

Fig. 2.10 Schematic diagram for **(a)** sample holder and **(b)** experimental setup for electrical conductivity measurement. 69

Fig. 2.11 Frequency dependence of ac conductivity in accordance with Jonscher's universal power law. 70

Fig. 2.12 **(a)** Block diagram of CV setup. **(b)** Block diagram of two electrode setup for measurement of electrochemical performance used in the present study. The setup is capable of wide temperature characterization. 74

Fig. 2.13 **(a)** A typical LSV curve showing ESW, **(b)** a Typical CV curve for redox reaction. 74

Fig. 2.14 A typical CV and GCD curve for EDLC, pseudo supercapacitor, and battery. 76

Chapter 3

- Fig. 3.1(a)** HT-XRD patterns for pristine sol-gel derived LTP, **(b)** HT-XRD patterns for LTP-13IL. 82
- Fig. 3.1 (c)** The unit cell volume as a function of temperature. 83
- Fig. 3.2 (a)** FESEM image of as prepared LTP, **(b)** FESEM image of LTP-13IL. 83
- Fig. 3.2 (c)** EDS mapping for LTP-13IL and elemental distribution maps. 84
- Fig. 3.3** TGA scan of the LTP-13IL. Inset of Fig. 3: TGA of pure ionic liquid. 85
- Fig. 3.4 (a)** Nyquist plots for LTP with equivalent circuit, **(b)** Nyquist plots for LTP-13IL with equivalent circuit. 85
- Fig. 3.4(c)** Frequency dependence of total conductivity at different temperatures for LTP-13IL. The σ_{total} was also extracted from plateau, at onset of dc to dispersion as shown for one temperature (165 °C). 86
- Fig. 3.5 (a)** Conductivity at three different temperatures with variation of IL content in the composite, **(b)** Temperature dependence of total conductivity for all the composites. 87
- Fig. 3.5 (c)** Temperature dependence of total conductivity (30-600 °C) for LTP-13IL and pristine LTP. After IL decomposition the composite attains conductivity of LTP, **(d)** Total conductivity with temperature (-50 °C to 10 °C) for LTP and LTP-13IL. 88
- Fig. 3.6** Electrical response (Z'' vs ω) for LTP and LTP-13IL. 89
- Fig. 3.7** Cyclic voltammetry scan of LTP-13IL. 90
- Fig. 3.8** Discharging of cell at different currents. 90
- Fig. 3.9 (a)** Temperature dependence of total conductivity for all the composites, **(b)** Discharging of cell at different currents. 92
- Fig. 3.10** Schematic diagram showing the movement of Li^+ ions in between LTP/LATP grains with the help of ionic liquid. 92

Chapter 4

Fig. 4.1 (a) HT-XRD patterns for pristine sol-gel derived LTP, **(b)** HT-XRD patterns for LTP-13 EMIMBF₄. 99

Fig. 4.2 Electrical conductivity at three different temperatures for LTP with different ILs (13 wt%), **(b)** Electrical conductivity at three different temperatures for LTP with different ILs (13 wt%). 100

Fig. 4.3 (a) FESEM image of the as prepared LTP, **(b)** FESEM image of LTP-13 EMIMBF₄ composite. 100

Fig. 4.4 (a) Nitrogen adsorption-desorption isotherm curve of the activated charcoal (inset: linear fitting with the BET equation), **(b)** Micropore distribution plot of the activated charcoal, **(c)** FESEM image for the activated charcoal deposited on copper collector. 101

Fig. 4.5 (a) Nyquist plots (10 mHz-0.1 MHz) for SSCs having different IL-dispersed LTPs as electrolyte. For comparison, thickness and area of the cross-section are kept the same for all the SSCs, **(b)** Nyquist plots (10 mHz-0.1 MHz) for SSCs having different IL dispersed LTPs as electrolyte. For comparison, thickness and area of the cross-section are kept the same for all the SSCs. 102

Fig. 4.5 (c) Imaginary capacitance (C'') of SSCs as a function of frequency, **(d)** Equivalent circuit for SSCs. 103

Fig. 4.6 (a) CV scans for the SSCs having electrolyte as different IL dispersed LTPs at a scan rate of 10 mV/s, **(b)** CV scans for the SSCs having electrolyte as different IL dispersed LTPs at a scan rate of 10 mV/s. 104

Fig. 4.6 (c) CV scans of SSC having LTP-13 EMIMBF₄ electrolyte up to 100 cycles. Typical EDLC nature is witnessed, **(d)** CV scans (at 10 mV/s) of SSC for LTP-13 EMIMBF₄ for different voltage ranges. 105

Fig. 4.7 (a) Galvanostatic charge-discharge (at 0.65 mA/cm²) cycles for SSCs having IL dispersed LTP composites, **(b)** Galvanostatic charge-discharge (at 0.65 mA/cm²) cycles for SSCs having IL

dispersed LATP composites, (c) GCD curves of LATP-13 EMIM BF₄ for the 10th cycle at different currents ranging from 0.11-1.7 A-g⁻¹ at 1 V with areal current densities mentioned in brackets. 106

Fig. 4.7 (d) Coulomb efficiency as a function of discharge current density, (e) GCD curves of LATP-13 EMIM BF₄ for different voltage ranges, (f) Conductivity versus capacitance for different composites. Here A: LATP-13 EMIMBF₄, B: LATP-13 EMIMCF₃SO₃, C: LTP-13 EMIMBF₄, D: LATP-13 BMIMBF₄, E: LTP-13 EMIMCF₃SO₃, F: LTP-13 BMIMBF₄, (g) Charge-discharge cycles for SSC having LATP-13 EMIMBF₄ composite as electrolyte obtained at different cycles at ~35 °C. 110

Fig. 4.7 (h) The specific capacitance and ESR vs cycle number at ~35 °C for SSC having electrolyte LATP-13 EMIMBF₄. INSET: coulomb efficiency vs cycle number up to 13000 cycles. 111

Fig. 4.7 (i) Specific capacitance rise and decay cycle between 30 °C - 100 °C, (j) Ragone plot for SSCs having IL dispersed LATP composites. 112

Fig. 4.8 (a) Glow of LED using two-coin cells (having LATP-13 EMIM BF₄ as electrolyte) connected in series, (b) Glow of LED using two-coin cells (having only EMIMBF₄ as electrolyte) connected in series. 113

Chapter 5

Fig. 5.1(a) Nitrogen adsorption-desorption isotherm curve of the activated charcoal (inset: linear fitting with the BET equation), (b) Micropore distribution plot of the activated charcoal. 118

Fig. 5.2 (a) The Nyquist plot and corresponding equivalent circuit for SSC at different temperatures having LATP-13 EMIMBF₄ composite as an electrolyte. 119

Fig. 5.2(b) The Nyquist plot and equivalent circuit for SSC for composites with different IL percentage at 100 °C. 120

Fig. 5.2 (c) CV scans for SSC at -10 °C up to 100 cycles, (d) CV scans for SSC at 100 °C up to 100 cycles. 121

Fig. 5.2 (e) Galvanostatic charge-discharge (at 0.56 A/g) cycles for SSCs at low temperatures. 122

Fig. 5.2 (f) Galvanostatic charge-discharge (at 0.56 A/g) cycles for the SSCs at 35 °C and 100 °C.	122
Fig. 5.2 (g) Comparison of conductivity and C_s value of the composites with different IL content.	124
Fig. 5.2 (h) GCD curves for SSC up to 100 cycles at 35 °C.	125
Fig. 5.2 (i) C_s vs Cycle number for first 100 GCD cycles at 35 °C.	125
Fig. 5.2 (j) GCD curves for SSC up to 100 cycles at -10 °C.	125
Fig. 5.2 (k) C_s vs Cycle number for first 100 cycles at -10 °C.	125
Fig. 5.2 (l) GCD curves for SSC up to ~30 cycles at 100 °C.	126
Fig. 5.2 (m) C_s vs Cycle number for first 30 cycles at 100 °C.	126
Fig. 5.2 (n) The C_s vs current density for SSC at 2 V.	127
Fig. 5.2 (o) Ragone plot for SSC at different temperatures.	127
Fig. 5.2 (p) Coulombic efficiency vs current density at different temperatures.	127
Fig. 5.3 (a) Nyquist plot for SSC in Swagelok assembly at different temperatures.	128
Fig. 5.3 (b) CV scans for SSC at different temperatures in Swagelok assembly.	128
Fig. 5.3 (c) GCD cycles for SSCs at 35 °C and 175 °C.	129
Fig. 5.3 (d) C_s vs cycle number at 175 °C.	129
Fig. 5.3 (e) C_s values at room temperature after heating at 175 °C.	129
Fig. 5.4 (a) Nyquist plot for annealed SSCs at room temperature.	130
Fig. 5.4 (b) CV scans for annealed SSCs at room temperature.	130
Fig. 5.4 (c) GCD cycles for annealed SSCs.	131
Fig. 5.4 (d) C_s for SSCs at different annealed temperatures.	131
Fig. 5.4 (e) Supercapacitors after annealing at higher temperatures.	131
Fig. 5.5 (a) Nyquist plot for laminated SSC.	132
Fig. 5.5 (b) CV plot for laminated SSC.	132

Fig. 5.5 (c) GCD cycles for laminated SSC.	132
Fig. 5.5 (d) C_s value as observed after cycling.	132
Fig. 5.5 (e) Laminated SSC picture before and after heating.	133

Chapter 6

Fig. 6.1(a) The IL-LALZO as prepared pellet used for electrical transport studies	137
Fig. 6.1(b) FESEM image of powders of pristine LALZO	137
Fig. 6.1(c) LALZO dispersed with ionic liquid (6wt%) at equal magnification	137
Fig. 6.2(a) Nyquist plots for LALZO-0.1 EMIMBF ₄ with equivalent circuit in the inset.	138
Fig 6.2 (b) Nyquist plots for LALZO-6 EMIMBF ₄ with equivalent circuit in the inset.	138
Fig 6.3 (a) Conductivity of the composite with variation of IL content (EMIMBF ₄) at three different temperatures.	139
Fig 6.3 (b) Temperature dependence of total conductivity for all the composites having LALZO and varied amount of EMIMBF ₄ .	139
Fig 6.3 (c) Electrical conductivity at three different temperatures for LALZO with different ILs. Amount fixed to ~ 6 wt% in the LALZO matrix.	140
Fig 6.4 (a) HT-XRD patterns of LALZO, (b) HT-XRD patterns of LALZO-6 EMIMBF ₄ .	140
Fig. 6.5 (a) FTIR in Attenuated total reflection (ATR) mode for pure IL, pristine LALZO, and the LALZO-IL composite.	141
Fig. 6.5 (b) Raman spectra for LALZO and LALZO-6EMIM BF ₄ composite (Inset: for EMIM BF ₄).	141
Fig. 6.6 (a) TGA plots for LALZO and LALZO-6 EMIM BF ₄ . Inset: TGA plot for EMIM BF ₄ .	143
Fig 6.6 (b) DSC plots for LALZO and its composite with different ILs. Inset: DSC plot of first and second heating cycle for LALZO-6 EMIMBF ₄ .	144
Fig 6.6 (c) Enthalpy values obtained from DSC for composites having LALZO and different.	144
Fig 6.7 (a) The dynamic conductivity temperature cycles for LALZO-6 EMIM BF ₄ composite in a temperature range of 30-340 °C.	145

Fig 6.7 (b) Nyquist plot for LALZO-6 EMIMBF ₄ at 220 °C.	145
Fig 6.7 (c) Conductivity isotherm (at ~220 °C) for composites containing LALZO and different percent of EMIMBF ₄ . Inset: Enthalpy value obtained from DSC versus $\Delta\sigma$ (obtained from Fig. 6.6(c)) for composites containing LALZO and different percent of EMIMBF ₄ .	147
Fig 6.8 (a) GCD cycle for lithium cell at different discharge rate, (b) Discharge capacity versus cycle number.	148
Fig. 6.9. The Nyquist plot and corresponding equivalent circuit for the SSC (2032 type) at different temperatures having LALZO-6 EMIMBF ₄ composite as an electrolyte. Inset: Temperature dependence of total conductivity for composite LALZO-6 EMIMBF ₄ .	150
Fig. 6.10 (a) CV scans (at 10 mV/s) of SSC for different voltage ranges at 35 °C, (b) CV scans (at 10 mV/s) for the SSC for the 10 th cycle at different temperatures.	151
Fig. 6.11 (a) GCD curves of SSCs for different voltage ranges at 0.57 A/g. Inset shows coulombic efficiency versus operating voltage.	152
Fig. 6.11 (b) GCD curves of SSCs for the 10 th cycle at different discharge currents ranging from 0.57-6.8 A/g with areal current densities mentioned in brackets.	152
Fig. 6.11 (c) GCD curves for SSCs at 0.57 A/g (1 mA) for different activated charcoal surface area electrodes.	153
Fig. 6.11 (d) Charge-discharge curves obtained at different cycles for SSC with LALZO-6 EMIM BF ₄ composite as electrolyte at room temperature at 0.57 A/g (1 mA).	154
Fig. 6.11 (e) Specific capacitance and ESR vs cycle number for SSC having electrolyte LALZO-6 EMIM BF ₄ . Inset shows coulombic efficiency vs cycle number up to 4000 cycles.	154
Fig. 6.11 (f) GCD curves (at 1.13 A/g) for SSC up to 200 cycles at 100 °C.	155
Fig. 6.11 (g) C _s vs Cycle number for first 200 cycles at 100 °C. Inset: coulombic efficiency versus cycle number.	155
Fig. 6.11 (h) GCD curves (at 1.73 A/g) for SSC up to 200 cycles at 0 °C.	156
Fig. 6.11 (i) C _s vs Cycle number for first 200 cycles at 0 °C. Inset: coulombic efficiency versus cycle number.	156

Fig. 6.11 (j) Ragone plot for SSC in 0-2 V range.	156
Fig. 6.12 (a) Nyquist plot for laminated SSC with corresponding equivalent circuit.	157
Fig. 6.12(b) CV (at 10 mV/s) scan for laminated SSC.	157
Fig. 6.12 (c) GCD (at 0.57 A/g) cycles for laminated SSC.	157
Fig. 6.13 Glow of LEDs using four cells connected in series.	158

List of Tables

Chapter 1

Table 1.1 Historical outline of the development of solid state ionic conductors.	3
Table 1.2 Various Li ⁺ -NASICONs at room temperature	10
Table 1.3 Various Li ⁺ ion garnets	12
Table 1.4 Various Li ⁺ ion perovskites at room temperature	15
Table 1.5 Ionic conductivities of various Li ⁺ ion based sulfide and oxide glasses	16
Table 1.6 Li ⁺ ion based glass-ceramic composites having various precipitated FICs	17
Table 1.7 Various polymer-salt complexes and polymer-filler composites	20
Table 1.8 Various gel polymer electrolytes	21
Table 1.9 Properties of Ionic Liquids	23

Chapter 2

Table 2.1 The interrelationship between four formalisms of impedance spectroscopy. ($j = \sqrt{-1}$)	68
Table 2.2 Nyquist plots of common interest and their corresponding equivalent circuit	72

Chapter 3

Table 3.1 Lattice parameters a, c and unit cell volume for LTP-13IL considering hexagonal unit cell	83
Table 3.2 Room temperature conductivity and activation energy of ionic conduction as obtained from Fig. 5(b)	87

Chapter 4

Table 4.1 Electrical conductivity, specific capacitance, energy, power, ESR, and coulomb efficiency for the SSCs with compositions containing different ILs dispersed LTP and LATP as an electrolyte. The range is specified for C_s , E, and P, and (*) represents values for a typical SSC used in the analysis that is close to the average performance of SSCs 109

Table 4.2 Areal capacitance, energy, and power density values for the SSCs with compositions containing different ILs dispersed LTP and LATP as an electrolyte 109

Chapter 5

Table 5.1 Specific capacitance (C_s), specific energy (E), specific power (P), equivalent series resistance (ESR), and coulombic efficiency (η_{CE}) for the SSCs of the composite LATP-13 EMIMBF₄ as an electrolyte at different temperatures (operating current and voltage are 1mA and 1V respectively). The range is specified for C_s and (*) represents values for a typical SSC used in the analysis that is close to the average performance of the SSC 123

Table 5.2 Areal capacitance, energy, and power density values for the SSCs with LATP-13 EMIMBF₄ as electrolyte at different temperatures. The range is specified for Areal capacitance and (*) represents values for a typical SSC used in the analysis that is close to the average performance of the SSC 124

Chapter 6

Table 6.1 Specific Capacitance (C_s), specific energy (E), specific power (P), Equivalent series resistance (ESR), areal capacitance, energy density (E_a), and power density (P_a) for the SSCs of the composite LALZO-6 EMIMBF₄ as electrolyte having different surface area activated carbon for electrodes and operating current and voltage as 1 mA (0.57 A/g) and 2 V respectively. The range is specified for C_s and (*) represents values for a typical SSC used in the analysis that is close to the average performance of the SSC 154

Chapter 7

Table 7.1 A comparison of electrical conductivity of the composites and device performance parameters obtained for the optimized composites of Li^+ -NASICON and garnet with IL 169

Abbreviations

LIBs: Li⁺ ion batteries

SSEs: Solid-state electrolytes

FICs: Fast ion conductors

SICs: Superionic solids

SSBs: Solid-state batteries

SSCs: Solid-state supercapacitors

NASICON: Sodium superionic conductor

Li⁺-NASICON: NASICON structured Li⁺ ion conductors

LTP: LiTi₂(PO₄)₃

LATP: Li_{1.3}Al_{0.3}Ti_{1.7}(PO₄)₃

GBI: Grain boundary impedance

LLZO: Li₇La₃Zr₂O₁₂

LISICON: Lithium super ionic conductor

IS: Impedance spectroscopy

SPEs: Solid polymer electrolytes

PEO: Polyethylene oxide

PVDF: Polyvinylidene fluoride

PAN: Polyacrylonitrile

CSPEs: Composite solid polymer electrolyte

GPEs: Gel polymer electrolytes

IL: Ionic liquid

EDLCs: Electric double-layer capacitors

NMP: 1-Methyl-2-pyrrolidinone

LFP: LiFePO₄

XRD: X-ray diffraction

HTXRD: High temperature X-ray diffraction

FESEM: Field emission scanning electron microscopy

EDS: Energy dispersive X-ray spectroscopy

FTIR: Fourier Transform Infrared

DSC: Differential scanning calorimetry

TGA: Thermogravimetric Analysis

CPE: Constant phase element

LSV: Linear sweep voltammetry

CV: Cyclic voltammetry

GCD: Galvanostatic charge discharge

ESW: Electrochemical stability window

ESR: Equivalent series resistance

AC: Activated charcoal

Notations

- σ : Electrical conductivity
- σ_e : Electronic conductivity
- σ_G : In-grain/ bulk conductivity
- σ_{GB} : Grain boundary conductivity
- E_σ : Activation energy for ionic conduction
- T_g : Glass transition temperature
- T_c : Crystallization temperature
- T_m : Melting temperature
- Z' : Real part of impedance
- Z'' : Imaginary part of impedance
- ϵ' : Real part of complex permittivity
- C_s : Specific capacitance
- E : Specific energy
- P : Specific power
- V_p : Total pore volume
- V_d : Average pore diameter
- R_b : Bulk resistance
- R_{ct} : Charge-transfer resistance
- W : Warburg impedance
- η_{CE} : Coulombic efficiency

Chapter 1

Introduction

1.1 General Background

A serious challenge for the current era is to have energy security and environmental sustainability amidst the increasing dependence on fossil fuels and their associated greenhouse gas emissions. In order to facilitate the transition towards a more sustainable future, renewable energy sources such as wind, solar, and hydroelectric power have been explored and are being increasingly utilized. These energy sources offer a promising alternative to fossil fuels, but they also pose challenges of intermittency and variability. To overcome these challenges, efficient and reliable electrochemical energy storage systems have been employed to balance the supply and demand of energy [1].

Rechargeable battery technology has undergone significant transformation since the development of the lead-acid battery in the 19th century which still dominates the commercial market. Initially used primarily in cars, lead-acid batteries being heavy and have a low energy density, making them unsuitable for most portable devices. This led to the development of nickel-cadmium, nickel-metal hydride, and other such batteries, which offered higher energy densities but were still limited in terms of efficiency and memory effect. However, in the 1990s, lithium-ion (Li^+ ion) batteries were commercialized and quickly became the most widely used and efficient battery technology [2]. Among various energy storage technologies, Li^+ ion batteries (LIBs) along with Li^+ ion capacitors have emerged as the dominant choice for portable electronics, electric vehicles, and grid-scale applications due to their high energy density, long cycle life, and low maintenance cost [3].

Although Li^+ ion batteries along with supercapacitors have revolutionized the portable electronics industry and have become the standard power source for electric vehicles, however, they have their share of problems. Still, many of the LIBs and other batteries available in the market use liquid/gel electrolytes that are toxic and flammable which restricts their large-scale application. Other issues related to them include leakage, limited temperature range, miniaturization, poor mechanical strength,

etc. Moreover, conventional LIBs are limited by the use of graphite as the anode material, which restricts the theoretical capacity and energy density of the battery [4].

To address these issues, solid-state electrolytes (SSEs) have been proposed, almost four decades back, as a potential solution and are being researched and developed for next-generation LIBs. This led to the development of a novel research field area of solid-state ionics. Solid-state electrolytes offer several advantages over liquid electrolytes, including improved safety, longer lifespan, non-leakage, nontoxic, wide temperature range, mechanical strength, etc. They also have the potential to be lighter and more compact, making them ideal for use in portable electronic devices and electric vehicles. They enable the use of lithium metal as the anode, which has a much higher capacity and energy density. As a result of these benefits, in recent years we have seen a surge of research on solid-state electrolytes for lithium energy storage devices [4-5].

1.2 Solid State Ionics

Solid state ionics is a field (coined by T. Takahashi) that studies the transport and reactions of ions in solid materials, such as ceramics, glasses, polymers, and composites [6]. These materials can exhibit high ionic conductivity values, comparable to or even exceeding those of liquid electrolytes, and are therefore attractive candidates for solid-state energy storage devices [7-8].

Search for fast ionic transport, in fact, started in the early 1830s when Faraday discovered that the heated solid substances Ag_2S and PbF_2 had remarkable ionic properties showing conductivities similar to metals [9]. Thereafter, a number of solid ionic conductors were discovered, and the “solid electrolyte” term was frequently used by researchers as shown in Table 1.1 [10-11]. However, in the 1960s, there was a notable shift in focus toward Solid State Electrolytes (SSEs) that had high ionic conductivity, and these areas of research were then referred to as "solid state ionics". This marked a crucial moment in the development of SSEs, as they were beginning to be recognized for their potential as a new class of materials with promising applications in various fields. During the beginning of the 1960s, T. Takahashi and O. Yamamoto introduced a novel solid-state electrolyte called Ag_3SI (which had a very high Ag^+ conductivity of $1 \times 10^{-2} \Omega^{-1}\text{cm}^{-1}$ at 20 °C), and proposed an all-solid-state battery of the type $\text{Ag}/\text{Ag}_3\text{SI}/\text{I}_2$ based on it [12-13]. In 1967, Y. Yao and J. Kummer

reported $\text{Na}_2\text{O} \cdot 11\text{Al}_2\text{O}_3$ (β -alumina) which exhibited high Na^+ ion conductivity [14]. Subsequently, J. Kummer and Y. Weber proposed the first Na/S battery using β -alumina as a solid-state electrolyte. The Na^+ ion conducting membrane of β - Al_2O_3 was used as a solid-state electrolyte with molten sodium and sulphur [15-16]. The crystal structure of Na- β - Al_2O_3 is shown in Fig. 1.1 (a). The movement of Na^+ ions was observed to occur along planar surfaces that separate the spine-like blocks of atoms in a two-dimensional manner. With the successful discovery of high-conductivity solid-state electrolytes such as Ag_3SI , β -alumina, and RbAg_4I_5 [17], there was swift progress in creating practical applications in terms of solid state ionic devices such as batteries, sensors, and fuel cells.

Table 1.1 Historical outline of the development of solid state ionic conductors.

Year	Materials	Description	Ref.
1834	Ag_2S and PbF_2	Remarkable ionic properties of Ag_2S (at 177 °C) and PbF_2 (at 500 °C).	[9]
1899	ZrO_2 with Y_2O_3 or CeO_2	Nernst produced the anionic conductor as a “glower”.	[18] [19]
1966	$\text{Ag}/\text{Ag}_3\text{SI}/\text{I}_2$	An all-solid-state battery was proposed by T. Takahashi and O. Yamamoto.	[12] [13]
1967	β -Alumina ($\text{Na}_2\text{O} \cdot 11\text{Al}_2\text{O}_3$)	Exhibited high Na^+ conductivity.	[14]
1966- 1967	Ag_4MI_5 (M = Rb, K, and NH_4)	A high-conductivity solid-state electrolyte proposed by Bradley and Greene.	[20] [21]
1973	PEO with Na^+ and K^+ salts	Discovery of solid polymer electrolyte.	[22]
1979	PEO with Li^+ salts	“PEO + Li salts” system.	[23]
1986- 1987	Zebra battery with β -alumina electrolyte	Practical specific energy of 130 Wh kg^{-1} , long life (41000 cycles), and high degree of safety.	[24] [25]
1986	PEO/ LiCF_3SO_3 /polystyrene	“PEO + Li salts” system.	[26]
1992	LIPON	Proposed inorganic lithium-ion solid-state electrolyte system.	[27] [28]

Various other Li^+ ion materials like Li_3N were developed which have shown a high ionic conductivity of $10^{-3} \Omega^{-1}\text{cm}^{-1}$ at room temperature. These materials exhibited a layered structure having sheets of Li_2N forming a N-Li-N bridge connected through Li^+ ions [29]. The Li^+ ion conduction took place through 2-D intersecting empty tunnels. Kwist and Luden discovered α phase of Li_2SO_4 that showed conductivity of the order $1 \Omega^{-1}\text{cm}^{-1}$ at high temperature ($\sim 575^\circ\text{C}$) [30]. They proposed paddle wheel model and explained the diffusion of Li^+ ions due to the fast rotation of SO_4^{2-} tetrahedron in α - Li_2SO_4 crystal lattice. The high ionic conductivity of α - Li_2SO_4 is due to the FCC arrangement of SO_4^{2-} tetrahedra that allow Li^+ ions to move easily between the tetrahedral sites as shown in Fig. 1.1 (b). These reported materials of Li and Ag exhibited low decomposition potential making them unsuitable for solid state batteries. In the 1970s high ionic conductivity was obtained by dispersing Al_2O_3 in LiI in a very small amount which was later used as electrolyte in Li/PbI_2 cells. The high conductivity of this electrolyte was due to the formation of a space charge region containing high carrier concentration at the interfaces/ grain boundaries. To explain this doping effect in different ionic conductors space charge layer model was proposed.

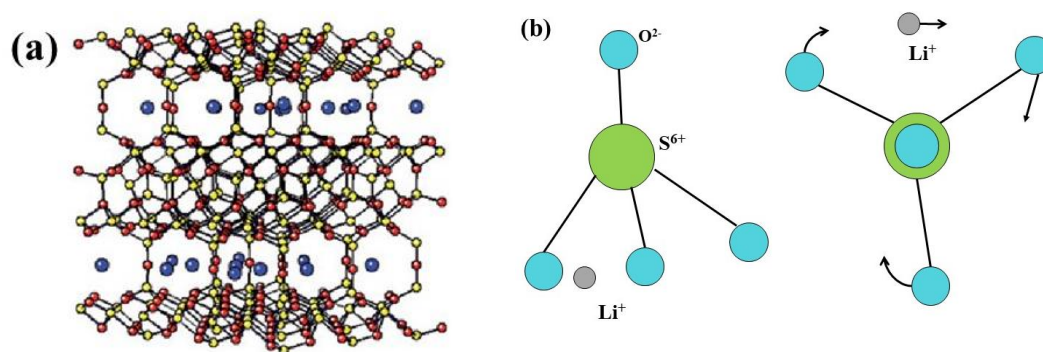


Fig. 1.1(a) Crystal structure of $\text{Na-}\beta\text{-Al}_2\text{O}_3$. The mobile sodium ions, oxygen, and aluminum atoms are represented by blue, red, and yellow colors, respectively [31]

(b) Li^+ ion transport in Li_2SO_4 depicted by paddle wheel mechanism.

Besides these inorganic materials, solid polymeric electrolytes were reported in 1973 [22]. These consist of crystalline complexes of sodium and potassium salts with PEO and this discovery extended the scope of SSE to organic materials. M. Armand and co-workers proposed the solid-polymer electrolytes of PEO + Li salts and it led to many studies reported in the 1980s exhibiting high lithium-ion conductivity.

Subsequently, different lithium-ion conductive polymer materials such as PVDF, PMMA, and PAN have been studied for lithium batteries [23, 26, 32-33].

In 1986, J. Coetzar et al. proposed a new high energy density battery system, known as a Zebra battery, which consists of a liquid sodium anode, a solid-state cathode, and a β -alumina electrolyte [24-25]. Since 1980, the term “solid-state ionics” has become widely used, and a journal with the same name was established in that year. Oak Ridge National Laboratory developed an inorganic Li^+ ion solid-state electrolyte named LIPON (lithium phosphorus oxynitride) in 1992 just after Sony commercialized its first lithium-ion battery in 1991 [27-28, 34]. After that, various investigations were done on materials including the oxides such as perovskite, NASICON, LISICON, and garnet; the sulfides such as $\text{Li}_2\text{S-P}_2\text{S}_5$, and $\text{Li}_2\text{S-P}_2\text{S}_5\text{-MS}_x$; and the hydrides and halides. Thus, these solid-state electrolytes which have been identified over the years led to the development of solid state ionics area. The solid-state electrolytes having exceptionally high ionic conductivities near room temperature were named as fast ionic solids (FICs)/ superionic solids (SICs).

1.3 Fast Ionic Solids

Fast ionic solids or superionic solids are materials that have exceptionally high ionic mobilities and diffusion coefficients, often due to structural defects or disorders. The structure of these materials lies between those of liquid electrolytes which have completely irregular and delocalized structure with all mobile ions, and the crystalline solids having regular and localized structure with immobile (frozen) ions. The main characteristics of FICs are (i) high ionic conductivity that lies between $10^{-1}\text{-}10^{-4} \Omega^{-1}\text{cm}^{-1}$ much below the melting point ($T \ll T_m$), (ii) negligible electronic conductivity ($\leq 0.01\%$ of ionic conductivity) with ionic transport number approaching unity (iii) low or moderate activation energy barrier, preferably $\ll 1$ eV, which helps in easy migration of ions (iv) crystal structure which has open tunnels for ion migration and interconnected sites for mobile ions [35]. Furthermore, for their applications in solid-state energy storage devices, they should inevitably be physically and chemically compatible with anode and cathode. Superionic solids can be classified based on structure as shown in Fig. 1.2.

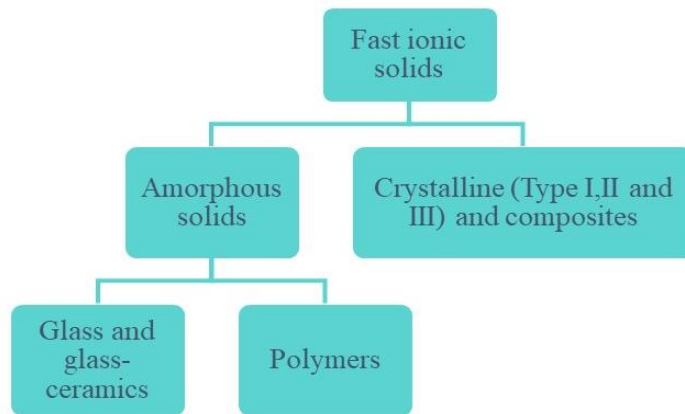


Fig. 1.2 Classification of fast ionic solids based on their structure.

According to Boyce and Huberman [36], the crystalline FICs can be divided into three types:

(i) Type I- This type of material exhibits a sudden and anomalous rise in ionic conductivity at some elevated temperature via a first order structural phase transition. At this superionic phase transition (T_c), there is a rearrangement of the immobile-ion sublattice along with a massive disordering of the mobile ion sublattice. The structures of the superionic phase of most of the type I materials are BCC or FCC and example includes AgI, Cu_2S , Li_2SO_4 , etc.

(ii) Type II- Unlike type I, in this type of material there is a gradual transition from normal ionic to conducting state. These materials undergo a second order phase transition to attain the superionic phase. There is a gradual disordering that occurs at an apparent onset temperature (T_c) for mobile sublattice, however, there is no change in the lattice of immobile ions. Most of these ionic conductors have fluorite structure. Examples: CaF_2 , PbF_2 , Na_2S , etc.

(iii) Type III- In these types of materials there is an exponential increase in ionic conductivity without any structural phase transition. They are mostly non-stoichiometric materials that exist in a given structural phase over a range of compositions. Examples: $\text{Na-}\beta\text{-Al}_2\text{O}_3$, Li_3N , $\text{Li}_2\text{Ti}_3\text{O}_7$, NASICON, $\text{Li}^+\text{-NASICON}$ etc.

Fig. 1.3 shows the ionic conductivities of various fast ionic solids as a function of temperature. The superionic phase can be clearly distinguished in these materials.

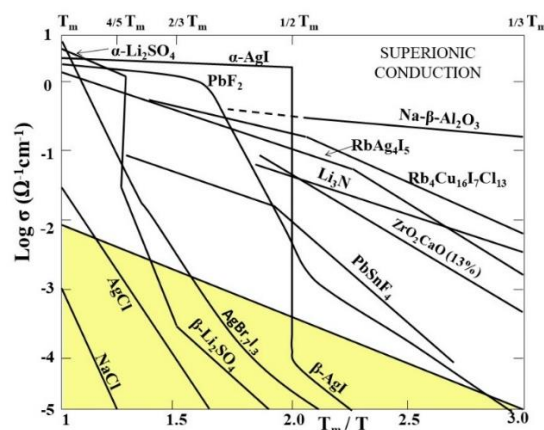


Fig. 1.3 Temperature dependence of electrical conductivity for various fast ionic solids [36].

The further discussion in the chapter is focused on various Li^+ ion based inorganic and organic solid-state electrolytes for solid-state batteries and supercapacitors (SSBs and SSCs, respectively) in view of the nature of work carried out in the thesis.

1.4 Inorganic solid-state electrolytes

Various FICs have got attention in the last four decades. Mainly NASICON (sodium superionic conductor), garnet, perovskite, LISICON, LIPON, and Li^+ ion based glass-ceramics have been considered potential candidates for solid state ionic devices.

1.4.1 NASICONs and NASICON structured Li^+ ion systems

To overcome the restrictions of β -alumina that is its layer structure and migration of the Na^+ ions in only two dimensional conductive planes, Hong, Goodenough et al. proposed a framework structure with proper tunnel size for Na^+ ion migration in three dimensions of $\text{Na}_{1+x}\text{Zr}_2\text{P}_{3-x}\text{Si}_x\text{O}_{12}$ ($0 \leq x \leq 3$), named as NASICON (Sodium (Na) Super (S) Ionic (I) Conductor (CON)). Its composition has been derived from $\text{NaZr}_2\text{P}_3\text{O}_{12}$ by partial replacement of P by Si with excess Na to balance the negatively charged framework to yield the above mentioned general formula [37]. Interestingly, its structure possesses a rhombohedral symmetry with $R\bar{3}c$ space group and consists of a three-dimensional network of PO_4 tetrahedra sharing corners with ZrO_6 octahedra [38]. The structural unit $(\text{Zr}_2\text{P}_3\text{O}_{12})^-$ is formed when each PO_4 tetrahedron shares corners with four of the octahedra, and each ZrO_6 octahedron sharing corners with six tetrahedra. This type of structure therefore has two Na^+ ion

sites, among which Na (1) is located between two ZrO_6 octahedra and an $O_3ZrO_3NaO_3-ZrO_3$ unit. The other Na (2) site is located between the structural strings along c axis formed when the PO_4 tetrahedra links $O_3ZrO_3NaO_3-ZrO_3$ groups which are further linked by PO_4 tetrahedra forming a 3-D skeleton. The crystal structure for all compositions remains the same as discussed above except in the range $1.8 \leq x \leq 2.2$ where a monoclinic transition occurred with space group $C2/c$ [39–42]. The highest room temperature ionic conductivity of $6.7 \times 10^{-4} \Omega^{-1}cm^{-1}$ is achieved particularly for $x = 2$ (i.e., $Na_3Zr_2Si_2PO_{12}$) [43–45].

There have been different preparation routes developed for the synthesis of NASICONs and they led to different compositions with varied conductivity values [46–49]. Also, there have been various reports on enhancing conductivity by using different substitutions of elements. For example, isovalent or heterovalent substitution at the Zr^{4+} site has led to an increase in the bulk conductivity in $Na_3Zr_2Si_2PO_{12}$. The substitution of Zr^{4+} has been done by various di (Mg^{2+} , Ca^{2+} , Sr^{2+}), tri (Sc^{3+} , Ti^{3+} , Cr^{3+} , Y^{3+} , Lu^{3+}), tetra (Ti^{4+} , Zr^{4+} , Si^{4+} , Ge^{4+}) and penta (V^{5+} , Nb^{5+} , Ta^{5+} , As^{5+}) valent ions [48, 50–52]. The Na^+ ions have also been replaced and studied by various alkali and alkaline ions. The substituting Li^+ ion having a relatively small size and high ionic mobility (as compared to Na^+ ion) leads to an analogue structure and is found to be a potential candidate for energy storage devices [53–54].

On replacing the Na^+ ion in the structure $Na_3Zr_2Si_2PO_{12}$ with Li^+ ion, the conductivity decreased by three orders of magnitude, thus ruling out the possibility of $Li_3Zr_2Si_2PO_{12}$ as a good ionic conductor [54]. However, another lithium analogue of NASICON, $LiM_2(PO_4)_3$ ($M = Zr, Sn, Hf, Ti$) got attention and was thoroughly investigated due to its high bulk (in-grain) conductivity [55].

Interestingly, $LiM_2(PO_4)_3$ consists of a network of three-dimensional pathways for Li^+ ions with a skeleton of vertex sharing PO_4 tetrahedra and MO_6 octahedra. These NASICON structured Li^+ ion conductors are abbreviated as Li^+ -NASICON. They have been reported with different crystal structures such as orthorhombic, monoclinic, and triclinic (rarely) depending up on their synthesis conditions, their compositions, and temperature [56]. There are mainly two sites for Li^+ ions in these NASICON structures, namely the M1 site which is coordinated by six oxygen atoms between two MO_6 octahedra units along the c -axis. The M2 site lies between two M1 sites and each M1 site is concurrently surrounded by six M2 sites. Among these Li^+ -NASICON compounds, $LiTi_2(PO_4)_3$ (LTP) is one of the promising Li^+ ion conductor, which

exhibits phenomenally high bulk conductivity of the order of $\sim 10^{-4} \Omega^{-1}\text{cm}^{-1}$, due to its unique structure [57-58]. This makes it a promising candidate for device application. However, high grain boundary impedance (GBI) causes a drop in conductivity to $\sim 10^{-6} - 10^{-7} \Omega^{-1}\text{cm}^{-1}$. Many groups have reported different substitutions in LTP to enhance conductivity. Partial substitution by larger trivalent cations like Sc^{3+} , Ga^{3+} , In^{3+} resulted in enhanced Li^+ ion conduction through the modification of bottlenecks in the structure of Li^+ -NASICON [58–60]. Aono et al. added smaller trivalent cation Al^{3+} and it led Li^+ ions to occupy more sites with the formula $\text{Li}_{1+x}\text{M}_x\text{M}_{2-x}(\text{PO}_4)_3$ [61]. These newly occupied sites were identified as M3 sites which are formed by splitting of M2 sites into two positions [62-63]. Figure 1.4 shows the structure for $\text{Li}_{1.5}\text{Al}_{0.5}\text{Ti}_{1.5}(\text{PO}_4)_3$. Among these Li^+ -NASICON ionic conductors, the Al^{3+} substituted LTP compound i.e., $\text{Li}_{1+x}\text{Al}_x\text{Ti}_{2-x}(\text{PO}_4)_3$ (LATP) is mostly investigated because it exhibits a very high bulk ionic conductivity of the order of $10^{-3} \Omega^{-1}\text{cm}^{-1}$ for $x = 0.3$, attributed to a large concentration of charge carriers and low activation energy [61].

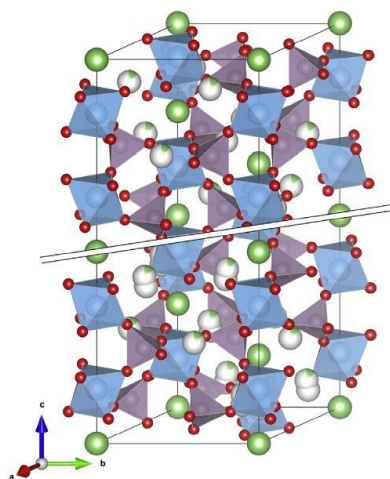


Fig. 1.4 Rhombohedral structure of Li^+ NASICON, $\text{Li}_{1.5}\text{Al}_{0.5}\text{Ti}_{1.5}(\text{PO}_4)_3$. The oxygen at red and blue octahedral sites represents $(\text{Al}/\text{Ti})\text{O}_6$, while the one at purple tetrahedral sites shows PO_4 sites. The Li^+ ions at M1 sites are shown in green colour with Wyckoff position 6b. Additional Li^+ ions in the top half occupy the M2 site in the 18e position while the bottom half are at the M3 site at the 36f position [56].

There have been other modified LTP compounds as well, which show high ionic conductivity. These are obtained through the substitution of Ge, Cr, Ga, Ce for Ti in the LTP, with conductivity in the range of 10^{-3} - $10^{-4} \Omega^{-1}\text{cm}^{-1}$. The electrical

conductivity with compositions has been given in Table 1.2 for various Li⁺-NASICONs that have been developed.

Table 1.2 Various Li⁺-NASICONs at room temperature

S. No.	Composition	Total Conductivity ($\Omega^{-1}\text{cm}^{-1}$)	Total E_{σ} (eV)	References
1.	$\text{LiTi}_2(\text{PO}_4)_3$	$\sim 10^{-6}-10^{-7}$	0.47	[61, 64-65]
2.	$\text{LiZr}_2(\text{PO}_4)_3$	3.3×10^{-6}	0.79	[59]
3.	$\text{LiGe}_2(\text{PO}_4)_3$	1.23×10^{-8}	0.78	[66]
4.	$\text{LiZr}_{0.2}\text{Ti}_{1.8}(\text{PO}_4)_3$	8.5×10^{-8}	0.29	[59]
5.	$\text{Li}_{1.3}\text{Al}_{0.3}\text{Ti}_{1.7}(\text{PO}_4)_3$	$\sim 10^{-3}$	0.21	[61]
6.	$\text{Li}_{1.3}\text{In}_{0.3}\text{Ti}_{1.7}(\text{PO}_4)_3$	4×10^{-4}	0.38	[38]
7.	$\text{Li}_{1+x}\text{Ga}_x\text{Ti}_{2-x}(\text{PO}_4)_3$	2.1×10^{-5}	0.31	[67]
8.	$\text{Li}_{1.5}\text{Al}_{0.5}\text{Ge}_{1.5}(\text{PO}_4)_3$	$\sim 10^{-4}$	0.41	[68, 69]
9.	$\text{Li}_{1.4}\text{Al}_{0.4}\text{Ge}_{0.2}\text{Ti}_{1.4}(\text{PO}_4)_3$	1.53×10^{-3}	0.29	[70]
10.	$\text{Li}_{1.3}\text{Al}_{0.3}\text{Ti}_{1.7}(\text{PO}_4)_3$	$\sim 1 \times 10^{-3}$	0.23	[71]
11.	$\text{Li}_{1.3}\text{Eu}_{0.3}\text{Ti}_{1.7}(\text{PO}_4)_3$	$\sim 6 \times 10^{-5}$	0.32	[72]
12.	$\text{Li}_{1.1}\text{Fe}_{0.1}\text{Hf}_{1.9}(\text{PO}_4)_3$	$\sim 1 \times 10^{-3}$	0.42	[73]

Grain boundaries, which are present in polycrystalline materials, have a significant impact on the transport of charge and mass. These were first discovered in ceramic materials by Burggraf et al. in the 1980s [74]. Fleig and Maier introduced the Brick Layer Model as a means of comprehending the electrical transport mechanism occurring in both the bulk and grain boundaries of polycrystalline materials [75]. This model considers a polycrystalline material as a collection of grains that have a uniform and finite size and a cubic shape and solid-state electrolyte is considered to have the same collection [76]. Fig. 1.5 shows the Brick layer model for a solid-state electrolyte.

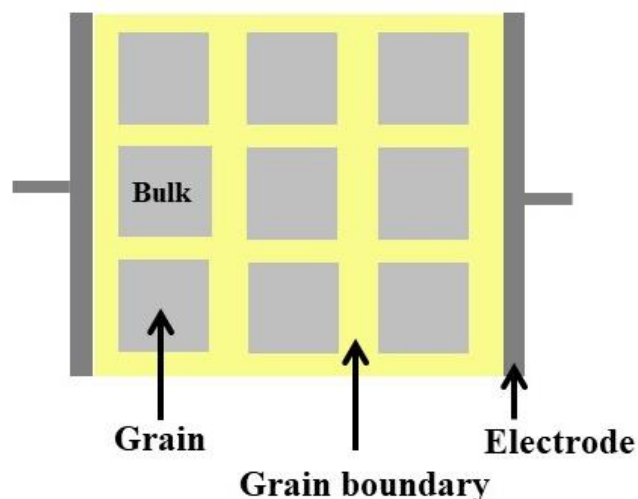


Fig. 1.5 A schematic diagram based on the Brick layer model showing grains and grain boundaries in a solid-state electrolyte placed between two symmetric electrodes

1.4.2 Garnets

Garnet-type Li^+ -ion conductors have gained significant attention in recent years as solid-state electrolytes for lithium-ion batteries (LIBs). This interest was sparked by the first report by Thangadurai et al., which demonstrated the potential of garnet-type materials as a solid-state electrolyte for LIBs [77-78]. Since then, researchers have been working to improve the performance of these materials in terms of their ionic conductivity, electrochemical stability, and compatibility with electrode materials. Garnet-type Li^+ -ion conductors are considered promising candidates for the next generation of solid-state electrolytes for LIBs due to their high Li^+ -ion conductivity, excellent chemical stability, and compatibility with various cathode and anode materials [7, 79–82].

Garnets are a group of orthosilicates having a general formula of $\text{A}_3^{\text{II}}\text{B}_2^{\text{III}}(\text{SiO}_4)_3$ ($\text{A} = \text{Ca, Mg}$ and $\text{B} = \text{Cr, Al, Fe}$). A, B, Si cations respectively occupy the eight, six, and four coordination sites, which crystallize in cubic structure [78, 83]. Li-containing garnets, such as $\text{Li}_x\text{M}_2\text{M}'_3\text{O}_{12}$, are derived from the structural prototype $\text{Ca}_3\text{Al}_2\text{Si}_3\text{O}_{12}$ through a substitution process. Two octahedral AlO_6 , three antiprismatic CaO_8 , and three tetrahedral SiO_4 polyhedra form each unit formula of $[\text{Ca}_3][\text{Al}_2](\text{Si}_3)\text{O}_{12}$. Li analogous of this garnet type structure is $\text{Li}_3\text{La}_3\text{Te}_2\text{O}_{12}$ in which Li replaces the tetrahedral Si^{4+} which however exhibits poor conductivity [84]. This led to the development of Li-stuffed garnet compositions which can give higher conductivity values.

These garnet type electrolytes can be categorised into four different subtypes, viz. Li_3 , Li_5 , Li_6 , and Li_7 . In Li containing garnets, it is observed that their ionic conductivity increases almost exponentially with Li content. In order to study the relationship between Li site occupation and Li^+ -ion conductivity, O'Callaghan et al. developed garnet-type $\text{Li}_3\text{Ln}_3\text{Te}_2\text{O}_{12}$ ($\text{Ln}=\text{Y, Pr, Nd, Sm, Lu}$) [85]. In $\text{Li}_3\text{Ln}_3\text{Te}_2\text{O}_{12}$, Li^+ ions are located exclusively at tetrahedral sites. The low ionic conductivity with a high activation energy in these compounds exhibited that Li^+ ions at tetrahedral positions are less mobile. Then partial substitution of the trivalent La^{3+} with divalent ions in $\text{Li}_5\text{La}_3\text{M}_2\text{O}_{12}$ gave Li_6 phase which can be represented as $\text{Li}_6\text{ALa}_2\text{M}_2\text{O}_{12}$ ($\text{A} = \text{Mg, Ca, Sr, Ba}$, and $\text{M} = \text{Nb, Ta}$) [86]. In 2007, Murugan et al. synthesized cubic-

structured $\text{Li}_7\text{La}_3\text{Zr}_2\text{O}_{12}$ which exhibited the highest conductivity of $3 \times 10^{-4} \Omega^{-1}\text{cm}^{-1}$ with the lowest activation energy of 0.3 eV for a garnet structure material [87]. This Li_7 phase has been obtained by replacing M with Zr in $\text{Li}_5\text{La}_3\text{M}_2\text{O}_{12}$ along with excess Li^+ stuffing for charge balancing. Various chemical compositions reported by different doping in a garnet type structure are shown in Table 1.3.

Table 1.3 Various Li^+ ion garnets

S. No.	Composition	Total Conductivity ($\Omega^{-1}\text{cm}^{-1}$)	Total E_σ (eV)	References
1.	$\text{Li}_3\text{Nd}_3\text{Te}_2\text{O}_{12}$	1×10^{-5} (600 °C/air)	1.22	[85]
2.	$\text{Li}_{3.05}\text{Nd}_3\text{Te}_{1.95}\text{Sb}_{0.05}\text{O}_{12}$	3×10^{-5} (400 °C/air)	0.67	[84]
3.	$\text{Li}_{5.5}\text{BaLa}_2\text{Ta}_2\text{O}_{11.75}$	3.55×10^{-5} (50 °C/air)	0.47	[88]
4.	$\text{Li}_5\text{La}_3\text{Nb}_2\text{O}_{12}$	1×10^{-5} (22 °C/air)	0.43	[89]
5.	$\text{Li}_5\text{La}_3\text{Ta}_2\text{O}_{12}$	1.54×10^{-6} (25 °C/air)	0.57	[90]
6.	$\text{Li}_5\text{La}_3\text{Nb}_{1.95}\text{Y}_{0.05}\text{O}_{12}$	1.34×10^{-5} (23 °C/air)	0.45	[91]
7.	$\text{Li}_6\text{BaLa}_2\text{Nb}_2\text{O}_{12}$	6×10^{-6} (22 °C/air)	0.44	[92]
8.	$\text{Li}_6\text{La}_3\text{SnSbO}_{12}$	2.2×10^{-5} (20 °C/air)	0.50	[93]
9.	$\text{Li}_{6.5}\text{La}_3\text{Zr}_{1.75}\text{Te}_{0.25}\text{O}_{12}$	1.02×10^{-3} (30 °C/air)	0.38	[94]
10.	$\text{Li}_7\text{La}_3\text{Zr}_2\text{O}_{12}$	2.85×10^{-6} (25 °C/air)	0.36	[95]
11.	$\text{Li}_7\text{La}_3\text{Hf}_2\text{O}_{13}$	2.4×10^{-4} (23 °C/air)	0.29	[96]
12.	$\text{Li}_7\text{La}_3\text{Ta}_2\text{O}_{13}$	5.0×10^{-6} (40 °C/air)	0.55	[97]
13.	$\text{Li}_7\text{Nd}_3\text{Zr}_2\text{O}_{12}$	4.9×10^{-7} (100 °C/air)	0.66	[98]

The $\text{Li}_7\text{La}_3\text{Zr}_2\text{O}_{12}$ (LLZO) garnet exists in two stable phases depending on the sintering conditions. One of the phases is a tetragonal form with $I41/acd$ space group and it contains ordered lithium-ion distribution. The second phase is a cubic form with space group $Ia\bar{3}d$, and it contains disordered lithium-ion distribution. As the sintering temperature increases LLZO changes its phase from tetragonal to cubic [87]. The conductivity of the cubic phase has been found to be higher than the tetragonal phase by almost two orders of magnitude. LLZO and the Al doped LLZO (LALZO) have been extensively used in practical applications in devices due to their high conductivity and other features like high voltage window [99]. The structures for tetragonal and cubic LLZO are shown in Fig. 1.6.

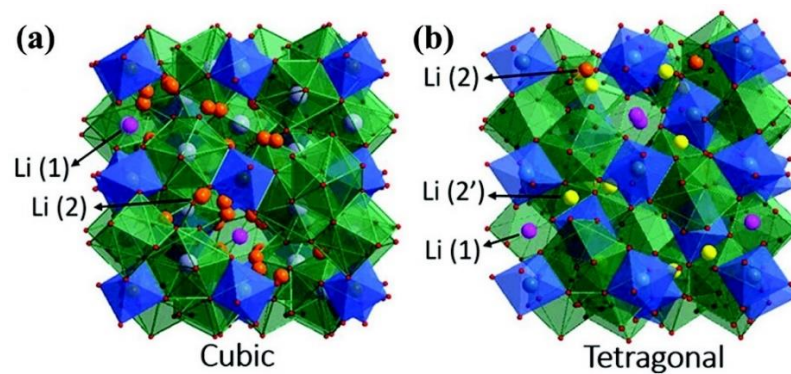


Fig. 1.6 Crystal structures of $\text{Li}_7\text{La}_3\text{Zr}_2\text{O}_{12}$ with (a) cubic and (b) tetragonal phases [100].

Different preparation routes for the synthesis of NASICONs and garnets

1. Solid-state reaction route: This method involves the mixing and grinding of stoichiometric amounts of metal oxides, carbonates, or hydroxides followed by high-temperature sintering to obtain the desired phase. This method is simple and low-cost, but it may result in large particle sizes, poor homogeneity, and undesired secondary phase. This method requires high temperature for sintering which also limits its application [101–104].
2. Sol-gel technique: This method involves the hydrolysis and condensation of metal alkoxides or nitrates in a solvent, followed by drying and calcination to obtain the desired phase. This method can produce homogeneous and fine powders with good crystallinity and purity. It requires relatively low sintering temperatures as compared to the solid-state reaction method [105-106].
3. Hydrothermal synthesis: In this method the dissolution and precipitation of metal salts or oxides in a high-pressure and high-temperature aqueous solution, followed by filtration and drying to obtain the desired phase. This method can produce fine and uniform powders with high purity and crystallinity, but it requires special equipment and long reaction times [107–109].
5. Microwave-assisted synthesis: In this technique microwave electromagnetic radiation is used to heat up and activate the reactants or solvents in a chemical reaction, resulting in a faster and more efficient synthesis of ceramics. This method has been used recently in the preparation of garnets and it reduces the sintering time, however, it requires special furnaces that can sustain high temperatures [104, 110].

4. Electrospinning method: This technique is used to produce ultrafine fibers from various ceramic materials by applying a high voltage to a solution or melt and collecting the fibers on a conductive substrate. This can produce nanofibers with high surface area, and porosity which can enhance the conductivity and mechanical properties [111-112].

Some other techniques include spray pyrolysis, co-precipitation method, solid-state diffusion method, etc. The choice of method also depends on factors such as the desired purity, crystal size, morphology, and cost. However, the sol-gel method has been frequently used for the preparation of NASICONs and garnets due to its unique properties [104-110].

1.4.3 Perovskites

Perovskite-type materials have a general formula of (ABO_3) , where A and B are six and twelve oxygen-coordinated cation sites. A-site can be occupied with cations having large ionic radius such as Na^+ , K^+ , Ca^{2+} , La^{3+} , etc, and B-site can be occupied by small ionic radius cations such as Sc^{3+} , Al^{3+} , Ga^{3+} , Ti^{4+} , etc. The perovskite-type Li^+ -ion solid-state electrolytes that have been developed in recent years include $Li_{3x}La_{2/3-x}TiO_3$ which exhibits a tetragonal structure and $(Li, Sr)(B, B')O_3$ ($B = Zr, Hf, Ga, \text{etc.}$, $B' = Nb, Ta, \text{etc.}$) that exhibits cubic structure [113-114]. There have been many advantages of these electrolytes including simple crystal structure, high bulk Li^+ -ion conductivity, better chemical stability against Li, etc. The crystal structures of the cubic and tetragonal perovskite materials are shown in Fig. 1.7.

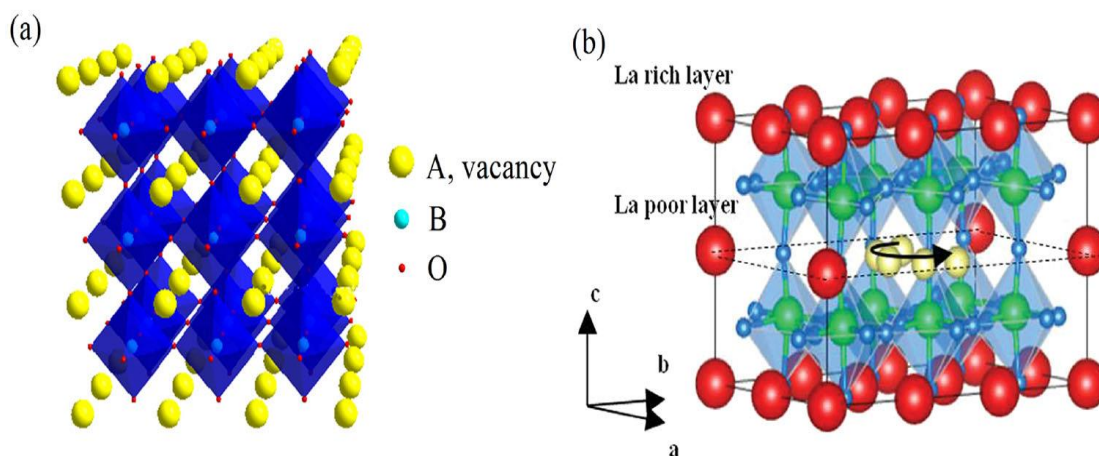


Fig. 1.7 Crystal structures (a) cubic and (b) tetragonal perovskite [115].

To improve the ionic conductivity and stability of the perovskites different dopants have been introduced. Also, some other strategies have been used like increasing Li^+ ion concentration, increasing the concentration of A-site vacancy, and expanding the size of lithium-ion transport channels [115]. Different reported perovskite-type Li^+ -ion solid-state electrolytes have been shown in Table 1.4.

Table 1.4 Various Li^+ ion perovskites at room temperature

S. No.	Composition	Total Conductivity ($\Omega^{-1}\text{cm}^{-1}$)	Total E_{σ} (eV)	References
1.	$\text{Li}_{2/7}\text{La}_{4/7}\text{TiO}_3$	4.01×10^{-4}	0.3	[116]
2.	$\text{Li}_{0.35}\text{La}_{0.557}\text{TiO}_3$	9.55×10^{-5}	0.01	[117]
3.	$\text{La}_{0.56}\text{Li}_{0.36}\text{Ti}_{0.995}\text{Al}_{0.005}\text{O}_3$	1.1×10^{-3}	0.28	[118]
4.	$\text{Li}_{0.33}\text{La}_{0.46}\text{Y}_{0.1}\text{TiO}_3$	8.03×10^{-5}	-	[119]
5.	$\text{Li}_{0.43}\text{La}_{0.56}\text{Ti}_{0.95}\text{Ge}_{0.05}\text{O}_3$	1.2×10^{-5}	-	[120]
6.	$\text{Li}_{3/8}\text{Sr}_{7/16}\text{Zr}_{1/4}\text{Nb}_{3/4}\text{O}_3$	2.0×10^{-5}	0.26	[121]
7.	$\text{LiSr}_{1.65}\text{Ti}_{1.3}\text{Ta}_{1.7}\text{O}_9$	4.9×10^{-5}	0.35	[122]
8.	$\text{Li}_{3/8}\text{Sr}_{7/16}\text{Hf}_{1/4}\text{Ta}_{3/4}\text{O}_3$	3.8×10^{-4}	0.36	[123]

1.4.4 LISICON-type

The LISICON (lithium super ionic conductor) type materials include Li_4SiO_4 and $\gamma\text{-Li}_3\text{PO}_4$. They consist of XO^{4-} ($\text{X} = \text{Al}, \text{Si}, \text{S}, \text{Ge}, \text{etc.}$) based tetrahedral units and Li-O polyhedral units. H. Hong et al. discovered the first LISICON-type electrolyte with the general formula as $\text{Li}_{16-2x}\text{D}_x(\text{TO}_4)_4$ ($\text{D} = \text{Mg}^{2+}, \text{Zn}^{2+}$, and $\text{T} = \text{Si}^{4+}, \text{Ge}^{4+}$) [124]. LISICON-type electrolytes exhibit ionic conductivity around $10^{-5} \Omega^{-1}\text{cm}^{-1}$, which is in the lower range of oxide solid-state electrolytes. However, substitution led to an increase in the lattice volume per Li atom within a given structure which enhanced the conductivity and decreased the activation energy. The substitution of P^{5+} by Si^{4+} in $\gamma\text{-Li}_3\text{PO}_4$ gave a novel series of compositions [125]. Tachez et al. found a new sulfide electrolyte Li_3PS_4 [126]. In 2011, Kanno et al. replaced O^{2-} with S^{2-} to create a thio-LISICON-type SSE with the composition $\text{Li}_{10}\text{GeP}_2\text{S}_{12}$ (LGPS). $\text{Li}_{14}\text{Zn}(\text{GeO}_4)_4$ composition gave high ionic conductivity of $1.3 \times 10^{-3} \Omega^{-1}\text{cm}^{-1}$ at 300°C [127]. Other LISICON-type electrolytes with different compositions include $\text{Li}_{3.4}\text{Si}_{0.4}\text{P}_{0.6}\text{S}_4$, $\text{Li}_{3.6}\text{Si}_{0.5}\text{P}_{0.5}\text{O}_4$, $\text{Li}_{3.25}\text{Ge}_{0.25}\text{P}_{0.75}\text{S}_4$, etc. [128]. These materials show high stability in moist air and can be easily synthesized and handled.

1.4.5 Li⁺ ion-based glass ceramics

Glasses are amorphous solid materials, also referred to as super cooled liquids. In a glass matrix, there is a large free volume essentially due to this frozen ‘liquid-like’ structure [129]. If free ions are available, the free volume in the glass facilitates electrical transport. Different types of ion conducting glasses like Li⁺, Na⁺, Ag⁺ have been developed and studied as solid-state electrolytes for energy storage device applications [130]. In particular, Li⁺ ion-based glasses have received much attention among all due to the ion’s small size. Otto reported the first highly conducting Li⁺ ion borate glass with a conductivity value approaching $\sim 10^{-1} \Omega^{-1}\text{cm}^{-1}$ at 350 °C [131]. Extensive work has been done on Li⁺ ion sulphide and oxide glasses in the last three decades both in theory and applications [132].

Malguni and Robert in 1980 developed the first sulfide based LiI-Li₂S-P₂S₅ glassy system [133]. The glass composition 0.37Li₂S-0.18P₂S₅-0.45LiI exhibited conductivity of $10^{-3} \Omega^{-1}\text{cm}^{-1}$ at 20 °C [134]. Besides this, Li⁺ ion-based oxide glasses have also been widely studied as they are thermally more stable. Ionic conductivity in these glasses could be increased substantially by salt (Li₂SO₄, LiCl, etc.) addition [135]. Alternatively, the use of mixed glass former (P₂O₅-B₂O₃) was found to be effective in enhancing conductivity by increasing the free volume [136]. Table 1.5 shows some important Li⁺ ion based sulfide and oxide glasses developed in the past.

Thermally stable partially crystallized glasses i.e., glass-ceramic electrolytes have also been developed by crystallization of precursor glasses and by direct addition of glass into ceramics. Sulfide based glass ceramics such as Li₂S-P₂S₅ exhibited conductivity of the order of $10^{-3} \Omega^{-1}\text{cm}^{-1}$ [143].

Table 1.5 Ionic conductivities of various Li⁺ ion based sulfide and oxide glasses

S. No.	Li ⁺ Ion Oxide Glasses	Conductivity ($\Omega^{-1}\text{cm}^{-1}$)	Total E _σ (eV)	References
1.	Li ₂ S-P ₂ S ₅ -LiI	$\sim 10^{-3}$ (25 °C)	0.29	[134]
2.	67Li ₂ S-10P ₂ S ₅ -23B ₂ S ₃	$\sim 10^{-4}$ (25 °C)	0.40	[137]
3.	70Li ₂ S-30P ₂ S ₅	$\sim 10^{-5}$ (25 °C)	0.40	[138]
4.	63Li ₂ S-36SiS ₂ -1Li ₂ SO ₄	$\sim 10^{-3}$ (25 °C)	0.30	[139]
5.	56Li ₂ O-8LiF-36B ₂ O ₃	$\sim 6 \times 10^{-4}$ (300 °C)	0.70	[140]
6.	Li ₂ O-TiO ₂ -P ₂ O ₅	$\sim 10^{-2}$ - 10^{-5} (127 °C)	0.07	[141]
7.	0.3Li ₂ O-0.275B ₂ O ₃ -0.475V ₂ O ₅	$\sim 7.4 \times 10^{-5}$ (RT)	0.22	[142]

The Li⁺-NASICON based glass-ceramics have been extensively studied owing to their amorphous and partially crystalline phase which gives it characteristics of both glass and ceramic. Fu et al. synthesized Li₂O-Al₂O₃-TiO₂-P₂O₅ with frozen NASICON crystallites by thermal cycling/annealing the glass above its crystallization temperature [144]. Kwatek et al. studied the effect of the addition of Li_{2.9}B_{0.9}S_{0.1}O_{3.1} (LBSO) and Li₃BO₃ glass in LTP [145-146]. The addition of these glasses makes the composite denser and in turn, enhances the conductivity. In garnets, the addition of these additives helps in reducing sintering time and temperature [147]. A list of various glass-ceramic composites is shown in table 1.6.

Table 1.6 Li⁺ ion based glass-ceramic composites having various precipitated FICs.

S. No.	Glass-Ceramics	Conductivity (Ω ⁻¹ cm ⁻¹ at 300 K)	Total E _σ (eV)	References
1.	(1+x)Li ₂ O-6.6CaO-(4-2x)TiO ₂ -xAl ₂ O ₃ -5.2P ₂ O ₅	5×10 ⁻⁵	0.30	[148]
2.	Li ₂ O-Al ₂ O ₃ -TiO ₂ -P ₂ O ₅	6.53×10 ⁻⁴	0.28	[149]
3.	Li _{1.5} Al _{0.5} Ge _{1.5} (PO ₄) ₃ - 0.05Li ₂ O	7.2×10 ⁻⁴	0.25	[150]
4.	Li _{1+x+y} Ti _{2-x} Al _x P _{3-y} Si _y O ₁₂	1.8×10 ⁻⁴	0.40	[151]
5.	LiTi ₂ (PO ₄) ₃ -0.3 Li _{2.9} B _{0.9} S _{0.1} O _{3.1}	1.79×10 ⁻⁴	0.36	[145]
6.	LiTi ₂ (PO ₄) ₃ -0.3Li ₃ BO ₃	1.43×10 ⁻⁴	0.37	[146]

So, from the above discussion, it can be concluded that different types of inorganic solid-state electrolytes and glass-ceramics have been explored extensively in the last few decades. Different ways have been adopted to enhance the conductivity and stability of these solid systems, still, they could not be used directly in commercial devices due to certain reasons and constraints. These are assessed and discussed below.

1.4.6 Shortcomings of Li⁺ ion-based inorganic solid and glass-ceramic electrolytes

Solid-state electrolytes consisting of inorganic crystalline solids and glass-ceramics have overcome many limitations of liquid electrolytes such as flammability, toxicity, miniaturization, leakage, etc. However, they also face some limitations for example:

-
- These solid-state electrolytes have high grain boundary impedance. Ionic conductivity of the orders of magnitude lower than liquid electrolytes especially at room temperature, reduces the power output and thus the performance of the devices. Despite various strategies being adopted such as doping, nano structuring, compositing, etc. the total conductivity still has not been achieved to a satisfactory level [152-153]. Solid-state electrolytes have poor interfacial stability with metal electrodes, especially with lithium anodes. This can cause unwanted reactions and side effects such as dendrite formation, interfacial resistance, and electrolyte decomposition. These problems lead to issues such as short circuits, capacity loss, and safety hazards [154].
 - Solid ionic electrolytes have high mechanical stiffness and brittleness compared to liquid electrolytes, due to which they are more prone to cracks and fractures under mechanical stress or thermal expansion. These defects can cause loss of contact and electrical isolation between the electrodes and the electrolyte, which reduces the performance and reliability of the devices [152].
 - Solid-state electrolytes have complex fabrication processes compared to liquid electrolytes. Also, their scaling for mass production is, again, challenging. The fabrication processes often involve high temperatures, high pressure, vacuum, or special equipment that increase energy consumption and environmental impact [155-156].
 - Solid electrolytes, particularly glasses/glass-ceramics cannot be molded to desired shapes. They lose their properties when converted to powders of small grain size via grinding [153,157].

These limitations and drawbacks are actively being addressed through research and development efforts in these materials.

In parallel, there has been significant work on soft solid-state electrolyte materials realizing the limitations of solid ionic compounds. Organic polymeric electrolytes along with their composites with salts, glasses, and ceramics have been widely studied. Gel polymer electrolytes and ionogels have also been explored well. These soft ionic systems along with hybrid (solid-liquid composites) are discussed below.

1.5 Organic solid-state electrolytes

These electrolytes consist of mainly polymer and their composites, solid and gel polymer electrolytes. Unlike crystalline inorganic electrolytes, which are brittle and rigid, these organic soft electrolyte materials are light, flexible, and scalable in nature. They have also been studied due to their good interfacial stability as compared to inorganic electrolytes.

1.5.1 Polymers and their composites

The solid polymer electrolytes (SPEs) generally consist of a polymer matrix and an ionic salt. The first ion conducting SPE with alkali metal salts was reported by Fenton et al. in 1973 and then Armand et al. further explored these materials [22]. Different forms of Li^+ ion-based polymer complexes have been developed and studied for electrolytic applications in both batteries and supercapacitors. Various types of host polymer matrix such as polyethylene oxide (PEO), polyvinylidene fluoride (PVDF), polyacrylonitrile (PAN), etc. have been used and these play an important role in the properties of SPEs. Among these polymer electrolytes, PEO has been widely studied as it has the ability to solvate a variety of salts [158]. Some of the commonly used salts are LiPF_6 , LiClO_4 , LiBF_4 , LiCF_3SO_3 , etc. Mobile cation-PEO chain coupling is considered a prominent mechanism of ionic transport in these systems. Inadequate ionic conductivity at room temperature has been again an issue in these ‘liquid free’ electrolytes. Different methods have been employed to enhance electrical transport. For example, increasing salt concentration up to a certain limit has been a simple approach to enhance conductivity. Another famous approach to enhance ionic conductivity is incorporating inorganic fillers into solid polymer electrolytes to obtain composite solid polymer electrolytes (CSPEs). This technique not only enhances conductivity substantially but also improves mechanical strength and electrochemical stability. Inorganic fillers can be classified into two types inactive and active fillers. Inactive fillers include inert ceramics, ferroelectric ceramics, oxygen-ion conducting ceramics, and clays with small crystallite size. These cannot directly offer transport pathways for Li^+ ions in electrolytes but can facilitate Li^+ ion transport via amorphization of polymers [159]. On the other hand, active fillers include fast Li^+ ion conductors such as Li_3N , $\text{Li}_{7-x}\text{La}_3\text{Zr}_{2-x}\text{Ta}_x\text{O}_{12}$, $\text{Li}_{1.6}\text{Al}_{0.6}\text{Ge}_{0.8}(\text{PO}_4)_3$, $\text{Li}_{3-2x}(\text{Al}_{1-x}\text{Ti}_x)_2(\text{PO}_4)_3$, etc. [62, 124, 159]. These can exhibit high ionic conductivity and Li^+ ion transference number. Inorganic fillers with different morphologies such as

nanoparticles, nanowires, nanofibers, etc. have also been explored. Some of the reported polymer-salt composites and polymer-filler composites are given in table 1.7.

Table 1.7 Various polymer-salt complexes and polymer-filler composites

S. No.	Composition	Conductivity ($\Omega^{-1}\text{cm}^{-1}$ at 300 K)	Total E_{σ} (eV)	References
1.	PEO ₁₂ -LiI	$\sim 10^{-6}$	1.98	[160]
2.	PEO-15wt% LiCF ₃ SO ₃	1.0×10^{-6}	0.27	[161]
3.	90PEO-10LiAsF ₆	1.43×10^{-4}	0.32	[162]
4.	PEO-15wt% LiPF ₆	1.82×10^{-5}	0.29	[163]
5.	P(EO) ₁₆ -LiClO ₄ -10 wt% SiO ₂	$10^{-5.5}$	0.19	[164]
6.	P(EO) ₈ -LiClO ₄ -10 wt% Al ₂ O ₃	10^{-5}	0.33	[165]
7.	PEO-LiClO ₄ -10 wt% SiO ₂ nanospheres	$4.4 \times 10^{-5.5}$		[166]
8.	PEO-LiTFSI-Li _{0.3} La _{0.557} TiO ₃	1.8×10^{-4}	0.38	[167]
9.	P(EO) ₁₈ -LiTFSI-1 wt% Li ₁₀ GeP ₂ S ₁₂	1.21×10^{-3}	0.35	[168]
10.	PEO ₁₆ -LiTFSI-Li ₇ La ₃ Zr ₂ O ₁₂	2.3×10^{-4}	0.37	[169]

1.5.2 Gel polymers

Gel polymer electrolytes (GPEs) consist of a polymer matrix which is generally a cross-linked polymer, and a liquid electrolyte. The polymer matrix acts as a framework that immobilizes the liquid electrolyte [170]. GPEs have the advantage of being highly flexible and can be moulded into any shape or form. They can be mainly categorized into four types (i) aqueous gel polymer electrolytes, (ii) organic gel polymer electrolytes, (iii) redox-active gel electrolytes, and (iv) ionic liquid-based gel polymer electrolytes. Aqueous gel polymer electrolyte or hydrogels consists of a host polymer matrix, an electrolytic salt, and a plasticizer. These electrolytes have an issue of narrow operating voltage window which can be overcome by organic gel polymer electrolytes [171]. Many groups have added redox-active species into the electrolyte which undergo oxidation and reduction, thus producing pseudocapacitance. K₃Fe(CN)₆/K₄Fe(CN)₆ redox couple is generally used due to its high stability, low toxicity, and high capacitance [171]. Another class of GPEs includes ionic liquid (IL)

based gel electrolytes which have many advantages over aqueous and organic electrolytes. They are used as plasticizing salts in GPEs which increases the amorphous phase of the gels, improving the ionic conductivity, thermal, mechanical, and chemical properties [172-173]. There have been various reports based on these GPEs which have been tabulated in table 1.8.

Table 1.8 Various gel polymer electrolytes

S. No.	Composition	Conductivity ($\Omega^{-1}\text{cm}^{-1}$ At 300 K)	Total E_{σ} (eV)	References
1.	PVA/H ₃ PO ₄ /H ₂ O	9.6×10^{-4}	0.20	[174]
2.	PVA/H ₃ PO ₄ /PEG/H ₂ O	8.6×10^{-5}	0.25	[175]
3.	PVA/H ₃ PO ₄ /EMIMBF ₄ /H ₂ O	3.3×10^{-4}	0.21	[176]
4.	PEO/LiCF ₃ SO ₃ /Al ₂ O ₃	8.64×10^{-5}	0.15	[161]
5.	PEO/LiTFSI/[BMP][TFSI]	2.5×10^{-5}	0.28	[177]
6.	PEO/LiClO ₄ / BMIMPF ₆	10^{-4}	0.25	[178]

From the above literature review, one finds that different types of soft materials have been developed with relatively higher ionic conductivity. Soft electrolytes improve the interface with the electrodes which was the main concern in ceramic and other inorganic based solid-state electrolytes. Soft electrolytes have also addressed the issue of flexibility and scalability. They are developed in a wide composition range with low flammability and toxicity. However, there are some major issues related to these electrolytes which have been discussed in the section below.

1.5.3 Shortcomings of Li⁺ ion based organic solid-state electrolytes: polymers, gels polymers

- CSPEs themselves have poor ionic conductivity and need the addition of salts or other dopants to enhance their conductivity. The addition of salts or any dopants can be done up to a certain limit only, as it leads to a decrease in mechanical strength [179].
- Liquid free soft electrolytes still suffer from inadequate ionic conductivity problem even after the development of various hybrid composites. Their Interfacial stability with electrodes has not been achieved up to the mark. Some electrolytes have limited stability at high voltages which leads to premature degradation and electrolyte breakdown [7, 180].

- Thermal stability is quite poor in polymer and gel polymer electrolytes. Polymers (particularly PEO) start melting around 60 °C restricting device performance to a certain temperature range. This also leads to the issue of flammability in devices. Also, these devices have poor performance at low temperatures. Some polymers are sensitive to moisture which can lead to reduced conductivity [180-181].

1.6 Ionogel

Ionogels are a type of electrolyte that combines an ionic liquid (IL) with a porous solid matrix. The IL confined (incorporated) solid matrix is used as a solid/quasi-solid electrolyte. They are promising for overcoming the issues related to liquid electrolytes and creating a flexible and mechanically stable device. Depending upon the host material for the entrapment of ILs, ionogels can be classified as organic, inorganic, and hybrids [182]. Chio et al. synthesized ionogel by incorporating 80% IL BMIMTFSI with polymer electrolyte PEO-LiTFSI by hot-press method and obtained a conductivity of $3.2 \times 10^{-4} \Omega^{-1}\text{cm}^{-1}$ [183]. ILs BMIMBF₄, BMIMCF₃SO₃ were also blended with PEO-LiTFSI electrolyte to obtain ionogels [184]. Generally, the ionic conductivity of ionogels used to increase with increasing amount of IL, however, this increase can be only up to a certain limit. So, optimization of IL content as well as salt addition has an important role. Fericola et al. developed PVDF-HFP based ionogel using 80 wt% of LiTFSI+[PP24][TFSI] solution and obtained ionic conductivity of the order of $10^{-4} \Omega^{-1}\text{cm}^{-1}$ [185]. Another PVDF-HFP+LiTf+[EMIM][Tf] ionogel has been synthesized with a conductivity value of $4.5 \times 10^{-3} \Omega^{-1}\text{cm}^{-1}$ [186]. There have been many reports on ionogels which are inorganic materials such as SiO₂ and TiO₂ based and are more thermally stable than organic materials based systems [182].

It is important to stress the fact that the ionogels are not pure solid-state electrolytes. The mobile ions are mostly from IL, and the host solid provides pathways through micropores and mechanical stability. They are in quasi solid form as they contain large amount of ionic liquid that sometimes occupies ~80% or more volume fraction of the matrix. They are thus prone to leakage and possess poor mechanical strength due to large liquid content.

Different types of electrolytes have been discussed so far with their electrical properties and challenges. These electrolytes have either hard ceramic solid-state

electrolyte like NASICONs, garnets, perovskites, glass-ceramics, or soft organic solid-state electrolytes like polymers, gels, or ionogels. Soft electrolyte materials have paved the way to overcome various issues existing in inorganic solid-state electrolytes, however, they themselves have many challenges regarding conductivity, mechanical strength, temperature range, leakage, etc. Various types of hybrid electrolytes have also been developed within these systems which have achieved better conductivity and improvement in other properties.

The above literature also suggests that hybrids are more suitable as electrolytes to achieve excellent performance parameters. Importantly, ionic transport in ionic solids/ceramics can be drastically tailored by adding ionic liquid in a suitable amount to hard ceramics. The idea of creating aqueous/liquid phase regions between the ceramic grains is essentially facilitating a ‘coupling’ so that mobile ions, from the solid state, can perform long range diffusive motion. The next section elaborates these novel hybrid composites developed recently.

1.7 Ionic liquid and fast ionic solids dispersed with ionic liquids

Ionic liquids are molten salts consisting of self-dissociated organic cations and organic/inorganic anions. To call a salt an ionic liquid the melting point of the salt should not be very high (should be around or less than 100 °C). These substances consist of ammonium, phosphonium based cations, saturated heterocyclic cations, etc. and anions can be halides, fluorides, amide anions, etc.

Table 1.9 Properties of Ionic Liquids

Ionic Liquid	Conductivity ($\Omega^{-1}\text{cm}^{-1}$) (at RT)	Viscosity (mPas)	ECS window	Cation ionic radii (nm)	anion ionic radii (nm)
EMIMBF ₄	13×10^{-3}	43	4-6 V	0.310	0.227
BMIMBF ₄	3.1×10^{-3}	110		0.331	0.227
EMIMCF ₃ SO ₃	9.5×10^{-3}	35		0.310	0.270

ILs have high ionic conductivity, negligible vapor pressure, high thermal and chemical stability, wide electrochemical window, and high flame resistance [187].

These properties make them suitable candidates to be used in electrolytes. Ionic liquids have been used in devices since the 1960s either directly as liquid electrolytes in the starting and then later on in the form of ionogels, gel polymers, and other composites [188-189]. Table 1.9 shows properties of few ionic liquids.

Different researchers have reported the enhancement in conductivity by the addition of a small amount of IL in fast ionic systems like ceramics and glasses. As IL is being added in a very small amount so it does not lead to any compromise in the mechanical strength of the resulting solid composites. These composites provide good interfacial contacts along with stability. In most of the systems, ionic liquid stays as a separate phase in the composites occupying the grain boundaries and enhancing the conductivity by reducing impedance and improving interfacial contacts. Hayashi et al. developed these solid composites by dispersion of IL- EMIMBF₄ in the 50Li₂SO₄-50Li₃BO₃ oxide glassy matrix [190]. A maximum conductivity value of $10^{-4} \Omega^{-1}\text{cm}^{-1}$ was achieved by just 10 mol% addition of IL, which was found to be three orders of magnitude higher than that of the pristine glass. In another report, Kwatek et al. synthesized LTP/LATP-IL composites, and a conductivity enhancement of three to four orders of magnitude was reported by the addition of ~10 wt% of BMIMBF₄ [191]. It was emphasized that ionic liquid plays the role of connector between neighboring grains which facilitates the ion transport. Another ionic solid, BCN 18 (Ba₃Ca_{1.18}Nb_{1.82}O_{8.73}) on addition of IL- BMIMBF₄ exhibited a total conductivity of $10^{-5} \Omega^{-1}\text{cm}^{-1}$ which is about seven orders of magnitude higher than that of BCN 18 [192]. It was suggested that the grain boundary effects are eliminated due to the addition of IL. Rathore et al. dispersed 5 wt % of IL- BMIMBF₄ in Li⁺ ion oxide glass 60Li₂SO₄-40(0.5Li₂O-0.5P₂O₅) and obtained a conductivity enhancement by ~2-4 orders of magnitude [189]. They proposed a mechanism according to which Li⁺ ions at the interface of glass-IL or glass-ceramic-IL become more mobile after IL addition which results in a rise in conductivity. The mobile Li⁺ ions move along the grain boundaries in the presence of IL. IL confined silica glasses have been prepared using the sol-gel route giving high ionic conductivity [187]. The garnet-IL based solid-state electrolyte with composition 80%LLZO-20% IL (Py14TFSI) has been developed with ionic conductivity $\sim 0.4 \times 10^{-3} \Omega^{-1}\text{cm}^{-1}$ [193]. It has been proposed that IL addition helps to reduce energy barriers for Li⁺ ion conduction by facilitating Li⁺ ion motion.

1.8 Energy storage: Batteries and Supercapacitors

Batteries and supercapacitors are both devices that can store and deliver electrical energy, but they have different characteristics and applications. Batteries have a higher energy density and breakdown voltage which means they can hold more charge and operate at higher voltages. Supercapacitors on the other hand have a higher power density and lifespan, meaning they can deliver and receive charge faster and longer. Supercapacitors store charge electrically, while batteries store charge chemically. They both can work together as a hybrid system for applications such as electric vehicles. A brief description of batteries and supercapacitors is given below as the thesis deals with the fabrication of such devices using the novel materials synthesized for this work.

Battery is an electrochemical device that can store energy in the form of chemical energy. It translates to electric energy when the battery is connected in a circuit due to the flow of electrons. Primary battery is the non-rechargeable battery whereas secondary battery is rechargeable. Some common rechargeable batteries are lead-acid battery, Nickel-cadmium battery, nickel-metal hydride battery, lithium-ion battery. Lithium-ion battery is successful in the market due to its lightweight, higher energy density, and low self-discharge as compared to other types of battery. It consists of anode (negative electrode), cathode (positive electrode), electrolyte, and separator. While at present the electrolyte in these batteries available in the market consists of generally liquid electrolyte, recently gels and polymer are being used. The separator is a porous material placed between anode and cathode to prevent direct contact and avoid short circuits while allowing the passage of lithium ions. In a complete all solid-state battery, the electrolyte itself acts as a separator. Fig. 1.8 shows the modern Li^+ ion battery.

During discharging a load is connected to the battery, such as an electronic device or an electric vehicle the lithium ions move from the anode back to the cathode through the electrolyte. This movement creates an electron flow through the external circuit, generating an electrical current to power the connected device. Simultaneously, the cathode receives the lithium ions and undergoes a reduction reaction.

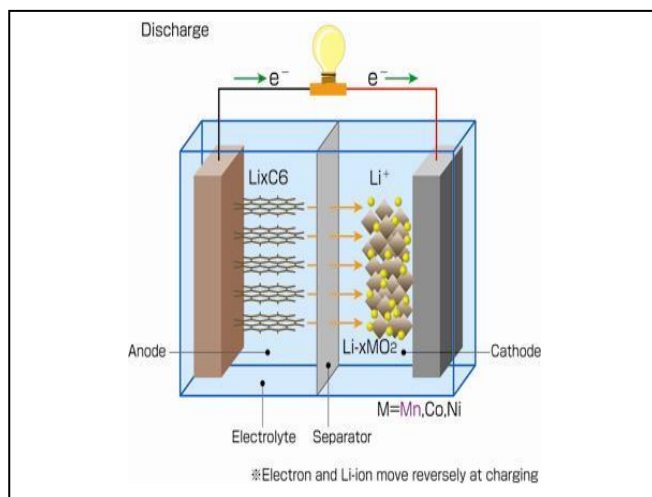


Fig. 1.8 Li⁺ ion battery

During the charging process, a voltage higher than the battery's current voltage is applied across the terminals. This causes lithium ions to move from the cathode to the anode through the electrolyte. The anode, with its layered structure, provides spaces between its carbon layers where the lithium ions can intercalate and be stored.

Supercapacitors, also known as ultracapacitors or electrochemical capacitors, are energy storage devices that store energy through the physical separation of charges. Unlike batteries, they do not rely on chemical reactions to store energy. Instead, supercapacitors use electrostatic double-layer capacitance and/or pseudo-capacitance to store charge at the electrode-electrolyte interface. Supercapacitors have a high power density, which means they can deliver and absorb energy rapidly.

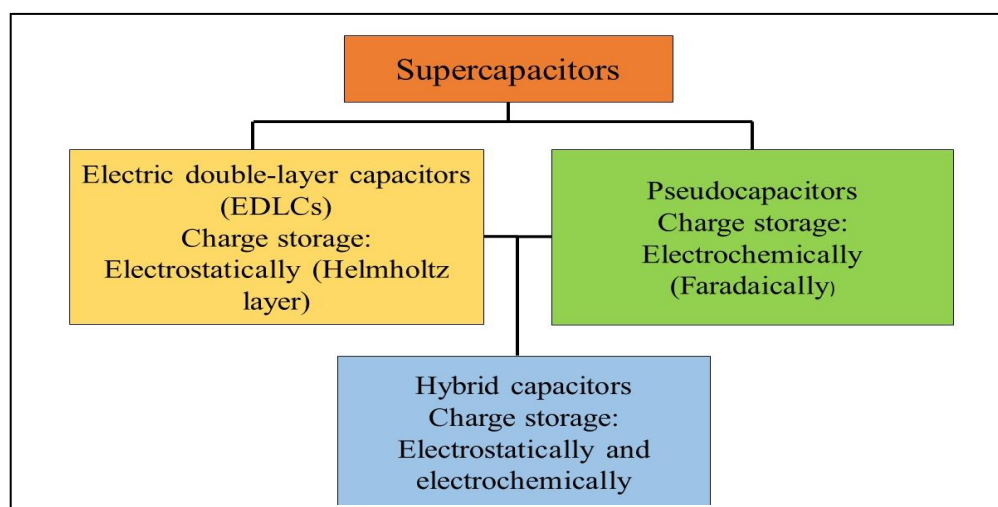


Fig. 1.9. Classification of supercapacitors

They can charge and discharge quickly, making them suitable for applications that require bursts of power or regenerative energy capture, such as hybrid vehicles, electronic devices, and grid energy storage. They can be categorized into different types as shown in Fig. 1.9.

The Stern model is a theoretical model used to describe the structure and behavior of the electric double layer (EDL) that forms at the interface between an electrode and an electrolyte in EDLCs. It is a combination of both the Helmholtz and Gouy-Chapman model (Fig. 1.10). As suggested by this model when a supercapacitor is charged, cations within the electrolyte concentrate near one electrode and anions near another electrode forming EDL which compensates the external charge imbalance as shown in Fig. 1.10 c. During the discharge, electrons travel from the negative electrode to the positive electrode through an external circuit, and simultaneously ions at the interface forming EDL travel back to the electrolyte until the cell is discharged.

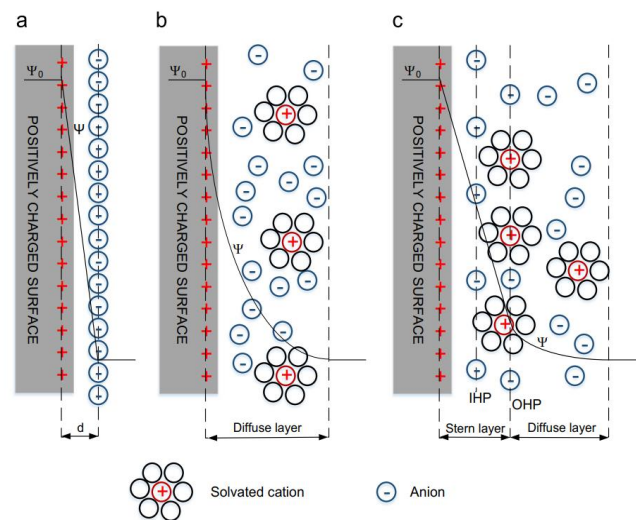


Fig. 1.10. EDL models, (a) Helmholtz model, (b) Gouy-Chapman model, and (c) Stern model [194].

From the above literature survey, it may be concluded that:

- (a) Significant efforts have been dedicated over the past four decades to developing solid-state electrolytes with conductivity comparable to that of liquid electrolytes. Remarkably, Li^+ ion superionic conductors in NASICONs, garnets have achieved conductivity values as high as 10^{-3} - $10^{-4} \text{ } \Omega^{-1}\text{cm}^{-1}$ near room temperature.

-
- (b) Among inorganic fast ionic conductors Li^+ -NASICON and recently garnets too have received much attention due to their high ionic conductivity and have also been widely applied for all solid-state batteries.
 - (c) Polymers, ionogels, and gel polymer electrolytes have also been extensively explored as soft organic electrolyte materials due to their better ionic conductivity and interfacial stability.
 - (d) There has been significant work done on the theoretical understanding, particularly the mechanism of electrical transport, and conductivity-structure correlations.
 - (e) Recently hybrid electrolytes for devices have garnered much importance as they can overcome the shortcomings of both hard and soft fast ionic systems. Composites like “polymer in ceramic” and “ceramic in polymer” have been synthesized to overcome the difficulties in interfacial stability between electrode and electrolyte, to achieve high ionic conductivity, to maintain mechanical strength, etc.
 - (f) There have been a few reports on ceramic-IL based solid-state electrolytes. These electrolytes have been found to be very stable with high ionic conductivity and mechanical strength along with maintaining solid-state nature.

1.9 Gaps in the existing research

Various solid-state electrolytes have been developed in the last few decades which have ionic conductivity comparable to liquid electrolytes. However, there are many other issues related to these solid-state electrolytes which need to be focussed. Applicability of these electrolytes in devices has many challenges that need to be addressed as listed below:

- (i) There have been many solid systems developed but either they are hard ceramics, ionic glasses, or soft electrolytes like polymers, gels, etc. Hard ionic systems suffer from high grain boundary impedance and high interfacial resistance whereas soft systems suffer from poor mechanical strength and narrow temperature range. The conductivity of solid polymer electrolytes (SPEs), Glass-ceramics, and composite SPE is not adequate

for the device applications. Besides, there are limitations in tailoring properties e.g., mechanical strength, thermal stability is often compromised.

- (ii) There is a subtle but significant work on ceramic-ionic liquid based electrolytes. Ionogels suffer mechanical stability. Further, in these, the mobile ions from the host (solid) matrix do not contribute significantly to the conductivity.
- (iii) In the case of novel hybrids in IL-ceramic composites, ionic liquid's presence is found to improve interfacial stability. Various workers have demonstrated a large conductivity enhancement, but no generalized mechanism has been brought out so far. For example, it is still under discussion how the IL helps improve ionic conductivity and which ions participate in ionic conduction. These composites need more studies by exploring different ceramics and ionic liquids. The electrical transport mechanism, information about majority charge carriers, and the conductivity structure correlation in these solid-liquid systems require a better understanding.
- (iv) It is well known that most of the ceramics as well as ILs are generally stable. The stability of their composites in a wide temperature range has not been emphasized so far. Low ($T < 0$ °C, when IL freezes) and high ($T > 100$ °C when IL decomposes) temperature studies of ceramic-ionic liquid systems need more exploration.
- (v) Despite high ionic conductivity comparable to gels, and aqueous solutions, the practical application of these IL-ceramic solid-state systems in batteries and supercapacitors has not yet been explored thoroughly.
- (vi) IL-solid composites in solid-state batteries (SSBs) are less explored. Further, the above review suggests that their use in solid-state supercapacitors (SSCs) has never been explored. For example, NASICONS and garnets have not been used in supercapacitors so far. Solid-state supercapacitors are mostly based on liquids, gels, ionogels, and polymer-based electrolytes.

1.10 Statement of problem and objectives

With the increasing demand for all-solid-state energy storage devices, there has been a great exploration in the field of fast ionic systems for electrolytes. These electrolytes are expected to meet requirements such as high conductivity, leakage proof, good mechanical strength, non-flammability, great interfacial stability, etc. Solid-state electrolytes such as Li^+ -NASICON, and Garnets have attained much attention due to high bulk conductivity. However, grain boundary impedance (GBI) restricts their use, and to overcome this, different types of ceramic-polymer hybrids, ionogels, and gel polymers have been explored. Despite all these research developments, there have been issues regarding ionic conductivity, leakage, flammability, mechanical strength, interfacial stability, etc. However, a solid-liquid hybrid composite can overcome these issues to a large extent. Dispersion of small amounts of ionic liquids in ceramics can lead to a composite having better conductivity with all other desired properties for a solid-state electrolyte. Mechanism understanding and device fabrication of such composites need thorough studies.

So, keeping this in view, the present work focuses on (i) the development of different IL dispersed ceramic composites, (ii) attempts to propose a fundamental model of the mechanism of ionic transport based on experimental evidence, and to study structural, thermal properties, and (iii) to explore the application of these developed electrolytes in all-solid-state batteries and supercapacitors.

Objectives

- (i) Synthesis of ionic liquid dispersed Li^+ -NASICON and garnet hybrid composites.
- (ii) To understand the mechanism of ionic transport by exploring the electrical, structural, and thermal properties of these hybrid composites.
- (iii) Fabrication of solid-state batteries (SSBs)/button cells using these composites as electrolytes, and to assess the device performance.
- (iv) Developing solid-state supercapacitors (SSCs) with these composites as electrolytes in different geometries and assessing the device performance.
- (v) To develop wide temperature stable EDLCs from these IL-ceramic composites.

In order to achieve the above objectives, the following systems have been chosen for investigation:

- (i) IL (EMIMBF₄, EMIMCF₃SO₃, and BMIMBF₄) dispersed in LiTi₂(PO₄)₃ (LTP) and Li_{1.3}Al_{0.3}Ti_{1.7}(PO₄)₃ (LATP) NASICONs.
- (ii) IL (EMIMBF₄, EMIMCF₃SO₃, and BMIMBF₄) dispersed in Li_{6.4}Al_{0.2}La₃Zr₂O₁₂ (LALZO) garnet.

The NASICON and garnets have been synthesized using the sol-gel route. For all the developed systems batteries and supercapacitors have been fabricated. Different geometries of supercapacitors have been explored such as coin cell, laminated, and swagelok assembly. EDLCs with wide temperature window have also been developed with a temperature range of -10 °C - 200 °C.

References

- [1] S. M. Benoy, M. Pandey, D. Bhattacharjya, and B. K. Saikia, "Recent trends in supercapacitor-battery hybrid energy storage devices based on carbon materials," *Journal of Energy Storage*, vol. 52, pp. 104938, 2022, doi: 10.1016/j.est.2022.104938.
- [2] D. Di Lecce, R. Verrelli, and J. Hassoun, "Lithium-ion batteries for sustainable energy storage: Recent advances towards new cell configurations," *Green Chemistry*, vol. 19, pp. 3442–3467, 2017, doi: 10.1039/c7gc01328k.
- [3] D. Deng, "Li-ion batteries: Basics, progress, and challenges," *Energy Science and Engineering*, vol. 3, pp. 385–418, 2015, doi: 10.1002/ese3.95.
- [4] C. Bubulinca, N. E. Kazantseva, V. Pechancova, N. Joseph, H. Fei, M. Venher, A. Ivanichenko, P. Saha, "Development of All-Solid-State Li-Ion Batteries: From Key Technical Areas to Commercial Use," *Batteries*, vol. 9, 2023, doi: 10.3390/batteries9030157.
- [5] F. Zheng, M. Kotobuki, S. Song, M. O. Lai, and L. Lu, "Review on solid electrolytes for all-solid-state lithium-ion batteries," *Journal of Power Sources*, vol. 389, pp. 198–213, 2018, doi: 10.1016/j.jpowsour.2018.04.022.
- [6] P. Knauth and H. L. Tuller, "Solid-state ionics: Roots, status, and future

- prospects,” *Journal of the American Ceramic Society*, vol. 85, pp. 1654–1680, 2002, doi: 10.1111/j.1151-2916.2002.tb00334.x.
- [7] T. Ye, L. Li, and Y. Zhang, “Recent Progress in Solid Electrolytes for Energy Storage Devices,” *Advanced Functional Materials*, vol. 30, pp. 1–20, 2020, doi: 10.1002/adfm.202000077.
- [8] Q. Abbas, M. Mirzaeian, A. G. Olabi, and D. Gibson, “Solid State Electrolytes,” *Encyclopedia of Smart Materials*, vol. 4, pp. 382–392, 2021, doi: 10.1016/B978-0-12-803581-8.11740-0.
- [9] M. Faraday, *Philos. Trans. R. Soc. London*, vol. 132, no. 675, 1833.
- [10] S. C. Singhal and K. Kendall, *High Temperature Solid Oxide Fuel Cells (SOFCs): Fundamentals, Design and Applications*,. Variorum Publishing Ltd, Lancaster and Rugby, 2003.
- [11] F. V. G. Wiedemann, Die Lehre von der Elektrizität and Braunschweig, *The Science of Electricity*, 2nd edn., 1893.
- [12] T. T. and O. Yamamoto, “The Ag/Ag₃SI/I₂ solid-electrolyte cell,” *Electrochim. Acta*, vol. 11, pp. 779–789, 1966.
- [13] T. Takahashi, “Early History of Solid State Ionics,” *MRS Proc.*, vol. 135, no. 3, 1988.
- [14] Y. Y. Yao, and J. T. Kummer, “Ion exchange properties of and rates of ionic diffusion in beta-alumina,” *J. Inorg. Nucl. Chem.*, vol. 29, pp. 2453–2466, 1967.
- [15] J. T. K. and N. Weber, “A Sodium-Sulfur Secondary Battery,” *Proc. SAE Cong.*, vol. 670179, pp. 1003–1028, 1967.
- [16] N. Weber, J. T. Kummer, “Thermo-Electric Generator,” US3458356A, 1969.
- [17] J. N. Bradley, and P. D. Greene, “Potassium iodide and silver iodide phase diagram high ionic conductivity of KAg₄I₅,” *Trans. Faraday Soc.*, vol. 62, pp. 2069–2075, 1966.
- [18] H. W. C. Heraeus, “Über die elektrolytische Leitung fester Körper bei sehr

- hohen Temperaturen,” *Zeitschrift für Elektrochemie*, vol. 6, pp. 41–43, 1899.
- [19] W. Nernst, “Material for electric-lamp glowers,” US685730A, 1899.
- [20] J. N. Bradley and P. D. Greene, “Potassium iodide + silver iodide phase diagram. High ionic conductivity of KAg_4I_5 ,” *React. Wkly.*, vol. 62, pp. 2069–2975, 1966.
- [21] J. N. Bradley and P. D. Greene, “Solids with high ionic conductivity in group 1 halide systems,” *Trans. Faraday Soc.*, vol. 63, pp. 424–430, 1967.
- [22] J. M. Parker, P. Wright, and D. Fenton, “Complexes of alkali metal ions with poly(ethylene oxide),” *Polymer*, vol. 14, pp. 589, 1973.
- [23] J. M. Chabagno, M. J. Duclot, and M. Armand, *Fast ion transport in solids electrodes and electrolytes conference*, vol. 131, 1979.
- [24] J. Coetzer, “A new high energy density battery system,” *J. Power Sources*, vol. 18, pp. 377–380, 1986.
- [25] R. C. Galloway, D. A. Teagle, R. J. Bones, and J. Coetzer, “A Sodium/Iron(II) Chloride Cell with a Beta Alumina Electrolyte,” *J. Electrochem. Soc.*, vol. 134, pp. 2379–2382, 1987.
- [26] J. R. MacCallum, Colin. A. Vincent, and F. M. Gray, “Poly(ethylene oxide) - LiCF_3SO_3 - polystyrene electrolyte systems,” *Solid State Ionics*, vol. 18–19, pp. 282–286, 1986.
- [27] C. F. Luck, J. D. Robertson, N. J. Dudney, J. B. Bates, and R. A. Zuhr, “Sputtering of lithium compounds for preparation of electrolyte thin films,” *Solid State Ionics*, vol. 53–56, pp. 655–661, 1992.
- [28] A. Choudhary, C. F. Luck, J. B. Bates, N. J. Dudney, G. R. Gruzalski, and R. A. Zuhr, “Electrical properties of amorphous lithium electrolyte thin films,” *Solid State Ionics*, vol. 53–56, pp. 647–654, 1992.
- [29] P. R. Gandhi, V. K. Deshpande, and K. Singh, “Conductivity enhancement in Li_2SO_4 incorporated $\text{Li}_2\text{O}:\text{B}_2\text{O}_3$ glass system” *Solid State Ionics*, vol. 36, pp. 97–102, 1989.

-
- [30] Z. N. A. Kwist, A. Lund'en, vol. A20, p. 235, 1965.
- [31] B. N. Pal, B. M. Dhar, K. C. See, and H. E. Katz, "Solution-deposited sodium beta-alumina gate dielectrics for low-voltage and transparent field-effect transistors," *Nature Materials*, vol. 8, pp. 898–903, 2009, doi: 10.1038/nmat2560.
- [32] M. M. W. Gorecki, R. Andreani, C. Berthier, M. Armand and J. R. and D. Brinkmann, "NMR, DSC, and conductivity study of a poly(ethylene oxide) complex electrolyte : PEO(LiClO₄)_x," *Solid State Ionics*, vol. 18–19, pp. 295–299, 1986.
- [33] A. Manthiram, X. Yu, and S. Wang, "Lithium battery chemistries enabled by solid-state electrolytes," *Nature Reviews Materials*, vol. 2, pp. 1–16, 2017, doi: 10.1038/natrevmats.2016.103.
- [34] M. Armand and J. Tarascon, "Building better batteries," *Nature*, vol. 451, pp. 652–657, 2008.
- [35] P. Knauth, L. Mate, C. S. Charles, C. M. Cedex, and H. L. Tuller, "Solid-State Ionics : Roots , Status , and Future Prospects," vol. 80, pp. 1654–1680, 2002.
- [36] J. B. Boyce, and B. A. Huberman, "Superionic conductors: Transitions, structures, dynamics", *Physics Reports*, vol. 51, pp. 189-265, 1979.
- [37] J. B. Goodenough, H. Y-P. Hong, and J. A. Kafalas, "Fast Na⁺-ion transport in skeleton structures," *Mat. Res. Bull.*, vol. 11, pp. 203–220, 1976.
- [38] Lin Zuxiang, Li Shichun, Tian Shunbao, and Yu Huijun, "Fast Ion Conductors of Nasicon Structure.," *Scientia Sinica, Series A: Mathematical, Physical, Astronomical & Technical Sciences*, vol. 27, pp. 889–896, 1984.
- [39] L. P. D. Boilot J, Salanie J, Desplanches G, "Phase transformation in Na_{1+x}Si_xZr₂P_{3-x}O₁₂ compounds," *Mater Res Bull.*, vol. 14, pp. 1469–1477, 1979.
- [40] W. W. P. Von Alpen U, Bell M, "Phase transition in NASICON (Na₃Zr₂Si₂PO₁₂)," *Mater Res Bull.*, vol. 14, pp. 1317–1322, 1979.

-
- [41] M. O. Kohler H, Schulz H, “Composition and conduction mechanism of the NASICON structure X-ray diffraction study on two crystals at different temperatures,” *Mater Res Bull.*, vol. 18, pp. 1143–1152, 1983.
- [42] A. G. Jolley, D. D. Taylor, N. J. Schreiber, and E. D. Wachsman, “Structural Investigation of Monoclinic-Rhombohedral Phase Transition in $\text{Na}_3\text{Zr}_2\text{Si}_2\text{PO}_{12}$ and Doped NASICON,” *Journal of the American Ceramic Society*, vol. 98, pp. 2902–2907, 2015, doi: 10.1111/jace.13692.
- [43] C. P. Boilot JP, Collin G, “Relation structure-fast ion conduction in the NASICON solid solution,” *Solid State Chem.*, vol. 73, pp. 160–171, 1988.
- [44] R. J. Gordon R, Miller G, McEntire B, Beck E, “Fabrication and characterization of Nasicon electrolytes,” *Solid State Ionics*, vol. 3, pp. 243–248, 1981.
- [45] E. J. Yde-Andersen S, Lundsgaard JS, Møller L, “Properties of NASICON electrolytes prepared from alkoxide derived gels: ionic conductivity, durability in molten sodium and strength test data,” *Solid State Ion.*, vol. 14, pp. 73–39, 1984.
- [46] A. Jalalian-Khakshour, C. O. Phillips, L. Jackson, T. O. Dunlop, S. Margadonna, and D. Deganello, “Solid-state synthesis of NASICON ($\text{Na}_3\text{Zr}_2\text{Si}_2\text{PO}_{12}$) using nanoparticle precursors for optimisation of ionic conductivity,” *Journal of Materials Science*, vol. 55, pp. 2291–2302, 2020, doi: 10.1007/s10853-019-04162-8.
- [47] J. A. Dias, S. H. Santagneli, and Y. Messaddeq, “Methods for Lithium Ion NASICON Preparation: From Solid-State Synthesis to Highly Conductive Glass-Ceramics,” *Journal of Physical Chemistry C*, vol. 124, pp. 26518–26539, 2020, doi: 10.1021/acs.jpcc.0c07385.
- [48] Y. B. Rao, K. K. Bharathi, and L. N. Patro, “Review on the synthesis and doping strategies in enhancing the Na ion conductivity of $\text{Na}_3\text{Zr}_2\text{Si}_2\text{PO}_{12}$ (NASICON) based solid electrolytes,” *Solid State Ionics*, vol. 366–367, p. 115671, 2021, doi: 10.1016/j.ssi.2021.115671.
- [49] Z. Yang, B. Tang, Z. Xie, and Z. Zhou, “NASICON-Type $\text{Na}_3\text{Zr}_2\text{Si}_2\text{PO}_{12}$

- Solid-State Electrolytes for Sodium Batteries**,” *ChemElectroChem*, vol. 8, pp. 1035–1047, 2021, doi: 10.1002/celec.202001527.
- [50] L. Zhang, Y. Liu, Y. You, A. Vinu, and L. Mai, “NASICONs-type solid-state electrolytes: The history, physicochemical properties, and challenges,” *Interdisciplinary Materials*, vol. 2, pp. 91–110, 2023, doi: 10.1002/idm2.12046.
- [51] C. Li, R. Li, K. Liu, R. Si, Z. Zhang, and Y. Hu, “NaSICON: A promising solid electrolyte for solid-state sodium batteries,” *Interdisciplinary Materials*, vol. 1, pp. 396–416, 2022, doi: 10.1002/idm2.12044.
- [52] S. K. Pal, R. Saha, G. V. Kumar, and S. Omar, “Designing High Ionic Conducting NASICON-type $\text{Na}_3\text{Zr}_2\text{Si}_2\text{PO}_{12}$ Solid-Electrolytes for Na-Ion Batteries,” *Journal of Physical Chemistry C*, vol. 124, pp. 9161–9169, 2020, doi: 10.1021/acs.jpcc.0c00543.
- [53] R. D. Shannon, B. E. Taylor, A. D. English, And T. Berzins, *New Li Solid Electrolytes*, vol. 22, Pergamon Press Ltd, 1977.
- [54] B. E. Taylor, A. D. English, and T. Berzins, “New solid ionic conductors,” *Materials Research Bulletin*, vol. 12, pp. 171–181, 1977, doi: 10.1016/0025-5408(77)90161-1.
- [55] M. Catti and S. Stramare, “Lithium location in NASICON-type Li^+ conductors by neutron diffraction: II. Rhombohedral $\alpha\text{-LiZr}_2(\text{PO}_4)_3$ at $T = 423 \text{ K}$,” *Solid State Ionics*, vol. 136, pp. 489–494, 2000, doi: 10.1016/S0167-2738(00)00459-8.
- [56] A. Rossbach, F. Tietz, and S. Grieshammer, “Structural and transport properties of lithium-conducting NASICON materials,” *Journal of Power Sources*, vol. 391, pp. 1–9, 2018, doi: 10.1016/j.jpowsour.2018.04.059.
- [57] H. Aono, N. Imanaka, and G. ya Adachi, “High Li^+ Conducting Ceramics,” *Accounts of Chemical Research*, vol. 27, pp. 265–270, 1994, doi: 10.1021/ar00045a002.
- [58] Z.-X. Lin, H.-J. Yu, S.-C. Li, and S.-B. Tian, “Phase Relationship and Electrical Conductivity of $\text{Li}_{1+x}\text{Ti}_{2-x}\text{Ga}_x\text{P}_3\text{O}_{12}$ and $\text{Li}_{1+2x}\text{Ti}_{2-x}\text{Mg}_x\text{P}_3\text{O}_{12}$

- Systems,” *Solid State Ionics*, vol. 18 & 19, pp. 549–552, 1986.
- [59] M. A. Subramanian, R. Subramanian, and A. Clearfield, “Lithium ion conductors in the system $AB(IV)_2(PO_4)_3$ (B = Ti, Zr and Hf),” *Solid State Ionics*, vol. 18–19, pp. 562–569, 1986, doi: 10.1016/0167-2738(86)90179-7.
- [60] K. Iwamoto, N. Aotani, K. Takada, and S. Kondo, “Application of Li_3PO_4 - Li_2S - SiS_2 glass to the solid state secondary batteries,” *Solid State Ionics*, vol. 79, pp. 288–291, 1995, doi: 10.1016/0167-2738(95)00076-I.
- [61] H. Aono, E. Sugimoto, Y. Sadaoka, N. Imanaka, and G. Adachi, “Ionic Conductivity of Solid Electrolytes Based on Lithium Titanium Phosphate,” *Journal of The Electrochemical Society*, vol. 137, pp. 1023–1027, 1990, doi: 10.1149/1.2086597.
- [62] M. Monchak *et al.*, “Lithium Diffusion Pathway in $Li_{1.3}Al_{0.3}Ti_{1.7}(PO_4)_3$ (LATP) Superionic Conductor,” *Inorganic Chemistry*, vol. 55, pp. 2941–2945, 2016, doi: 10.1021/acs.inorgchem.5b02821.
- [63] G. J. Redhammer *et al.*, “A single crystal X-ray and powder neutron diffraction study on NASICON-type $Li_{1+x}Al_xTi_{2-x}(PO_4)_3$ ($0 \leq x \leq 0.5$) crystals: Implications on ionic conductivity,” *Solid State Sciences*, vol. 60, pp. 99–107, 2016, doi: 10.1016/j.solidstatesciences.2016.08.011.
- [64] J. S. M. A. Paris, A.M. Juarez, J. M. Rojo, “Lithium mobility in the NASICON-type compound $LiTi_2(PO_4)_3$ by nuclear magnetic resonance and impedance spectroscopies,” *J. Phys.: Condens. Matter*, vol. 8, pp. 5355–5366, 1996.
- [65] A. H. Adachi B.G., Imanaka N., “Fast Li^+ Conducting Ceramic Electrolytes,” *Advanced Materials*, pp. 127–135, 1996.
- [66] J. Kang, H. Chung, C. Doh, B. Kang, and B. Han, “Integrated study of first principles calculations and experimental measurements for Li-ionic conductivity in Al-doped solid-state $LiGe_2(PO_4)_3$ electrolyte,” *Journal of Power Sources*, vol. 293, pp. 11–16, 2015, doi: 10.1016/j.jpowsour.2015.05.060.

- [67] Y. Liang, C. Peng, Y. Kamiike, K. Kuroda, and M. Okido, “Gallium doped NASICON type $\text{LiTi}_2(\text{PO}_4)_3$ thin-film grown on graphite anode as solid electrolyte for all solid state lithium batteries,” *Journal of Alloys and Compounds*, vol. 775, pp. 1147–1155, 2019, doi: 10.1016/j.jallcom.2018.10.226.
- [68] M. Kotobuki and K. Hoshina, “Preparation of $\text{Li}_{1.5}\text{Al}_{0.5}\text{Ge}_{1.5}(\text{PO}_4)_3$ solid electrolyte by sol-gel method,” *Phosphorus Research Bulletin*, vol. 24, pp. 61–63, 2011.
- [69] C. R. Mariappan, C. Yada, F. Rosciano, and B. Roling, “Correlation between micro-structural properties and ionic conductivity of $\text{Li}_{1.5}\text{Al}_{0.5}\text{Ge}_{1.5}(\text{PO}_4)_3$ ceramics,” *Journal of Power Sources*, vol. 196, pp. 6456–6464, 2011, doi: 10.1016/j.jpowsour.2011.03.065.
- [70] N. Kyono, F. Bai, H. Nemori, H. Minami, D. Mori, Y. Takeda, O. Yamamoto, and N. Imanishi, “Lithium-ion conducting solid electrolytes of $\text{Li}_{1.4}\text{Al}_{0.4}\text{Ge}_{0.2}\text{Ti}_{1.4}(\text{PO}_4)_3$ and MO_x (M = Al, Ti, and Zr) composites,” *Solid State Ionics*, vol. 324, pp. 114–127, 2018, doi: 10.1016/j.ssi.2018.06.016.
- [71] K. Waetzig, A. Rost, C. Heubner, M. Coeler, K. Nikolowski, M. Wolter, and J. Schilm, “Synthesis and sintering of $\text{Li}_{1.3}\text{Al}_{0.3}\text{Ti}_{1.7}(\text{PO}_4)_3$ (LATP) electrolyte for ceramics with improved Li^+ conductivity,” *Journal of Alloys and Compounds*, vol. 818, p. 153237, 2020, doi: 10.1016/j.jallcom.2019.153237.
- [72] W. Zhao, L. Chen, R. Xue, J. Min, and W. Cui, “Ionic conductivity and luminescence of Eu^{3+} -doped $\text{LiTi}_2(\text{PO}_4)_3$,” *Solid State Ionics*, vol. 70–71, pp. 144–146, 1994, doi: 10.1016/0167-2738(94)90299-2.
- [73] H. Aono, E. Sugimoto, Y. Sadaoka, N. Imanaka, and G. ya Adachi, “Electrical properties and crystal structure of solid electrolyte based on lithium hafnium phosphate $\text{LiHf}_2(\text{PO}_4)_3$,” *Solid State Ionics*, vol. 62, pp. 309–316, 1993, doi: 10.1016/0167-2738(93)90387-I.
- [74] T. van Dijk, and A.J. Burggraaf, “Grain boundary effects on ionic conductivity in ceramic $\text{Gd}_x\text{Zr}_{1-x}\text{O}_{2-(x/2)}$ solid solutions,” *Physica status solidi (a)*, vol. 63, pp. 229–240, 1981.

-
- [75] J. Fleig, and J. Maier, “The impedance of ceramics with highly resistive grain boundaries: Validity and limits of the brick layer model,” *Journal of the European Ceramic Society*, vol. 19, pp. 693–696, 1999, doi: 10.1016/s0955-2219(98)00298-2.
- [76] J. Fleig, “The grain boundary impedance of random microstructures: Numerical simulations and implications for the analysis of experimental data,” *Solid State Ionics*, vol. 150, pp. 181–193, 2002, doi: 10.1016/S0167-2738(02)00274-6.
- [77] V. Thangadurai, H. Kaack, and W. J. F. Weppner, “Novel fast lithium ion conduction in garnet-type $\text{Li}_5\text{La}_3\text{M}_2\text{O}_{12}$ ($\text{M} = \text{Nb}, \text{Ta}$),” *Journal of the American Ceramic Society*, vol. 86, pp. 437–440, 2003, doi: 10.1111/j.1151-2916.2003.tb03318.x.
- [78] V. Thangadurai, S. Narayanan, and D. Pinzaru, “Garnet-type solid-state fast Li ion conductors for Li batteries: Critical review,” *Chemical Society Reviews*, vol. 43, pp. 4714–4727, 2014, doi: 10.1039/c4cs00020j.
- [79] G. V. Alexander, N. C. Rosero-Navarro, A. Miura, K. Tadanaga, and R. Murugan, “Electrochemical performance of a garnet solid electrolyte based lithium metal battery with interface modification,” *Journal of Materials Chemistry A*, vol. 6, pp. 21018–21028, 2018, doi: 10.1039/C8TA07652A.
- [80] C. Li, Z. Wang, Z. He, Y. Li, J. Mao, K. Dai, C. Yan, and J. Zheng, “An advance review of solid-state battery: Challenges, progress and prospects,” *Sustainable Materials and Technologies*, vol. 29, p. e00297, 2021, doi: 10.1016/j.susmat.2021.e00297.
- [81] S. Teng, J. Tan, and A. Tiwari, “Recent developments in garnet based solid state electrolytes for thin film batteries,” *Current Opinion in Solid State and Materials Science*, vol. 18, pp. 29–38, 2014, doi: 10.1016/j.cossms.2013.10.002.
- [82] V. T. Luu, Q. H. Nguyen, M. G. Park, H. L. Nguyen, M. Seo, S. Jeong, N. Cho, Y. Lee, Y. Cho, S. N. Lim, Y. Jun, and W. Ahn, “Cubic garnet solid polymer electrolyte for room temperature operable all-solid-state-battery,” *Journal of*

-
- Materials Research and Technology*, vol. 15, pp. 5849–5863, 2021, doi: 10.1016/j.jmrt.2021.11.055.
- [83] E. G. Cox, *Structural Inorganic Chemistry*, 4th ed. Clarendon Press: Oxford, 1951.
- [84] E. J. Cussen, M. P. O’Callaghan, A. S. pdf. Powell, J. J. Titman, and G. Z. Chen, “Switching on fast lithium ion conductivity in garnets: The structure and transport properties of $\text{Li}_{3+x}\text{Nd}_3\text{Te}_{2-x}\text{Sb}_x\text{O}_{12}$,” *Chemistry of Materials*, vol. 20, pp. 2360–2369, 2008, doi: 10.1021/cm703677q.
- [85] M. P. O’ Callaghan, D. R. Lynham, E. Cussen, and G. Z. Chen, “Structure and Ionic-Transport Properties of Lithium-Containing garnets $\text{Li}_3\text{Ln}_3\text{Te}_2\text{O}_{12}$ ” vol. 18, pp. 4681–4689, 2006.
- [86] V. Thangadurai and W. Weppner, “ $\text{Li}_6\text{ALa}_2\text{Ta}_2\text{O}_{12}$ (A=Sr, Ba): Novel garnet-like oxides for fast lithium ion conduction,” *Advanced Functional Materials*, vol. 15, pp. 107–112, 2005, doi: 10.1002/adfm.200400044.
- [87] R. Murugan, V. Thangadurai, and W. Weppner, “Fast lithium ion conduction in garnet-type $\text{Li}_7\text{La}_3\text{Zr}_2\text{O}_{12}$,” *Angewandte Chemie - International Edition*, vol. 46, pp. 7778–7781, 2007, doi: 10.1002/anie.200701144.
- [88] R. Murugan, V. Thangadurai, and W. Weppner, “Effect of lithium ion content on the lithium ion conductivity of the garnet-like structure $\text{Li}_{5+x}\text{BaLa}_2\text{Ta}_2\text{O}_{11.5+0.5x}$ ($x = 0-2$),” *Applied Physics A: Materials Science and Processing*, vol. 91, pp. 615–620, 2008, doi: 10.1007/s00339-008-4494-2.
- [89] H. Peng, Q. Wu, and L. Xiao, “Low temperature synthesis of $\text{Li}_5\text{La}_3\text{Nb}_2\text{O}_{12}$ with cubic garnet-type structure by sol-gel process,” *Journal of Sol-Gel Science and Technology*, vol. 66, pp. 175–179, 2013, doi: 10.1007/s10971-013-2984-y.
- [90] Y. X. Gao, X. P. Wang, W. G. Wang, and Q. F. Fang, “Sol-gel synthesis and electrical properties of $\text{Li}_5\text{La}_3\text{Ta}_2\text{O}_{12}$ lithium ionic conductors,” *Solid State Ionics*, vol. 181, pp. 33–36, 2010, doi: 10.1016/j.ssi.2009.11.015.
- [91] S. Narayanan and V. Thangadurai, “Effect of y substitution for Nb in $\text{Li}_5\text{La}_3\text{Nb}_2\text{O}_{12}$ on Li ion conductivity of garnet-type solid electrolytes,” *Journal*

- of Power Sources*, vol. 196, pp. 8085–8090, 2011, doi: 10.1016/j.jpowsour.2011.05.031.
- [92] V. Thangadurai and W. Weppner, “ $\text{Li}_6\text{ALa}_2\text{Nb}_2\text{O}_{12}$ (A = Ca, Sr, Ba): A new class of fast lithium ion conductors with garnet-like structure,” *Journal of the American Ceramic Society*, vol. 88, pp. 411–418, 2005, doi: 10.1111/j.1551-2916.2005.00060.x.
- [93] L. W. H. Xie, Y. Li, J. Han, Y. Dong, M. P. Paranthaman, M. N. M. Xu, A. Gupta, Z. Bi, C. A. Bridges, and A. P. S. and J. B. Goodenough, “ $\text{Li}_6\text{La}_3\text{SnMO}_{12}$ (M = Sb, Nb, Ta), a Family of Lithium Garnets with High Li-Ion Conductivity,” *J. Electrochem. Soc.*, vol. 159, pp. A1148–A1151, 2012.
- [94] C. Deviannapoorani, L. Dhivya, S. Ramakumar, and R. Murugan, “Lithium ion transport properties of high conductive tellurium substituted $\text{Li}_7\text{La}_3\text{Zr}_2\text{O}_{12}$ cubic lithium garnets,” *Journal of Power Sources*, vol. 240, pp. 18–25, 2013, doi: 10.1016/j.jpowsour.2013.03.166.
- [95] Y. L. and J. B. G. H. Xie, “Low-temperature synthesis of $\text{Li}_7\text{La}_3\text{Zr}_2\text{O}_{12}$ with cubic garnet-type structure,” *Mater. Res. Bull.*, vol. 47, pp. 1229–1232, 2012.
- [96] T. Zaiß, M. Ortner, R. Murugan, and W. Weppner, “Fast ionic conduction in cubic hafnium garnet $\text{Li}_7\text{La}_3\text{Hf}_2\text{O}_{12}$,” *Ionics*, vol. 16, pp. 855–858, 2010, doi: 10.1007/s11581-010-0486-2.
- [97] C. R. Mariappan, K. I. Gnanasekar, V. Jayaraman, and T. Gnanasekaran, “Lithium ion conduction in $\text{Li}_5\text{La}_3\text{Ta}_2\text{O}_{12}$ and $\text{Li}_7\text{La}_3\text{Ta}_2\text{O}_{13}$ garnet-type materials,” *Journal of Electroceramics*, vol. 30, pp. 258–265, 2013, doi: 10.1007/s10832-013-9792-1.
- [98] M. A. Howard *et al.*, “Synthesis, conductivity and structural aspects of $\text{Nd}_3\text{Zr}_2\text{Li}_{7-3x}\text{Al}_x\text{O}_{12}$,” *Journal of Materials Chemistry A*, vol. 1, pp. 14013–14022, 2013, doi: 10.1039/c3ta13252h.
- [99] A. Kim, S. Woo, M. Kang, H. Park, and B. Kang, “Research Progresses of Garnet-Type Solid Electrolytes for Developing All-Solid-State Li Batteries,” *Frontiers in Chemistry*, vol. 8, pp. 1–13, 2020, doi: 10.3389/fchem.2020.00468.

-
- [100] B. Chen, S. Sarkar, S. P. Kammampata, C. Zhou, and V. Thangadurai, “Li-stuffed garnet electrolytes: structure, ionic conductivity, chemical stability, interface, and applications,” vol. 319, pp. 311–319, 2022.
- [101] S. Yan, Q. Cui, C. Sun, J. Hao, X. Chu, H. Xie, S. Lin, and X. Zhang, “Enhancing the ionic conductivity and stabilizing cubic structure of garnet-type $\text{Li}_{6.25-x}\text{Al}_{0.25}\text{La}_3\text{Zr}_{2-x}\text{Ta}_x\text{O}_{12}$ by Al/Ta co-doping,” *Journal of Solid State Chemistry*, vol. 295, no. December 2020, p. 121949, 2021, doi: 10.1016/j.jssc.2020.121949.
- [102] C. K. Chan, T. Yang, and J. Mark Weller, “Nanostructured Garnet-type $\text{Li}_7\text{La}_3\text{Zr}_2\text{O}_{12}$: Synthesis, Properties, and Opportunities as Electrolytes for Li-ion Batteries,” *Electrochimica Acta*, vol. 253, pp. 268–280, 2017, doi: 10.1016/j.electacta.2017.08.130.
- [103] N. Sharma and A. Dalvi, “Mechanical milling assisted synthesis of novel $\text{LiTi}_2(\text{PO}_4)_3$ -glass-ceramic nanocomposites,” *Journal of Non-Crystalline Solids*, vol. 483, pp. 126–133, 2018, doi: 10.1016/j.jnoncrysol.2018.01.016.
- [104] A. Banik, T. Famprakis, M. Ghidui, S. Ohno, M. A. Kraft, and W. G. Zeier, “On the underestimated influence of synthetic conditions in solid ionic conductors,” *Chemical Science*, vol. 12, pp. 6238–6263, 2021, doi: 10.1039/d0sc06553f.
- [105] Y. Li and H. Wang, “Composite solid electrolytes with NASICON-type LATP and PVdF-HFP for solid-state lithium batteries,” *Industrial and Engineering Chemistry Research*, vol. 60, pp. 1494–1500, 2021, doi: 10.1021/acs.iecr.0c05075.
- [106] M. Kim, G. Kim, and H. Lee, “Tri-doping of sol-gel synthesized garnet-type oxide solid-state electrolyte,” *Micromachines*, vol. 12, pp. 1–14, 2021, doi: 10.3390/mi12020134.
- [107] D. Burova, I. Shakhova, P. Morozova, A. Iarchuk, O. A. Drozhzhin, M. G. Rozova, S. Praneetha, V. Murugan, J. M. Tarascon, and A. M. Abakumov, “The rapid microwave-assisted hydrothermal synthesis of NASICON-structured $\text{Na}_3\text{V}_2\text{O}_{2x}(\text{PO}_4)_2\text{F}_{3-2x}$ ($0 < x \leq 1$) cathode materials for Na-ion

- batteries,” *RSC Advances*, vol. 9, pp. 19429–19440, 2019, doi: 10.1039/c9ra02257k.
- [108] S. Ferdov and Z. Lin, “The first hafnium germanate with garnet-type of structure: Mild hydrothermal synthesis, crystal structure and new mechanism of hydroxyl inclusion,” *Journal of Solid State Chemistry*, vol. 273, pp. 117–121, 2019, doi: 10.1016/j.jssc.2019.02.031.
- [109] A. Clearfield, M. A. Subramanian, W. Wang, and P. Jerus, “The use of hydrothermal procedures to synthesize NASICON and some comments on the stoichiometry of NASICON phases,” *Solid State Ionics*, vol. 9–10, pp. 895–902, 1983, doi: 10.1016/0167-2738(83)90108-X.
- [110] R. DeWees and H. Wang, “Synthesis and Properties of NaSICON-type LATP and LAGP Solid Electrolytes,” *ChemSusChem*, vol. 12, pp. 3713–3725, 2019, doi: 10.1002/cssc.201900725.
- [111] A. L. Monaca, G. Girard, S. Savoie, G. Bertoni, S. Krachkovskiy, A. Vijh, F. Pierini, F. Rosei, and A. Paoella, “Synthesis of Electrospun NASICON $\text{Li}_{1.5}\text{Al}_{0.5}\text{Ge}_{1.5}(\text{PO}_4)_3$ Solid Electrolyte Nanofibers by Control of Germanium Hydrolysis,” *J. Electrochem. Soc.*, vol. 168, p. 110512, 2021.
- [112] S. Yu, Q. Xu, X. Lu, Z. Liu, A. Windmuller, C. L. Tsai, A. Buchheit, H. Tempel, H. Kungl, H. D. Weimhofer, and R. A. Eichel, “Single-Ion-Conducting ‘Polymer-in-Ceramic’ Hybrid Electrolyte with an Intertwined NASICON-Type Nanofiber Skeleton,” *ACS Applied Materials and Interfaces*, vol. 13, pp. 61067–61077, 2021, doi: 10.1021/acsami.1c17718.
- [113] S. Yan, C. H. Yim, V. Pankov, M. Bauer, E. Baranova, A. Weck, A. Merati, and Y. A. Lebdeh, “Perovskite solid-state electrolytes for Lithium metal batteries,” *Batteries*, vol. 7, 2021, doi: 10.3390/batteries7040075.
- [114] Y. Ren, K. Chen, R. Chen, T. Liu, Y. Zhang, and C. Nan, “Oxide Electrolytes for Lithium Batteries,” *Journal of the American Ceramic Society*, vol. 3623, 2015, doi: 10.1111/jace.13844.
- [115] J. Lu and Y. Li, “Perovskite-type Li-ion solid electrolytes: a review,” *Journal of Materials Science: Materials in Electronics*, vol. 32, pp. 9736–9754, 2021,

- doi: 10.1007/s10854-021-05699-8.
- [116] J. Lu, Y. Li, and Y. Ding, “Structure, stability, and ionic conductivity of perovskite $\text{Li}_{2x-y}\text{Sr}_{1-x-y}\text{La}_y\text{TiO}_3$ solid electrolytes,” *Ceramics International*, vol. 46, pp. 7741–7747, 2020, doi: 10.1016/j.ceramint.2019.11.277.
- [117] X. Hu, X. Cheng, S. Qin, G. Yan, J. Malzbender, W. Qiang, and B. Huang, “Mechanical and electrochemical properties of cubic and tetragonal $\text{Li}_x\text{La}_{0.557}\text{TiO}_3$ perovskite oxide electrolytes,” *Ceramics International*, vol. 44, pp. 1902–1908, 2018, doi: 10.1016/j.ceramint.2017.10.129.
- [118] V. Thangadurai and W. Weppner, “Effect of B-site substitution of $(\text{Li},\text{La})\text{TiO}_3$ perovskites by Di-, tri-, tetra- and hexavalent metal ions on the lithium ion conductivity,” *Ionics*, vol. 6, pp. 70–77, 2000, doi: 10.1007/BF02375549.
- [119] S. J. Lee, J. J. Bae, and J. T. Son, “Structural and Electrical Effects of Y-doped $\text{Li}_{0.33}\text{La}_{0.56-x}\text{Y}_x\text{TiO}_3$ Solid Electrolytes on All-Solid-State Lithium Ion Batteries,” *Journal of the Korean Physical Society*, vol. 74, pp. 73–77, 2019, doi: 10.3938/jkps.74.73.
- [120] Z. Hu, J. Sheng, J. Chen, G. Sheng, Y. Li, X. Fu, L. Wang, R. Sun, and C. P. Wong, “Enhanced Li ion conductivity in Ge-doped $\text{Li}_{0.33}\text{La}_{0.56}\text{TiO}_3$ perovskite solid electrolytes for all-solid-state Li-ion batteries,” *New Journal of Chemistry*, vol. 42, pp. 9074–9079, 2018, doi: 10.1039/c8nj01113c.
- [121] R. Yu, Q. X. Du, B. K. Zou, Z. Y. Wen, and C. H. Chen, “Synthesis and characterization of perovskite-type $(\text{Li},\text{Sr})(\text{Zr},\text{Nb})\text{O}_3$ quaternary solid electrolyte for all-solid-state batteries,” *Journal of Power Sources*, vol. 306, pp. 623–629, 2016, doi: 10.1016/j.jpowsour.2015.12.065.
- [122] V. Thangadurai, A. K. Shukla, and J. Gopalakrishnan, “ $\text{LiSr}_{1.650.35}\text{B}_{1.3}\text{B}'_{1.7}\text{O}_9$ (B = Ti, Zr; B' = Nb, Ta): New lithium ion conductors based on the perovskite structure,” *Chemistry of Materials*, vol. 11, pp. 835–839, 1999, doi: 10.1021/cm9810382.
- [123] B. Huang, B. Xu, Y. Li, W. Zhou, Y. You, S. Zhong, C. Wang, and J. B. Goodenough, “Li-Ion Conduction and Stability of Perovskite $\text{Li}_{3/8}\text{Sr}_{7/16}\text{Hf}_{1/4}\text{Ta}_{3/4}\text{O}_3$,” *ACS Applied Materials and Interfaces*, vol. 8, pp.

- 14552–14557, 2016, doi: 10.1021/acsami.6b03070.
- [124] H. Y. P. Hong, “Crystal structure and ionic conductivity of $\text{Li}_{14}\text{Zn}(\text{GeO}_4)_4$ and other new Li^+ superionic conductors,” *Materials Research Bulletin*, vol. 13, pp. 117–124, 1978, doi: 10.1016/0025-5408(78)90075-2.
- [125] H. Kim, Y. Ding, and P. A. Kohl, “LiSICON - Ionic liquid electrolyte for lithium ion battery,” *Journal of Power Sources*, vol. 198, pp. 281–286, 2012, doi: 10.1016/j.jpowsour.2011.10.005.
- [126] M. Tachez, J. P. Malugani, R. Mercier, and G. Robert, “Ionic conductivity of and phase transition in lithium thiophosphate Li_3PS_4 ,” *Solid State Ionics*, vol. 14, pp. 181–185, 1984, doi: 10.1016/0167-2738(84)90097-3.
- [127] N. Kamaya, K. Homma, Y. Yamakawa, M. Hirayama, R. Kanno, M. Yonemura, T. Kamiyama, Y. Kato, S. Hama, K. Kawamoto, and A. Mitsui, “A lithium superionic conductor,” *Nature Materials*, vol. 10, pp. 682–686, 2011, doi: 10.1038/nmat3066.
- [128] Y. Zheng, Y. Yao, J. Ou, M. Li, D. Luo, H. Dou, Z. Li, K. Amine, A. Yu, and Z. Chen, “A review of composite solid-state electrolytes for lithium batteries: Fundamentals, key materials and advanced structures,” *Chemical Society Reviews*, vol. 49, pp. 8790–8839, 2020, doi: 10.1039/d0cs00305k.
- [129] J. Zarzycki, *Glasses and vitreous state*. Cambridge University press, 1981.
- [130] H. L. Tuller, D. P. Button, and D. R. Uhlmann, “Fast ion transport in oxide glasses,” *Journal of Non-Crystalline Solids*, vol. 40, pp. 93–118, 1980, doi: 10.1016/0022-3093(80)90096-4.
- [131] D. Ravaine, “Ionic transport properties in glasses,” *Solid State Ionics*, vol. 73, pp. 287–303, 1985.
- [132] P. Knauth, “Inorganic solid Li ion conductors: An overview,” *Solid State Ionics*, vol. 180, pp. 911–916, 2009, doi: 10.1016/j.ssi.2009.03.022.
- [133] J. P. Malugani and G. Robert, “Preparation and electrical properties of the $0,37\text{Li}_2\text{S}-0,18\text{P}_2\text{S}_5-0,45\text{LiI}$ glass,” *Solid State Ionics*, vol. 1, pp. 519–523, 1980, doi: 10.1016/0167-2738(80)90048-X.

-
- [134] R. Mercier, J. P. Malugani, B. Fahys, and G. Robert, "Superionic conduction in $\text{Li}_2\text{S}-\text{P}_2\text{S}_5$ -LiI- glasses," *Solid State Ionics*, vol. 5, pp. 663–666, 1981, doi: 10.1016/0167-2738(81)90341-6.
- [135] M. Rathore and A. Dalvi, "Electrical transport in Li_2SO_4 - Li_2O - P_2O_5 ionic glasses and glass-ceramic composites: A comparative study," *Solid State Ionics*, vol. 239, pp. 50–55, 2013, doi: 10.1016/j.ssi.2013.03.022.
- [136] B. K. Money and K. Hariharan, "Glass formation and electrical conductivity studies of melt quenched and mechanically milled $50\text{Li}_2\text{O}:(50-x)\text{P}_2\text{O}_5:x\text{B}_2\text{O}_3$," *Solid State Ionics*, vol. 179, pp. 1273–1277, 2008, doi: 10.1016/j.ssi.2007.12.068.
- [137] Z. Zhang and J. H. Kennedy, "Synthesis and characterization of the $\text{B}_2\text{S}_3\text{Li}_2\text{S}$, the $\text{P}_2\text{S}_5\text{Li}_2\text{S}$ and the $\text{B}_2\text{S}_3\text{P}_2\text{S}_5\text{Li}_2\text{S}$ glass systems," *Solid State Ionics*, vol. 38, pp. 217–224, 1990, doi: 10.1016/0167-2738(90)90424-P.
- [138] K. Minami, F. Mizuno, A. Hayashi, and M. Tatsumisago, "Lithium ion conductivity of the $\text{Li}_2\text{S}-\text{P}_2\text{S}_5$ glass-based electrolytes prepared by the melt quenching method," *Solid State Ionics*, vol. 178, pp. 837–841, 2007, doi: 10.1016/j.ssi.2007.03.001.
- [139] N. Aotani, K. Iwamoto, K. Takada, and S. Kondo, "Synthesis and electrochemical properties of lithium ion conductive glass, $\text{Li}_3\text{PO}_4\text{Li}_2\text{SSi}_2$," *Solid State Ionics*, vol. 68, pp. 35–39, 1994, doi: 10.1016/0167-2738(94)90232-1.
- [140] A. Levasseur, J. C. Brethous, J. M. Reau, P. Hagenmuller, and M. Couzi, "Synthesis and characterization of new solid electrolyte conductors of lithium ions," *Solid State Ionics*, vol. 1, pp. 177–186, 1980, doi: 10.1016/0167-2738(80)90002-8.
- [141] T. M. N. Machida, K. Fujii, "Preparation and ionic conductivity of the rapidly quenched glasses in the system $\text{Li}_2\text{O}-\text{TiO}_2-\text{P}_2\text{O}_5$," *Chemistry letters*, pp. 367–370, 1991.
- [142] N. S. Saetova, A. A. Raskovalov, B. D. Antonov, T. V Yaroslavtseva, O. G. Reznitskikh, and E. V Zabolotskaya, "Conductivity and spectroscopic studies

- of $\text{Li}_2\text{O-V}_2\text{O}_5\text{-B}_2\text{O}_3$ glasses,” *Ionics*, vol. 5, pp. 1929–1938, 2018.
- [143] F. Mizuno, A. Hayashi, K. Tadanaga, and M. Tatsumisago, “New, highly ion-conductive crystals precipitated from $\text{Li}_2\text{S-P}_2\text{S}_5$ glasses,” *Advanced Materials*, vol. 17, pp. 918–921, 2005, doi: 10.1002/adma.200401286.
- [144] J. Fu, “Superionic conductivity of glass-ceramics in the system $\text{Li}_2\text{O-Al}_2\text{O}_3\text{-TiO}_2\text{-P}_2\text{O}_5$,” *Solid State Ionics*, vol. 96, pp. 195–200, 1997, doi: 10.1016/s0167-2738(97)00018-0.
- [145] K. Kwatek and J. L. Nowiński, “Solid lithium ion conducting composites based on $\text{LiTi}_2(\text{PO}_4)_3$ and $\text{Li}_{2.9}\text{B}_{0.9}\text{S}_{0.1}\text{O}_{3.1}$ glass,” *Solid State Ionics*, vol. 322, pp. 93–99, 2018, doi: 10.1016/j.ssi.2018.05.007.
- [146] K. Kwatek, M. Świniarski, and J. L. Nowiński, “The Li^+ conducting composite based on $\text{LiTi}_2(\text{PO}_4)_3$ and Li_3BO_3 glass,” *Journal of Solid State Chemistry*, vol. 265, pp. 381–386, 2018, doi: 10.1016/j.jssc.2018.06.028.
- [147] P. Wakudkar and A. V. Deshpande, “ CeO_2 modified $\text{Li}_{6.6}\text{La}_3\text{Zr}_{1.6}\text{Sb}_{0.4}\text{O}_{12}$ composite ceramic electrolyte for lithium battery application,” *Journal of Physics and Chemistry of Solids*, vol. 155, p. 110092, 2021, doi: 10.1016/j.jpics.2021.110092.
- [148] H. Hosono and Y. Abe, “Fast lithium conducting glass-ceramics in the $\text{Li}_2\text{O-CaO-TiO}_2\text{-Al}_2\text{O}_3\text{-P}_2\text{O}_5$ system,” *Solid State Ionics*, vol. 44, pp. 293–297, 1991, doi: 10.1016/0167-2738(91)90021-3.
- [149] G. D. L. K. Jayasinghe, M. A. K. L. Dissanayake, P. W. S. K. Bandaranayake, J. L. Souquet, and D. Foscallo, “Electronic to ionic conductivity of glasses in the $\text{Li}_2\text{O-V}_2\text{O}_5\text{-TeO}_2$ system,” *Solid State Ionics*, vol. 121, pp. 19–23, 1999, doi: 10.1016/S0167-2738(98)00336-1.
- [150] X. Xu, Z. Wen, Z. Gu, X. Xu, and Z. Lin, “Lithium ion conductive glass ceramics in the system $\text{Li}_{1.4}\text{Al}_{0.4}(\text{Ge}_{1-x}\text{Ti}_x)_{1.6}(\text{PO}_4)_3$ ($x=0\text{-}1.0$),” *Solid State Ionics*, vol. 171, pp. 207–213, 2004, doi: 10.1016/j.ssi.2004.05.009.
- [151] Y. Shimonishi, T. Zhang, P. Johnson, N. Imanishi, A. Hirano, Y. Takeda, O. Yamamoto, and N. Sammes, “A study on lithium/air secondary batteries-

- Stability of NASICON-type glass ceramics in acid solutions,” *Journal of Power Sources*, vol. 195, pp. 6187–6191, 2010, doi: 10.1016/j.jpowsour.2009.11.023.
- [152] R. Chen, Q. Li, X. Yu, L. Chen, and H. Li, “Approaching Practically Accessible Solid-State Batteries: Stability Issues Related to Solid Electrolytes and Interfaces,” *Chemical Reviews*, vol. 120, pp. 6820–6877, 2020, doi: 10.1021/acs.chemrev.9b00268.
- [153] V. Deshpande *et al.*, “Journal of Physics : Energy 2020 roadmap on solid-state batteries,” *Journal of Physics: Energy*, vol. 2, p. 32008, 2020, <https://doi.org/10.1088/2515-7655/ab95f4>.
- [154] Z. Tong, S. B. Wang, Y. K. Liao, S. F. Hu, and R. S. Liu, “Interface between solid-state electrolytes and li-metal anodes: Issues, materials, and processing routes,” *ACS Applied Materials and Interfaces*, vol. 12, pp. 47181–47196, 2020, doi: 10.1021/acsami.0c13591.
- [155] Y. S. Jung, D. Y. Oh, Y. J. Nam, and K. H. Park, “Issues and challenges for bulk-type all-solid-state rechargeable lithium batteries using sulfide solid electrolytes,” *Israel Journal of Chemistry*, vol. 55, pp. 472–485, 2015, doi: 10.1002/ijch.201400112.
- [156] R. Wei, S. Chen, T. Gao, and W. Liu, “Challenges, fabrications and horizons of oxide solid electrolytes for solid-state lithium batteries,” *Nano Select*, vol. 2, pp. 2256–2274, 2021, doi: 10.1002/nano.202100110.
- [157] M. Lechartier, L. Porcarelli, H. Zhu, M. Forsyth, A. Gueguen, L. Castro, and D. Mecerreyes, “Single-ion polymer/LLZO hybrid electrolytes with high lithium conductivity,” *Materials Advances*, vol. 3, pp. 1139–1151, 2022, doi: 10.1039/d1ma00857a.
- [158] J. Mindemark, M. J. Lacey, T. Bowden, and D. Brandell, “Beyond PEO—Alternative host materials for Li⁺-conducting solid polymer electrolytes,” *Progress in Polymer Science*, vol. 81, pp. 114–143, 2018, doi: 10.1016/j.progpolymsci.2017.12.004.
- [159] A. Manuel Stephan and K. S. Nahm, “Review on composite polymer

- electrolytes for lithium batteries,” *Polymer*, vol. 47, pp. 5952–5964, 2006, doi: 10.1016/j.polymer.2006.05.069.
- [160] A. Karmakar and A. Ghosh, “Poly ethylene oxide (PEO)-LiI polymer electrolytes embedded with CdO nanoparticles,” *Journal of Nanoparticle Research*, vol. 13, pp. 2989–2996, 2011, doi: 10.1007/s11051-010-0194-x.
- [161] S. Klongkan and J. Pumchusak, “Effects of nano alumina and plasticizers on morphology, ionic conductivity, thermal and mechanical properties of PEO-LiCF₃SO₃ Solid Polymer Electrolyte,” *Electrochimica Acta*, vol. 161, pp. 171–176, 2015, doi: 10.1016/j.electacta.2015.02.074.
- [162] C. V. S. Reddy, G. P. Wu, C. X. Zhao, W. Jin, Q. Y. Zhu, W. Chen, and S. Mho, “Mesoporous silica (MCM-41) effect on (PEO + LiAsF₆) solid polymer electrolyte,” *Current Applied Physics*, vol. 7, pp. 655–661, 2007, doi: 10.1016/j.cap.2007.03.001.
- [163] S. Ibrahim and M. R. Johan, “Conductivity, thermal and neural network model nanocomposite solid polymer electrolyte system (PEO-LiPF₆-EC-CNT),” *International Journal of Electrochemical Science*, vol. 6, pp. 5565–5587, 2011, doi: 10.1016/S1452-3981(23)18428-8.
- [164] L. Fan, C. W. Nan, and S. Zhao, “Effect of modified SiO₂ on the properties of PEO-based polymer electrolytes,” *Solid State Ionics*, vol. 164, pp. 81–86, 2003, doi: 10.1016/j.ssi.2003.08.004.
- [165] F. Croce, G. B. Appetecchi, L. Persi, and B. Scrosati, “(Al₂O₃, TiO₂) Nanocomposite polymer electrolytes for lithium batteries, F. Croce, B. Scrosati, Nature (1998),” *Nature letters*, vol. 394, pp. 456–458, 1998, <https://www-nature-com.gaelnomade-2.grenet.fr/articles/28818.pdf>.
- [166] D. Lin, W. Liu, Y. Liu, H. R. Lee, P. Hsu, K. Liu, and Y. Cui, “High Ionic Conductivity of Composite Solid Polymer Electrolyte via in Situ Synthesis of Monodispersed SiO₂ Nanospheres in Poly(ethylene oxide),” *Nano Letters*, vol. 16, pp. 459–465, 2016, doi: 10.1021/acs.nanolett.5b04117.
- [167] X. Wang, Y. Zhang, X. Zhang, T. Liu, Y. Lin, L. Li, Y. Shen, and C. Nan, “Lithium-Salt-Rich PEO/Li_{0.3}La_{0.55}7TiO₃ Interpenetrating Composite

- Electrolyte with Three-Dimensional Ceramic Nano-Backbone for All-Solid-State Lithium-Ion Batteries,” *ACS Applied Materials and Interfaces*, vol. 10, pp. 24791–24798, 2018, doi: 10.1021/acsami.8b06658.
- [168] Y. Zhao, C. Wu, G. Peng, X. Chen, X. Yao, Y. Bai, F. Wu, S. Chen, and X. Xu, “A new solid polymer electrolyte incorporating $\text{Li}_{10}\text{GeP}_2\text{S}_{12}$ into a polyethylene oxide matrix for all-solid-state lithium batteries,” *Journal of Power Sources*, vol. 301, pp. 47–53, 2016, doi: 10.1016/j.jpowsour.2015.09.111.
- [169] Z. Wan, D. Lei, W. Yang, C. Liu, K. Shi, X. Hao, L. Shen, W. Lv, B. Li, Q. Yang, F. Kang, and Y. He, “Low Resistance–Integrated All-Solid-State Battery Achieved by $\text{Li}_7\text{La}_3\text{Zr}_2\text{O}_{12}$ Nanowire Upgrading Polyethylene Oxide (PEO) Composite Electrolyte and PEO Cathode Binder,” *Advanced Functional Materials*, vol. 29, 2019, doi: 10.1002/adfm.201805301.
- [170] X. Cheng, J. Pan, Y. Zhao, M. Liao, and H. Peng, “Gel Polymer Electrolytes for Electrochemical Energy Storage,” *Advanced Energy Materials*, vol. 8, pp. 1–16, 2018, doi: 10.1002/aenm.201702184.
- [171] S. Alipoori, S. Mazinani, S. H. Aboutalebi, and F. Sharif, “Review of PVA-based gel polymer electrolytes in flexible solid-state supercapacitors: Opportunities and challenges,” *Journal of Energy Storage*, vol. 27, p. 101072, 2020, doi: 10.1016/j.est.2019.101072.
- [172] A. K. Tripathi, “Ionic liquid based solid electrolytes (ionogels) for application in rechargeable lithium battery,” vol. 20, 2021, doi: 10.1016/j.mtener.2021.100643.
- [173] R. Jamil and D. S. Silvester, “Ionic liquid gel polymer electrolytes for flexible supercapacitors: Challenges and prospects,” *Current Opinion in Electrochemistry*, vol. 35, pp. 1–8, 2022, doi: 10.1016/j.coelec.2022.101046.
- [174] C. Zhao, C. Wang, Z. Yue, K. Shu, and G. G. Wallace, “Intrinsically stretchable supercapacitors composed of polypyrrole electrodes and highly stretchable gel electrolyte,” *ACS Applied Materials and Interfaces*, vol. 5, pp. 9008–9014, 2013, doi: 10.1021/am402130j.

- [175] G. K. Prajapati, R. Roshan, and P. N. Gupta, "Effect of plasticizer on ionic transport and dielectric properties of PVAH₃PO₄ proton conducting polymeric electrolytes," *Journal of Physics and Chemistry of Solids*, vol. 71, pp. 1717–1723, 2010, doi: 10.1016/j.jpcs.2010.08.023.
- [176] H. Seok Jang, C. Justin Raj, W. G. Lee, B. Chul Kim, and K. Hyun Yu, "Enhanced supercapacitive performances of functionalized activated carbon in novel gel polymer electrolytes with ionic liquid redox-mediated poly(vinyl alcohol)/phosphoric acid," *RSC Advances*, vol. 6, pp. 75376–75383, 2016, doi: 10.1039/c6ra15070e.
- [177] H. Gupta, Shalu, L. Balo, V. K. Singh, S. K. Singh, A. K. Tripathi, Y. L. Verma, and R. K. Singh, "Effect of temperature on electrochemical performance of ionic liquid based polymer electrolyte with Li/LiFePO₄ electrodes," *Solid State Ionics*, vol. 309, pp. 192–199, 2017, doi: 10.1016/j.ssi.2017.07.019.
- [178] S. K. Chaurasia, R. K. Singh, and S. Chandra, "Dielectric relaxation and conductivity studies on (PEO:LiClO₄) polymer electrolyte with added ionic liquid [BMIM][PF₆]: Evidence of ion-ion interaction," *Journal of Polymer Science, Part B: Polymer Physics*, vol. 49, pp. 291–300, 2011, doi: 10.1002/polb.22182.
- [179] A. Varzi, R. Raccichini, S. Passerini, and B. Scrosati, "Challenges and prospects of the role of solid electrolytes in the revitalization of lithium metal batteries," *Journal of Materials Chemistry A*, vol. 4, pp. 17251–17259, 2016, doi: 10.1039/c6ta07384k.
- [180] K. S. Ngai, S. Ramesh, K. Ramesh, and J. C. Juan, "A review of polymer electrolytes: fundamental, approaches and applications," *Ionics*, vol. 22, pp. 1259–1279, 2016, doi: 10.1007/s11581-016-1756-4.
- [181] S. A. Hashmi, N. Yadav, and M. K. Singh, "Polymer electrolytes for supercapacitor and challenges," *Polymer Electrolytes: Characterization Techniques and Energy Applications*, pp. 231–297, 2019, doi: 10.1002/9783527805457.ch9.

-
- [182] A. K. Tripathi, “Ionic liquid–based solid electrolytes (ionogels) for application in rechargeable lithium battery,” *Materials Today Energy*, vol. 20, p. 100643, 2021, doi: 10.1016/j.mtener.2021.100643.
- [183] J. W. Choi, G. Cheruvally, Y. Kim, J. Kim, J. Manuel, P. Raghavan, J. Ahn, K. Kim, H. Ahn, D. S. Choi, and C. E. Song, “Poly(ethylene oxide)-based polymer electrolyte incorporating room-temperature ionic liquid for lithium batteries,” *Solid State Ionics*, vol. 178, pp. 1235–1241, 2007, doi: 10.1016/j.ssi.2007.06.006.
- [184] Y. H. Kim, G. Cheruvally, J. W. Choi, J. H. Ahn, K. W. Kim, H. J. Ahn, D. S. Choi, C. E. Song, “Electrochemical properties of PEO-based polymer electrolytes blended with different room temperature ionic liquids,” *Macromolecular Symposia*, vol. 249–250, pp. 183–189, 2007, doi: 10.1002/masy.200750330.
- [185] B. S. and A. S. A. Fernicola, F. C. Weise, S. G. Greenbaum, J. Kagimoto, “Lithium-Ion-Conducting Electrolytes: From an Ionic Liquid to the Polymer Membrane,” *Journal of The Electrochemical Society*, vol. 156, p. A514, 2009.
- [186] Y. Kumar, G. P. Pandey, and S. A. Hashmi, “Gel polymer electrolyte based electrical double layer capacitors: Comparative study with multiwalled carbon nanotubes and activated carbon electrodes,” *Journal of Physical Chemistry C*, vol. 116, pp. 26118–26127, 2012, doi: 10.1021/jp305128z.
- [187] R. Kaswan, S. C. Sivasubramanian, Y. Kumar, and A. Dalvi, “Conductivity and Capacitance Studies of Silica Glass Composites Containing [BMIM] Br and LiCl,” *Materials Research Express*, vol. 6, 105202, 2019.
- [188] H. Nakagawa, S. Izuchi, K. Kuwana, T. Nukuda, and Y. Aihara, “Liquid and Polymer Gel Electrolytes for Lithium Batteries Composed of Room-Temperature Molten Salt Doped by Lithium Salt,” *Journal of the Electrochemical Society*, vol. 150, 2003, doi: 10.1149/1.1568939.
- [189] M. Rathore, A. Dalvi, A. Kumar, W. Tubowska, and J. L. Nowinski, “Ionic liquid dispersed Li⁺ ion oxide glasses and glass-ceramics: Assessment of electrical transport and thermal stability,” *Solid State Ionics*, vol. 282, pp. 76–

- 81, 2015, doi: 10.1016/j.ssi.2015.09.028.
- [190] A. Hayashi, H. Morishima, K. Tadanaga, and M. Tatsumisago, “Characterization of solid electrolytes prepared from ionic glass and ionic liquid for all-solid-state lithium batteries,” *Solid State Ionics*, vol. 192, pp. 126–129, 2011, doi: 10.1016/j.ssi.2010.07.011.
- [191] K. Kwatek and J. L. Nowiński, “Electrical properties of $\text{LiTi}_2(\text{PO}_4)_3$ and $\text{Li}_{1.3}\text{Al}_{0.3}\text{Ti}_{1.7}(\text{PO}_4)_3$ solid electrolytes containing ionic liquid,” *Solid State Ionics*, vol. 302, pp. 54–60, 2017, doi: 10.1016/j.ssi.2016.11.020.
- [192] K. G. S. Pannu, T. Pannu, T. Fürstenthaupt, and V. Thangadurai, “Electrical properties of ionic liquid and double perovskite-type metal oxide composites - A new method to tailor grain-boundary impedance of ceramic electrolytes,” *Solid State Ionics*, vol. 232, pp. 106–111, 2013, doi: 10.1016/j.ssi.2012.11.009.
- [193] H. W. Kim, P. Manikandan, Y. J. Lim, J. H. Kim, S. C. Nam, and Y. Kim, “Hybrid solid electrolyte with the combination of $\text{Li}_7\text{La}_3\text{Zr}_2\text{O}_{12}$ ceramic and ionic liquid for high voltage pseudo-solid-state Li-ion batteries,” *Journal of Materials Chemistry A*, vol. 4, pp. 17025–17032, 2016, doi: 10.1039/c6ta07268b.
- [194] A. González, E. Goikolea, J. A. Barrena, and R. Mysyk, “Review on supercapacitors: Technologies and materials,” *Renewable and Sustainable Energy Reviews*, vol. 58, pp. 1189–1206, 2016, doi: 10.1016/j.rser.2015.12.249.

Chapter 2

Experimental Procedures

A brief overview of the synthetic routes adopted for the preparation of the samples and other experimental techniques used in the characterization and electrical conductivity studies of the samples are presented in this chapter. The chapter also includes a discussion on the preparation/fabrication steps involved in Li⁺ ion based solid-state batteries (SSBs) and solid-state supercapacitors (SSCs).

2.1 Ionic Liquid dispersed Li⁺ NASICON and garnet preparation

To prepare IL dispersed ceramic composites, firstly Li⁺ ion conduction NASICONs (LiTi₂(PO₄)₃ and Li_{1.3}Al_{0.3}Ti_{1.7}(PO₄)₃) and garnet (Li_{6.75}Al_{0.25}La₃Zr₂O₁₂) were synthesized by sol-gel route [1-3]. Using these fine and homogeneously prepared powdered ceramics, IL-ceramic composites were prepared. The preparation routes have been discussed in detail below.

- (i) LiTi₂(PO₄)₃ (LTP) synthesis: In the first step, LiTi₂(PO₄)₃ sol was prepared using high purity materials CH₃COOLi·2H₂O, Ti(OC₄H₉), and H₃PO₄ in a weight ratio 10:63:27 [1]. For this purpose, CH₃COOLi·2H₂O and phenolic resin were gradually added to a homogeneous solution containing Ti(OC₄H₉) and C₂H₅OH to obtain the desired sol. In the second step, another solution of concentrated H₃PO₄ + C₂H₅OH was added dropwise to the sol. This mixture was continuously stirred at 50 °C for 3 h in a water bath to obtain a gel. It was further heated to 65 °C for ethanol evaporation. Subsequently, the gel was dried at 80 °C overnight and further annealed at 750 °C for 6 h to get LiTi₂(PO₄)₃ compound.
- (ii) Li_{1.3}Al_{0.3}Ti_{1.7}(PO₄)₃ (LATP) synthesis: LATP composite has been prepared by sol-gel method using citric acid [2]. Stoichiometric amount of Ti(OC₄H₉)₄ was added to ethylene glycol to get a homogeneous solution. This solution was then added to a 0.2 M aqueous solution of citric acid while stirring at 100 °C for 10 h. To this homogeneous solution stoichiometric amounts of LiNO₃, Al(NO₃)₃·9H₂O, and NH₄H₂PO₄ were

added with the molar ratio of citric acid to ($\text{Li}^+ + \text{Al}^{3+} + \text{Ti}^{4+}$) as 4:1. This mixture was continuously stirred to obtain a homogeneous gel solution. This gel was heated at 150 °C in an oven for water evaporation. The dried gel was heated at 500 °C for 5 h and then this black powder was crushed and finally sintered at 800 °C to get rid of all the organic residues and obtain the final white LATP powder.

- (iii) $\text{Li}_{6.75}\text{Al}_{0.25}\text{La}_3\text{Zr}_2\text{O}_{12}$ (LALZO) synthesis: For this, stoichiometric amounts of LiNO_3 , $\text{La}(\text{NO}_3)_3 \cdot 6\text{H}_2\text{O}$, $\text{ZrO}(\text{NO}_3) \cdot \text{H}_2\text{O}$, and $\text{Al}(\text{NO}_3)_3 \cdot 9\text{H}_2\text{O}$ have been added to a beaker with deionised water [3]. This mixture was stirred till all the components dissolved completely. Following this, citric acid and ethylene glycol (twice the number of moles of cations in the precursor solution) in a mole ratio of 1:1 were added. After stirring and heating at 70 °C for ~5 hrs, a blackish brown mixture was obtained that was subsequently kept in a furnace at ~200 °C for ~5 hrs. Following these steps, a yellowish-brown foam was obtained that was thoroughly ground and kept at 850 °C for ~5 hrs, and the powder thus obtained was again ground and annealed at 1100 °C for 10 hrs.

The ionic liquid composites were prepared by mixing these powder samples uniformly with different ILs in a planetary ball mill (Fritsch-P6). For this purpose, the powder sample and ionic liquid were taken in an agate pot for 1 h at 100 rpm having the ball to sample mass ratio as 5:1. Subsequently, the composite mixture was kept in a vacuum oven for drying for ~4 h to get rid of the moisture. Different ILs have been used in various weight percentages. The final composites with ILs used and their weight percentages have been mentioned in specific chapters.

2.2 Device fabrication

The prepared composites were examined as electrolytes for applications in SSBs and SSCs.

- (i) Electrode for battery: For the cathode preparation, the slurry was prepared in 1-Methyl-2-pyrrolidinone (NMP) solvent using LiCoO_2 , acetylene black, and PVdF in the stoichiometric ratio of 85:7.5:7.5. After stirring for ~12 h, the mixture was coated on aluminum foil and subsequently dried overnight in a vacuum oven. Also, the cathode LiFePO_4 (LFP) was

prepared using active material (LFP), PVdF, and acetylene black in a stoichiometric ratio of 80:10:10. The slurry was prepared in NMP solvent using a centrifugal mixer (Thinky mixer) and subsequently coated over an aluminium foil followed by vacuum drying at 120 °C for approximately 24 hours. Further, to remove the porosity due to solvent evaporation, the obtained cathode was calendared at 80 °C and subsequently punched into a ~10 mm diameter electrode using a disk cutter. Li metal was used as the anode.

- (ii) Electrode for supercapacitor: The device was prepared using high surface area (~1050 m²/g and ~1500 m²/g) activated charcoal from Merck. The surface area, pore diameter, and pore distribution were measured using BET surface area analyser BELSORP-MINI X. The electrode slurry was prepared by mixing activated charcoal, acetylene black, and binder PVDF-HFP in a weight ratio of 80:10:10 in 1-Methyl-2-pyrrolidinone (NMP) solvent and stirring overnight, and subsequently coated on copper foil (current collector) by doctor blade technique with a mass loading of ~1.2 mg/cm². The coated foil was further dried at 100 °C for 10-12 hrs for solvent evaporation
- (iii) Fabrication of lithium cell: To study the potential of the ionic liquid containing composite as a solid electrolyte, Swagelok type cells with configuration LiCoO₂|sample|Li and LFP|sample|Li were fabricated in an argon-filled glove box (Fig. 2.1).

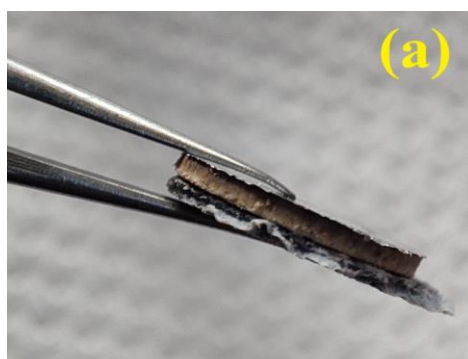




Fig. 2.1 (a) A picture of the composite pellet with electrodes, (b) A picture of Swagelok cell used for battery testing, and (c) Glove box (MTI) filled with Argon for fabrication.

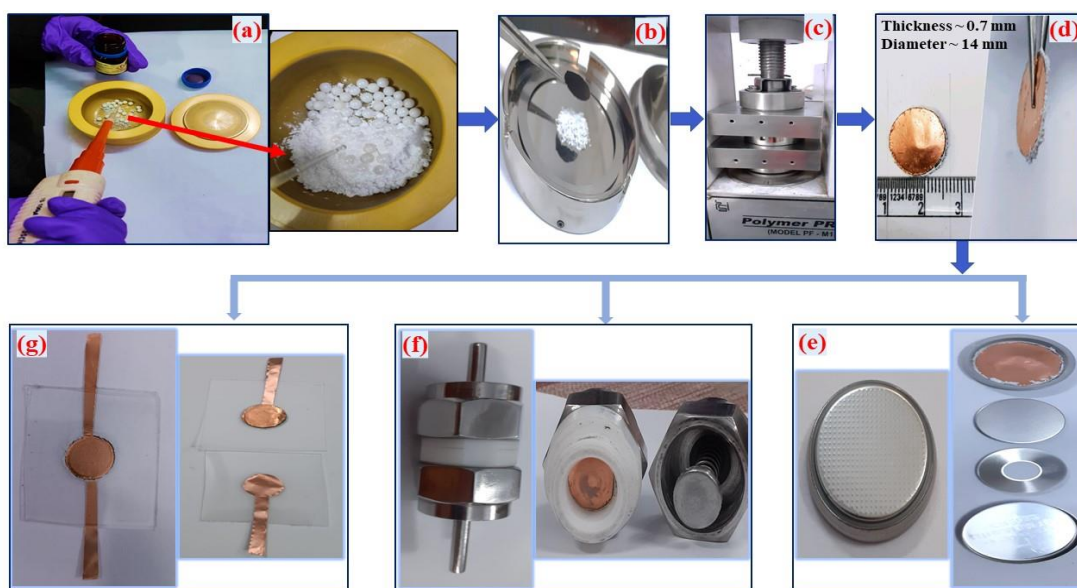


Fig. 2.2 Fabrication process steps for SSC having electrodes as activated charcoal coated copper foil, and IL dispersed ceramic composite as electrolyte. (a) Composite preparation: IL mixing with LATP in a ball mill, (b) Sprinkling composite powder on the activated charcoal electrode (coated on Cu foil) of diameter ~ 14mm, (c) Sandwich to press with ~ 3 tons/cm² in a hydraulic press (room temperature) for 10 minutes, (d) The SSC Cu|AC|LATP-IL|AC|Cu as obtained from the press in step (c). For casing the supercapacitor, the following geometries were chosen: (e) 2032 cell assembly, (f) Swagelok assembly, (g) Hot roll lamination.

-
- (iv) Fabrication of supercapacitors: Electrodes of diameter ~ 14 mm were cut in circular shapes using a puncher and used for the device fabrication. The composite electrolyte powder (LATP-13 EMIMBF₄) was sandwiched between electrodes and pressed in a hydraulic press by applying pressure up to ~ 3 -4 tons/cm² (Fig. 2.2 b-c). Finally, this sandwiched configuration of electrodes and electrolyte was transferred to three different geometries such as 2032-coin cell assembly, lamination, and Swagelok cell for cell fabrication (Fig. 2.2 e-g). These three different types have been developed to demonstrate the versatility of the developed composite for its potential to adopt various geometries. These different types of SSCs have been described in the chapters with detailed characterizations.

2.3 Characterization techniques

A brief discussion of various techniques used for the analysis and characterization of the prepared composites has been presented below.

2.3.1 X-ray diffraction

X-ray diffraction (XRD) is the most useful technique to study the crystalline structure, the ratio of crystalline to non-crystalline (amorphous) regions, crystal size, the arrangement patterns of the crystal, and the distance between the planes of the crystal. Max von Laue discovered in 1912 that crystalline structure behaves like a 3-D diffraction grating for X-rays with wavelengths comparable to the atomic spacing of the planes [4].

Samples have been analyzed using an X-ray diffractometer (Rigaku Miniflex-II) having CuK α radiation of the wavelength ~ 1.54 Å at room temperature. The filament current and voltage required for this operation of XRD were 30 mA and 30 kV respectively. In-situ high temperature X-ray diffraction (HTXRD) measurements were done on using a Rigaku Smartlab X-ray diffractometer with CuK α , 1.54 Å to examine the structural stability at higher temperatures. The samples were structurally characterized in a temperature range of 30-500 °C at a heating rate of 10 °C/min. After attaining the temperature, XRD scans were carried out at 5°/min. Using Rigaku Smart

lab studio II fitting software, lattice parameters and lattice volume were obtained as a function of temperature for the best conducting systems in each chapter.

An X-ray diffractometer consists of three main components: a cathode ray tube that generates X-rays, a sample holder that positions the sample, and an X-ray detector that measures and records the diffracted X-rays. The sample is rotated in the path of these X-rays at an angle θ and these diffracted X-rays are then collected by an X-ray detector which rotates at an angle of 2θ . In the present study, the 2θ range is varied from 10° - 90° at a scan speed of $2^\circ/\text{min}$. Bragg's law is used to study the interaction between the electromagnetic waves (X-rays) and a crystal [5]:

$$\lambda = 2nds\sin\theta \quad (2.1)$$

where θ is the angle of incidence, d is the perpendicular distance between pairs of adjacent planes, λ is the wavelength of the X-ray beam, and n gives the order of reflection. Further, considering two beams incident on a crystal plane at an angle θ_1 and θ_2 ,

$$2t \left(\frac{\theta_1 - \theta_2}{2} \right) \cos \theta = \lambda \quad (2.2)$$

$$t = \frac{\lambda}{\beta \cos \theta} \quad (2.3)$$

where β is the full width at half maximum to the peak corresponding to $\theta_1 - \theta_2$.

Further, the correction factor for instrumental broadening is as follows:

$$\beta = \sqrt{W_s - W_{Si}} \quad (2.4)$$

where W_s and W_{Si} are FWHM values of the sample and silicon, respectively [5].

After adding the correction factor from eq. 2.4,

$$t = \frac{K\lambda}{\beta \cos \theta} \quad (2.5)$$

where t is the average crystallite size, K is the dimensionless shape factor, and is taken to be 0.9 for most of the crystallites and λ is the wavelength of the X-rays used (1.54 Å). This relation is referred to as the Debye Scherrer's formula and is used to find the average crystallite size of the sample.

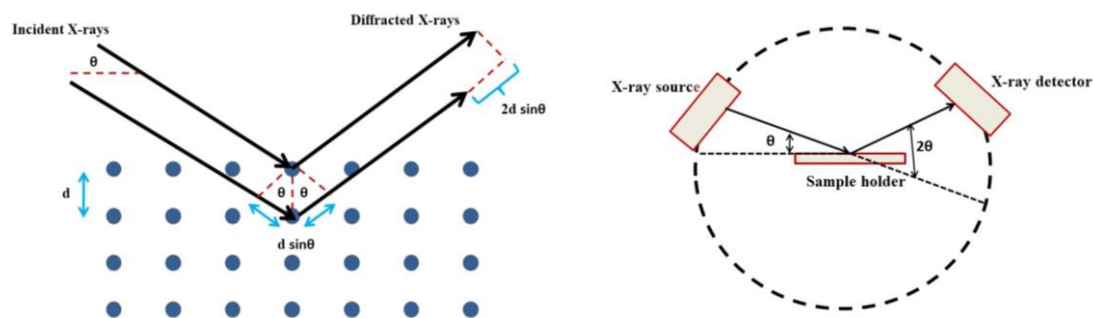


Fig. 2.3 (a) Geometrical representation of Bragg's law, (b) Block diagram of XRD setup.

For the present work, XRD has been used to characterize the formation of NASICONs (LTP and LATP) and garnet (LALZO). Then the IL-ceramic composites were analyzed at higher temperatures for thermal stability and to check the formation of any new crystalline phases in these composites. The lattice parameters and crystallite sizes have been found using this technique.

2.3.2 Field emission scanning electron microscopy

Field emission scanning electron microscopy (FESEM) is an advanced technology used to capture the microstructure image of the materials and to obtain information about the surface topography. In this instrument a beam of electrons is produced from a field emission (cold cathode) source and the electrons are accelerated in a high electric field gradient [6]. The block diagram of the experimental setup is given in Fig. 2.4.

The primary electrons liberated are then focused and deflected by electromagnetic lenses to produce a beam that scans the object. From each spot of the object where the primary electrons have hit, secondary electrons are emitted. The surface properties determine the angle and velocity of the secondary electrons. In the end, an electronic signal is produced when the detector spots the secondary electrons. This electronic signal is then amplified to produce an image that can be seen on the monitor. The basic difference between FESEM and conventional SEM is the way electrons are generated from a gun. FESEM uses a field emission gun that provides extremely focused electron beams which improves resolution. In SEM, electrical current from thermionic emitters is used to heat the filament, while, in FESEM, heating of the

filament is not required [8-9]. In order to observe FESEM images, the sample surface is made conductive by sputtering it with gold, platinum, carbon, etc.

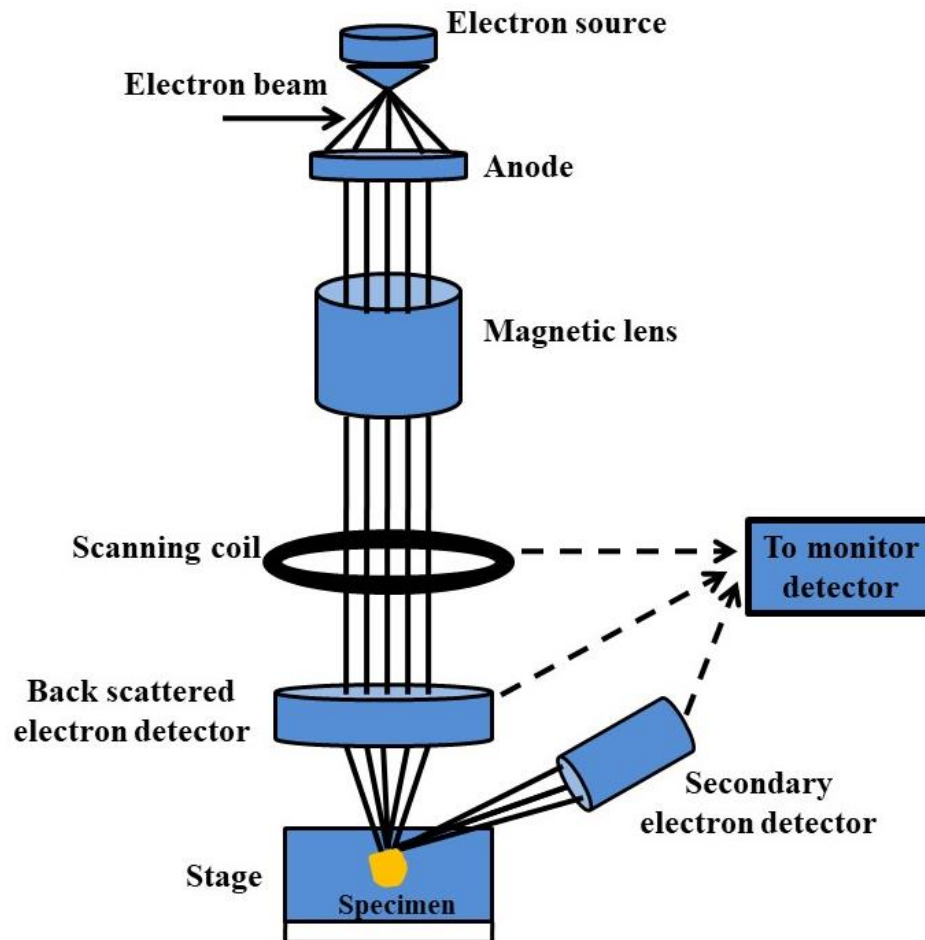


Fig. 2.4 Block diagram for experimental setup for FESEM [7].

Energy Dispersive X-ray spectroscopy (EDS or EDX) is another important technique to identify the elemental distribution and chemical composition in a sample [10]. In the FESEM experiment in addition to secondary electrons, X-rays and other emissions also occur. The EDS system consists of an X-ray detector and software to analyze energy spectra. The EDS detector absorbs the energy of incoming X-rays by ionization yielding free mobile electrons. Thus, the energy of individual X-rays is converted into electrical voltages of proportional size by X-ray absorption. The electrical pulses correspond to characteristic X-rays of elements. EDS spectrum is a plot between X-ray counts and energy (keV). Various elements in the sample are

indicated by different energy peaks. Further, elemental distribution maps can also be generated over an FESEM image.

In the present work, the surface morphology of pristine sol-gel derived NASICONs and garnets was investigated using the Thermo Fisher Scientific FEI Apreo-S instrument. Then, the IL dispersed composites were analyzed using this technique to check the surface condition of ceramics after IL addition. The samples were coated with gold (1.5-3 nm) by an ion sputtering mechanism in a high vacuum chamber. The images were taken using 20 kV accelerating voltage. Also, X-ray mapping was done for the composites to know about the qualitative elemental distribution across the specimen to check the homogeneity of IL distribution in the ceramic-IL composites.

2.3.3 Fourier Transform InfraRed (FTIR) Spectroscopy

Fourier Transform InfraRed (FTIR) Spectroscopy is an analytical technique used to study the interaction of materials with infrared (IR) radiation. It provides information about the molecular structure, functional groups, and chemical bonds present in a sample [11].

An IR source emits a broad spectrum of IR radiation covering a range of wavelengths (normally $400 - 4000 \text{ cm}^{-1}$). This IR radiation contains photons of varying energies corresponding to different vibrational (and in rare cases, rotational) states of molecules. After passing through the sample, the polychromatic IR radiation is split into two beams by an interferometer. When the sample beam and the reference beam recombine, they generate an interference pattern known as an interferogram which is processed (Fourier Transformed) by a computer to obtain the spectrum.

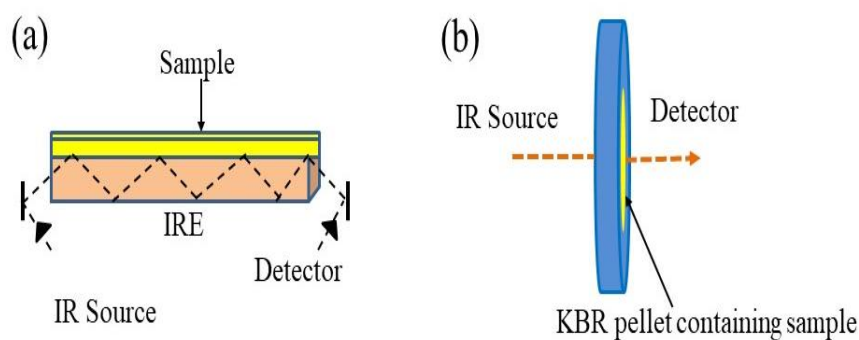


Fig. 2.5 Schematic diagram for sample analysis in FTIR Spectrophotometer in (a) ATR mode and (b) Transmission mode.

To ascertain the fundamental vibrations of diatomic molecules, Hooke's law is used. For the harmonic oscillator, vibration frequency can be expressed as

$$\bar{\nu} = \frac{1}{2\pi c} \sqrt{\frac{K}{\mu}} \quad (2.6)$$

where, c = speed of light, K = force constant, and μ = reduced mass ($m_1 \cdot m_2 / (m_1 + m_2)$). Molecules having stronger bonds with light atoms vibrate at a high stretching frequency. Only vibrations where the electric dipole moment changes during the vibration are visible in this technique. To identify other vibrations, techniques such as Raman Spectroscopy have to be used.

In the present work, ATR mode has been used to obtain FTIR spectra using an IRAffinity-1S instrument from SCHIMADZU. The composites have been analyzed by this technique to know if there is any new bond formation or complexation on the addition of IL to ceramics.

2.3.4 Raman Spectroscopy

Raman spectroscopy is a technique used to study the interaction of light with matter, providing information about the vibrational and rotational energy levels of molecules [12]. It is named after Sir C.V. Raman, an Indian physicist who discovered the Raman effect in 1928. In Raman spectroscopy, a sample is irradiated with monochromatic light (visible or UV region), typically from a laser. The incident light interacts with the sample, and most of it is scattered without any change in frequency (Rayleigh scattering). However, a small fraction of the scattered light undergoes inelastic scattering, resulting in a change in frequency. This is known as Raman scattering.

The energy difference between the incident and scattered light corresponds to the vibrational and rotational energy of the molecules in the sample. By analyzing the scattered light, information about the chemical composition, molecular structure, and bonding within the sample can be obtained. This technique has been used in the present work to study the formation of new chemical bonds or complexation in IL-ceramic composites [13].

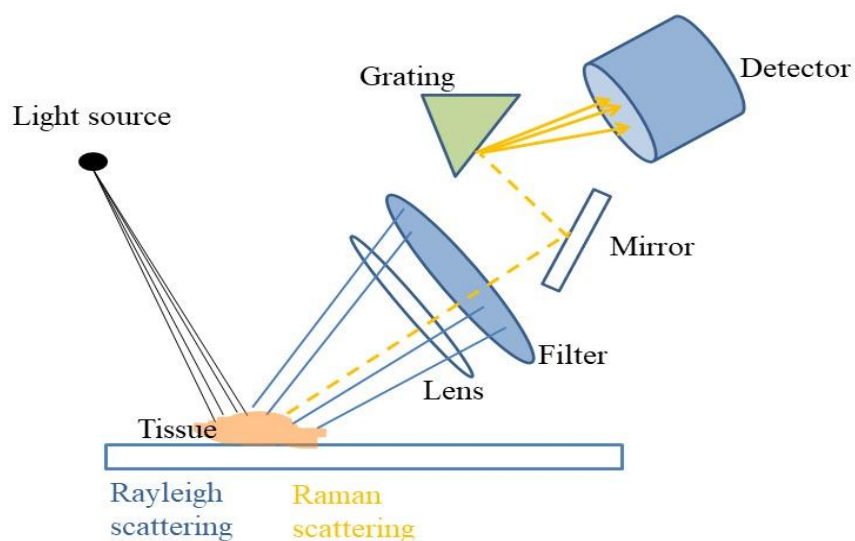


Fig. 2.6 Schematic diagram of a typical Raman spectrometer.

2.3.5 Differential Scanning Calorimetry (DSC)

Differential Scanning Calorimetry (DSC) is a thermal analysis technique used to study the thermal behavior of materials [14]. It measures the heat flow into or out of a sample as a function of temperature or time, allowing the determination of various thermal properties and phase transitions.

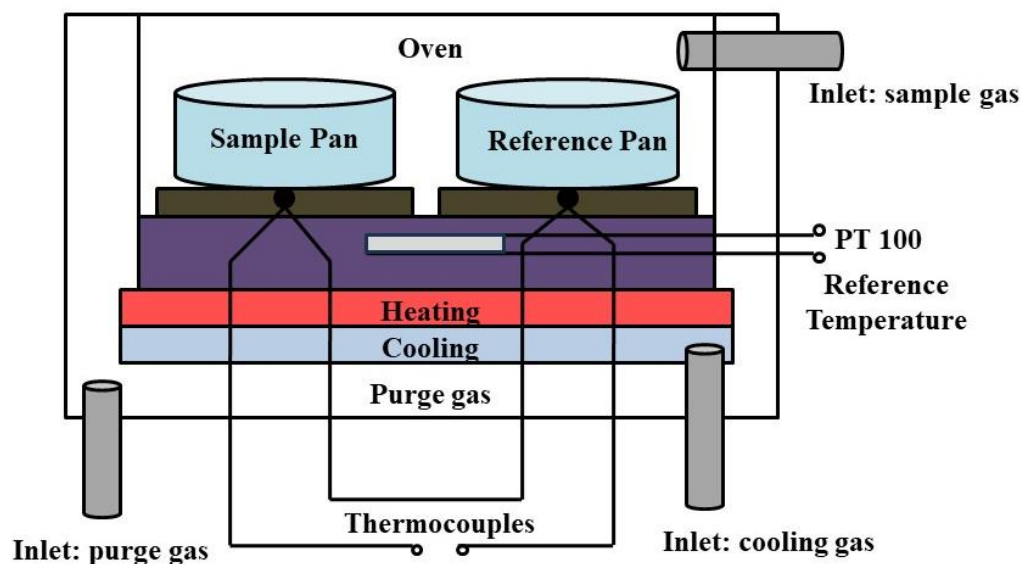


Fig. 2.7 Block diagram of DSC setup [15].

Differential Scanning Calorimeters can be broadly classified into two categories (i) Heat Flux instruments and (ii) Power Compensation instruments, based on the method

by which these instruments measure the change in the heat flow rate. During analysis, the temperature is increased for both the sample as well as the reference at a constant rate and pressure. Enthalpy changes (heat flow) can be observed as:

$$\left(\frac{dq}{dt}\right)_p = \left(\frac{dH}{dt}\right) \quad (2.7)$$

where (dH/dt) is Heat flow mcal sec^{-1} . Therefore, the heat flow difference between the sample and reference can be measured as:

$$\left(\frac{\Delta dH}{dt}\right) = \left(\frac{dH}{dt}\right)_{\text{Sample}} - \left(\frac{dH}{dt}\right)_{\text{Reference}} \quad (2.8)$$

Here, $(\Delta dH/dt)$ could be positive (endothermic process) for heat absorbed events or negative (exothermic process) for heat evolving events.

The sample and reference pans are placed in separate sample holders within the DSC instrument. The instrument then subjects both pans to a controlled temperature program, typically heating from a lower temperature to a higher temperature at a constant rate. The temperature range and heating rate are selected based on the properties of the sample and the information sought. As the temperature increases, heat flows into or out of the sample and reference pans due to changes in the sample's thermal properties or phase transitions. The DSC instrument measures the heat flow difference between the sample and reference pans, which is why it is called "differential" scanning calorimetry [16-17]. For the present work, measurements were done on a DSC 60 plus series SHIMADZU instrument, with a heating rate of 10 °C/minute to understand their thermal behavior and kinetics.

2.3.6 Thermo-gravimetric Analysis (TGA)

Thermogravimetric Analysis (TGA) is a thermal analysis technique used to study the weight changes of a sample as a function of temperature or time. It provides information about the thermal stability, composition, and decomposition behavior of materials [18].

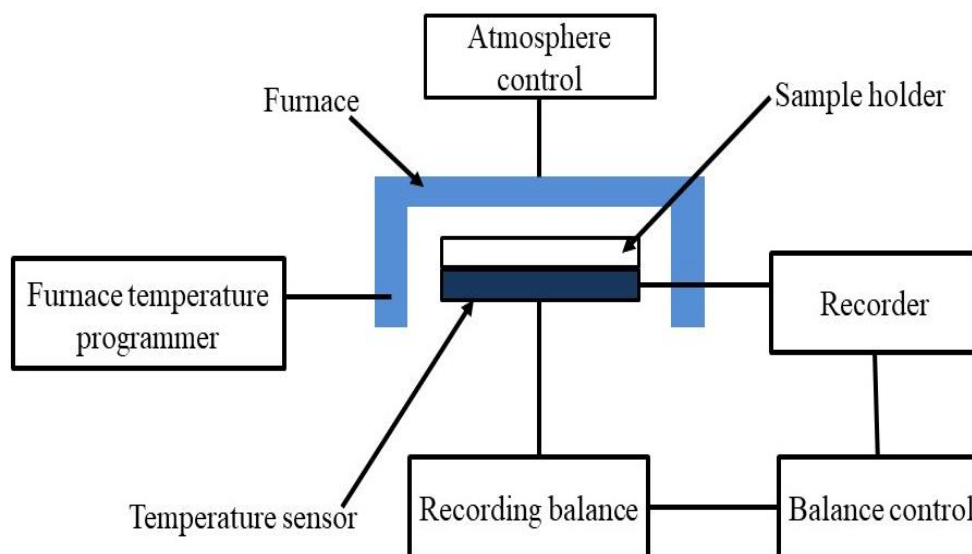


Fig. 2.8 Schematic diagram of TGA instrument.

The instrument of TGA consists of a sample pan attached to a heater and a precise micro-balance. The pan is heated and cooled during the experiment to record the thermal events. As the temperature changes, the sample undergoes various thermal events, such as decomposition, evaporation, oxidation, or desorption. The TGA instrument continuously monitors the weight of the sample by measuring the change in mass of the crucible and sample assembly. The weight loss or gain data obtained from TGA is recorded and analyzed to obtain information about the sample. By studying the mass change patterns, characteristic peaks, plateaus, or slopes can be observed [19]. For the present studies, TGA measurements have been done on TGA 60 plus series SHIMADZU instrument, with heating rates of 10 °C for pristine ceramics and their composites with IL to analyse the thermal stability of these samples.

2.3.7 BET surface area analysis

BET surface area analysis, named after its inventors Brunauer, Emmett, and Teller, is a widely used method to measure the specific surface area of solid materials including the pore size distribution [20]. The specific area determined by BET corresponds to the total surface area (reactive surface) as all porous structures adsorb the small gas molecules. The specific area is calculated by the physical adsorption of a gas on the surface of the solid and by determining the amount of adsorbate gas corresponding to a monomolecular layer on the surface. The schematic diagram of the BET analyzer is

shown in Fig. 2.9. The amount of gas adsorbed can be measured by a volumetric or continuous flow procedure.

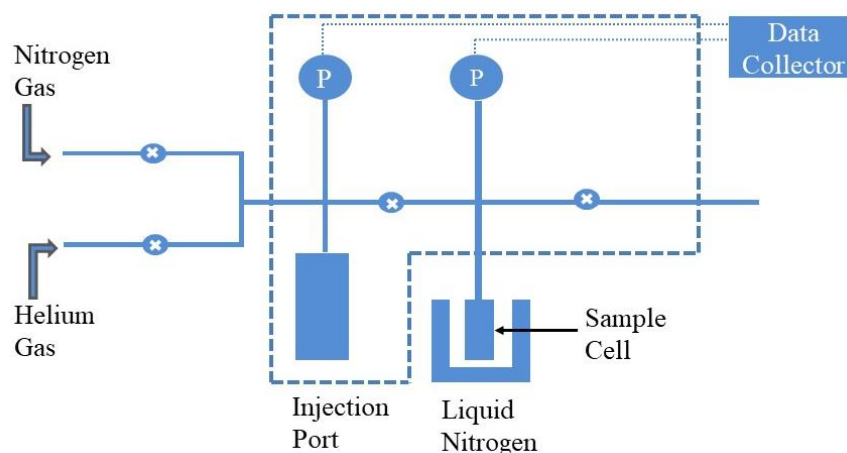


Fig. 2.9 Schematic diagram of BET surface area analyzer.

The data is analyzed as per BET adsorption isotherm equation as follows:

$$\frac{1}{[V_a \left(\frac{P_0}{P} - 1 \right)]} = \frac{C-1}{V_m C} \times \frac{P}{P_0} + \frac{1}{V_m C} \quad (2.9)$$

where P is the partial vapour pressure in pascals of adsorbate gas in equilibrium with the surface at a fixed temperature, P_0 is the saturated pressure of adsorbate gas in Pascals, V_a is the volume in ml of gas adsorbed at the experimental temperature and pressure, V_m is the volume in ml of gas adsorbed at the experimental conditions (T and P) to produce an apparent monolayer on the sample surface, and C is the dimensionless constant which is related to the enthalpy of adsorption of the adsorbate gas on the powder sample. This technique has been used mainly in this work to know about the surface area, pore volume, and pore diameter of the activated charcoal used for the preparation of electrodes for the supercapacitors.

2.3.8 Electrical characterization: Impedance spectroscopy

To study the electrical properties of the samples, different techniques were used. Impedance spectroscopy (IS) is an efficient method that utilizes an AC signal to excite or perturb a system under investigation and measure the response (current or voltage) [21-22]. The real and imaginary impedances are calculated and plotted against each other over different perturbation frequencies by using the measured data

to obtain impedance spectra. In order to measure quantitatively the electric and dielectric properties in the bulk and interfacial regions of solid and liquid materials IS data can be used.

In impedance spectroscopy, a sinusoidal alternating voltage $V = V_0 e^{j\omega t}$ is applied across the sample and the frequency response output current $I = I_0 e^{j\omega t + \theta}$ is recorded [23]. According to Ohm's law, the impedance (Z) of the circuit at any frequency (ω) can be given as [24]

$$Z^* = \frac{V}{I} = \frac{V_0 e^{j\omega t}}{I_0 e^{j\omega t + \theta}} = \frac{V_0}{I_0} e^{-j\theta} \quad (2.10)$$

Or,

$$Z^* = |Z| e^{-i\theta} = |Z| \cos\theta - i|Z| \sin\theta \quad (2.11)$$

$$Z^*(\omega) = Z' - iZ'' \quad (2.12)$$

Where Z' and Z'' are respectively the real and imaginary parts of the impedance. The phase angle is given as follows:

$$\theta = \tan^{-1} \left(\frac{Z''}{Z'} \right) \quad (2.13)$$

The impedance spectroscopy can also be used to measure the behaviour of the materials in terms of complex conductivity (σ^*), complex modulus (M^*), and complex permittivity (ϵ^*) as shown in Table 2.1.

Table 2.1 The interrelationship between four formalisms of impedance spectroscopy. ($j = \sqrt{-1}$)

Formalism	Symbol	Relation	Complex Form
Impedance	Z^*	$(V_0/I_0) e^{-j\theta}$	$Z' + jZ''$
Conductivity	σ^*	$L/(Z^*A)$	$\sigma' + j\sigma''$
Modulus	M^*	$j\omega C_0 Z^*$	$M' + jM''$
Permittivity	ϵ^*	$1/j\omega C_0 Z^*$	$\epsilon' + j\epsilon''$

Among these formalisms, the impedance and conductivity representations are used for analyzing the electrical behaviour of the sample in terms of bulk resistance (R) and its

electrical equivalent circuits. While the complex permittivity and modulus representations are generally used for analyzing the dielectric response of the sample.

In the present study, the electrical properties of the NASICONs, garnets, and their composites with IL were studied using an impedance analyzer (Hioki IM3570) in a frequency range of 4 Hz-5 MHz. Conductive silver paste or graphite paste was used for the electrical contacts. The cylindrical cells were obtained using pellets of ~ 9mm diameter with conductive paste on both sides and sandwiched between stainless steel discs to be used for the electrical measurements. The temperature dependent electrical properties were studied by keeping the sample holder in a PID-controlled furnace. The schematic diagram of the sample holder and measurement arrangement is shown in Fig. 2.10. The measurements were carried out mostly in a steady state mode in the temperature range of 30-165 °C. Some high and low temperature studies have also been performed. The complex conductivity (σ^*) of the composites has been calculated using the equation below:

$$\sigma^* = \frac{l}{Z^* A} \quad (2.14)$$

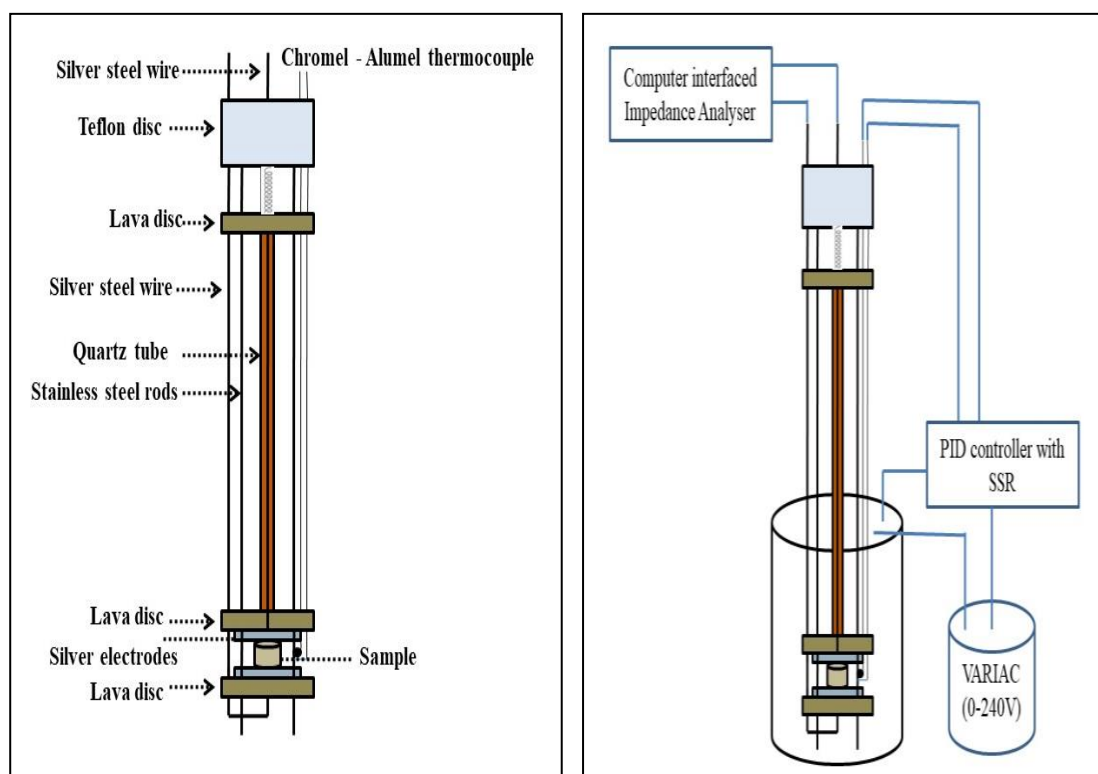


Fig. 2.10 Schematic diagram for (a) sample holder and (b) experimental setup for electrical conductivity measurement.

On simplifying,

$$\sigma^* = \frac{l \cos\theta}{|Z|A} - \frac{l \sin\theta}{|Z|A} = \sigma' - j\sigma'' \quad (2.15)$$

where l and A are the length and cross-sectional areas of the sample. The real and imaginary parts of the σ^* give the ac conductivity and conductivity loss of the composites respectively.

The σ - ω spectra for fast ionic conducting ceramic solids can be broadly divided into three regions as shown in Fig. 2.11. Region I shows a drastic fall in conductivity (at lower frequencies) due to the interfacial polarization. In region II, conductivity almost saturates for a wide range of frequency and refers to the long-range diffusive motion of ions; the value at the plateau is known as dc conductivity. Now, region III at higher frequencies gives a dispersion that corresponds to a short-range ionic motion. This behaviour of conductivity spectra obeys the universal Jonscher power law (JPL) characteristics [23] as:

$$\sigma = \sigma_{dc} + A\omega^n \quad (2.16)$$

where σ_{dc} is the frequency-independent conductivity at a plateau, A is the pre-exponential factor and n is the fractional exponent which generally lies between 0 and 1.

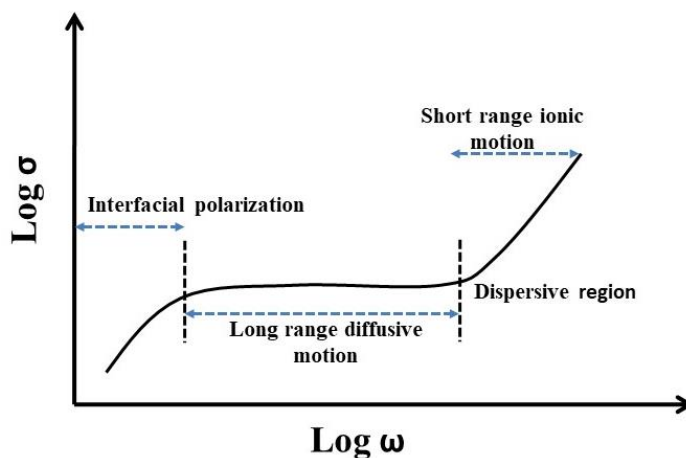


Fig. 2.11 Frequency dependence of ac conductivity in accordance with Jonscher's universal power law.

The value of n infers about the different types of ion conduction processes taking place in disordered materials. This relationship has been derived as a special case for materials in which the a.c. conductivity is accurately frequency-independent at low frequencies.

The modified form of JPL is the Almond-West formalism [25] defines the hopping rate for materials that do not show a frequency-independent conductivity plateau and according to this formalism, the hopping rate (ω_p) was defined as

$$\sigma(\omega) = \sigma_{dc}[1+(\omega/\omega_p)^n] \quad (2.17)$$

An ion conducting solid is an electronic insulator but allows ionic transport through it. Thus, acts like a leaky/lossy capacitor. So, an ion-conducting sample can be modelled as a parallel combination of the loss-less capacitor (C) with a resistor (R), and its impedance is given as

$$Z^* = \frac{R/i\omega C}{R + \frac{1}{i\omega C}} \quad (2.18)$$

On simplifying,

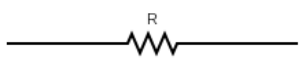
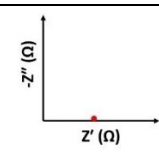
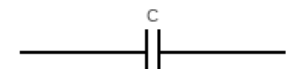
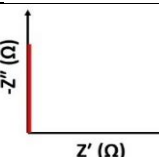
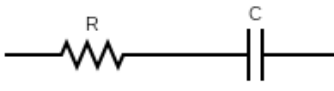
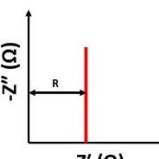
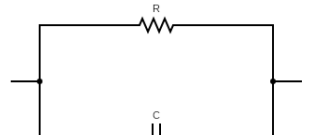
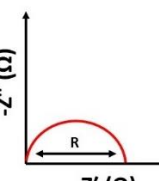
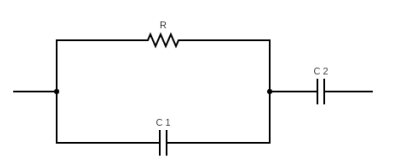
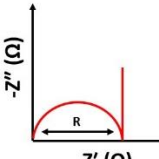
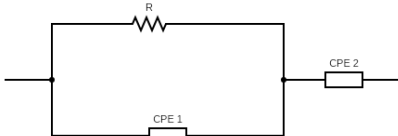
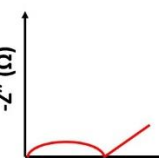
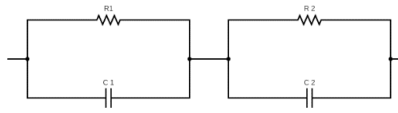
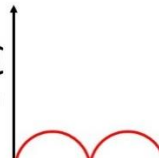
$$Z' = \frac{R}{1+(\omega CR)^2} \quad \text{and} \quad Z'' = \frac{\omega CR^2}{1+(\omega CR)^2}$$

Eliminating ω , one gets,

$$\left(Z' - \frac{R}{2}\right)^2 + Z'' = \frac{R^2}{4} \quad (2.19)$$

So, the Nyquist plot ($|Z'|$ versus $|Z''|$) exhibits a perfect semicircle with its center on the real axis (single relaxation, Debye type). The resistance of the material is given by its diameter. In a practical situation, the semicircle is seen to be depressed (non-Debye type), attributed to the distribution of relaxation times. The different relaxations are attributed to grain orientation/mismatch, and load charge accumulation due to grain, grain boundaries, and interface.

Table 2.2 Nyquist plots of common interest and their corresponding equivalent circuit.

Electrical circuit	Z^*	Plot
	$Z' = R, Z'' = 0$ $Z^* = R$	
	$Z' = 0, Z'' = \frac{1}{\omega C}$ $Z^* = \frac{1}{i\omega C}$	
	$Z' = R, Z'' = \frac{1}{\omega C}$ $Z^* = R + \frac{1}{i\omega C}$	
	$Z^* = \frac{R \cdot \frac{1}{i\omega C}}{R + \frac{1}{i\omega C}}$ $\left(Z' - \frac{R}{2}\right)^2 + Z''^2 = Z_a$	
	$Z^* = \frac{R}{1 + i\omega C_1 R} + \frac{1}{i\omega C_2}$	
	$Z^* = \frac{R \cdot CPE_1}{R + CPE_1} + CPE_2$ Where $CPE = \frac{Z_0}{(i\omega)^\alpha}$ CPE ₁ is lossy capacitor CPE ₂ is lossy capacitor at interface	
	$Z_1^* + Z_2^*$ $Z_1^* = \frac{R_1}{1 + i\omega C_1 R_1}$ $Z_2^* = \frac{R_2}{1 + i\omega C_2 R_2}$	

Thus, instead of a perfect capacitor, a constant phase element (CPE) [24] in parallel combination with a resistor (R) is used as an appropriate model for the Nyquist plots. CPE is viewed as a leaky/lossy capacitor and is defined as:

$$Z_{CPE} = \frac{Z_0}{(i\omega)^\alpha} \tag{2.20}$$

Here, α lies between 0 and 1. When $\alpha=0$, Z_{CPE} becomes frequency independent indicative of pure resistive nature, $Z_0 = R$. On the other hand, when $\alpha=1$, Z_{CPE} is written as $\frac{Z_0}{i\omega}$ with Z_0 becoming $\frac{1}{C}$. Thus, CPE acts as a pure capacitor with an impedance as $1/i\omega C$. CPE behaves as an intermediate between a resistor and a capacitor for all other values of α lying between 0 and 1.

Based on the ion transport mechanism in the composites, various impedance circuits can be designed to fit the Nyquist plots. Some of the configurations are given in Table 2.2. In the present work, EIS impedance analysis software has been used for fitting various models as given in table 2.2 above.

2.3.9 Electrochemical cell characterization

To check the electrochemical performance and properties of devices three main techniques are commonly used. These techniques include linear sweep voltammetry (LSV), cyclic voltammetry (CV), and galvanostatic charge-discharge (GCD) studies. CV and LSV are used to measure the current by varying potential against time and GCD deals with applying a current with time and measuring voltage.

Particularly for liquid electrolytes, a three-electrode system is used. These electrodes are known as working, counter, and reference [26]. The reference electrode maintains constant voltage and at the working electrode (or test electrode) reduction-oxidation takes place. The counter electrode, also known as the auxiliary electrode, serves as the source/sink of electrons. The current from the external circuit passes through the counter electrode. The use of these three electrodes mainly in highly conducting liquid electrolytes makes it possible the concurrent measurement of current and voltage accurately. The schematic diagram of a typical three electrode system is shown in Fig. 2.12(a). By joining reference and counter electrodes, these three electrode systems can be tailored into two electrode system, mainly used for studying solid electrolytes or sandwich geometry cells as shown in Fig 2.12(b).

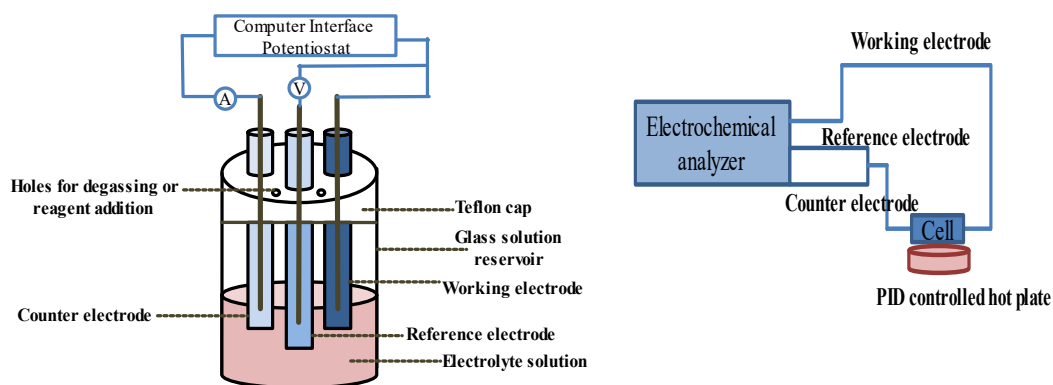


Fig. 2.12 (a) Block diagram of CV setup. (b) Block diagram of two electrode setup for measurement of electrochemical performance used in the present study. The setup is capable of wide temperature characterization.

Linear sweep voltammetry: It involves applying a linearly increasing or decreasing voltage waveform to the working electrode while measuring the resulting current response. The electrochemical stability window (ESW) of the composites has been studied using reversible and blocking electrodes [27-28]. To check the electrolyte's decomposition potential, the cell was prepared by sandwiching the pellet of the composite between blocking electrodes of silver. Also, to understand the potential stability of the composites, symmetric cells of type $\text{Li}|\text{sample}|\text{Li}$ were prepared in an argon filled glove box (MTI corp.).

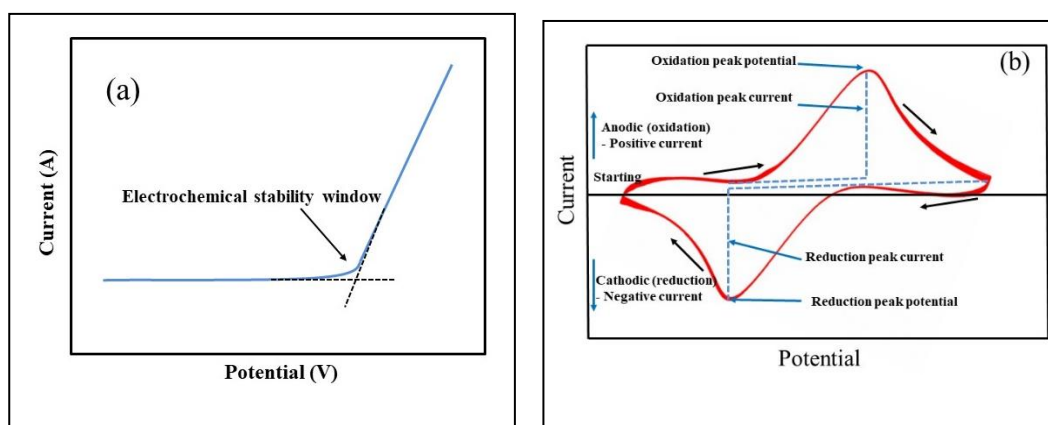


Fig. 2.13 (a) A typical LSV curve showing ESW, (b) a Typical CV curve for redox reaction.

The potential breakdown where the current shows abrupt rise was measured as shown in Fig. 2.13 (a), and the onset voltage was considered as the ESW limit. This limit may vary for blocking electrode configuration.

Cyclic Voltammetry (CV): This electrochemical technique has been used to investigate the redox properties and behaviour of chemical systems. It provides information about the electrochemical reactions that occur at an electrode surface as a function of applied voltage. According to the convention, a peak appearing in the direction of increasing voltage is considered oxidation and the one in the opposite direction belongs to reduction. A typical CV scan is shown in Fig. 2.13(b). In the present study, the CV scan was carried out for the battery to check the oxidation and reduction peaks. The intensity of these peaks also gives information about how chemical reactions are taking place at the working electrode. The reversible nature was also seen in repeated cycles of CV scans.

For supercapacitors, the CV scans were carried out to investigate the formation of interfacial supercapacitors, and operating voltage. The stability of these fabricated supercapacitors was checked by cycling the cell with various scan rates and also by doing a large number of scans at a single scan rate. From the hysteresis curves formed, the charge storage ability of the devices was assessed. The specific capacitance of these supercapacitors has been calculated from the CV scans using the equation:

$$C = \frac{Q}{mV} = \frac{I}{m\left(\frac{V}{t}\right)} \quad (2.21)$$

where, I is the corresponding current, m is the mass of a single electrode, and V/t is the voltage scan rate and is given as K. So, equation 2.21 can be written as

$$I = C \times m \times K \quad (2.22)$$

In the CV curve, the current changes by changing the potential from V1 to V2. Therefore, equation 2.22 can be written as

$$\int_{V_1}^{V_2} I(V)dV = \int_{V_1}^{V_2} (C \times m \times K)dV \quad (2.23)$$

$\int_{V_1}^{V_2} I(V)dV$ refers to the area under the CV curve. Therefore, specific capacitance can be calculated for the CV curve by the following equation:

$$C_p = \frac{\text{Area under CV curve}}{(V_2 - V_1)mK} \quad (2.24)$$

Galvanostatic charge-discharge (GCD): This technique helps in understanding the charge storage mechanisms, capacity fade, cycling stability, and overall performance of batteries and supercapacitors for various applications [29-30]. In GCD, a repetitive loop of charging and discharging is monitored. The set operating voltage of devices is optimized using LSV and CV scans. Then, charge discharge cycles are conducted at a constant current. A typical result of the GCD cycle for battery and EDLC is shown in Fig. 2.14 (a) and (b) respectively. In the present work, the GCD cycles were carried out for battery and supercapacitors to check their performance. In batteries, specific capacitance can be calculated using the discharge time and stable voltage value.

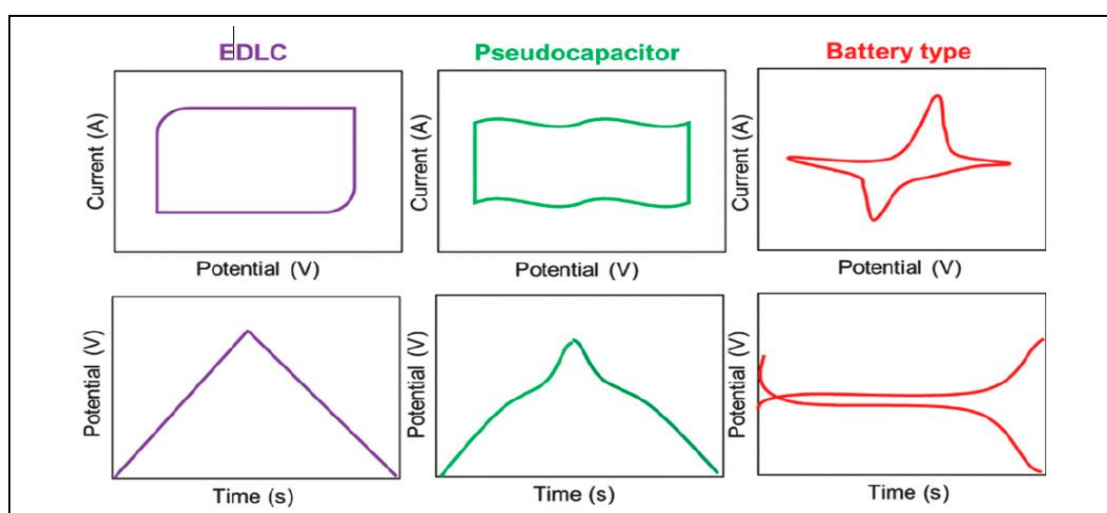


Fig. 2.14 A typical CV and GCD curve for EDLC, pseudo supercapacitor, and battery [31].

In the case of supercapacitors, while discharging a small voltage drop is observed due to equivalent series resistance (ESR) of the current collector and electrode contact. The ESR value gives information about contact resistance and helps in the study of interfacial charge transport reactance. The ESR with current density is calculated using the equation given below:

$$\text{ESR} = \frac{\text{Voltage drop (IR drop)}}{2 \text{ Discharge current}}$$

The specific capacitance (F/g) for a single electrode and specific energy (Wh/kg) and power (W/kg) for the device is calculated from the charging-discharging curve by using the following equations:

$$\text{Specific capacitance (C}_s\text{)} = \frac{2I\Delta t}{m\Delta V}$$

$$\text{Specific energy (E)} = \frac{C_s\Delta V^2}{7.2}$$

$$\text{Specific power (P)} = \frac{3600E_s}{\Delta t}$$

where Δt is the discharging time, ΔV is the voltage window excluding IR drop, I is the constant discharge current, and m is the average mass of the active material (charcoal) deposited on a single electrode. All these equations have been elaborated in the specific chapters in detail.

The systematic discussion on different composites is presented from next chapter onwards.

References:

- [1] Z. Jiang, L. Yuehua, C. Han, Z. He, W. Meng, L. Dai, and L. Wang, "K doping on Li site enables $\text{LiTi}_2(\text{PO}_4)_3/\text{C}$ excellent lithium storage performance," *Solid State Ionics*, vol. 341, pp. 115036, 2019, doi: 10.1016/j.ssi.2019.115036.
- [2] P. Zhang, M. Matsui, Y. Takeda, O. Yamamoto, and N. Imanishi, "Water-stable lithium ion conducting solid electrolyte of iron and aluminum doped NASICON-type $\text{LiTi}_2(\text{PO}_4)_3$," *Solid State Ionics*, vol. 263, pp. 27–32, 2014, doi: 10.1016/j.ssi.2014.04.017.
- [3] Y. Shimonishi, A. Toda, T. Zhang, A. Hirano, N. Imanishi, O. Yamamoto, and Y. Takeda, "Synthesis of garnet-type $\text{Li}_{7-x}\text{La}_3\text{Zr}_2\text{O}_{12-1/2x}$ and its stability in aqueous solutions," *Solid State Ionics*, vol. 183, pp. 48–53, 2011, doi: 10.1016/j.ssi.2010.12.010.
- [4] A. A. Bunaciu, E. G. Udristioiu, and H. Y. Aboul-Enein, "X-Ray Diffraction : Instrumentation and Applications," *Critical Reviews in Analytical Chemistry*,

-
- vol. 8347, pp. 289-299, 2015, doi: 10.1080/10408347.2014.949616.
- [5] B. D. Cullity, *Elements of X-ray diffraction*, 2nd Editio. Addison-Wesley Publishing Company, Inc., Reading, Massachusetts, 1956.
- [6] B. M. Collett, “Scanning Electron Microscopy: A Review and Report of Research in Wood Science,” *Wood and Fiber Science*, vol. 2, pp. 113–133, 1970.
- [7] A. Mayeen, L. Shaji, A. K. Nair, and N. Kalarikkal, “Morphological Characterization of Nanomaterials,” *Characterization of Nanomaterials*, pp. 335-364, 2018.
- [8] K. P. Severin, *Energy Dispersive Spectrometry of Common Rock Forming Minerals*. Kluwer Academic Publishers, 2004.
- [9] R. G. N. Brodusch, H. Demers, “Field emission scanning electron microscopy: New perspectives for materials characterization,” *Springer, Singapore*, 2018.
- [10] A. V. Gira, G. Caputo, M. C. Ferro, and C. Outline, “Application of Scanning Electron Microscopy e Energy Dispersive X-Ray Spectroscopy,” *Comprehensive Analytical Chemistry*, 75, 2017, doi: 10.1016/bs.coac.2016.10.002.
- [11] T. Tyner and J. Francis, “Hydrochloric Acid,” *ACS Reagent Chemicals*, 2016, doi: 10.1021/acsreagents.
- [12] L. A. Lyon, C. D. Keating, A. P. Fox, B. E. Baker, L. He, S. R. Nicewarner, S. P. Mulvaney, and M. J. Natan, “Raman Spectroscopy,” *Analytical Chemistry*, vol. 70, no. 12, pp. 341–362, 1998.
- [13] G. V. Alexander, N. C. Rosero-Navarro, A. Miura, K. Tadanaga, and R. Murugan, “Electrochemical performance of a garnet solid electrolyte based lithium metal battery with interface modification,” *Journal of Materials Chemistry A*, vol. 6, pp. 21018–21028, 2018, doi: 10.1039/C8TA07652A.
- [14] G.W. H. Hohne, W. F. Hemminger, and H. J. Flammersheim, “Applications of Differential scanning calorimetry,” *Springer-Veriag, Berlin*, 2003, doi: 10.1007/978-3-662-06710-9.

-
- [15] W. Steinmann, S. Walter, M. Beckers, G. Seide, and T. Gries, “Thermal analysis of phase transitions and crystallization in polymeric fibers,” *Applications of calorimetry in a wide context- differential scanning calorimetry, isothermal titration calorimetry and microcalorimetry*, 2013.
- [16] M. J. Vold, “Differential thermal analysis,” *Anal. Chem.*, vol. 21, pp. 683–688, 1949.
- [17] E. Pungor, “A Practical Guide to Instrumental Analysis,” *Florida: Boca Raton*, pp. 181–191, 1995.
- [18] Peter J. Haines, *Thermal Methods of Analysis: Principles, Applications and Problems*. Dordrecht: Springer Science + Business Media, 1995.
- [19] J. S. Ko, C. S. Choi, B. Dunn, and J. W. Long, “Electrochemical Characterization of Na-Ion Charge-Storage Properties for Nanostructured $\text{NaTi}_2(\text{PO}_4)_3$ as a Function of Crystalline Order,” *Journal of The Electrochemical Society*, vol. 164, pp. A2124–A2130, 2017, doi: 10.1149/2.1391709jes.
- [20] E. P. Barrett, L. G. Joyner, and P. P. Halenda, “The Determination of Pore Volume and Area Distributions in Porous Substances. I. Computations from Nitrogen Isotherms,” *Journal of the American Chemical Society*, vol. 73, pp. 373–380, 1951, doi: 10.1021/ja01145a126.
- [21] J. Ross Macdonald, *Impedance Spectroscopy*. New York: John Wiley & Sons, 1987.
- [22] A. K. Arof, S. Amirudin, S. Z. Yusof, and I. M. Noor, “A method based on impedance spectroscopy to determine transport properties of polymer electrolytes,” *Physical Chemistry Chemical Physics*, vol. 16, pp. 1856–1867, 2014, doi: 10.1039/c3cp53830c.
- [23] A. K. Jonscher, “Dielectric relaxation in solids,” *Journal of Physics D: Applied Physics*, vol. 32, 1999, doi: 10.1088/0022-3727/32/14/201.
- [24] J. R. Macdonald, “Impedance spectroscopy: Models, data fitting, and analysis,” *Solid State Ionics*, vol. 176, pp. 1961–1969, 2005, doi:

- 10.1016/j.ssi.2004.05.035.
- [25] D. P. Almond, C. C. Hunter, and A. R. West, “The extraction of ionic conductivities and hopping rates from a.c. conductivity data,” *Journal of Materials Science*, vol. 19, pp. 3236–3248, 1984, doi: 10.1007/BF00549810.
- [26] N. Elgrishi, K. J. Rountree, B. D. McCarthy, E. S. Rountree, T. T. Eisenhart, and J. L. Dempsey, “A Practical Beginner’s Guide to Cyclic Voltammetry,” *Journal of Chemical Education*, vol. 95, pp. 197–206, 2018, doi: 10.1021/acs.jchemed.7b00361.
- [27] A. Méry, S. Rousselot, D. Lepage, and M. Dollé, “A Critical Review for an Accurate Electrochemical Stability Composite Electrolytes,” *Materials*, vol. 14, pp. 3840, 2021.
- [28] Y. Benabed, M. Rioux, S. Rousselot, G. Hautier, and M. Dollé, “Assessing the Electrochemical Stability Window of NASICON-Type Solid Electrolytes,” *Frontiers in Energy Research*, vol. 9, pp. 1–13, 2021, doi: 10.3389/fenrg.2021.682008.
- [29] Y. Liu, S. P. Jiang, and Z. Shao, “Intercalation pseudocapacitance in electrochemical energy storage: recent advances in fundamental understanding and materials development,” *Materials Today Advances*, vol. 7, pp. 100072, 2020, doi: 10.1016/j.mtadv.2020.100072.
- [30] F. Licht, M. A. Davis, and H. A. Andreas, “Charge redistribution and electrode history impact galvanostatic charging/discharging and associated figures of merit,” *Journal of Power Sources*, vol. 446, 2019, pp. 227354, 2020, doi: 10.1016/j.jpowsour.2019.227354.
- [31] S. Nahirniak, A. Ray, and B. Saruhan, “Challenges and Future Prospects of the MXene-Based Materials for Energy Storage Applications,” *Batteries*, vol. 9, 2023, doi: 10.3390/batteries9020126.

Chapter 3*

Ionic Liquid Dispersed Sol-Gel Derived $\text{LiTi}_2(\text{PO}_4)_3$ Composites

In this chapter, the effect of ionic liquid (IL) dispersion on Li^+ -NASICON has been discussed. The most basic NASICON structured Li^+ ion system $\text{LiTi}_2(\text{PO}_4)_3$ (LTP) has been used for the IL dispersion. LTP has been synthesized by the sol-gel route (as discussed in section 2.1) to accommodate ionic liquid (IL) in a significant amount. Ionic liquid EMIMBF₄ has been used in the composites with LTP. The composites are labelled as LTP-xIL, where x=2,5,13, and 17 weight percentage of IL. Compositions with IL > 17 wt% were avoided as they did not yield a uniform distribution of IL over LTP, rather the excess IL spills out. The electrical, thermal, and structural properties of the composites have been discussed in detail and mechanism of ionic transport is proposed.

This chapter thus provides various experimental evidences to suggest a mechanism for enhanced ionic transport for the composites that have been developed. The IL content in the composites is varied systematically and it is revealed that even a small amount of IL addition can enhance the conductivity. It is therefore suggested that the grain boundary effects are suppressed due to presence of IL. Ionic liquid's presence just helps in facilitating the motion of Li^+ ions in the NASICON matrix. Solid state of the composites is well preserved as there are sufficient proofs of transport through LTP grains.

The composites have been further explored as a potential electrolyte for the lithium batteries.

* Parts of the results of this chapter are published in: G. Kaur, M. D. Singh, S. C. Sivasubramanian, A. Dalvi, "Investigations on enhanced ionic conduction in ionic liquid dispersed sol-gel derived $\text{LiTi}_2(\text{PO}_4)_3$ ", *Materials Research Bulletin*. 145 (2022) 111555.

3.1 Structural studies

At the outset, we present the structural characterization of the hybrid composites developed by us, by using various techniques. Detailed results are discussed here.

3.1.1 X-Ray diffraction (XRD)

High temperature in situ XRD patterns for pristine LTP (Fig. 3.1a) are shown in a wide range of temperatures (34-500 °C). The HT-XRD was also carried out on a composition LTP-13IL (Fig. 3.1b) for which IL content almost reaches its saturation. Other investigations (as discussed later) were also performed on this sample with adequate IL content. All peaks corresponding to sol-gel-derived LTP match well with the literature reported values [1].

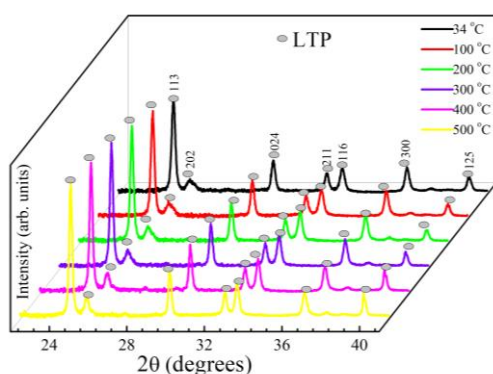


Fig. 3.1(a) HT-XRD patterns for pristine sol-gel derived LTP.

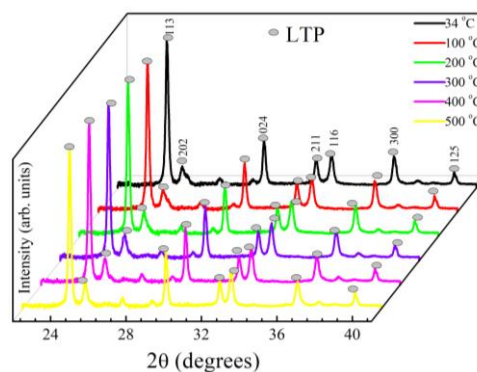


Fig. 3.1(b) HT-XRD patterns for LTP-13IL.

The crystallite size calculated using the Debye Scherer relation was found to be ~36 nm. Further, even after the addition of IL, there is no shift in LTP peak positions and all the peaks remain intact in a wide temperature range. Further, IL addition does not lead to any new peak that suggests no new crystalline compound formation. Thus at least up to 500 °C LTP structure is stable. The lattice parameters for the LTP-13IL composite are shown in Table 3.1. A significant expansion with temperature is seen for the *c* value, which leads to a monotonic rise in unit cell volume.

Table 3.1: Lattice parameters a, c and unit cell volume for LTP-13IL considering hexagonal unit cell.

T (°C)	a (Å)	c (Å)	volume(Å ³)
34	8.4945	20.8157	1300.7757
100	8.4980	20.8434	1303.5796
200	8.4972	20.9010	1306.9451
300	8.4969	20.9850	1312.0951
400	8.4964	21.0461	1315.7717
500	8.4991	21.1121	1320.7351

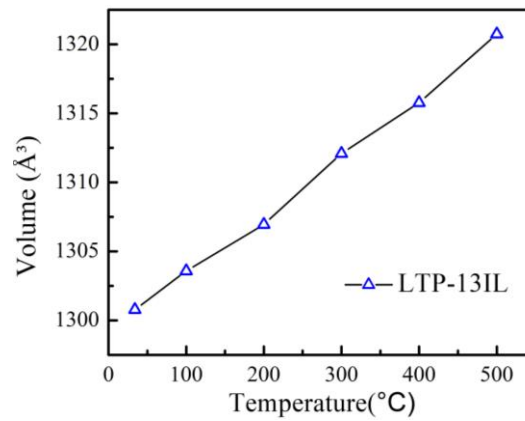


Fig. 3.1(c) The unit cell volume as a function of temperature.

Unit cell volume of LTP-13IL is plotted as a function of temperature in Fig. 3.1(c). The volume is found to be comparable with that reported in previous studies on LTP [2].

3.1.2 Field emission scanning electron microscopy (FESEM)

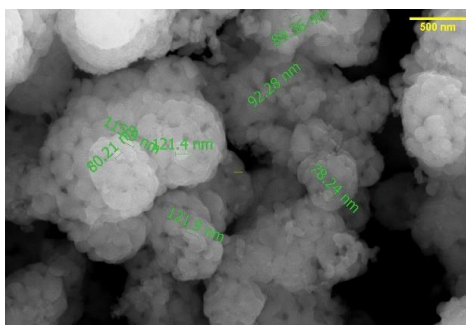


Fig. 3.2(a) FESEM image of as prepared LTP.

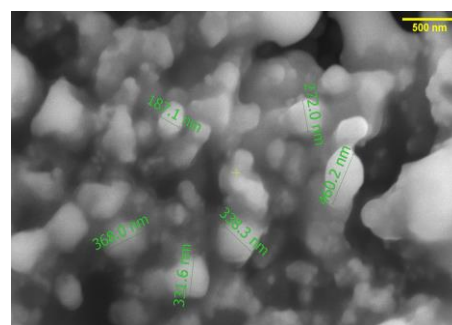


Fig. 3.2(b) FESEM image of LTP-13IL.

Fig. 3.2(a) and 3.2(b) show FESEM images of LTP and LTP-13IL composites, respectively. As evident, sol-gel synthesized LTP exhibits a porous structure where particles of size 60-80 nm appear to exist in a sphere-like structure. The porous nature is not seen when IL is added to the matrix. Apparently, the size of LTP grains and the pore volume decrease. The IL seems to be occupying the pore volume, and also the space between grains (Fig. 3.2b).

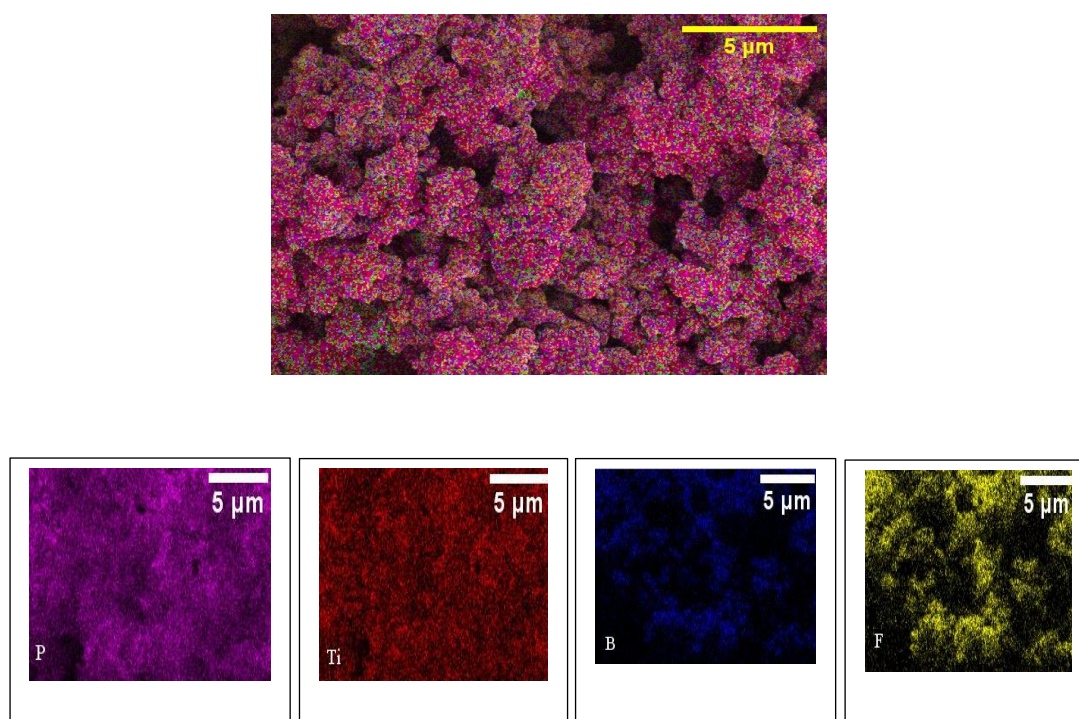


Fig. 3.2 (c) EDS mapping for LTP-13IL and elemental distribution maps.

EDS mapping (qualitative) over FESEM image on LTP-13IL is shown in Fig. 3.2(c). The elemental distribution map suggests that Ti and P are densely present and evenly distributed. Further, F and B are homogeneously present, but in a relatively lesser amount due to the small amount of IL in the matrix. There is an apparent homogeneity throughout the composite with no visible segregation.

3.2 Thermogravimetric analysis (TGA)

TGA analysis was done for LTP-13IL to check the thermal stability of the composites. As seen in Fig. 3.3 in the LTP-13IL composite, a weight loss is seen in the range 300-425 °C due to IL evaporation/decomposition. On the other hand, TGA of pure IL exhibits the same process starting at significantly high temperatures (350 °C). The

~13% weight loss indicates all the IL incorporated in the composite is removed at 425 °C. The evaporation/decomposition process, in the case of LTP-13IL composite, starting at a lower temperature could be due to (i) the presence of trace amounts of impurities in grain-grain interfaces, (ii) interaction of IL ions with the LTP matrix of the interface (LTP surface - IL ion adsorptions, compared to IL ion - IL ion interactions in the liquid.). Impurities are known to reduce T_d as reported earlier [3-4]. These along with HT-XRD results suggest that the two phases viz., IL and LTP coexist at least up to ~300 °C. Accordingly, electrical measurements were performed in an appropriate temperature range (30-200 °C) where the structure is likely to be thermally stable.

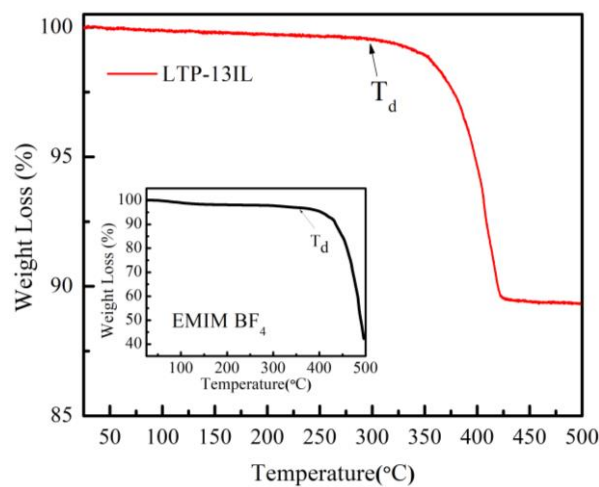


Fig. 3.3 TGA scan of the LTP-13IL. Inset of Fig. 3: TGA of pure ionic liquid.

3.3 Electrical conductivity

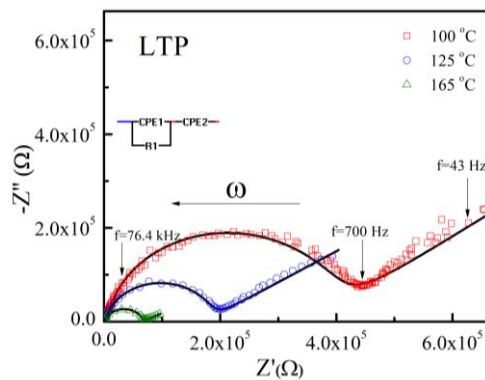


Fig. 3.4(a) Nyquist plots for LTP with equivalent circuit.

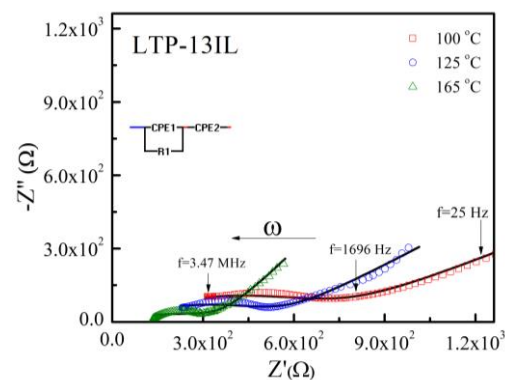


Fig. 3.4(b) Nyquist plots for LTP-13IL with equivalent circuit.

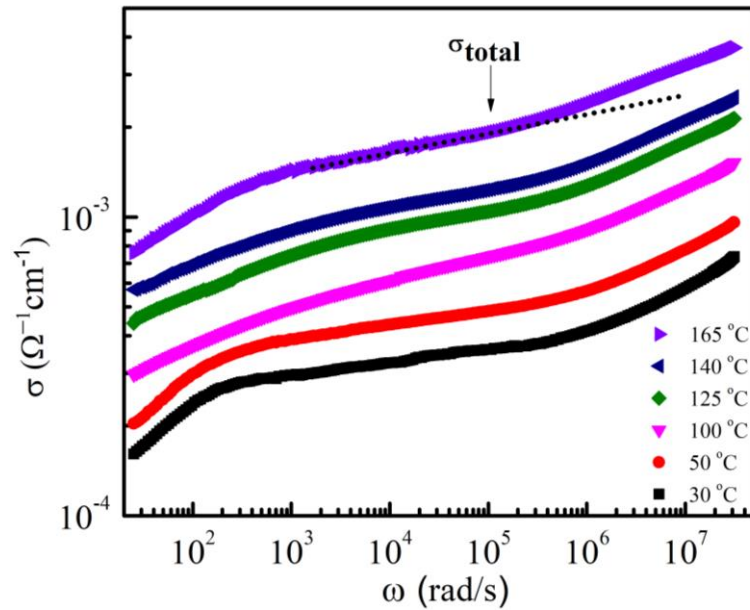


Fig. 3.4(c) Frequency dependence of total conductivity at different temperatures for LTP-13IL. The σ_{total} was also extracted from plateau, at onset of dc to dispersion as shown for one temperature (165 °C).

Fig. 3.4(a) and 3.4(b) show the Nyquist plot for LTP and LTP-13IL at different temperatures along with the equivalent circuit used for fitting. A single broad semicircle is seen in both the composites followed by an inclined line/spur at lower frequencies. However, the semicircle is more depressed in the case of an IL-containing composite. Possibly due to high resistance, the semicircle expected for bulk is not evident and hence total contribution (bulk + grain boundary) for conductivity is obtained from the diameter of the observable semicircle. The frequency dependence of the conductivity i.e., σ - ω plot for LTP-13IL composite is shown in Fig. 3.4(c). The σ_{total} obtained from the Nyquist plot also matches well with the corresponding value obtained from the plateau of the σ - ω plot.

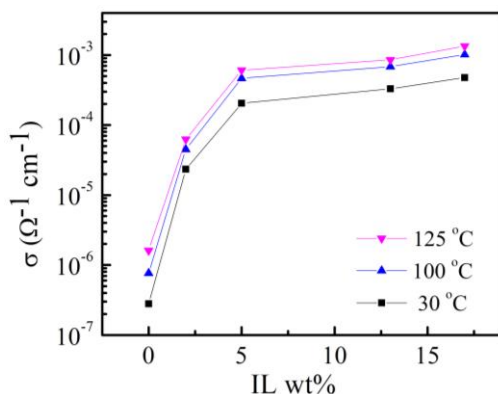


Fig. 3.5(a) Conductivity at three different temperatures with variation of IL content in the composite.

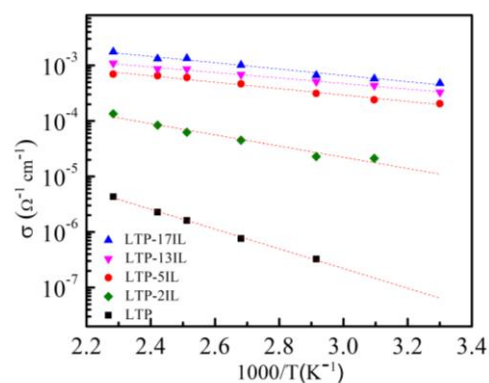


Fig. 3.5(b) Temperature dependence of total conductivity for all the composites.

Table 3.2: Room temperature conductivity and activation energy of ionic conduction as obtained from Fig. 5(b).

Composition	$\sigma_{\text{total}} (\Omega^{-1}\text{cm}^{-1})$ at 300 K	E_{σ} (eV)
LTP	2.8×10^{-7}	0.35
LTP-2IL	2.3×10^{-5}	0.20
LTP-5IL	2×10^{-4}	0.12
LTP-13IL	3.3×10^{-4}	0.10
LTP-17IL	4.8×10^{-4}	0.11

The conductivity values obtained have been plotted with the wt% of IL at three different temperatures in Fig. 3.5(a). It has been observed that with an increase in IL content conductivity exhibits a notable rise. The total conductivity value for all the composites has been plotted as a function of temperature (30-165 °C). As seen in Fig. 3.5(b) there is a systematic rise with Arrhenius type behaviour and the maximum conductivity is found to be in the range of 10^{-3} - 10^{-4} $\Omega^{-1}\text{cm}^{-1}$. There is a ~ 3 order of rise in conductivity for LTP-17IL as compared to pristine LTP. Further, the activation energy values of ionic liquid-containing composites are significantly smaller than that of pristine LTP as given in Table 3.2. The E_{σ} value initially drops with IL content and stabilizes for higher IL content to an almost constant value. Thus, looking at the conductivity trends we may

say, IL added up to 5 wt % of the sample increases the conductivity drastically. Further addition of IL only incrementally increases the conductivity. We may explain this as: initially up to 5 wt % the IL fills the gap in grain boundaries which restrict conduction; above 5 wt % the IL goes only to complete the monolayer above the surface of LTP; and beyond 17 wt% of the IL, the surface cannot hold the additional IL. To validate the above hypothesis, we may require further surface studies.

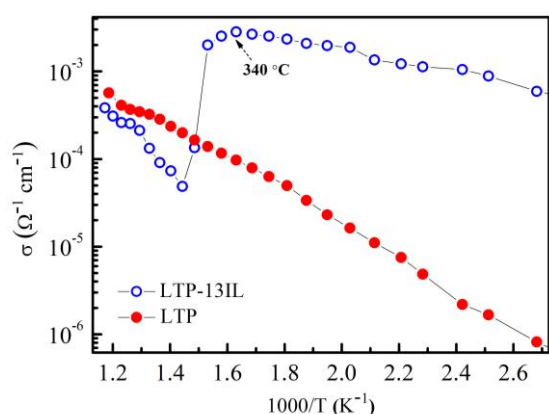


Fig. 3.5(c) Temperature dependence of total conductivity (30-600 °C) for LTP-13IL and pristine LTP. After IL decomposition the composite attains conductivity of LTP.

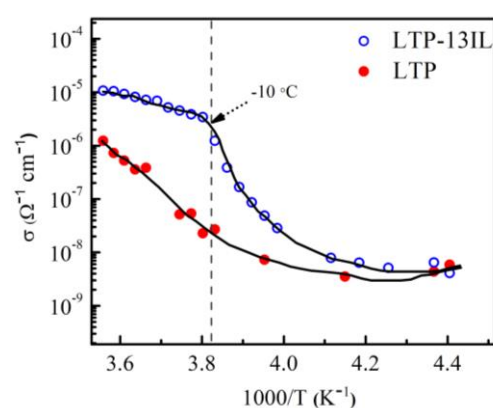


Fig. 3.5(d) Total conductivity with temperature (-50 °C to 10 °C) for LTP and LTP-13IL.

High temperature (30-600 °C) conductivity investigations were performed on LTP-13IL to comprehend the role of IL in transport. Conductivity was measured for $T \geq T_d$ of the ionic liquid. As depicted from Fig. 3.5(c) conductivity exhibits a systematic rise up to 340 °C followed by a drastic fall. The temperature where this conductivity drop occurs corresponds to the evaporation/decomposition temperature of IL [5-6] as has been also complemented in TGA thermograms. Temperature dependence of the conductivity of pristine LTP along with that of LTP-13IL is also shown for comparison. As evident, after the drop, the conductivity of LTP-13IL composite almost matches with that of LTP. It is well known that the conductivity of pristine LTP is dominated by large grain boundary impedance. Therefore, decomposition of the IL in the composite again introduces grain boundary impedance in the composite. This behaviour readily suggests an important role of IL in suppressing the grain boundary impedance.

Similarly, the temperature dependence of conductivity below room temperature is also investigated to understand the effect of low-temperature thermal events in the IL (Fig. 3.5 d). Interestingly, for LTP-13IL, the conductivity around $-10\text{ }^{\circ}\text{C}$ falls notably. At this temperature IL freezes. Further, the saturation below $-20\text{ }^{\circ}\text{C}$ may be attributed to poor thermal activation. Thus, poor conductivity of IL below its freezing again seems to play important role in degrading the electrical transport. On the other hand, for pristine LTP conductivity decreases gradually and reaches to a saturation, again due to poor thermally activated behaviour of mobile charge carriers [3]. A notable fall in the conductivity at T_d or freezing temperatures of IL is due to different reasons but suggests a role of IL in dictating the electrical transport. The melting point for IL depends on the way it is confined in the solid state and happens in the range of -10 to $-40\text{ }^{\circ}\text{C}$ [7]. Below the freezing temperature, the structural relaxation of IL units is likely to freeze which may be the reason for a sharp notable fall in the conductivity of the composite. Thus, both these conductivity variations suggest a major role of IL in electrical transport.

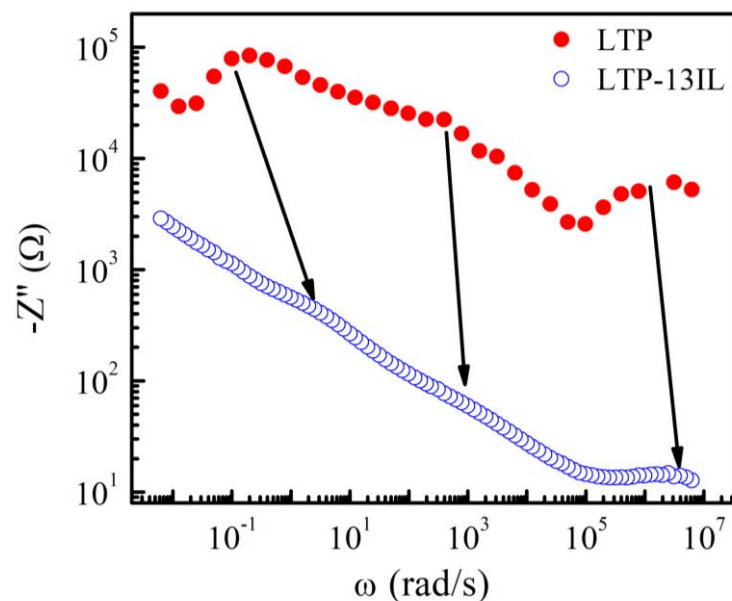


Fig. 3.6 Electrical response (Z'' vs ω) for LTP and LTP-13IL.

To further examine the mechanism, an electrical response from bulk, interfaces (grain boundaries and electrode-electrolyte) Z'' vs ω is plotted for $200\text{ }^{\circ}\text{C}$ (Fig. 3.6). The frequency dependence of the imaginary part of impedance (Z'') gives information about the hopping polarization loss [8]. The relaxation peak in the spectra corresponds to a

frequency where the fastest depolarization occurs at interfaces or bulk regions. In a way, it provides good qualitative information about electrical transport at various regions in the material. In Fig. 3.6, Z'' vs ω in a wide range of frequencies (1 mHz to 1 MHz) is plotted for LTP and LTP-13IL composites. As apparent in the case of LTP, three well-separated relaxation peaks are evident that may correspond to (lowest to highest frequency) electrode-electrolyte interface, grain-grain interface, and inter-grain/bulk relaxations. Apparently, for LTP-13IL the three peaks (though weak) are again evident with a much lower value of Z'' and shifted to higher frequencies. It may be therefore suggested that the polarization loss at grain boundaries and interface is suppressed. This, in turn, indicates significant depression in Z'' value in the case of IL-LTP composite which clearly suggests suppression of the grain boundary impedance. This may be due to the high conductivity in presence of IL in these regions. Interestingly, in this wide frequency region no new relaxation peak has appeared, thus pointing out that the relaxation processes (depolarization) correspond to only mobile Li^+ ions. The Z'' vs ω behaviour in BMIMBF_4 dispersed perovskite BCN-18 was also studied by Pannu et al. [8]. A huge suppression in the peaks corresponding to grain boundary was reported and attributed to suppression of grain boundary impedance.

3.4 The hybrid electrolyte under battery conditions:

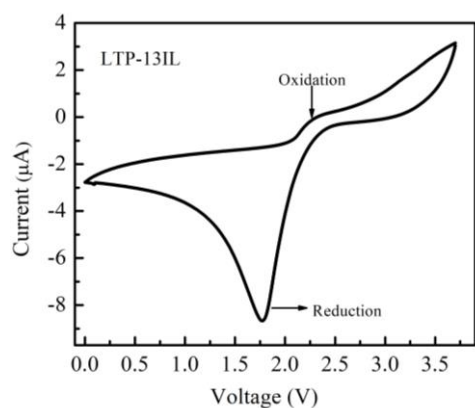


Fig. 3.7 Cyclic voltammety scan of LTP-13IL.

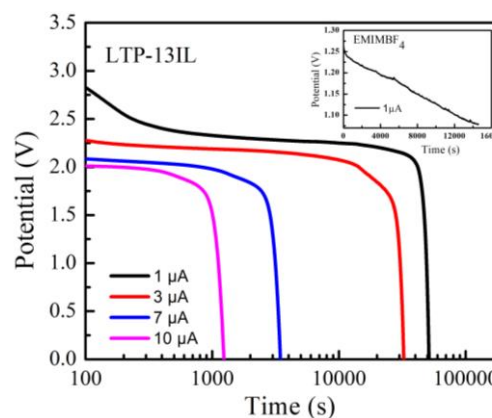
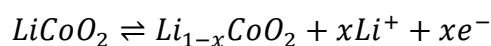


Fig. 3.8 Discharging of cell at different currents.

To study the potential of the ionic liquid containing composite as an electrolyte, Swagelok type cells with configuration $\text{LiCoO}_2|\text{sample}|\text{Li}$ were fabricated. A typical composite with 13 wt% IL i.e., LTP-13IL has been used for this study. The pellet of

composites was made of thickness $\sim 500 \mu\text{m}$. The active material loading on the cathode was $2\text{-}3 \text{ mg cm}^{-2}$. Firstly, a CV scan was performed in a range of $0\text{-}3.7 \text{ V}$. The oxidation and reduction peaks are visible at $\sim 2.25 \text{ V}$ and 1.76 V , respectively as shown in Fig. 3.7. The oxidation peak is though weak as compared to the reduction peak. CV scans were taken using LiCoO_2 as a working electrode against lithium metal. The following reaction may be suggested [9]:



The reversible nature of the reaction was also seen in repeated cycles of CV.

Further, the discharging at different currents was again studied for the same cell configuration and plotted in Fig. 3.8. Safely, $1 \mu\text{A}$ current can be drawn for around 11-12 hours. For higher load, the cell discharges fast. Voltage stability of around $2\text{-}2.5 \text{ V}$ is observed. The plots depict that electrolyte is stable under battery conditions. The current withdrawn is though less. These are the results of our very first fundamental study and they simply suggest stability of the composite electrolyte under battery conditions. It needs further engineering of the electrolyte-electrode interfaces and the thickness of the electrolyte material for applicability to high currents, which was not primary objective of the current study.

The electrochemical cell with pure IL as electrolyte (in Polypropylene membrane) were also fabricated for comparison. As seen in the inset of Fig. 3.8 the cell exhibits a maximum voltage of 1.26 V and while discharging it shows a gradual fall even at $1 \mu\text{A}$ current. Thus, IL alone in this geometry does not appear to be a suitable electrolyte for the batteries. However, its presence in a small amount in LTP leads to a stable electrolyte formation.

3.5 Replacing LTP by its superior version LATP

As it has been reported in literature that LTP's analogue $\text{Li}_{1.3}\text{Al}_{0.3}\text{Ti}_{1.7}(\text{PO}_4)_3$ (LATP) has better ionic conductivity [10]. So here LTP has been replaced by LATP to check about the role of this ceramic. For this similar to LTP, composites of LATP with EMIMBF_4 (IL) have been prepared with different weight percentage of IL. It can be seen from Fig. 3.9 (a) that there is a systematic rise with Arrhenius type behaviour giving maximum conductivity in the range of $10^{-2}\text{-}10^{-3} \Omega^{-1}\text{cm}^{-1}$. The conductivity as

expected is better here for the specific IL wt percentage as compared to LTP -IL composites. This shows that ceramic in the composite influence the electrical transport.

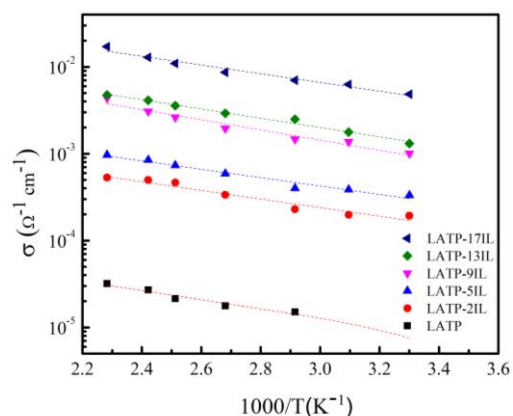


Fig. 3.9(a) Temperature dependence of total conductivity for all the composites.

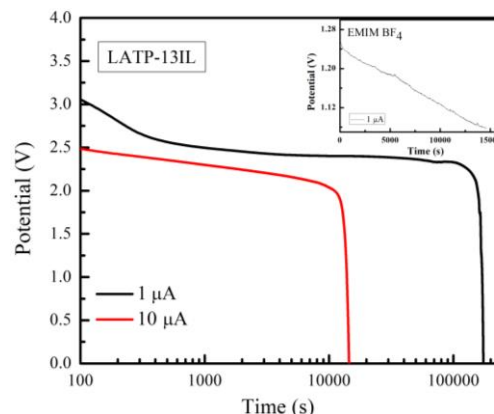


Fig. 3.9(b) Discharging of cell at different currents.

The potential of the LTP-IL composite as an electrolyte has been studied in Swagelok type cells with configuration $\text{LiCoO}_2|\text{sample}|\text{Li}$. The cell has been discharged at different currents. LTP-IL composite based cell discharges for longer time as compared to LTP-IL based composites. $10 \mu\text{A}$ current can be withdrawn for 4-5 hours depicting that this electrolyte is stable under battery conditions with higher discharge currents as compared to LTP-IL based composites.

3.6 A possible mechanism for ionic transport

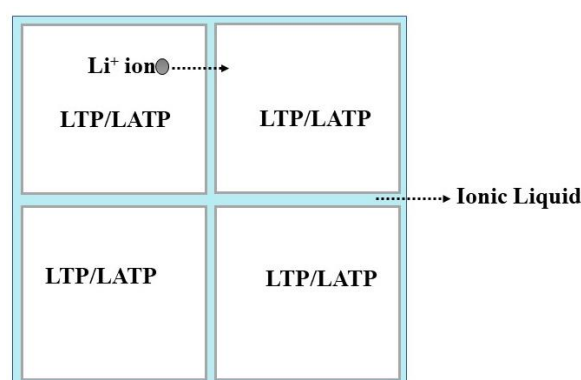


Fig. 3.10 Schematic diagram showing the movement of Li^+ ions in between LTP/LATP grains with the help of ionic liquid.

Based on the above findings a mechanism has been proposed for the ionic transport in LTP/LATP-IL composites as shown in Fig. 3.10. Although the mechanism is

qualitative, it is based on firm experimental observations. IL is confined between the grains of LTP/LATP. Its presence significantly reduces the grain boundary impedance and therefore facilitates inter-grain transport. Inspired by the Brick Layer model [11-13] one may propose that IL occupies the space between the LTP/LATP grains and provides a coupling [10].

The above hypothesis is based on the following evidences: (i) Ionic liquid cations and anions though exist in a molten state, the possibility of their contribution to electrical transport is rather weak in the current case. In such a compact and mechanically dense system, the long-range diffusive motion of ions with large radii [14] appears unlikely. The grain-grain interface is crowded with big IL ions. Thus, the possibility of electrical transport along the grain boundaries only due to IL is also less.

(ii) Z'' vs ω behaviour for the LTP-IL composites exhibits no new relaxation peak corresponding to IL. This strongly suggests that IL does not undergo any conductivity relaxation. Further, a notably small value of Z'' again compliments the possibility that IL facilitates Li^+ ion conduction across the grain boundaries. The subtle but notable relaxation peaks in the composite correspond only to mobile Li^+ ions.

(iii) In various systems (e.g., polymers, perovskites, glass-ceramics) IL incorporation leads to enhanced electrical transport [7, 15-16]. In polymer-based electrolyte systems, it is known that IL acts like a plasticizer and its role is to facilitate host ionic motion. For e.g., in some Mg^{2+} ion-containing gel polymer electrolytes, Mg^{2+} ions transference number dramatically increases only when IL occupies the host matrix [17]. Kwatek et al. [10] in their investigation on IL dispersed LTP/LATP suggested the role of IL in coupling the grains. In the present work as shown in the SEM image, the IL occupies the space in the matrix uniformly thus likely to facilitate inter-grain transport of small ions such as Li^+ .

(iv) The characteristic temperature dependence of conductivity for various pristine ionic liquids in a wide range of temperatures was systematically studied by Stoppa et al. [18]. According to which the ILs viz., EMIMBF₄, BMIMBF₄, HMIMBF₄ etc. follow Vogel-Fulcher-Tammann behaviour. Unlike the pristine ILs, in the present case, all the samples exhibit Arrhenius behaviour and thus rules out the possibility of long range diffusive contribution of IL ion to the electrical transport.

(v) At temperatures less than the IL freezing, a notable fall suggests that the regions at the grain boundaries, Li^+ ion migration is no longer supported by IL. Possibly, the frozen IL acts like an insulating barrier for Li^+ ion migration. On further cooling, even the thermally activated behaviour vanishes thus the total conductivity reaches saturation. On the other hand, at a temperature close to the decomposition of IL, conductivity again falls drastically to a value of LTP. This drastic fall (due to IL decomposition) further confirms IL's role in facilitating Li^+ ion transport.

(vi) The low activation energy for ionic transport as seen for high IL content samples matches well with the bulk conductivity of LTP as reported in various studies that further compliments the proposed model.

(vii) The electrochemical characterization does suggest a stable voltage and corresponding current only in the case of the cells with IL-LTP/LATP composites. Such stability is not seen for cells with IL alone as an electrolyte. This further suggests a predominant role of Li^+ ions in transport [19,10].

The above observations strongly suggest that IL ions have very low mobility and therefore do not act as mobile ions. However, their presence at the interfaces reduces the grain boundary impedance and offers moderate energy barriers for mobile Li^+ ions conduction.

The above tentative mechanism needs further verification with more theoretical inputs, and new practical studies with different ILs.

3.7 Summary

- (i) It has been demonstrated that IL-LTP/LATP composites are thermally and electrochemically stable and exhibit high ionic conductivity at room temperature.
- (ii) The LATP-IL composites show superior performance compared to LTP-IL composites.
- (iii) Importantly, in both cases of LTP and LATP, the IL content in the matrix is small, and the "solid-state of the electrolyte" is also preserved.
- (iv) The present investigation suggests that these composites essentially behave like Li^+ ion conductors, and the role of IL is to facilitate electrical transport

by lowering the barriers for Li⁺ ion movement, and providing inter-grain coupling.

- (v) It is encouraging to note that these composites are extremely stable with lithium and LiCoO₂. Therefore, with proper engineering of the interfaces and electrolyte thickness/contact area, high power lithium cells can be developed.

References

- [1] Z. Jiang, L. Yuehua, C. Han, Z. He, W. Meng, L. Dai, and L. Wang, “K doping on Li site enables LiTi₂(PO₄)₃/C excellent lithium storage performance,” *Solid State Ionics*, vol. 341, no. April, p. 115036, 2019, doi: 10.1016/j.ssi.2019.115036.
- [2] N. Sharma and A. Dalvi, “Vanadium substituted Li⁺-NASICON systems: Tailoring electronic conductivity for electrode applications,” *Journal of Alloys and Compounds*, vol. 861, p. 157954, 2021, doi: 10.1016/j.jallcom.2020.157954.
- [3] M. Rathore, A. Dalvi, A. Kumar, W. Tubowska, and J. L. Nowinski, “Ionic liquid dispersed Li⁺ ion oxide glasses and glass-ceramics: Assessment of electrical transport and thermal stability,” *Solid State Ionics*, vol. 282, pp. 76–81, 2015, doi: 10.1016/j.ssi.2015.09.028.
- [4] A. L. Saroj, R. K. Singh, and S. Chandra, “Thermal, vibrational, and dielectric studies on PVP/LiBF₄+ionic liquid [EMIM][BF₄]-based polymer electrolyte films,” *Journal of Physics and Chemistry of Solids*, vol. 75, no. 7, pp. 849–857, 2014, doi: 10.1016/j.jpcs.2014.02.005.
- [5] K. Soeda, M. Yamagata, and M. Ishikawa, “Outstanding features of alginate-based gel electrolyte with ionic liquid for electric double layer capacitors,” *Journal of Power Sources*, vol. 280, pp. 565–572, 2015, doi: 10.1016/j.jpowsour.2015.01.144.
- [6] C. Maton, N. De Vos, and C. V. Stevens, “Ionic liquid thermal stabilities: Decomposition mechanisms and analysis tools,” *Chemical Society Reviews*, vol. 42, no. 13, pp. 5963–5977, 2013, doi: 10.1039/c3cs60071h.
- [7] R. Kaswan, M. D. Singh, S. Chandrasekara Sivasubramanian, and A. Dalvi,

- “Preparation and characterization of novel solid electrolytes based on [EMIM] BF₄ and lithium nitrate confined silica gels,” *Electrochimica Acta*, vol. 323, p. 134841, 2019, doi: 10.1016/j.electacta.2019.134841.
- [8] K. G. S. Pannu, T. Pannu, T. Fürstenhaupt, and V. Thangadurai, “Electrical properties of ionic liquid and double perovskite-type metal oxide composites - A new method to tailor grain-boundary impedance of ceramic electrolytes,” *Solid State Ionics*, vol. 232, pp. 106–111, 2013, doi: 10.1016/j.ssi.2012.11.009.
- [9] D. E. Sonja Laubach, Stefan Laubach, Peter C. Schmidt, K. N. Stefan Schmid, Wolfram Jaegermann, Andreas Thißen, and H. Ehrenberge, “Changes in the crystal and electronic structure of LiCoO₂ and LiNiO₂ upon Li intercalation and de-intercalation,” *Physical Chemistry Chemical Physics*, vol. 11, pp. 3278–3289, 2009.
- [10] K. Kwatek and J. L. Nowiński, “Electrical properties of LiTi₂(PO₄)₃ and Li_{1.3}Al_{0.3}Ti_{1.7}(PO₄)₃ solid electrolytes containing ionic liquid,” *Solid State Ionics*, vol. 302, pp. 54–60, 2017, doi: 10.1016/j.ssi.2016.11.020.
- [11] N. J. Kidner, N. H. Perry, T. O. Mason, and E. J. Garboczi, “The brick layer model revisited: Introducing the nano-grain composite model,” *Journal of the American Ceramic Society*, vol. 91, no. 6, pp. 1733–1746, 2008, doi: 10.1111/j.1551-2916.2008.02445.x.
- [12] A. Mertens, S. Yu, N. Schon, D. C. Gunduz, H. Tempel, R. Schierholz, F. Hausen, H. Kungl, J. Granwehr, and R. A. Eichel, “Superionic bulk conductivity in Li_{1.3}Al_{0.3}Ti_{1.7}(PO₄)₃ solid electrolyte,” *Solid State Ionics*, vol. 309, no. April, pp. 180–186, 2017, doi: 10.1016/j.ssi.2017.07.023.
- [13] H. Chung and B. Kang, “Increase in grain boundary ionic conductivity of Li_{1.5}Al_{0.5}Ge_{1.5}(PO₄)₃ by adding excess lithium,” *Solid State Ionics*, vol. 263, pp. 125–130, 2014, doi: 10.1016/j.ssi.2014.05.016.
- [14] A. Boruń and A. Bald, “Ionic association and conductance of ionic liquids in dichloromethane at temperatures from 278.15 to 303.15 K,” *Ionics*, vol. 22, no. 6, pp. 859–867, 2016, doi: 10.1007/s11581-015-1613-x.
- [15] R. Kaswan, S. C. Sivasubramanian, Y. Kumar, and A. Dalvi, “Conductivity and

Capacitance Studies of Silica Glass Composites Containing [BMIM] Br and LiCl

Keywords : Sol-gel process ; Lithium Silica glasses ; electrical conductivity ; high capacitance ; ionic liquids .,” pp. 1–48.

- [16] P. Dabas and K. Hariharan, “Influence of an ionic liquid on the conduction characteristics of lithium niobophosphate glass,” *AIP Conference Proceedings*, vol. 1512, pp. 584–585, 2013, doi: 10.1063/1.4791172.
- [17] G. P. Pandey, Y. Kumar, and S. A. Hashmi, “Ionic liquid incorporated PEO based polymer electrolyte for electrical double layer capacitors: A comparative study with lithium and magnesium systems,” *Solid State Ionics*, vol. 190, no. 1, pp. 93–98, 2011, doi: 10.1016/j.ssi.2011.03.018.
- [18] A. Stoppa, O. Zech, W. Kunz, and R. Buchner, “The conductivity of imidazolium-based ionic liquids from (-35 to 195) °c. A. variation of cations alkyl chain,” *Journal of Chemical and Engineering Data*, vol. 55, no. 5, pp. 1768–1773, 2010, doi: 10.1021/je900789j.
- [19] N. Sharma and A. Dalvi, “Mechanical milling assisted synthesis of novel $\text{LiTi}_2(\text{PO}_4)_3$ -glass-ceramic nanocomposites,” *Journal of Non-Crystalline Solids*, vol. 483, no. September 2017, pp. 126–133, 2018, doi: 10.1016/j.jnoncrysol.2018.01.016.

Chapter 4

Li⁺-NASICONs-IL Composites as Electrolyte for Solid-State Supercapacitors*

In the previous chapter, we discussed about ionic conductivity enhancement mechanism for IL-LTP/LATP composites along with their application as electrolytes in Solid-State Batteries (SSBs). In this chapter, these electrolytes have been explored for application to solid-state supercapacitors (SSCs).

For this work, three different ILs have been explored viz., EMIMBF₄, EMIMCF₃SO₃, and BMIMBF₄ to synthesize the corresponding composites with LTP and LATP (Li_{1.3}Al_{0.3}Ti_{1.7}(PO₄)₃). The supercapacitor fabrication process and electrode preparation have been discussed in detail in chapter 2. This chapter provides a thorough characterization of developed all-solid-state supercapacitors (SSCs). The role of IL ions and Li⁺ ions from the NASICON framework in the device performance has been assessed in detail. Thus, the chapter attempts to explore how the electrical conductivity of the composite electrolyte correlates with the performance of supercapacitors. The work therefore elaborates the influencing factors affecting the device performance.

The composites are labelled as LTP/LATP-xIL, where x is the weight percentage of IL added to the matrix and x is fixed to 13 wt% as that corresponds to the maximum weight percentage of IL that can be added without any leakage etc. as discussed in chapter 3.

* Parts of the results of this chapter are published in: G. Kaur, S. C. Sivasubramanian, A. Dalvi, "Solid-state supercapacitors using ionic liquid dispersed Li⁺-NASICONs as electrolytes", *Electrochimica Acta*. 434 (2022) 141311.

4.1. Li⁺-NASICONs-IL solid composite electrolyte characterization

The HT-XRD has been carried out on pristine LTP (Fig. 4.1(a)) and LTP-13IL (IL-EMIMBF₄) (Fig. 4.1(b)) in a wide temperature range (30- 500 °C). All the peaks related to LTP match well with the literature reported values and even after the addition of IL there is no shift in peak positions and no new crystalline compound formation was observed [1]. The HT-XRD for LTP and LTP-13 EMIMBF₄ have been shown in chapter 3 [2-3].

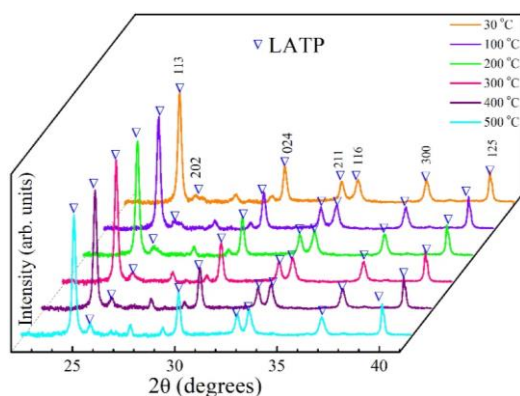


Fig. 4.1(a) HT-XRD patterns for pristine sol-gel derived LTP.

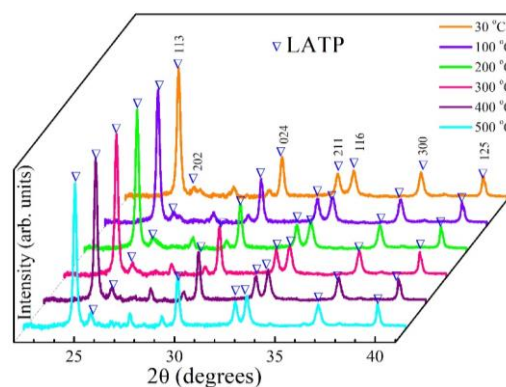


Fig. 4.1(b) HT-XRD patterns for LTP-13 EMIMBF₄.

The electrical conductivity values at three different temperatures for compositions containing LTP and LTP dispersed with various ILs are shown in Fig. 4.2(a) and Fig. 4.2(b), respectively. It is evident that for every composition the conductivity rises with temperature. Also, (i) dispersion of EMIMBF₄ in LTP/LTP leads to better conductivity, and (ii) LTP-based composites exhibit relatively better electrical conductivity than those of LTP-based composites. A maximum conductivity of $1.7 \times 10^{-3} \Omega^{-1} \text{cm}^{-1}$ at 40 °C is achieved for LTP dispersed with 13 wt. % of IL (EMIMBF₄). This is possibly due to the relatively smaller cation/anion size of EMIMBF₄ as compared to the other two ILs [4-5]. Thus, ionic radii of the IL seem to play an important role here. It may be therefore suggested that the ceramic, as well as the IL content in the composite influence the electrical transport. The conductivity in these IL dispersed composites was found to be quite adequate for electrolytic applications.

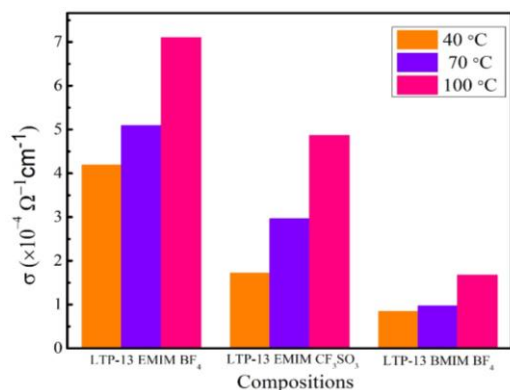


Fig. 4.2(a) Electrical conductivity at three different temperatures for LTP with different ILs (13 wt%).

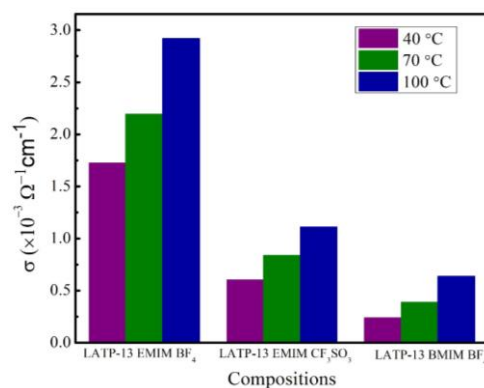


Fig. 4.2(b) Electrical conductivity at three different temperatures for LATP with different ILs (13 wt%).

Fig. 4.3(a) and 4.3(b) show FESEM images for LATP and LATP-13 EMIMBF₄, respectively. Importantly, these sol-gel derived NASICONs exhibit a porous structure with a typical grain size of 170-200 nm. Further, in the composites, IL fills the pores as evident in Fig. 4.3(b).

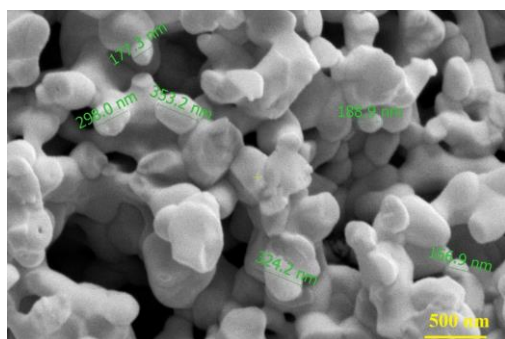


Fig. 4.3(a) FESEM image of the as prepared LATP.

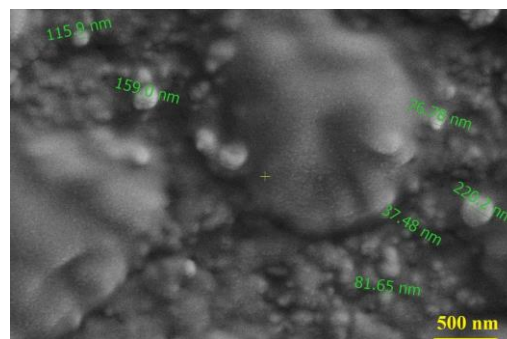


Fig. 4.3(b) FESEM image of LATP-13 EMIMBF₄ composite.

4.2 Activated Charcoal (electrode) characterization

The commercially procured activated charcoal (AC) was first characterized by BET surface area measurements. The N₂ adsorption-desorption isotherm and pore size distribution of the activated charcoal powder are shown in Fig. 4.4(a) and 4.4(b). According to the IUPAC classification, the material shows the type I isotherm [6]. The steep rising behaviour for $P/P_0 \leq 0.005$ of the isotherm, suggests a major N₂ uptake,

followed by a moderate rise in adsorption for the whole range of P/P_0 . The steep rise in the curve (below $P/P_0 \leq 0.005$) depicts a predominant microporous structure. The gradual increase in adsorption over a long range ($0.1 \leq P/P_0 \leq 1$) suggests the presence of mesopores with narrow pore size distribution. Micropores distribution (MP) plot for activated charcoal shows distribution maxima at $\sim 0.6\text{-}0.8$ nm. The pore size distribution was calculated using the BJH method and the specific area calculated from the linear form of the BET equation (inset of Fig. 4.4(a)) is found to be ~ 1050 m²/g. The total pore volume (V_p) and average pore diameter (V_d) were found to be ~ 0.58 cm³/gm and ~ 2.25 nm, respectively.

The FESEM images of the top surface of the deposited activated charcoal exhibit a quite homogeneous distribution of pores as seen in Fig. 4.4(c). These results suggest the suitability of the activated charcoal for SSC fabrication.

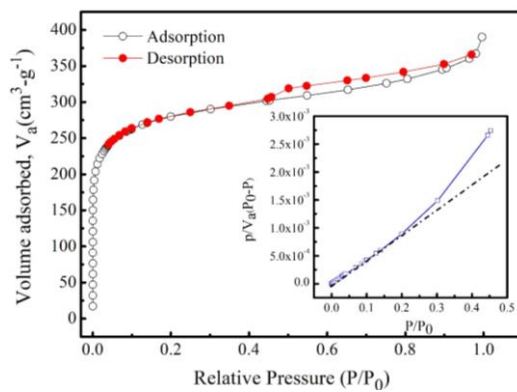


Fig. 4.4(a) Nitrogen adsorption-desorption isotherm curve of the activated charcoal (inset: linear fitting with the BET equation).

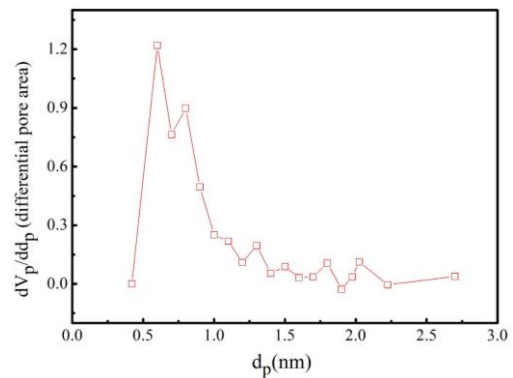


Fig. 4.4(b) Micropore distribution plot of the activated charcoal.

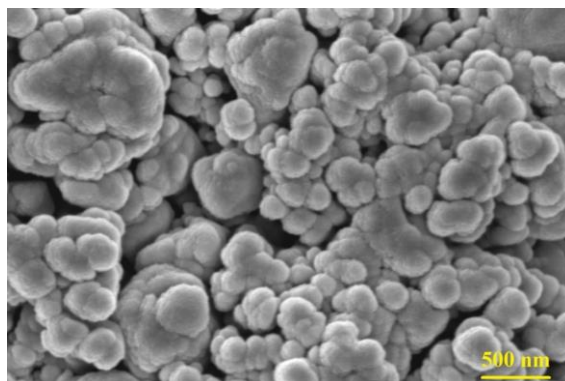


Fig. 4.4(c) FESEM image for the activated charcoal deposited on copper collector.

4.3 SSC Characterization

SSCs were fabricated using different composites containing LTP/ LATP dispersed with different ILs and the electrochemical properties were studied at room temperature (~35 °C). All the devices have been fabricated using electrodes having mass loading of ~1.2 mg/cm². Firstly, the Nyquist plots in a frequency range of 10 mHz to 0.1 MHz for various SSCs having different composite electrolytes are shown in Fig. 4.5. All the SSCs with various composite electrolytes, exhibit a semicircle (more apparent on the extended scale in the inset) followed by a steep vertical line which confirms the supercapacitor formation. The high-frequency features give the bulk and interfacial charge transfer characteristics, and the steep vertical line at the low frequency region shows the predominant capacitive nature of the cells. As apparent in the insets of Fig. 4.5(a) and 4.5(b), the bulk resistance (R_b), charge-transfer resistance (R_{ct}), and a resistive contribution corresponding to ion diffusion, i.e., Warburg impedance (W) regions are marked in the Nyquist plots [7]. The total cell impedance also termed equivalent series resistance (ESR) of the overall device (ESR) comprised of R_b , R_{ct} , and W , can be inferred from the intercept of the vertical line on the Z' (real) axis. The charge transfer process corresponding to R_{ct} is faradaic in nature and not expected in electric double layer supercapacitors (EDLCs). However, notable small values suggest weak faradic reactions at the electrode-electrolyte interface, as reported previously in some EDLCs [8]. Further, the Warburg nature is also observed in the mid-frequency region, which suggests a diffusive mechanism at the interface, i.e., from bulk to the pores of activated charcoal, as reported earlier [8].

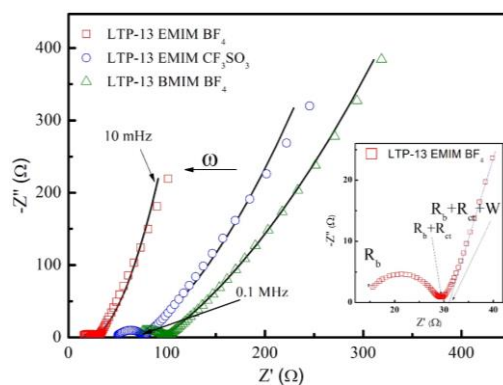


Fig. 4.5(a) Nyquist plots (10 mHz-0.1 MHz) for SSCs having different IL dispersed LTPs as electrolyte. For comparison, thickness and area of the cross-section are kept the same for all the SSCs.

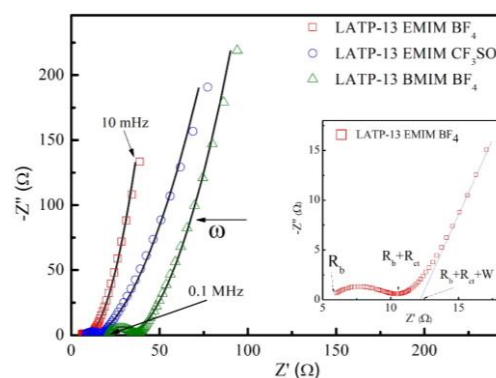


Fig. 4.5(b) Nyquist plots (10 mHz-0.1 MHz) for SSCs having different IL dispersed LATPs as electrolyte. For comparison, thickness and area of the cross-section are kept the same for all the SSCs.

The Nyquist plots (Fig. 4.5(a) and 4.5(b)) have been fitted using the equivalent circuit given in Fig. 4.5(d). The circuit fits well with many of the gel-based supercapacitors reported earlier [9]. The data obtained from fitting as in Fig. 4.5(d) have higher values of R_b than R_{ct} . R_b and R_{ct} have the lowest values for the best conducting electrolyte and gradually increase as the conductivity of the electrolyte decreases.

It is interesting to observe that with a decrease in the ionic radii of IL ions, the ESR gradually decreases, and the low frequency vertical line appears steeper. Smaller ions possibly contribute more significantly to the capacitor action. Secondly, the conductivity of ceramic (LTP/LATP) also seems to affect the Nyquist plots, i.e., low ESR and steeper low frequency inclined line is again observed for better conducting ceramic (LATP). Nyquist plots thus suggest a role of IL as well as Li⁺ NASICON in facilitating the charge storage process. This is further examined. The imaginary (C'') part of the capacitance values are obtained from the following equations [9-11]:

$$C''(\omega) = \frac{-Z'(\omega)}{\omega |Z|^2} \quad (4.1)$$

As seen in Fig. 4.5 (c), the C'' versus ω apparently exhibits a relaxation that corresponds to the charge storage process in the electrode pores [8]. The peak gradually shifts towards high frequency when the conductivity of the SSC composite electrolyte increases. This suggests that charges take a relatively smaller time to reach the pores for the capacitive action [12]. This again suggests the role of electrolyte conductivity in the charge storage process.

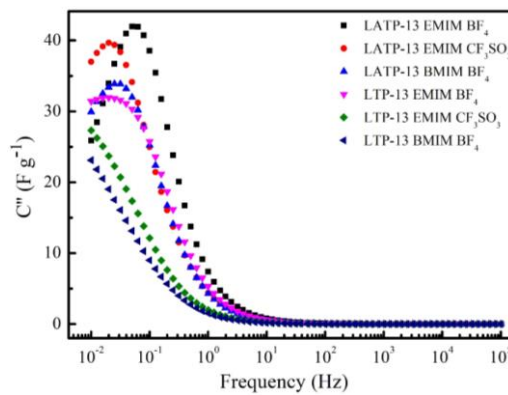


Fig. 4.5(c) Imaginary capacitance (C'') of SSCs as a function of frequency.

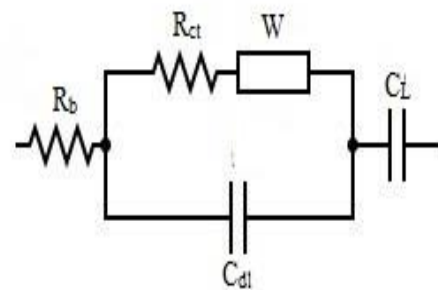


Fig. 4.5(d) Equivalent circuit for SSCs.

The electrochemical performance of the SSCs has been recorded at room temperature (~35 °C) and the optimal voltage of these cells was obtained from the CV. Fig. 4.6(a) and 4.6(b) show CV scans (10 mV/s) for different ionic liquid composites with LTP and LAMP, respectively. The CV scans in the range of 0-1 V for all the composites show appreciable hysteresis which suggests substantial charge storage ability in these devices. The absence of any noticeable oxidation-reduction peak suggests the formation of EDLC. When LTP is replaced with LAMP, a significant increase in the area under the CV scans is observed, which indicates a substantial increase in charge storage ability. Also, for fixed LTP/LAMP incorporation of different ILs exhibits interesting results. The shapes of the CVs are more rectangular for better conducting electrolyte in the SSC. Thus, the fast ionic transport in the electrolyte also enables significant charge transfer at the interface. It may be inferred from the area under the CV curve that the SSCs having IL EMIMBF₄ in the LAMP do exhibit maximum storage capacity. These results again confirm the ideal capacitor nature of the cells as also suggested by Nyquist plots. Further, these results strongly suggest that both Li⁺-NASICON and IL content in the electrolyte matrix play an important role in the ionic activity at the interface, thus in supercapacitor formation.

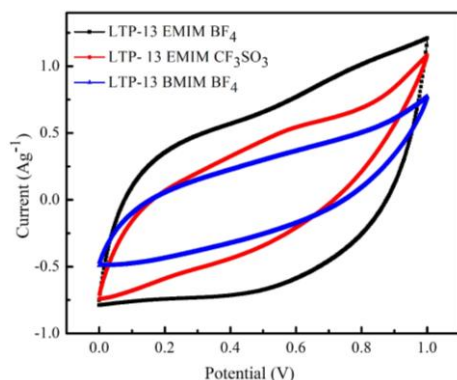


Fig. 4.6(a) CV scans for the SSCs having electrolyte as different IL dispersed LTPs at a scan rate of 10 mV/s.

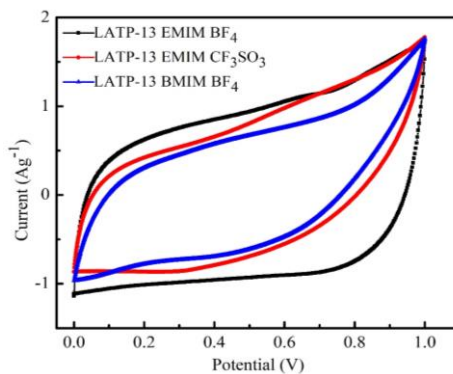


Fig. 4.6(b) CV scans for the SSCs having electrolyte as different IL dispersed LAMPs at a scan rate of 10 mV/s.

To further evaluate the device's capability for charge storage CV scans were obtained at 10 mV/s in a voltage range of 0-1 V for subsequent 100 cycles Fig. 4.6(c). A constant

current response is observed up to 1 V with a smooth featureless profile, which suggests a predominantly non-faradic event in cycling and is typical of an electric double layer capacitor (EDLC) nature.

Further, the CV patterns for the cell containing the highest conducting composite L ATP-13 EMIMBF₄ have been recorded by gradually increasing the voltage range up to 1.8 V as seen in Fig. 4.6 (d). With an increasing voltage limit, the shape of the CV curves almost remains box-like, up to a value of ~ 1.5 V, above which a notable deviation is witnessed. Hence further studies were carried out up to ~ 1 V only, below which the features are quite stable and reproducible.

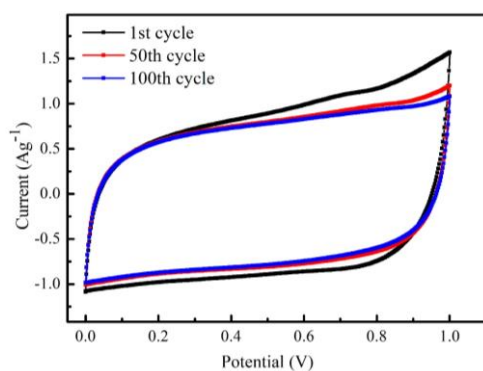


Fig. 4.6(c) CV scans of SSC having L ATP-13 EMIMBF₄ electrolyte up to 100 cycles. Typical EDLC nature is witnessed.

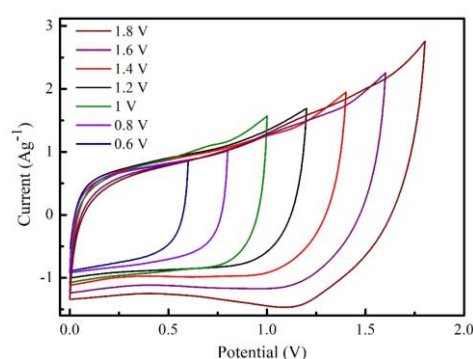


Fig. 4.6(d) CV scans (at 10 mV/s) of SSC for L ATP-13 EMIMBF₄ for different voltage ranges.

The galvanostatic charge-discharge (GCD) cycling was carried out for the cells with different IL-LTP/L ATP composites as electrolytes. The GCD cycles obtained are shown in Fig. 4.7(a) and 4.7(b) for SSC with LTP and L ATP-containing composites with different ILs as electrolytes, respectively. Similarly, the SSC containing L ATP-13 EMIMBF₄ composite GCD cycles are separately shown at different current densities (0.11-1.7 A-g⁻¹) Fig. 4.7(c).

From these plots, different performance parameters such as specific capacitance (F-g⁻¹), specific energy (Wh-kg⁻¹), specific power (W-kg⁻¹), and equivalent series resistance (ESR) (Ω cm²) were obtained to study quantitative analysis for the SSCs using the following relations.

The overall device capacitance is given by:

$$C = \frac{I \Delta t}{\Delta V} \quad (4.2)$$

where Δt is the discharge time in seconds, ΔV is the voltage window of the discharge cycle. This window excludes IR drop.

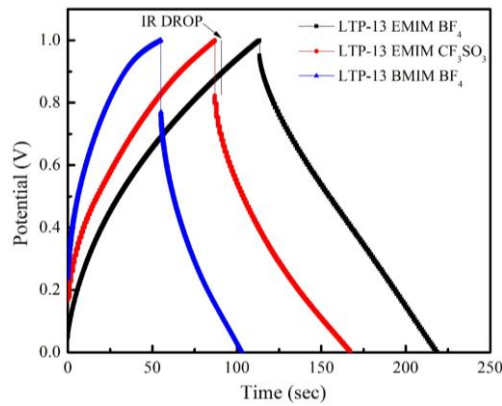


Fig. 4.7(a) Galvanostatic charge-discharge (at 0.65 mA/cm^2) cycles for SSCs having IL dispersed LTP composites.

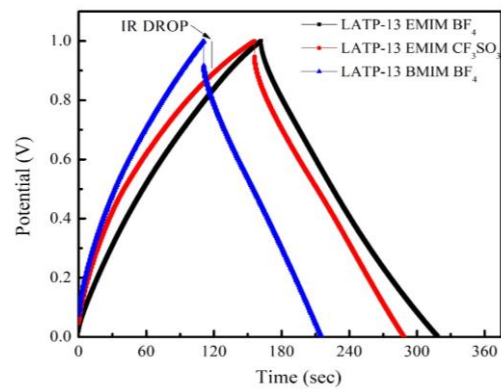


Fig. 4.7(b) Galvanostatic charge-discharge (at 0.65 mA/cm^2) cycles for SSCs having IL dispersed LATP composites.

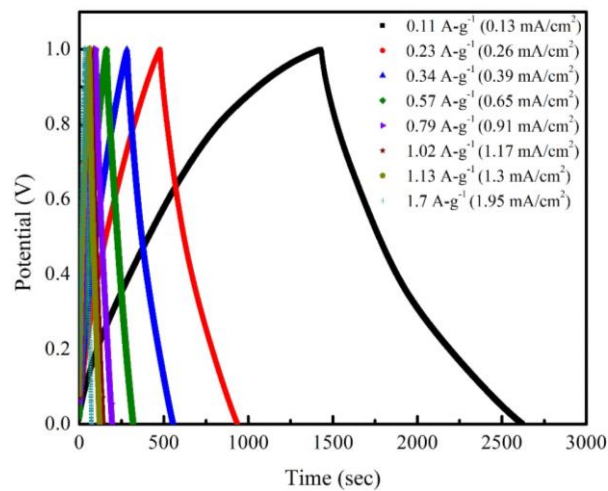


Fig. 4.7(c) GCD curves of LATP-13 EMIM BF₄ for the 10th cycle at different currents ranging from $0.11\text{-}1.7 \text{ A-g}^{-1}$ at 1 V with areal current densities mentioned in brackets.

The specific capacitance (F-g⁻¹) per electrode is calculated from the discharging curve as:

$$C_s = \frac{4C}{m_{total}} \quad (4.3)$$

where m_{total} is the total mass of active material (in grams) on the electrodes.

Moreover, the specific energy (Wh-kg⁻¹) for the device is calculated as:

$$E = \frac{1}{2} \cdot \frac{C(\Delta V)^2}{3.6 m_{total}} \quad (4.4)$$

For the device, the specific power (W-kg⁻¹) is obtained using the following equation:

$$P = \frac{3600 \cdot E_s}{\Delta t} \quad (4.5)$$

In addition, the equivalent series resistance (ESR) is also obtained from the initial voltage drop ΔV_{IR} and discharge current I (A) during the discharge cycle as:

$$ESR = \frac{\Delta V_{IR}}{2I} \quad (4.6)$$

Further, the coulomb efficiency (η_{CE}) obtained from charging and discharging time is given by:

$$\eta_{CE} = \frac{\Delta t_{discharge}}{\Delta t_{charge}} \times 100 \quad (4.7)$$

For comparison, the areal capacitance (F-cm⁻²) of the device is obtained by dividing (1) by the electrode area (A):

$$C = \frac{I \Delta t}{\Delta V A} \quad (4.8)$$

Further, the energy density (Wh-cm⁻²) is obtained from the areal capacitance of the device as follows:

$$E_a = \frac{1}{2} \cdot \frac{C(\Delta V)^2}{3600} \quad (4.9)$$

and the power density (W-cm⁻²) obtained for the device is given as:

$$P_a = \frac{3600 \cdot E_s}{\Delta t} \quad (4.10)$$

It is evident from Fig. 4.7(a) and 4.7(b) that the discharge cycle for all the cells is linear, and the discharging time is relatively higher in the case of cells with better conducting electrolyte. For a fixed IL content, cells with LATP exhibit a notably longer discharge time. Also, as seen in Nyquist plots and CV cycles of these cells, the smaller the size of IL ions, the higher the discharging time. Therefore, it appears that both Li⁺-NASICON and IL affect the GCD profile of cells. Specific capacitance (C_s) and other parameters obtained for all the cells having different electrolyte composites are tabulated (Table 4.1). The areal capacitance values with specific energy and power density values are also reported in Table 4.2.

Table 4.1 Electrical conductivity, specific capacitance, energy, power, ESR, and coulomb efficiency for the SSCs with compositions containing different ILs dispersed LTP and LATP as an electrolyte. The range is specified for C_s , E, and P, and (*) represents values for a typical SSC used in the analysis that is close to the average performance of SSCs.

Electrolyte composition	σ ($\Omega^{-1} \text{ cm}^{-1}$)	C_s ($\text{F}\cdot\text{g}^{-1}$)	E ($\text{Wh}\cdot\text{kg}^{-1}$)	P ($\text{W}\cdot\text{kg}^{-1}$)	ESR ($\Omega \text{ cm}^2$)		η_{CE} (0.65 $\text{mA}\cdot\text{cm}^{-2}$ / 0.56A- g^{-1})
					From GCD	From IS	
LTP-13 EMIM BF ₄	4.18×10^{-4}	127-131 129*	4.0-4.13 4.07*	136*	36*	(47)	94%
LTP-13 EMIM CF ₃ SO ₃	1.72×10^{-4}	113-117 115*	2.68-2.77 2.7*	115*	133*	(124)	95%
LTP-13 BMIM BF ₄	8.48×10^{-5}	70-74 72*	1.43-1.51 1.5*	110*	177*	(168)	88%
LATP-13 EMIMBF ₄	1.72×10^{-3}	179-184 181*	6.08-6.14 6.1*	140*	12*	(18)	99%
LATP-13 EMIM CF ₃ SO ₃	6.01×10^{-4}	157-161 159*	4.94-5.06 4.98*	134*	37*	(27)	85%
LATP-13 BMIM BF ₄	2.39×10^{-4}	126-130 128*	3.70-3.82 3.7*	128*	61*	(58)	95%

The highest value of specific capacitance, specific energy, and specific power has been observed for the SSCs having LATP-13 EMIMBF₄ composite as an electrolyte that exhibits superior conductivity. Further, the ESR values (calculated using IR drop)

match quite well with those obtained from Nyquist plots. The ESR gradually decreases when (i) IL with relatively smaller radii ions are introduced in the electrolyte and also when (ii) Li⁺-NASICON conductivity is high, i.e., LTP is replaced by LATP.

Interesting to note that the ESR for these SSC cells is found to be quite low and comparable to those of gels [12-14] and some liquid electrolyte [15-17] based EDLCs.

Table 4.2 Areal capacitance, energy, and power density values for the SSCs with compositions containing different ILs dispersed LTP and LATP as an electrolyte.

Electrolyte composition	Areal Capacitance (mF-cm ⁻²)	E _a (μWh-cm ⁻²)	P _a (μW-cm ⁻²)
	From GCD		
LTP-13 EMIMBF ₄	74	9.3	310
LTP-13 EMIMCF ₃ SO ₃	65.6	6.23	267
LTP-13 BMIMBF ₄	41.4	3.4	249
LATP-13 EMIMBF ₄	104	14	321
LATP-13 EMIMCF ₃ SO ₃	90.7	11.4	308
LATP-13 BMIMBF ₄	73.4	8.62	290

Galvanostatic charge-discharge cycles were also performed for the cells containing LATP-13 EMIMBF₄ composite electrolyte at various current densities from 0.11-1.7 A-g⁻¹ (areal currents of 0.13-1.95 mA/cm²) as shown in Fig. 4.7(c). The discharge is almost linear for higher currents and suggests predominantly electric double layer capacitor (EDLC) behavior. Apparently, the IR drop during discharge reduces gradually with decreasing discharge current density. As expected, for smaller discharge currents it takes a longer time to discharge. Fig. 4.7(d) shows a variation of coulomb efficiency (η_{CE}) with discharge currents. It initially rises notably with discharge currents and further saturates to ~ 97-99 % for I ≥ 0.34 A/g. The GCD curves were also obtained for different cut-off voltages essentially to optimize the operating voltage limits (Fig. 4.7e). Beyond 1 V, the coulombic efficiency values decrease rapidly along with a substantial increase in the ESR. These results along with CV curves suggest that the optimal operating voltage is close to ~1 V for these devices.

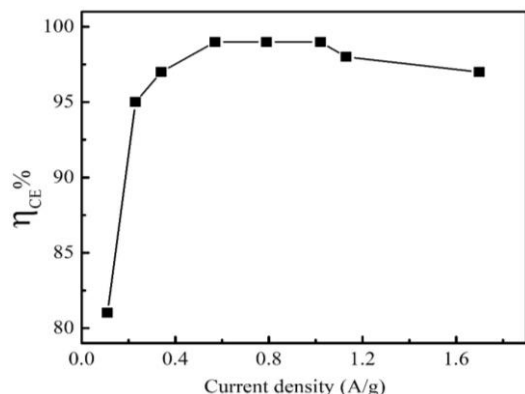


Fig. 4.7(d) Coulomb efficiency as a function of discharge current density.

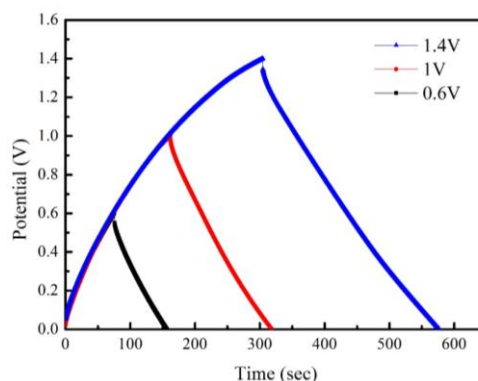


Fig. 4.7(e) GCD curves of LATP-13 EMIM BF₄ for different voltage ranges.

An interesting correlation is seen between the conductivity and C_s (Fig. 4.7f). With a rise in the conductivity of the electrolyte, cell performance dramatically improves.

Electrochemical cycling stability was also examined and the SSCs exhibited satisfactory performance. For the SSC having electrolyte that showed the best performance Fig. 4.7(g) shows potential versus specific capacitance for different charging-discharging cycles. The discharge characteristics remain the same even after ~13000 cycles. The specific capacitance and ESR for these cycles are also shown as a function of cycle number in Fig. 4.7(h).

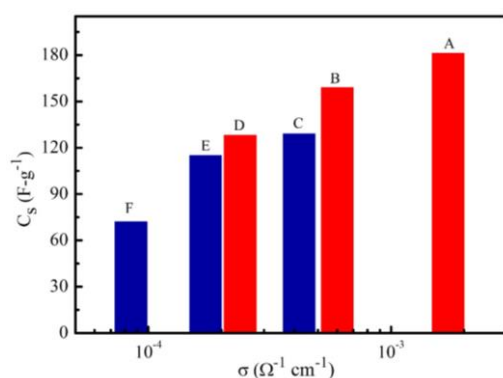


Fig. 4.7(f) Conductivity versus capacitance for different composites. Here A: LATP-13 EMIMBF₄, B: LATP-13 EMIMCF₃SO₃, C: LTP-13 EMIMBF₄, D: LATP-13 BMIMBF₄, E: LTP-13 EMIMCF₃SO₃, F: LTP-13 BMIMBF₄.

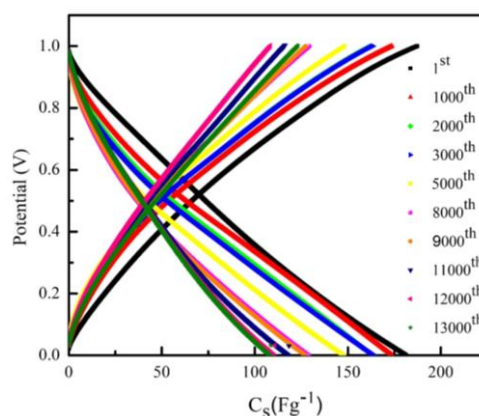


Fig. 4.7(g) Charge-discharge cycles for SSC having LATP-13 EMIMBF₄ composite as electrolyte obtained at different cycles at ~35 °C.

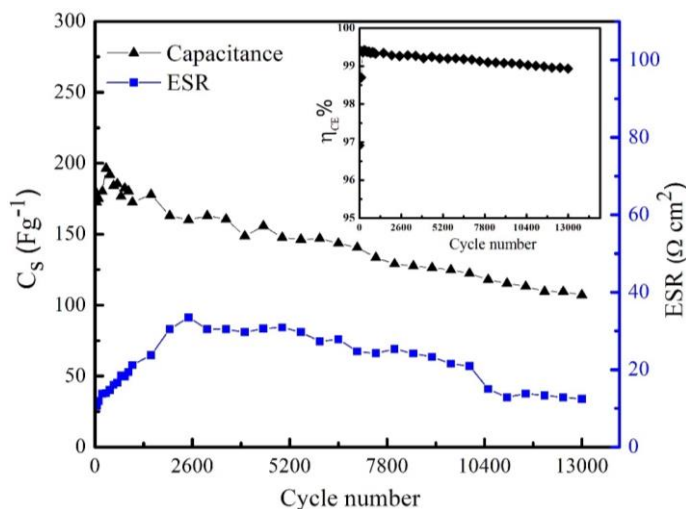


Fig. 4.7(h) The specific capacitance and ESR vs cycle number at ~ 35 °C for SSC having electrolyte LTP-13 EMIMBF₄. INSET: coulomb efficiency vs cycle number up to 13000 cycles.

The specific capacitance remains almost constant around ~ 180 F-g⁻¹ for nearly 1500 cycles, subsequently decreasing very slowly to ~ 110 F-g⁻¹ at ~ 13000 cycles. Further, the ESR value rises in initial cycles and then decreases continuously afterward with a value of 14 Ω cm² up to ~ 13000 cycles. This is consistent with the specific capacitance. The cells show a coulomb efficiency of around 99% throughout the charging-discharging up to ~ 13000 cycles indicating excellent electrochemical stability and a stable electrode-electrolyte interface. After ~ 7000 and ~ 13000 cycles, the capacitance is found to be able to sustain 81% and 61% of its initial value. This again confirms excellent cycling performance.

Fig. 4.7 (i) shows that with an increase in temperature, capacitance increases rapidly. Thus, the rise may be attributed to the enhanced conductivity of the composite electrolyte, which in turn facilitates ionic diffusion at the interface. Interestingly, the capacitance value reaches ~ 640 F-g⁻¹ at 100 °C. Further on cooling, the cell attains almost the same capacitance value at room temperature which suggests excellent thermal stability of the SSCs. Coulomb efficiency, however, generally decreases with a temperature rise, from 98.5% at 50 °C to 71% at 100 °C. On cooling, the cell attains almost the same value. The coulomb efficiency and capacity retention are also plotted

(in the inset of Fig. 4.7(i)) at 35 °C after each heating cycle. Almost the same coulomb efficiency is obtained with nearly 100% capacity retention at least up to ~10 cycles. Fig. 4.7(j) shows the Ragone plot for the cells for comparison. The cell with LATP-13 EMIMBF₄ electrolyte exhibits the highest specific energy and power of 9 Wh·kg⁻¹ (at 0.11 A/g) and 280 W·kg⁻¹ (at 1.13 A/g), respectively among the three.

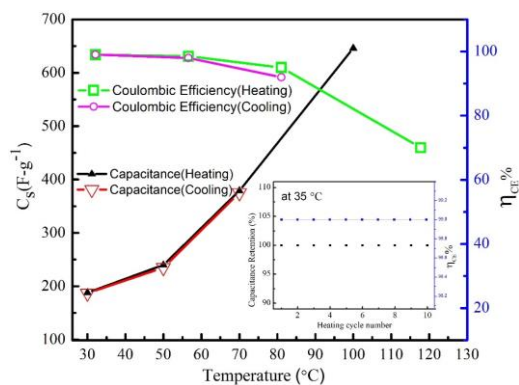


Fig. 4.7(i) Specific capacitance rise and decay cycle between 30 °C - 100 °C.

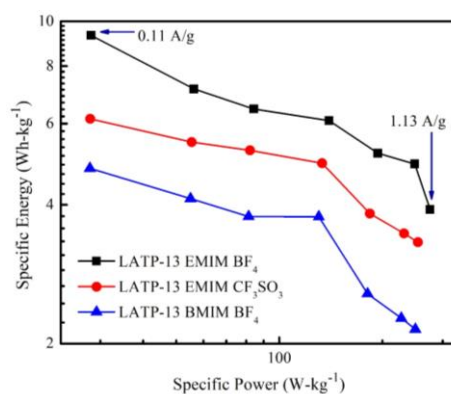


Fig. 4.7(j) Ragone plot for SSCs having IL dispersed LATP composites.

To demonstrate the practical applicability of the SSCs, the series combination of two cells having LATP-13 EMIMBF₄ as an electrolyte has been used to glow a white LED (3V) as seen in Fig. 4.8(a). The LED during direct discharge could glow for ~30 minutes at a fairly low temperature of ~ 15 °C. However, for SSCs having only IL EMIMBF₄ as electrolyte supported in Whatman filter paper (1), this LED could glow only for ~5 minutes (Fig. 4.8b) which readily suggests the importance of Li⁺-NASICON in the device performance in this geometry.

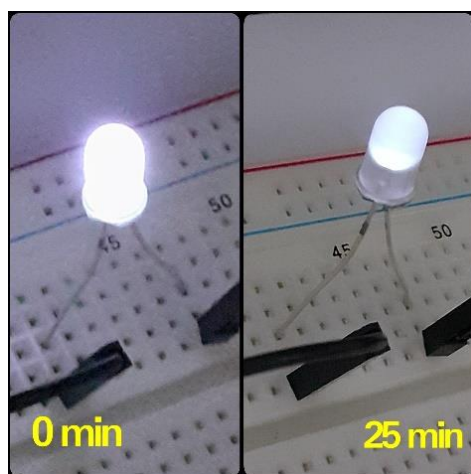


Fig. 4.8(a) Glow of LED using two-coin cells (having LATP-13 EMIM BF₄ as electrolyte) connected in series.

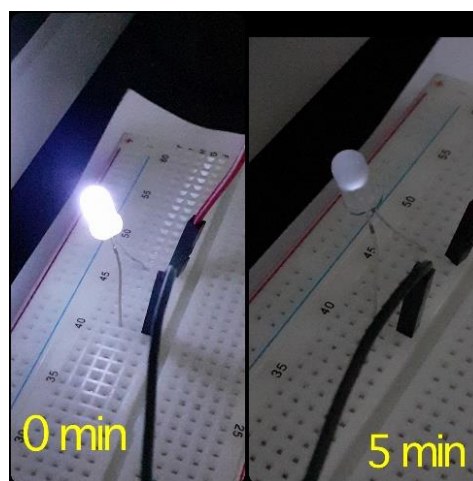


Fig. 4.8(b) Glow of LED using two-coin cells (having only EMIMBF₄ as electrolyte) connected in series.

The results may be summarized as (i) the composites consisting of LTP / LATP and various ILs show excellent conductivity at room temperature, and (ii) the cells fabricated using these exhibits excellent stability against cycling. It is important to explore a tentative mechanism, i.e., the role of various ions in the composite in supercapacitor action and performance. The mobile ions in the composites viz. Li⁺, and cation/anion of ILs that are indeed weakly bonded to the matrix. Thus, the following possibilities may be suggested, supported by the present experimental observations:

- The electrochemical characterization suggests predominantly electric double layer capacitor (EDLC) behavior of the supercapacitors, particularly at higher (≥ 0.56 A/g) discharge currents. At very low currents (e.g., at 0.11 A/g) however, the SSCs possibly exhibit faradic charge transfer at the interface, and thus pseudo effects are noticed (Fig. 4.7c). The conductivity of the composite electrolyte influences the performance of the device (Fig. 4.7f). Because of high ionic conductivity, the electroactive species can reach the electrode-electrolyte interface relatively faster and contribute to charge storage. This has also been complemented by the C'' - ω relaxation.
- The Li⁺ ions possibly act as capacitor ions. When LTP is replaced by a relatively better Li⁺ ion conducting system- LATP, the device performance improves notably. Also, the addition of IL enhances device performance further in both cases; this is supported by our work on IL-LTP composites. IL presence in such composites essentially lowers the energy barriers for mobile Li⁺ ions and facilitates long-range Li⁺ ion migration in the matrix.
- Further, results also suggest that the type/size of IL ions also seem to influence device performance. They exist uniformly in the matrix and also at the electrode-electrolyte interface. It was also seen in the present study that SSC cells with relatively smaller IL ions exhibit better storage ability, and the variation of cation, as well as anion size, plays a crucial role in EDLC performance. Thus, the IL ions also contribute to capacitor action as their short-range migration is not unlikely.
- The cells consisting of pure IL electrolytes (without the ceramic host) do exhibit capacitor action, but their device performance is quite poor.

In view of the above facts, it may be suggested that Li⁺ ions from the host and IL ions both contribute to capacitor action. More detailed studies are further required.

4.4 Summary

(i) IL dispersed NASICON solid composites having high electrical conductivity have been successfully used as electrolytes for solid-state supercapacitors. These electrolytes are stable under supercapacitor conditions.

(ii) High specific capacitance values have been obtained by varying IL and NASICON in the composite. The specific (gravimetric) and areal parameters found are much improved than reported before for many ionogels and gel-based electrolytes.

(iii) The electrical conductivity of the electrolyte influences the device's performance. An interesting correlation suggests that IL cation and anion, along with mobile Li⁺ ions actively contribute to predominant electric double-layer capacitance at the interface. At lower currents, weak pseudo-capacitive behaviour is witnessed that needs further investigation.

(iv) The long cycling stability with high coulomb efficiency has been obtained showing the electrochemical stability of the device. These cells are stable at least up to ~100 °C with remarkably high specific capacitance values. The promising energy storage capability of the device has been shown by glowing an LED for ~30 minutes. The higher surface area activated charcoal, if used (>1050 m²/g) may further improve the performance parameters.

(v) Present work strongly emphasizes the role of Li⁺ conducting ceramic host matrix in the supercapacitor performance.

References

- [1] P. Zhang, M. Matsui, Y. Takeda, O. Yamamoto, and N. Imanishi, "Water-stable lithium ion conducting solid electrolyte of iron and aluminum doped NASICON-type LiTi₂(PO₄)₃," *Solid State Ionics*, vol. 263, pp. 27–32, 2014, doi: 10.1016/j.ssi.2014.04.017.
- [2] Z. Jiang *et al.*, "K doping on Li site enables LiTi₂(PO₄)₃/C excellent lithium storage performance," *Solid State Ionics*, vol. 341, pp. 115036, 2019, doi: 10.1016/j.ssi.2019.115036.
- [3] N. Sharma and A. Dalvi, "Vanadium substituted Li⁺-NASICON systems:

-
- Tailoring electronic conductivity for electrode applications,” *Journal of Alloys and Compounds*, pp. 1–23, 2020, doi: 10.1016/j.jallcom.2020.157954.
- [4] A. Boruń and A. Bald, “Ionic association and conductance of ionic liquids in dichloromethane at temperatures from 278.15 to 303.15 K,” *Ionics*, vol. 22, pp. 859–867, 2016, doi: 10.1007/s11581-015-1613-x.
- [5] T. R. Jow, K. Xu, and S. P. Ding, “Nonaqueous Electrolyte Development for Electrochemical Capacitors,” no. June 2015, pp. 1–39, 1999, doi: 10.2172/15050.
- [6] S. A. Borghei *et al.*, “Synthesis of multi-application activated carbon from oak seeds by KOH activation for methylene blue adsorption and electrochemical supercapacitor electrode,” *Arabian Journal of Chemistry*, vol. 14, pp. 102958, 2021, doi: 10.1016/j.arabjc.2020.102958.
- [7] G. P. Pandey and S. A. Hashmi, “Solid-state supercapacitors with ionic liquid based gel polymer electrolyte: Effect of lithium salt addition,” *Journal of Power Sources*, vol. 243, pp. 211–218, 2013, doi: 10.1016/j.jpowsour.2013.05.183.
- [8] N. Yadav, N. Yadav, and S. A. Hashmi, “High-Energy-Density Carbon Supercapacitors Incorporating a Plastic-Crystal-Based Nonaqueous Redox-Active Gel Polymer Electrolyte,” *ACS Applied Energy Materials*, vol. 4, pp. 6635–6649, 2021, doi: 10.1021/acsaem.1c00703.
- [9] N. Yadav, N. Yadav, and S. A. Hashmi, “Ionic liquid incorporated, redox-active blend polymer electrolyte for high energy density quasi-solid-state carbon supercapacitor,” *Journal of Power Sources*, vol. 451, pp. 227771, 2020, doi: 10.1016/j.jpowsour.2020.227771.
- [10] G. P. Pandey, T. Liu, C. Hancock, Y. Li, X. S. Sun, and J. Li, “Thermostable gel polymer electrolyte based on succinonitrile and ionic liquid for high-performance solid-state supercapacitors,” *Journal of Power Sources*, vol. 328, pp. 510–519, 2016, doi: 10.1016/j.jpowsour.2016.08.032.
- [11] P. L. Taberna, P. Simon, and J. F. Fauvarque, “Electrochemical Characteristics and Impedance Spectroscopy Studies of Carbon-Carbon Supercapacitors,” *Journal of The Electrochemical Society*, vol. 150, pp. A292, 2003, doi:

10.1149/1.1543948.

- [12] N. Yadav, M. K. Singh, N. Yadav, and S. A. Hashmi, “High performance quasi-solid-state supercapacitors with peanut-shell-derived porous carbon,” *Journal of Power Sources*, vol. 402, pp. 133–146, 2018, doi: 10.1016/j.jpowsour.2018.09.032.
- [13] K. S. Lee and H. T. Jeong, “Development and optimization of ionic liquid based gel polymer electrolyte for all solid-state supercapacitor,” *Journal of Energy Storage*, vol. 42, pp. 103001, 2021, doi: 10.1016/j.est.2021.103001.
- [14] V. Chaudoy, F. Tran Van, M. Deschamps, and F. Ghamouss, “Ionic liquids in a poly ethylene oxide cross-linked gel polymer as an electrolyte for electrical double layer capacitor,” *Journal of Power Sources*, vol. 342, pp. 872–878, 2017, doi: 10.1016/j.jpowsour.2016.12.097.
- [15] B. Asbani, C. Douard, T. Brousse, and J. Le Bideau, “High temperature solid-state supercapacitor designed with ionogel electrolyte,” *Energy Storage Materials*, vol. 21, pp. 439–445, 2019, doi: 10.1016/j.ensm.2019.06.004.
- [16] S. T. Senthilkumar, R. K. Selvan, N. Ponpandian, J. S. Melo, and Y. S. Lee, “Improved performance of electric double layer capacitor using redox additive (VO²⁺/VO₂⁺) aqueous electrolyte,” *Journal of Materials Chemistry A*, vol. 1, pp. 7913–7919, 2013, doi: 10.1039/c3ta10998d.
- [17] A. Laheäär, A. Jänes, and E. Lust, “NaClO₄ and NaPF₆ as potential non-aqueous electrolyte salts for electrical double layer capacitor application,” *Electrochimica Acta*, vol. 82, pp. 309–313, 2012, doi: 10.1016/j.electacta.2012.04.149.

Chapter 5*

Li_{1.3}Al_{0.3}Ti_{1.7}(PO₄)₃-EMIMBF₄ electrolyte with wide thermal stability for SSCs

In Chapters 3 and 4, we have discussed LTP/LATP-IL composites and observed enhancement in conductivity. A tentative mechanism for ionic transport was also proposed. Also, it was revealed that among all the composites LATP-13 EMIMBF₄ exhibits the highest ionic conductivity. These composites were explored for electrolytic application in solid-state batteries (SSBs) and solid-state supercapacitors (SSCs).

This chapter emphasizes applying composite as an electrolyte in solid-state supercapacitors for wide thermal stability applications. To the best of the literature explored, the high as well as low temperature application of supercapacitors has not got sufficient emphasis so far. No supercapacitors specific to high temperature requirements exist in the market.

In this work, LATP-13 EMIMBF₄ composite has been used as an electrolyte considering its high conductivity and the electrochemical stability window. The supercapacitors are fabricated in different geometries according to their need in various applications. The SSCs have been developed to demonstrate the versatility of the novel IL-NASICON composite for its potential to adopt various geometries.

*Part of the results of this chapter are filed in an Indian patent by A. Dalvi, G. Kaur, S. C. Sivasubramanian, "Development of Li_{1.3}Al_{0.3}Ti_{1.7}(PO₄)₃-EMIMBF₄ nanocomposite electrolyte with wide thermal stability for all-solid-state supercapacitors", No. 202211047554, August 2022.

5.1. Activated Charcoal (electrode) characterization

For the SSCs under investigation, a relatively high surface area activated charcoal was used. The surface area and pore size distribution of activated charcoal for the electrodes were measured by using the BET (Brunauer Emmett Teller) technique (BELSORP-MINI X) [1]. Fig. 5.1(a) shows the predominant microporous structure along with the presence of mesopores [2-3]. The distribution maxima are observable at a pore diameter of 0.7 nm (Fig. 5.1b). The specific area calculated from the linear form of the BET equation (inset of Fig. 5.1a) is found to be $\sim 1450 \text{ m}^2/\text{g}$. The total pore volume (V_p) and average pore diameter (V_d) were found to be $\sim 0.68 \text{ cm}^3/\text{g}$ and $\sim 1.85 \text{ nm}$, respectively. Secondly, electrodes for the supercapacitors were made using this high surface area ($1500 \pm 100 \text{ m}^2/\text{g}$) activated charcoal (AC) along with a binder (PVDF-HFP) and a conductive material acetylene black (AB).

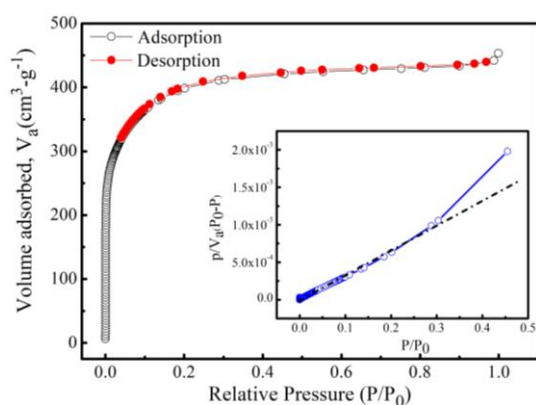


Fig. 5.1(a) Nitrogen adsorption-desorption isotherm curve of the activated charcoal (inset: linear fitting with the BET equation).

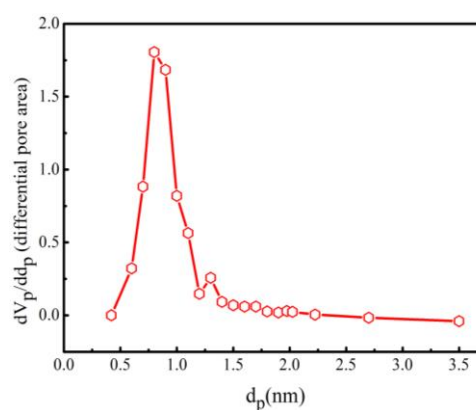


Fig. 5.1(b) Micropore distribution plot of the activated charcoal.

5.2 Description of three geometries

Using a high surface area ($1500 \pm 100 \text{ m}^2/\text{g}$), activated carbon the supercapacitors based on the composite electrolytes were prepared in various geometries. All the devices have been fabricated using electrodes having mass loading of $\sim 1.2 \text{ mg}/\text{cm}^2$. The fabrication process of these geometries has been discussed in chapter 2 and their importance is elaborated here.

- (I) **Coin cell Fabrication:** This is one of the nicely packed cell geometry conventionally used for supercapacitors. This can be used in applications

where a coin or button cell is required. In this geometry, the supercapacitor configuration gets packed properly with good contacts between electrodes and electrolytes thus giving less resistance. Since the cell is fully packed, it remains moisture free and good to go for a long lifetime retaining excellent mechanical stability. Since conventional liquid/gel electrolyte-based supercapacitors use this geometry, it was used primarily for comparison [4].

For the IL-LATP composites, this geometry is found to be suitable for a temperature range of -10 to 100 °C. For temperatures > 100 °C, the 2032 cell case material is not stable. For proper assessment of the potential of the developed material, for temperature > 100 °C Swagelok geometry was used.

- (II) **Swagelok Assembly:** This is a very bare and simple geometry that has been used in the present work for the high-temperature characterization of supercapacitors. The Swagelok cell was developed using Teflon material essentially to test device performance for temperatures > 100 °C to 300 °C.
- (III) **Laminated Supercapacitors:** This fabrication method is best suitable for developing these composite powder-based supercapacitors in a reasonably thin form [5-6]. The laminated ceramic supercapacitor is the first time being reported. It is found to be a cost-effective fabrication process that provides good contact between electrodes and electrolytes. This method has been used for SSC operations in a temperature range of 35 °C to 70 °C. Importantly, limitations are only due to the lamination sheet.

5.3 Important results for different geometries

(I) Coin cell Fabrication:

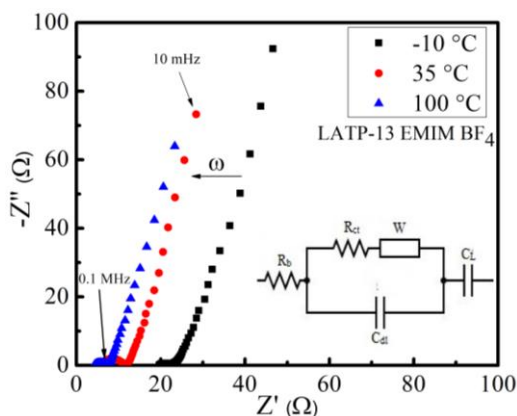


Fig. 5.2 (a) The Nyquist plot and corresponding equivalent circuit for SSC at different temperatures having LATP-13 EMIMBF₄ composite as an electrolyte.

Fig. 5.2 (a) shows the Nyquist plot for SSC having L ATP-13 EMIMBF₄ composite as an electrolyte in a frequency range of 10 mHz to 0.1 MHz from -10 °C to 100 °C. The nature of these plots confirms the supercapacitor formation [4,7-8]. The impedance nature is intact from -10 °C to 100 °C and it improves as the temperature approaches 100 °C. The equivalent circuit is given in the figure [9]. The results readily suggest that the interface is stable under such a temperature variation.

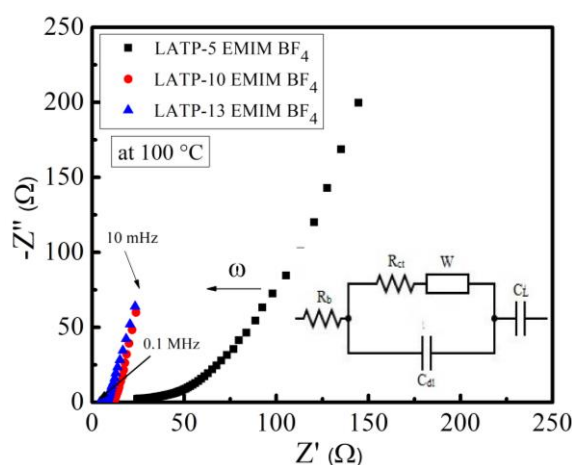


Fig. 5.2 (b) The Nyquist plot and equivalent circuit for SSC for composites with different IL percentage at 100 °C.

Fig. 5.2(b) gives the Nyquist plot (frequency range of 10 mHz to 0.1 MHz) for SSC having different weight percentages of ionic liquid EMIM BF₄ in the composite containing L ATP and EMIMBF₄ operating at 100 °C. It shows that IL is effective at a lower weight percentage too, but was with a slightly high equivalent series resistance (ESR), and spur at lower frequencies deviating from ‘vertical-line-like’ linearity. Thus, the optimized IL content of 10-13 wt% was found to be effective. Important to mention that we have not added IL beyond 13 wt% as it spills out from the pellet. Further, the amount is deliberately kept as low as possible so as not to compromise the ‘solid state’ of our electrolyte composite [4,10]. We have achieved a high ionic conductivity of $\geq 10^{-3} \Omega^{-1}\text{cm}^{-1}$ near room temperature for this composite having 13 wt% of IL, and quite a small value of ESR is witnessed in the devices based on these composites.

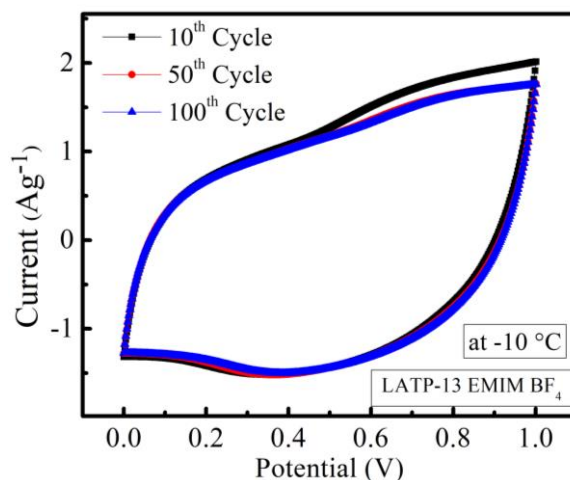


Fig. 5.2 (c) CV scans for SSC at -10 °C up to 100 cycles.

Fig. 5.2(c) shows the cyclic voltammetry (CV) scans at -10 °C obtained at 10 mV/s to evaluate the device's capability for charge storage at such a low temperature. With electrolyte L ATP-13 EMIMBF₄ composite the performance of the supercapacitor is noticeable even after 100 cycles, and the CV scans are intact with a reproducible and constant current response. Further, the box-like featureless profile confirms that the supercapacitors predominantly exhibit an 'electric-double-layer' type energy storage process. Furthermore, an appreciably large area under the curve again suggests significant charge storage.

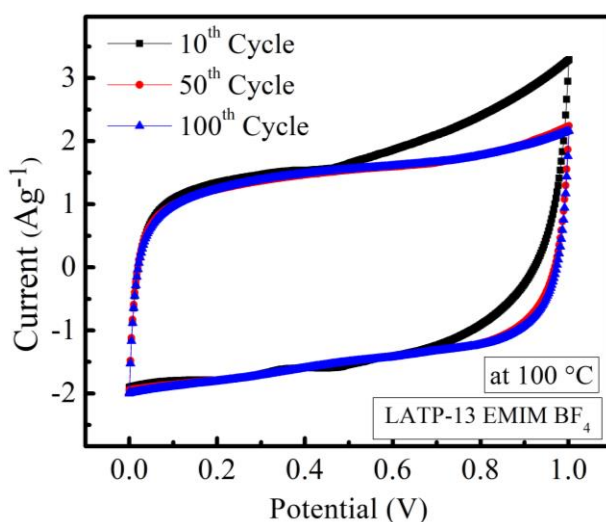


Fig. 5.2 (d) CV scans for SSC at 100 °C up to 100 cycles.

Fig. 5.2(d) demonstrates similar performance (CV) at 100 °C for supercapacitor having LATP-13 EMIMBF₄ composite as an electrolyte. At a scan rate 10 mV/s a more box-like feature-less profile is visible with intact and reproducible scans at least up to 100 cycles. The charge storage ability increases at higher temperatures due to improved ionic activity at the interface as expected.

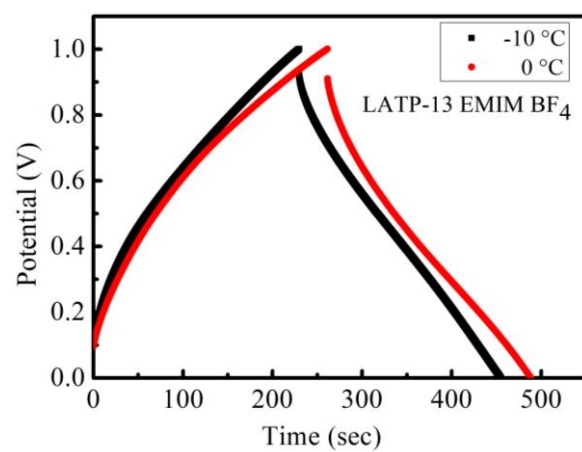


Fig. 5.2 (e) Galvanostatic charge-discharge (at 0.56 A/g) cycles for SSCs at low temperatures.

Fig. 5.2(e) shows the Galvanostatic charge-discharge (GCD) cycles for the supercapacitor at current density 0.56 A/g for two temperatures viz. -10 °C and 0 °C. Interestingly, the discharge time is quite large, even at such a low temperature. Further, the ESR is quite nominal. The nature of the curves shows predominantly the EDLC behaviour of the supercapacitor.

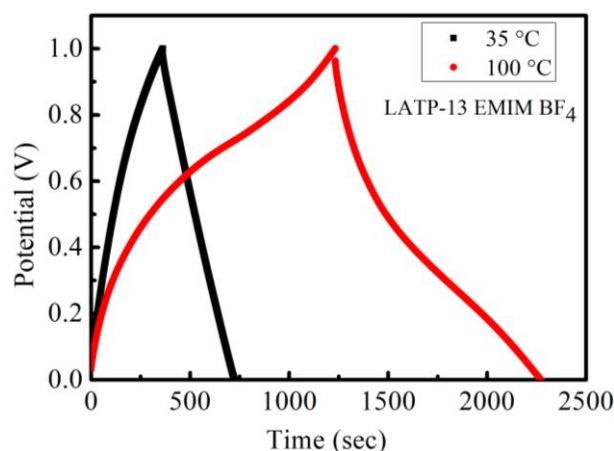


Fig. 5.2 (f) Galvanostatic charge-discharge (at 0.56 A/g) cycles for the SSCs at 35 °C and 100 °C.

Fig. 5.2 (f) shows the GCD cycles at room temperature ($\sim 35\text{ }^\circ\text{C}$) and $100\text{ }^\circ\text{C}$ at a current density of 0.56 A/g . The discharge time shows a rise as the temperature increases, which is in agreement with the CV profile. The value of ESR further drops down as compared to low temperature results shown in Fig. 5.2 (e). An important observation is the nature of the charge-discharge cycle that deviates from the ideal triangular shape when the device operates at $100\text{ }^\circ\text{C}$. This may be due to some pseudo capacitive effects. High temperature possibly facilitates chemical reaction or some charge transfer at the interface.

The different performance parameters obtained from these two GCD plots for the coin cells are tabulated (Table 1).

Table 5.1: Specific capacitance (C_s), specific energy (E), specific power (P), equivalent series resistance (ESR), and coulombic efficiency (η_{CE}) for the SSCs of the composite LATP-13 EMIMBF₄ as an electrolyte at different temperatures (operating current and voltage are 1mA and 1V respectively). The range is specified for C_s and (*) represents values for a typical SSC used in the analysis that is close to the average performance of the SSC.

Interestingly, C_s , E, and P have a very appreciable value even at $-10\text{ }^\circ\text{C}$.

Temperature	C_s (F/g)	E (Wh-kg ⁻¹)	P (W-kg ⁻¹)	ESR ($\Omega\text{ cm}^2$)	η_{CE} (0.65 mA-cm^{-2} / 0.56A-g^{-1})
$-10\text{ }^\circ\text{C}$	270-278 274*	8*	131*	58*	97%
$0\text{ }^\circ\text{C}$	281-289 285*	8.5*	130*	62*	92%
$35\text{ }^\circ\text{C}$	411-417 415*	14*	140*	14*	99%
$100\text{ }^\circ\text{C}$	1150-1250 1205*	40*	141*	23*	87%

Table 5.2: Areal capacitance, energy, and power density values for the SSCs with LATP-13 EMIMBF₄ as electrolyte at different temperatures. The range is specified for Areal capacitance and (*) represents values for a typical SSC used in the analysis that is close to the average performance of the SSC.

Temperature	Areal Capacitance (mF-cm ⁻²) (From GCD)	E _s (μWh-cm ⁻²)	P _s (μW-cm ⁻²)
-10 °C	154-159 157*	18.5*	297*
0 °C	158-162 160*	19*	298*
35 °C	235-240 238*	29*	320*
100 °C	660-720 690*	90*	317*

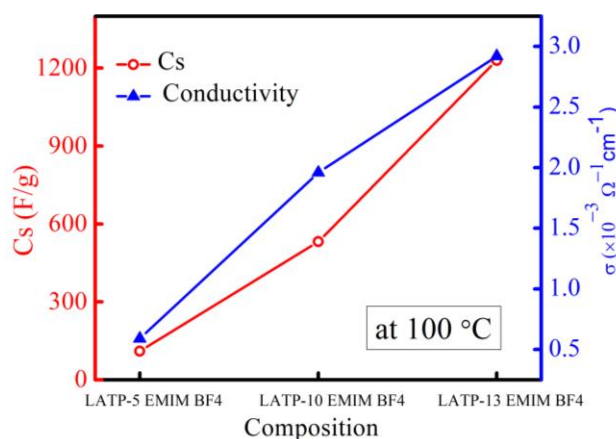


Fig. 5.2 (g) Comparison of conductivity and C_s value of the composites with different IL content.

Fig. 5.2(g) gives the C_s value for the SSC and conductivity of the composites of different IL contents. As the IL content increases, the C_s value and the conductivity both exhibit a rise. A systematic correlation between the conductivity of electrolyte and capacitance is thus observed. The C_s value sees a good rise in value as the IL amount in the composite increases from 5 to 13 wt%.

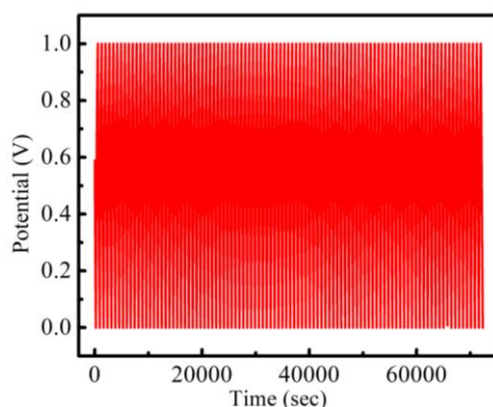


Fig. 5.2 (h) GCD curves for SSC up to 100 cycles at 35 °C.

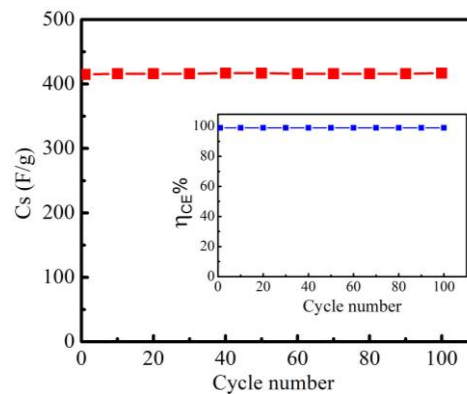


Fig. 5.2 (i) C_s vs Cycle number for first 100 GCD cycles at 35 °C.

Fig 5.2(h) gives the Galvanostatic Charge Discharge (GCD) curves up to 100 cycles (current density 0.56 A/g) for supercapacitor at ~ 35 °C having LATP-13 EMIMBF₄ composite as electrolyte. The cycles follow a constant pattern till 100 cycles and with negligible drop-in discharging time. Further, Fig 5.2(i) gives the C_s vs discharge cycle number for the first 100 cycles at ~ 35 °C for supercapacitor having LATP-13 EMIMBF₄ composite as electrolyte and shows that C_s remains almost constant around a value ~ 415 F/g with a good coulombic efficiency close to ~ 99 % throughout as shown in the inset. This readily indicates excellent electrochemical stability and a stable electrode-electrolyte interface.

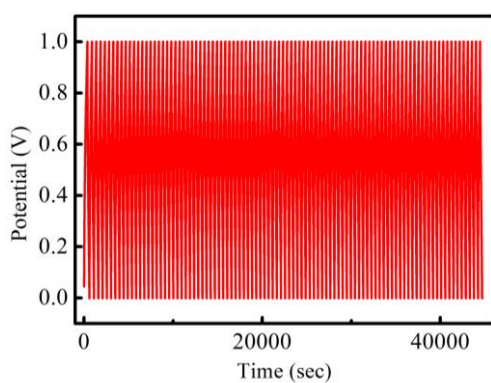


Fig. 5.2 (j) GCD curves for SSC up to 100 cycles at -10 °C.

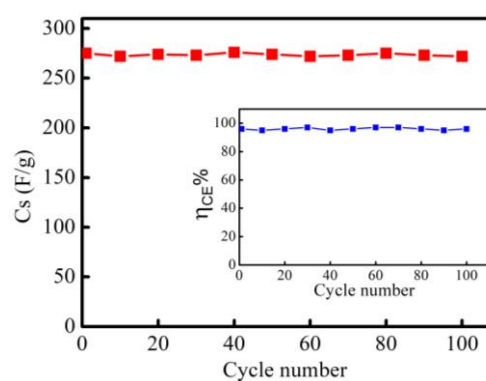


Fig. 5.2 (k) C_s vs Cycle number for first 100 cycles at -10 °C.

To further explore the device stability in adverse temperature conditions, GCD cycling was done at -10 °C as shown in Fig. 5.2(j) which gives the GCD curves up to 100 cycles

(current density 0.56 A/g) for the supercapacitor. Here GCD cycles are again stable and exhibit a continuous pattern with no specific change in the feature. Also, Fig. 5.2(k) shows the C_s vs cycle number for 100 cycles at -10°C . The C_s value remains almost constant around a value of ~ 275 F/g with appreciable columbic efficiency throughout ($\sim 98\%$) the cycle (inset). The nature of the graph demonstrates excellent electrochemical stability and a stable electrode-electrolyte interface even at such low temperatures.

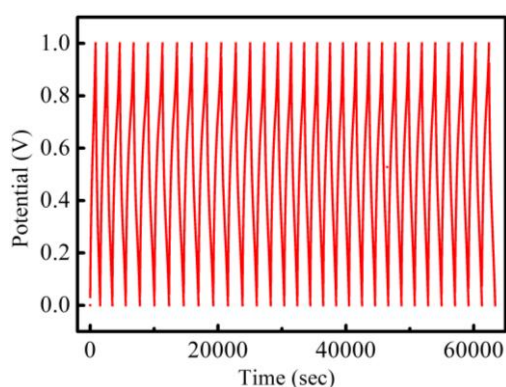


Fig. 5.2 (l) GCD curves for SSC up to ~ 30 cycles at 100°C .

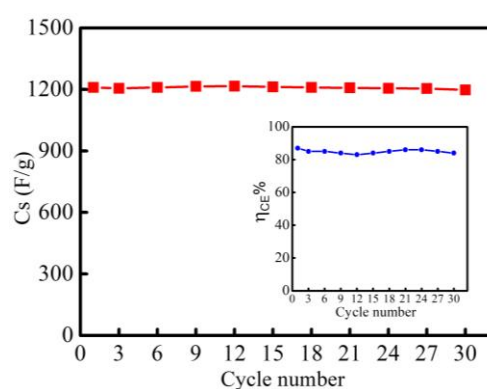


Fig. 5.2 (m) C_s vs Cycle number for first 30 cycles at 100°C .

The SSC device was again examined at 100°C . Fig. 5.2(l) depicts the GCD curves up to ~ 30 cycles (current density 0.56 A/g) for the supercapacitor at 100°C . The cycles exhibit almost a continuous trend without any deviation even at such a high temperature. The C_s vs cycle number for 30 cycles at 100°C is shown in Fig. 5.2 (m). As apparent, the C_s value remains almost constant to an appreciably high value around ~ 1200 F/g, and with good efficiency as shown in the inset. This indicates excellent electrochemical stability and a stable electrode-electrolyte interface. Moreover, the electrolyte is not only stable but also does not react with the electrode. This stability of the electrolyte and electrode-electrolyte interface leads to stable SSC performance.

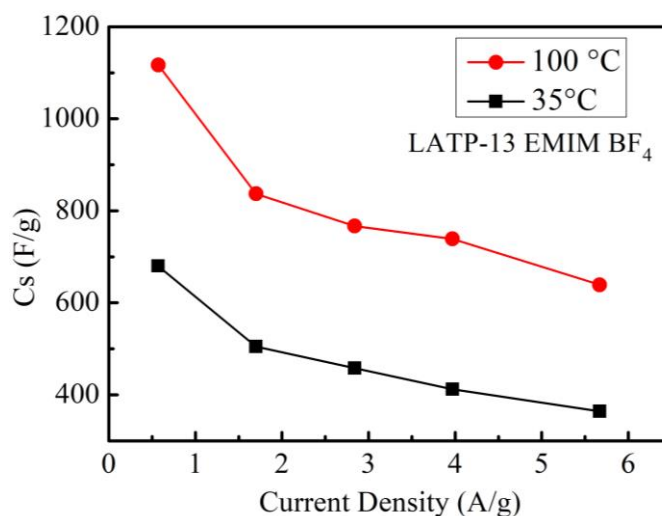


Fig. 5.2 (n) The C_s vs current density for SSC at 2 V.

Fig. 5.2 (n) The current density dependence of the specific capacitance for the supercapacitor at 2 V is shown. It can be seen that very high C_s values are obtained for low current densities, and even at high current densities the C_s values are quite significant. The trend is the same even at high temperature with the plot shifting upwards as C_s values rise.

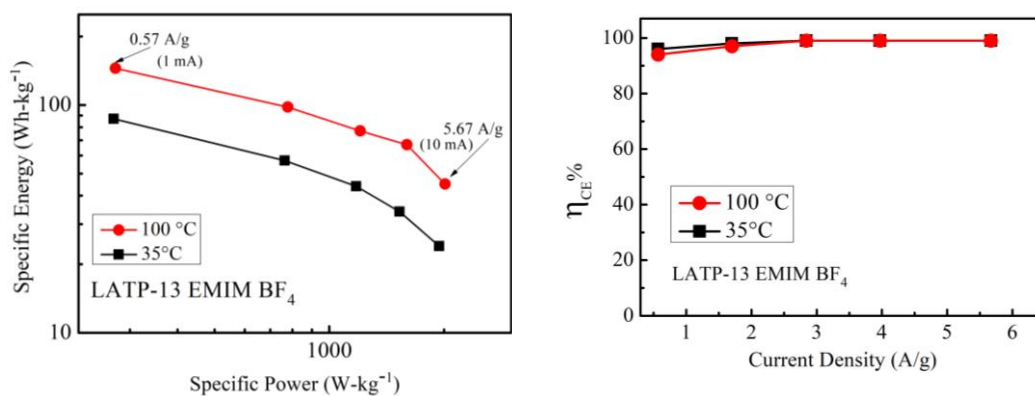


Fig. 5.2 (o) Ragone plot for SSC at different temperatures.

Fig. 5.2 (p) Coulombic efficiency vs current density at different temperatures.

In Fig. 5.2(o) Ragone plot for supercapacitor at different temperatures is shown in a voltage range of 0-2 V. The Specific energy (E) and specific power (P) values are appreciable from room temperature to 100 °C. At low specific power of 272 W/kg one

observes a high value of specific energy of 87 Wh/kg at 35 °C. Further, with increasing power output, the specific energy decreases. Higher values are obtained at high temperature with the plot shifting upwards with temperature rise. The highest specific energy and power of 145 Wh/kg (at 0.57 A/g) and 2012 W/kg (at 5.67 A/g), respectively at 100 °C. The coulombic efficiency as a function of current density is shown here at 35 °C and 100 °C for a voltage range of 0-2 V (Fig. 5.2 (p)). Coulombic efficiency rises from low to higher current densities and then saturates to 99 %.

(II) Swagelok Assembly:

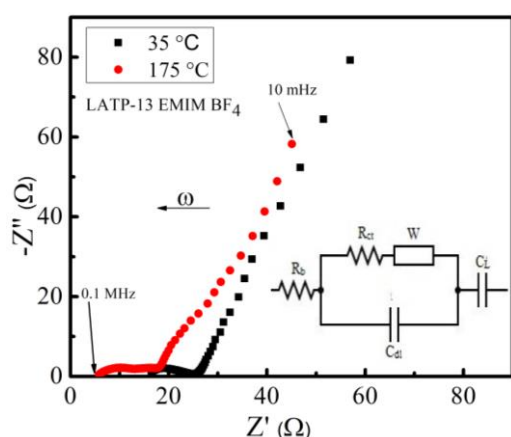


Fig. 5.3 (a) Nyquist plot for SSC in Swagelok assembly at different temperatures.

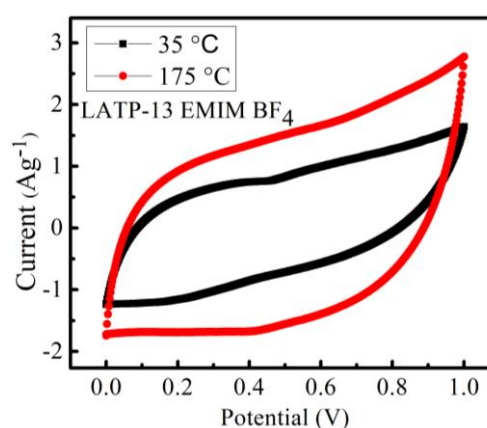


Fig. 5.3 (b) CV scans for SSC at different temperatures in Swagelok assembly.

Fig. 5.3(a) Nyquist plot at 35 °C and 175 °C (10 mHz-0.1 MHz) shows the supercapacitor formation for different temperatures. The equivalent circuit is given in the figure. In this fabrication method, the resistance is seen to be slightly high as compared to observed in SSC fabricated using the other two methods as it is a simple bare Swagelok geometry without any efforts to improve the contacts further. It is used only to show the performance of the SSC at temperatures > 100 °C where the other holders/ coin cell cases are not stable. CV scans (10 mV/s) give good charge storage capacity without any noticeable faradic process as shown in Fig. 5.3(b). The CV scan shows appreciable charge storage capacity without any distortion in the peak shape at 175 °C which makes the device capable of working at very high temperatures.

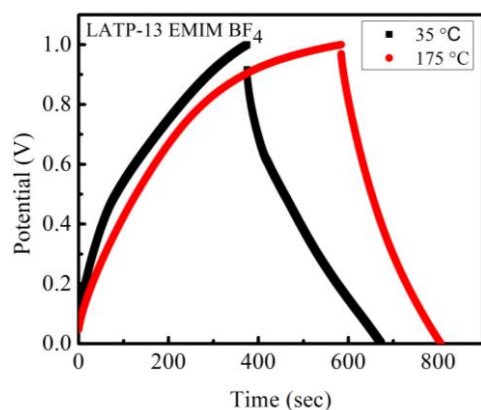


Fig. 5.3 (c) GCD cycles for SSCs at 35 °C and 175 °C.

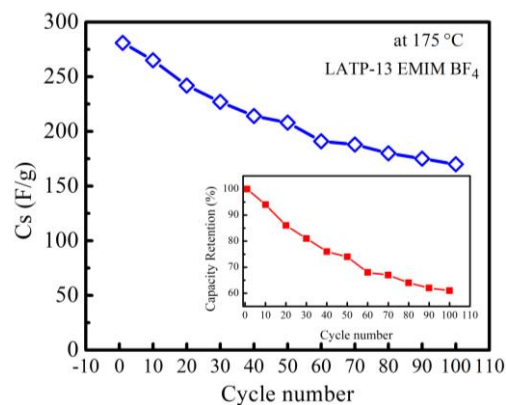


Fig. 5.3 (d) C_s vs cycle number at 175 °C.

The GCD cycles (at 0.56 A/g) for SSC at different temperatures in Swagelok assembly are shown in Fig. 5.3(c). The discharge time is quite large with a slightly high value of ESR as compared to SSC in coin cell fabrication. As has been already discussed above that it's a simple bare Swagelok geometry and resistance is more for device in this geometry so the rise in ESR is expected. However, it improves with an increase in temperature. To further explore the stability of the device at high temperature GCD cycling was performed up to 100 cycles at 175 °C and C_s vs cycle number has been plotted and shown in Fig. 5.3 (d). It can be seen that even after 100 cycles at such a high temperature the device performance is appreciable with a good C_s value of 170 F/g. The Inset of Fig. 5.3 (d) shows capacity retention with cycle number for the same supercapacitor at the same conditions which depicts that after 100 GCD cycles SSC attains 60% capacity retention.

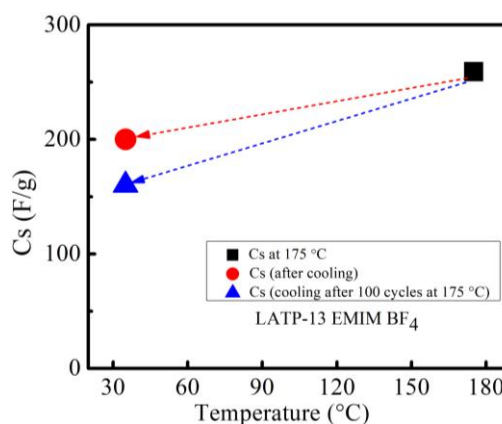


Fig. 5.3 (e) C_s values at room temperature after heating at 175 °C.

Fig. 5.3(e) shows that the C_s value even at 175 °C is quite appreciable in this simple bare Swagelok geometry too which shows the high-temperature stability of this electrolyte material under supercapacitor conditions. On cooling down to room temperature, the device is seen to be still working with a high C_s value of around 200 F/g. Also, even after 100 GCD cycles at 175 °C and then cooling to 35 °C the device is nicely working and has an appreciable value of capacitance. So, in this particular geometry at 175 °C it is possible to obtain a significant value of capacitance, and with a fairly high, stable value. On cooling, however, the value exhibits a subtle drop at room temperature.

Annealing of the device at higher temperatures and effect on performance:

Further to explore the thermal stability of the layered/sandwiched geometry beyond 175 °C the devices were annealed to specific high temperatures for 30 minutes and then furnace cooled to 35 °C and tested with their working condition using electrochemical characterization viz. impedance, CV, and GCD. These cells after annealing and cooling were fabricated in Swagelok geometry for studies.

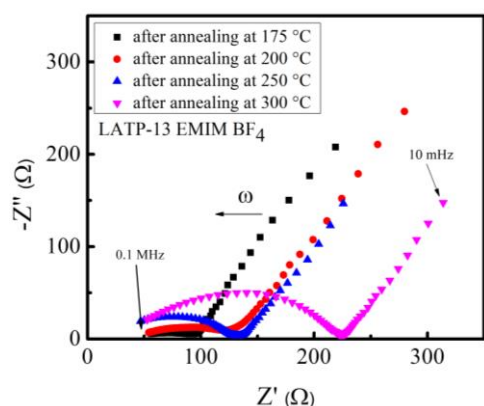


Fig. 5.4 (a) Nyquist plot for annealed SSCs at room temperature.

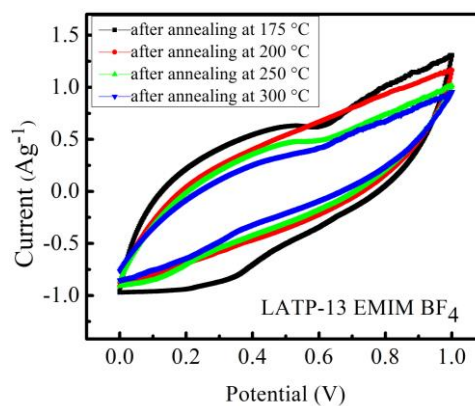


Fig. 5.4 (b) CV scans for annealed SSCs at room temperature.

Nyquist plot (10 mHz - 0.1 MHz) for supercapacitors annealed at high temperatures is shown in Fig. 5.4(a). With increase in annealing temperature resistance increases, however, the impedance nature is intact even after annealing up to 300 °C. The CV scans of SSC at room temperature after annealing at various temperatures at a scan rate of 10 mV/s. CV scans show good charge capacity (Fig. 5.4(b)). There are a few features in the CV scans which may be due to pseudo capacitive behavior initiated due to high

temperature treatment. High temperature annealing promotes diffusion across the interface and thus a charge transfer.

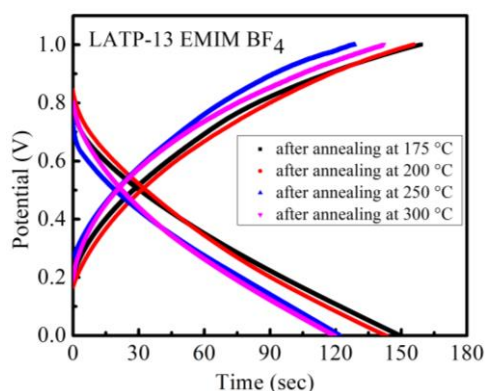


Fig. 5.4 (c) GCD cycles for annealed SSCs.

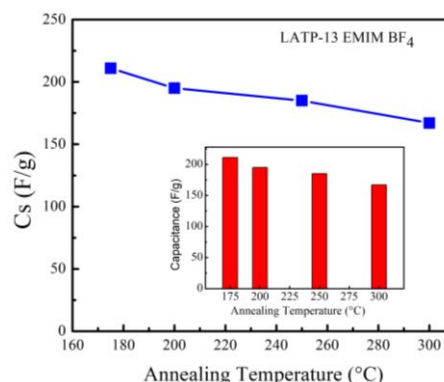


Fig. 5.4 (d) C_s for SSCs at different annealed temperatures.

GCD (at 0.56 A/g) cycles at room temperature for SSCs after annealing at high temperatures show good discharge time as shown in Fig. 5.4(c). Interestingly, the discharging time is significant even after annealing the SSC between 175 °C-300 °C. Fig. 5.4(d) gives specific capacitance at different annealed temperatures and even after annealing up to 300 °C the device shows an appreciably high C_s value of ~ 170 F/g.

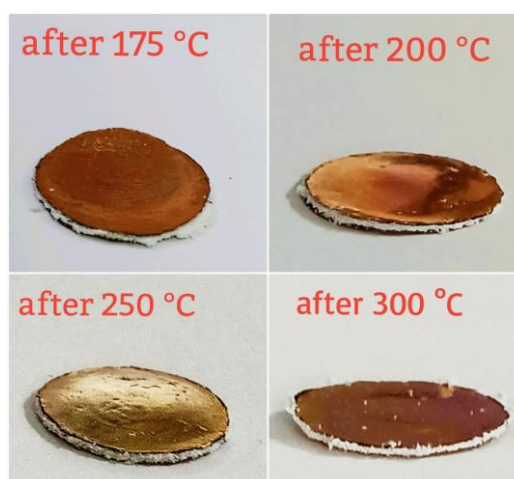


Fig. 5.4 (e) Supercapacitors after annealing at higher temperatures.

Fig. 5.4(e) shows picture of the condition of supercapacitors annealed up to 300 °C. There is not much change in their geometry. There are no significant swelling effects observed and the interfacial contacts also remain good.

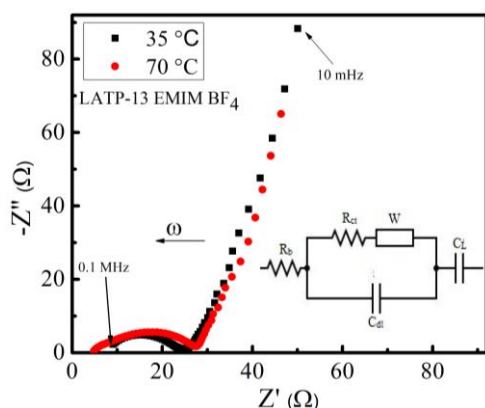
(III) Laminated Supercapacitors:

Fig. 5.5 (a) Nyquist plot for laminated SSC.

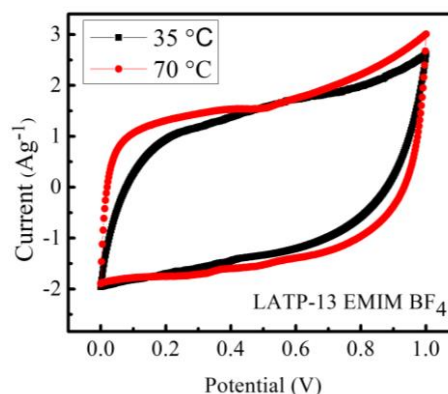


Fig. 5.5 (b) CV plot for laminated SSC.

Fig. 5.5(a) illustrates the Nyquist plot (frequency range of 10 mHz to 0.1 MHz) at two different temperatures with an equivalent circuit. In this fabrication method, the supercapacitor nature is clearly defined with very less resistance. So, the contact between electrodes and electrolyte is very reliable in this geometry. CV scans of SSC at different temperatures at a scan rate of 10 mV/s show a featureless profile with good charge storage ability (Fig. 5.5(b)).

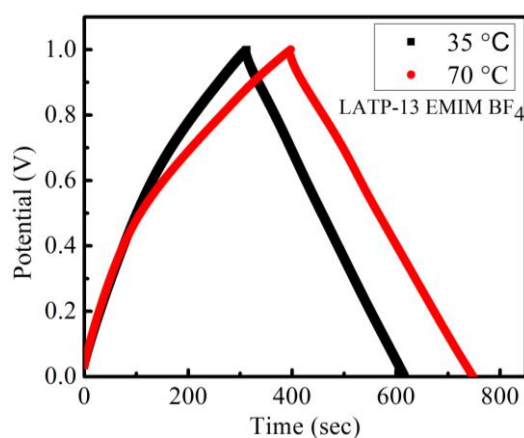


Fig. 5.5 (c) GCD cycles for laminated SSC.

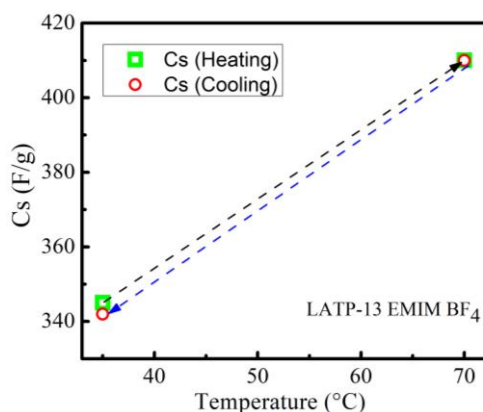


Fig. 5.5 (d) C_s value as observed after cycling.

Fig. 5.5(c) shows GCD (at 0.56 A/g) cycles for SSCs at 35 °C and 70 °C. It shows substantial discharge time, that again increases with temperature rise. The EDLC nature

is prominent. It is important to note that ESR is very less in this geometry which means good interfacial contacts and thus compliments the impedance results. Fig. 5.5(d) gives specific capacitance for the heating and cooling cycle of a laminated supercapacitor. It shows the C_s with temperature rise when the device is heated. Also, even after cooling to room temperature, the device exhibited almost the same capacitance which implies that the device does not get damaged or degraded even after heating up to 70 °C. Also, the electrode-electrolyte interface is stable.

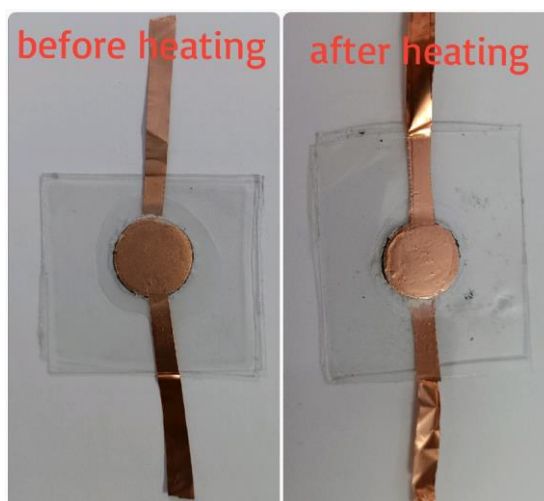


Fig. 5.5 (e) Laminated SSC picture before and after heating.

Fig. 5.5(e) shows that the device after heating up to 70 °C is in good condition. The layered stack which undergoes lamination, leads to a remarkable supercapacitor. The interfacial contacts are appreciable. The self-sustained geometry has significantly low mass than the 2032-coin cell geometry or the Swagelok assembly.

5.4 Summary

- (i) Work in this chapter demonstrates the use of LATP-IL composites in supercapacitors (SSCs). The amount of IL in the composites is small; thus, the solid state is not compromised.

- (ii) These SSCs can withstand a temperature from as low as $-10\text{ }^{\circ}\text{C}$ to as high as $300\text{ }^{\circ}\text{C}$.
- (iii) Application of these composites to supercapacitor technology is quite flexible. It has been demonstrated that supercapacitors in three different geometries exhibit excellent performance.
- (iv) We have shown that in the coin cell geometry, the SSCs work quite efficiently in a temperature range of $-10\text{ }^{\circ}\text{C}$ to $100\text{ }^{\circ}\text{C}$. SSC at $100\text{ }^{\circ}\text{C}$ in coin cells shows very high values of C_s ($\sim 1200\text{ F/g}$ at current density 0.57 A/g), E (145 Wh/kg at current density 0.57 A/g), and P (2000 W/kg at current density 5.67 A/g) and operating voltage of 2 V . The high-temperature limit is only due to the materials used in the coin cell casings.
- (v) SSC in Swagelok assembly works efficiently up to $\sim 175\text{ }^{\circ}\text{C}$ with high C_s values. This geometry is used only to demonstrate the application potential of the composites at high temperatures. Degradation in the performance near $175\text{ }^{\circ}\text{C}$ is attributed again to the quality of the material used in the Swagelok cell.
- (vi) For the first time, laminated ceramic supercapacitors have also been developed in this work. Direct use of ceramics in the supercapacitors has been shown in a simple sandwich geometry cell prepared using a simple hot roll laminator. This method also proved to be economically very efficient.
- (vii) High temperature annealing effects on these supercapacitors are quite novel. Annealing of the SSC at $\sim 300\text{ }^{\circ}\text{C}$ does not lead to any significant degradation. The subtle change in the values is due to copper oxidation. We have shown that these composites do not swell, or degrade when treated at higher temperatures. Thus, the electrode-electrolyte interface is quite stable.

References

- [1] E. P. Barrett, L. G. Joyner, and P. P. Halenda, "The Determination of Pore Volume and Area Distributions in Porous Substances. I. Computations from Nitrogen Isotherms," *Journal of the American Chemical Society*, vol. 73, pp. 373–380, 1951, doi: 10.1021/ja01145a126.
- [2] A. Kumar and H. M. Jena, "Preparation and characterization of high surface area activated carbon from Fox nut (*Euryale ferox*) shell by chemical activation with H_3PO_4 ," *Results in Physics*, vol. 6, pp. 651–658, 2016, doi:

- 10.1016/j.rinp.2016.09.012.
- [3] S. A. Borghei *et al.*, “Synthesis of multi-application activated carbon from oak seeds by KOH activation for methylene blue adsorption and electrochemical supercapacitor electrode,” *Arabian Journal of Chemistry*, vol. 14, pp. 102958, 2021, doi: 10.1016/j.arabjc.2020.102958.
- [4] G. Kaur, S. C. Sivasubramanian, and A. Dalvi, “Solid-state supercapacitors using ionic liquid dispersed Li^+ -NASICONs as electrolytes,” *Electrochimica Acta*, vol. 434, pp. 141311, 2022, doi: 10.1016/j.electacta.2022.141311.
- [5] S. Sharma, M. D. Singh, and A. Dalvi, “All-solid-state electric double layer supercapacitors using $\text{Li}_{1.3}\text{Al}_{0.3}\text{Ti}_{1.7}(\text{PO}_4)_3$ reinforced solid polymer electrolyte,” *Journal of Energy Storage*, vol. 49, 2022, doi: 10.1016/j.est.2022.104178.
- [6] S. Sharma and A. Dalvi, “Solid polymer electrolyte membranes using the ‘polymer-in-ceramic’ approach for all-solid-state supercapacitor applications,” *Solid State Ionics*, vol. 387, pp. 116063, 2022, doi: 10.1016/j.ssi.2022.116063.
- [7] G. P. Pandey and S. A. Hashmi, “Solid-state supercapacitors with ionic liquid based gel polymer electrolyte: Effect of lithium salt addition,” *Journal of Power Sources*, vol. 243, pp. 211–218, 2013, doi: 10.1016/j.jpowsour.2013.05.183.
- [8] N. Yadav, N. Yadav, and S. A. Hashmi, “High-Energy-Density Carbon Supercapacitors Incorporating a Plastic-Crystal-Based Nonaqueous Redox-Active Gel Polymer Electrolyte,” *ACS Applied Energy Materials*, vol. 4, pp. 6635–6649, 2021, doi: 10.1021/acsaem.1c00703.
- [9] N. Yadav, N. Yadav, and S. A. Hashmi, “Ionic liquid incorporated, redox-active blend polymer electrolyte for high energy density quasi-solid-state carbon supercapacitor,” *Journal of Power Sources*, vol. 451, pp. 227771, 2020, doi: 10.1016/j.jpowsour.2020.227771.
- [10] G. Kaur, M. D. Singh, S. C. Sivasubramanian, and A. Dalvi, “Investigations on enhanced ionic conduction in ionic liquid dispersed sol-gel derived $\text{LiTi}_2(\text{PO}_4)_3$,” *Materials Research Bulletin*, vol. 145, pp. 111555, 2022, doi: 10.1016/j.materresbull.2021.111555.

Chapter 6*

Ionic Liquid-garnet composites for Solid State Batteries (SSBs) and Solid State Supercapacitors (SSCs)

In this chapter, the effect of ionic liquid (IL) dispersion on LALZO ($\text{Li}_{6.75}\text{Al}_{0.25}\text{La}_3\text{Zr}_2\text{O}_{12}$) garnet has been studied. Different ILs viz. EMIMBF₄, EMIMCF₃SO₃, and BMIMBF₄ have been added in small amounts to garnet. The composites are labelled as LALZO-xIL, where x varies from 0.1 to 7 weight percentage of IL. Compositions with IL > 6 wt% have been avoided to maintain the solid-state nature of the electrolytes. The electrical (mainly conductivity-structure correlations), thermal (thermal stability), and structural properties of the composites have been discussed in detail.

The composites have been further explored as potential electrolytes for Li-ion batteries and supercapacitors. The synthesis of the electrodes and the fabrication process have been discussed in detail in chapter 2.

* Parts of the results of this chapter are published in: G. Kaur, S. Sharma, M. D. Singh, K. S. Nalwa, S. C. Sivasubramanian, A. Dalvi, "Ionic liquid composites with garnet-type $\text{Li}_{6.75}\text{Al}_{0.25}\text{La}_3\text{Zr}_2\text{O}_{12}$: Stability, electrical transport, and potential for energy storage applications", *Material Chemistry and Physics*.

6.1 FESEM

FESEM images of the pristine LALZO and LALZO-IL composite are shown in Fig. 6.1. Sol-gel derived LALZO exhibit grains of uniform size of ~80-100nm with no aggregations (Fig. 6.1(b)). In composite (Fig. 6.1(c)), ionic liquid appears dispersed uniformly in the matrix, surrounding the LALZO crystallites. The IL fills the pores and connects the grains with each other.

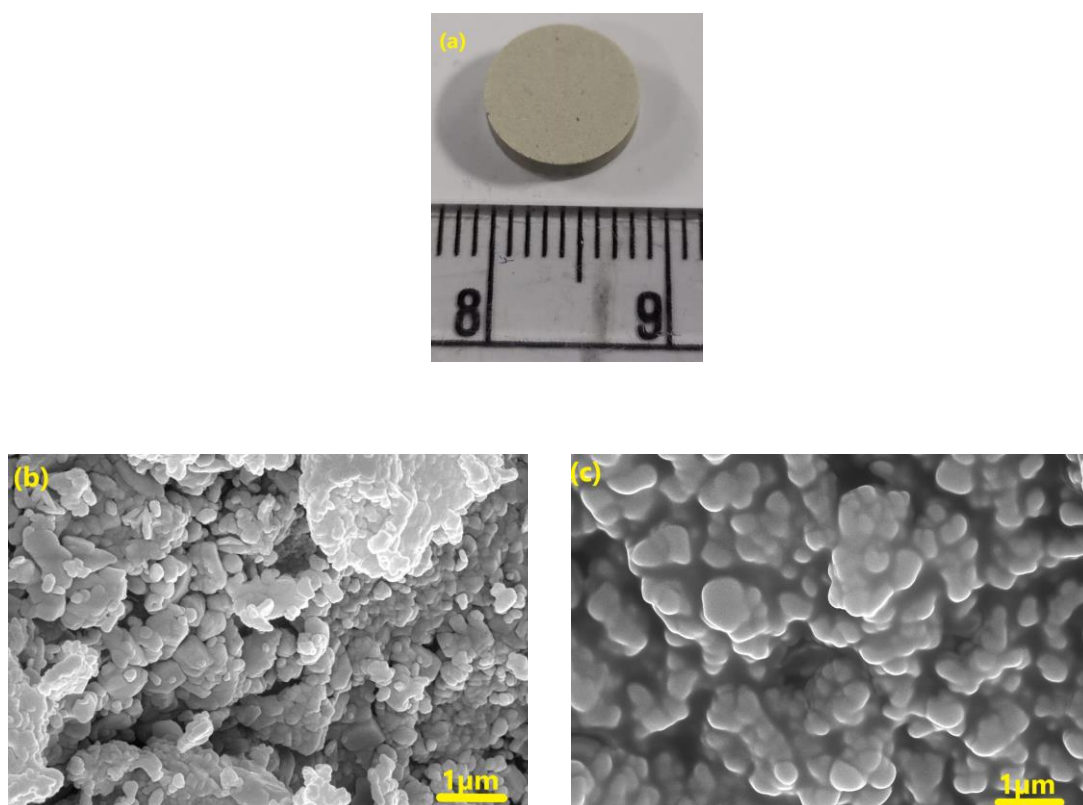


Fig. 6.1(a) The IL-LALZO as prepared pellet used for electrical transport studies **6.1(b)** FESEM image of powders of pristine LALZO and **6.1(c)** LALZO dispersed with ionic liquid (6wt%) at equal magnification.

6.2 Electrical Transport

At the outset, Nyquist plots for samples with low (LALZO-0.1 EMIMBF₄) and high (LALZO-6 EMIMBF₄) IL content are shown in Fig. 6.2(a) and 6.2(b), respectively. These spectra exhibit a similar pattern, consisting of a depressed semicircle at higher frequencies followed by a tail at lower frequencies. The tail is more prominent and the semicircle is relatively depressed in the case of a relatively high (6wt%) IL content sample.

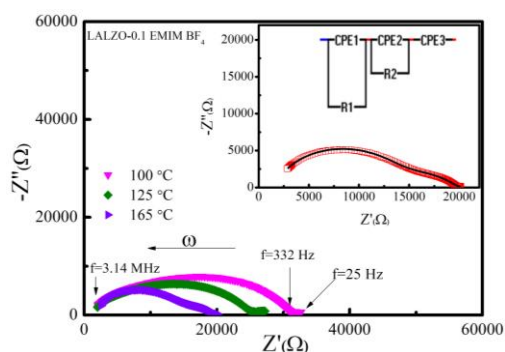


Fig 6.2 (a) Nyquist plots for LALZO-0.1 EMIMBF₄ with equivalent circuit in the inset.

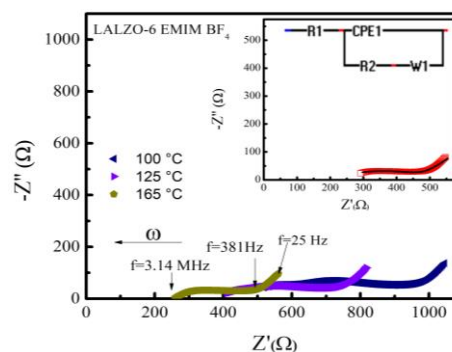


Fig 6.2 (b) Nyquist plots for LALZO-6 EMIMBF₄ with equivalent circuit in the inset.

The depressed semicircle consists of two merged-up semicircles, which may be attributed to impedance corresponding to bulk (high frequency) and grain-grain interface (low frequency) contributions. The equivalent circuits are also shown for both composites. The interfacial polarization though seen at the lower frequencies is not prominent (Fig. 6.2(a)), which may be attributed to ion intercalation in the partially non-blocking graphite electrodes. Polarization is relatively prominent in the high IL content samples. The total dc conductivity was obtained from the low-frequency intersection of the semicircle to the Z' axis (Fig. 6.2(a) and 6.2(b)).

The variation of conductivity (obtained from the Nyquist plot) with the IL content (wt%) is plotted in Fig. 6.3(a) for three different temperatures. It can be seen that with an increase in IL content, conductivity increases rapidly initially and exhibits a plateau above ~ 2 wt%, attaining a practically constant value. In the case of recently investigated LTP-IL composites, a relatively higher amount of IL was required (10-13 wt%) for the conductivity to reach the highest saturated value [1-2].

Fig. 6.3(b) shows the total conductivity (steady state) variation with temperature for all the IL-LALZO composites in a temperature range of 30-165 °C. Conductivity exhibits linear (Arrhenius) behaviour. The curves almost overlap for IL content ≥ 4 wt%. Thus, the highest conductivity (of $\sim 4 \times 10^{-4} \Omega^{-1} \text{cm}^{-1}$) is seen for the sample with 6 wt% IL content.

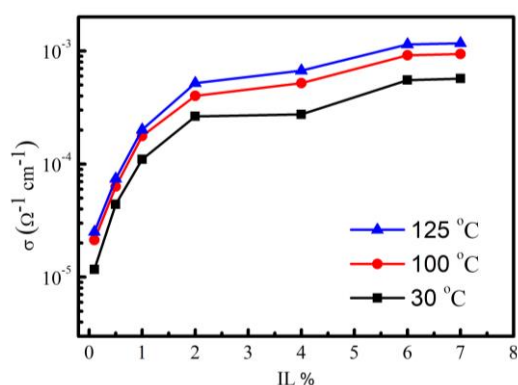


Fig 6.3 (a) Conductivity of the composite with variation of IL content (EMIMBF₄) at three different temperatures.

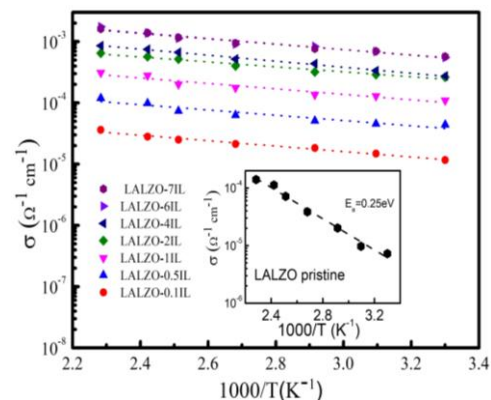


Fig 6.3 (b) Temperature dependence of total conductivity for all the composites having LALZO and varied amount of EMIMBF₄.

As evident in the inset of Fig. 6.3(b) the pristine garnet pellet exhibits a relatively low conductivity value with a higher activation energy of 0.25 eV. It is also observed that for composites with varied IL content, the activation energy remains almost constant, around a value, of 0.10 ± 0.02 eV. Thus, it is noticed that incorporating IL lowers the energy barriers for Li⁺ ions migration. For pure Li⁺ garnets, in-grain (bulk) activation energies have been reported in a range 0.1-0.6eV in various studies [3]. Such a moderate activation energy, as in present case, is seen for superionic solids e.g. α -AgI (above 147 °C) α -Li₂SO₄ (above 575°C) RbAg₄I₅ [3] near room temperature.

Such a noticeably low, activation energy in the IL-LALZO composites could also be due to migration of Li⁺ ions along the IL-LALZO interface bypassing the bulk (in grain) regions. This is similar to polymer-garnet composites where a very low activation energy of 0.07 eV is reported, and attributed to Li⁺ ion migration along the PEO-garnet interface [4]. Such a small value also suggest possibility of (i) saturation in the Li⁺ ion concentration and/or (ii) high Li⁺ ion mobility in presence of ionic liquid.

It is evident that a large variation in the conductivity is observed with a small change in the IL content in the LALZO matrix. Thus, a small quantity of the IL (2-6 wt%) is sufficient for a conductivity enhancement.

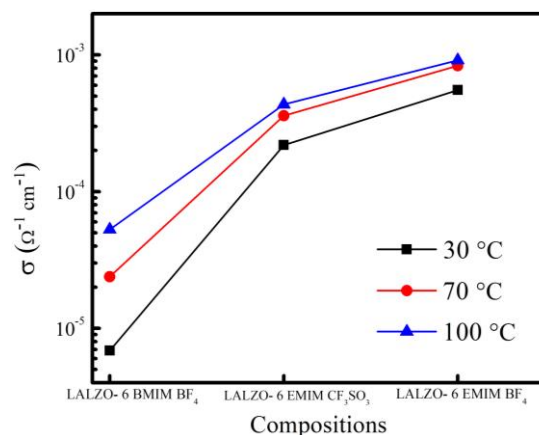


Fig 6.3 (c) Electrical conductivity at three different temperatures for LALZO with different ILs. Amount fixed to ~ 6 wt% in the LALZO matrix.

It is again interesting to see how ionic liquids of different types when added to the LALZO matrix, influence the electrical transport (Fig. 6.3(c)). Interestingly, the size of the anion, as well as the cation (of the IL), plays a role in tailoring conductivity. As discussed in our previous work, NASICON-IL composites have also shown varied conductivity trends for different ionic liquids. For example, about 13 wt% of EMIMBF₄ in the LATP/LTP matrix exhibited a maximum conductivity, attributed to the relatively smaller cation/anion size of EMIMBF₄ as compared to the other two ILs viz EMIMCF₃SO₃ and BMIMBF₄. The maximum conductivity has been observed for the LALZO-6 EMIMBF₄ composite, as seen in Fig. 6.3(c). Thus, smaller cation/anion size leads to a better rise in electrical transport.

6.3 Thermal Stability Investigations

The in-situ high-temperature XRD patterns obtained for pristine LALZO and LALZO-IL composite are shown in Fig. 6.4(a) and 6.4(b), respectively for three different temperatures.

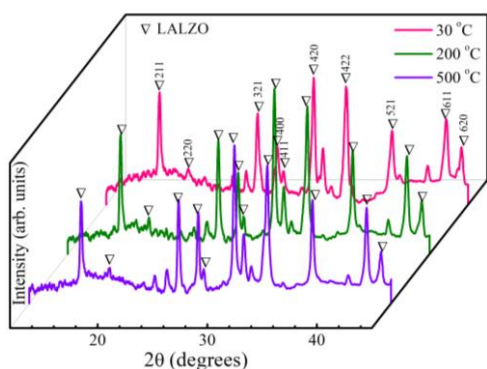


Fig 6.4 (a) HT-XRD patterns of LALZO.

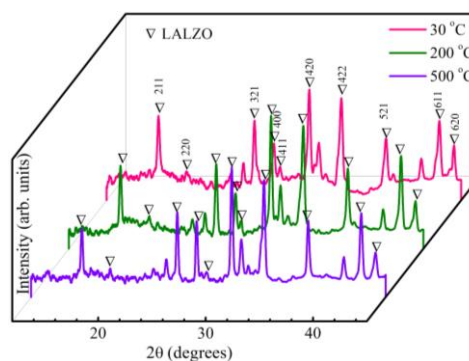


Fig 6.4 (b) HT-XRD patterns of LALZO-6 EMIMBF₄.

The peaks corresponding to LALZO match well with the literature-reported values [5], and the overall XRD patterns suggest a predominant cubic phase in LALZO. There are some unknown peaks, possibly due to the presence of the tetragonal phase (t-LALZO) along with Li_2CO_3 but in small amounts. The lattice parameter obtained ($a = 12.95 \text{ \AA}$) is comparable to cubic LALZO reported earlier [6]. All the peaks remain intact at their positions, even at higher temperatures. Furthermore, there is no new peak observed after the addition of IL to the LALZO, even at higher temperatures (Fig. 6.4(b)). This readily suggests that the LALZO phase in the composite is stable at elevated temperatures, and there is no evidence of any new crystalline compound formation due to the addition of IL. Further the IL addition does not distort the unit cell of LALZO.

FTIR and Raman spectra have been obtained to comprehend the nature of chemical bonding in the LALZO-IL composite and also to evaluate the way ionic liquid occupies the space within the LALZO matrix, thus creating possible new bonds, complexation, etc. A combination of Raman and FT-IR covers a wide energy range.

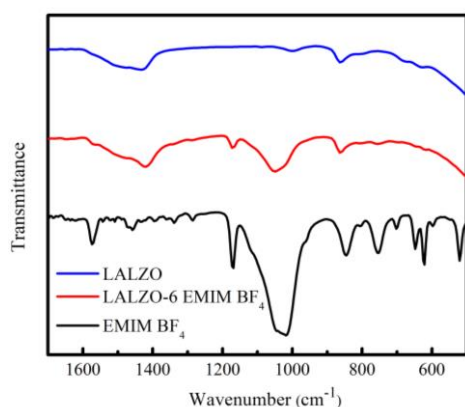


Fig 6.5 (a) FTIR in Attenuated total reflection (ATR) mode for pure IL, pristine LALZO, and the LALZO-IL composite.

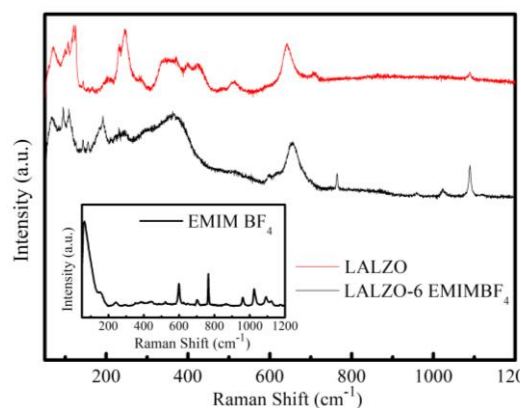


Fig 6.5 (b) Raman spectra for LALZO and LALZO-6EMIM BF_4 composite (Inset: for EMIM BF_4).

FTIR spectra for LALZO, LALZO-6 EMIMBF₄, and EMIMBF₄ are compared in Fig. 6.5(a), and similarly, Fig. 6.5(b) shows the Raman shifts up to 1200 cm^{-1} . The pristine LALZO shows absorption bands only at 1438 cm^{-1} and 863 cm^{-1} ; this observation, combined with the Raman shift at 1094 cm^{-1} , suggests the presence of impurity Li_2CO_3 . The weak and broad nature of these peaks again indicates that Li_2CO_3 precipitation is in small amounts and also distributed in a variety of environments. Further, the IR

spectrum of pure EMIMBF₄ is produced for comparison; of the many absorption bands in this spectrum, the dominant peak at 1049 cm⁻¹ corresponds to the asymmetric vibration of the B-F bond and the one at 1180 cm⁻¹ is due to the C-N stretching vibration of the imidazolium ring. A careful observation of the IR spectrum of the composite (shown in the middle) suggests that the absorption bands of the composite are either that of the LALZO or that of IL and no new absorption band is visible. This shows there is no possibility of any complexation or new bond formation in the composite, and the IL is adsorbed on the surface of LALZO only by weak forces.

The Raman shifts of LALZO prepared for this study interestingly provide some additional information. From the literature, we understand that in this case, the shifts, particularly apparent at < 300 cm⁻¹ correspond to the vibrations of the LiO₆ octahedral unit. Further, the shifts in the range 300–550 cm⁻¹ may be assigned to vibrational bending modes of the LiO₄ tetrahedral unit, and the shifts above 550 cm⁻¹ belong to the vibrations of the ZrO₆ octahedral unit [7]. All these peaks are visible in Fig. 6.5(b) (top spectrum), however, compared to the spectra reported for pure cubic phase in literature, in our case some peaks are split, suggesting the tetragonal phase may also be present at a much smaller concentration. Looking at Fig 6.5(b)-middle spectrum, we see the peaks discussed just above for pristine LALZO become broader with a subtle but significant red shift in the case of the composite. This broadening of peaks and their shift towards lower wavenumber strongly suggests (i) Li-O bonds are in a variety of environments (distributed environment) and, (ii) the bond weakening, i.e., the Li-O bonds are possibly getting elongated after the addition of IL in the matrix.

Thus, HT-XRD, FTIR along with Raman studies, suggest (i) due to IL addition, there is no other phase formation or chemical reaction leading to strong complexation; the IL is weakly adsorbed on the surface of LALZO providing a liquid-like environment (similar to amorphous structures) where the Li-O bonds are weakened; (ii) the presence of tetragonal phase of LALZO and lithium carbonate at trace levels cannot be ruled out; Even in the presence of these substances the conductivity values are substantially enhanced. The thermal analysis studies further confirm this proposition.

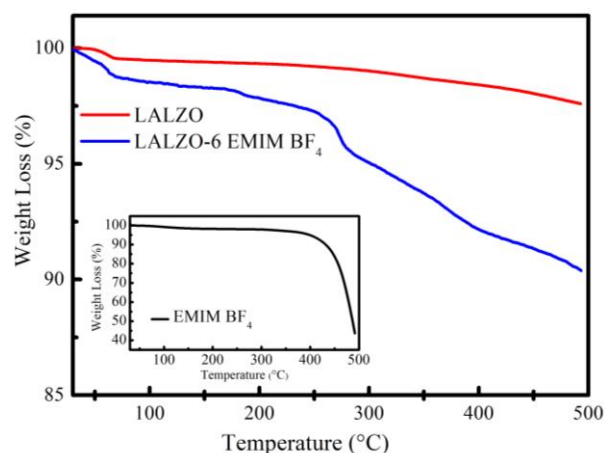


Fig 6.6 (a) TGA plots for LALZO and LALZO-6 EMIM BF₄. Inset: TGA plot for EMIM BF₄.

In Fig. 6.6(a) the TGA results of LALZO are compared with the LALZO-6 EMIMBF₄ composite. The pristine LALZO does not show any sudden weight loss; The small and gradual weight loss seen in the plot can be attributed to the slow removal of trace amounts of water and other organic moieties used during preparation and adsorbed on the surface of garnet [5]. In the case of LALZO-6 EMIM BF₄ composite, there is slight weight loss near 100 °C which may again be attributed to water evaporation. Further, a noticeable gradual weight loss initiates at $T \geq 200$ °C. As evident in the inset, the TGA of pristine IL exhibits a weight loss process at relatively higher temperatures (inset, Fig. 6.6(a)). Further, for pristine IL the weight loss around 400 °C is massive. On the other hand, for the composite, this weight loss may be attributed to the removal of adsorbed IL (or surface water) which is prolonged and gradual. This suggests in the composites, the IL is not bound by a unique strong chemical bond but held up by the adsorption of forces of different magnitudes.

This phenomenon has been again examined using differential scanning calorimetry (Fig. 6.6(b)). A small endothermic dip below ~100 °C for Pristine LALZO is due to water/solvent evaporation as also explained in the TGA thermogram. There are no other major peaks observed in pristine LALZO up to ~500 °C. On the other hand, surprisingly, for LALZO-6 EMIMBF₄ and LALZO-6 BMIMBF₄ exothermic broad peaks are seen around 200 °C which may be attributed to the gradual desorption of IL

and the consequent strengthening/ordering of other chemical bonds on the surface of garnet.

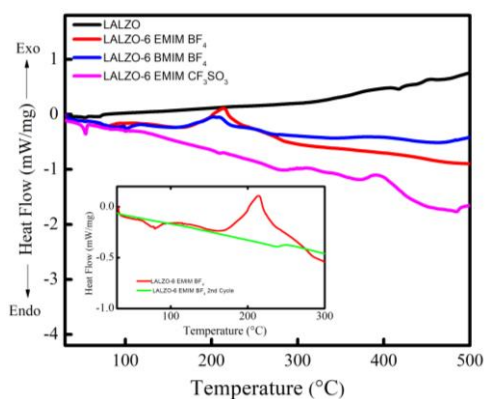


Fig 6.6 (b) DSC plots for LALZO and its composite with different ILs. Inset: DSC plot of first and second heating cycle for LALZO-6 EMIMBF₄.

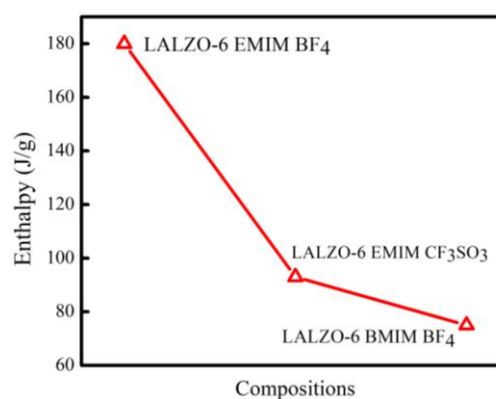


Fig 6.6 (c) Enthalpy values obtained from DSC for composites having LALZO and different ILs.

In LALZO-6 EMIMCF₃SO₃ composite this thermal event takes place above ~300 °C. The second heating cycle for LALZO-6 EMIMBF₄ is surprisingly featureless (inset Fig. 6.6(b)) and suggests an irreversible process of the process at the LALZO grain-grain interface. Thus, the desorbed IL does not form a bond with the LALZO surface again. In Fig. 6.6(c) enthalpy obtained corresponding to these exothermic peaks for these composites is plotted with composition. The behaviour shows that LALZO-6 EMIMBF₄ exhibits the highest enthalpy value among the three composites. Higher enthalpy release is suggestive of better strengthening of other bonds on the surface (for example Li ion – Garnet bonds) after desorption; and this process is better in EMIMBF₄ compared to other ILs. The exothermic peak indicates that disorder at the IL-grain interface. The exothermic peaks are weak, broad and suggest a slow ordering transformation. It appears that adsorption gives rise to an amorphous environment/domain at the grain-IL-grain interface that slowly transforms into a ordered phase above certain temperatures. IR-Raman studies are in conformity with DSC/TGA studies. The enthalpy obtained for these composites from DSC correlate well with the obtained conductivity values and suggest a major role of amorphous regions/ domains in facilitating the electrical transport.

In our earlier studies on LTP and LATP IL composites we found the adsorption of IL on the surface of these materials is a sort of physisorption [2,8]. The thermogravimetric plots of LTP and LATP-IL composites almost mimic the characteristics of pristine IL, suggesting no strong bonding of IL at the interface. Unlike LALZO-IL composites exhibit stronger adsorption with a wide range of distributed bond strengths. The irreversible DSC thermogram also suggests a strong possibility of chemisorption. Further, during the formation of the composite, these new bonds between the IL and the garnet surface may consequently weaken the bonds of lithium with LALZO on its surface thus increasing the conductivity of the Li^+ ion. We have said the broad exothermic peak seen in DSC is due to the ordering process after IL is desorbed, in which the lithium bonds are strengthened. This is further examined using dynamic conductivity studies.

6.4 Conductivity- structure correlation

To correlate the structural changes as suggested by DSC/TGA and other experiments with the electrical transport, dynamic conductivity measurements were performed where the electrical conductivity was measured at a typical heating rate of $1\text{ }^\circ\text{C}/\text{min}$ from room temperature to a temperature $T \geq T_c$, where T_c is the onset point of exothermic transformation (as observed in DSC).

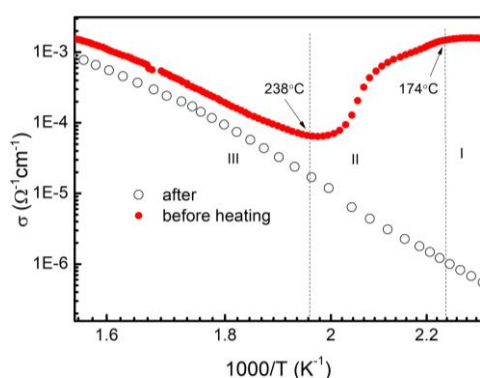


Fig 6.7 (a) The dynamic conductivity temperature cycles for LALZO-6 EMIM BF_4 composite in a temperature range of $30\text{-}340\text{ }^\circ\text{C}$.

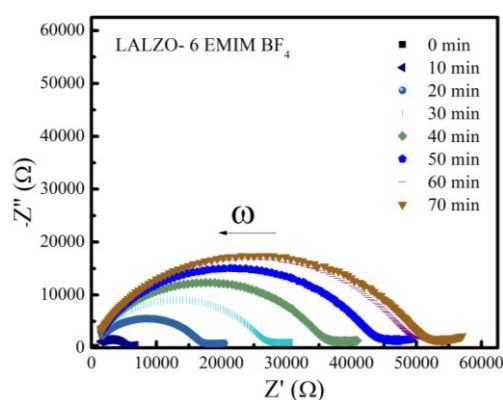


Fig 6.7 (b) Nyquist plot for LALZO-6 EMIM BF_4 at $220\text{ }^\circ\text{C}$.

Fig. 6.7(a) shows the temperature dependence of dynamic conductivity for LALZO-6 EMIM BF₄. This observation is aligned with the thermal events suggested by DSC and TGA. The plot is divided into three regions; the conductivity rises linearly in region-I, gradually decreases initially, and falls rapidly at 181°C (region-II). Further, it exhibits a dip at 190°C, and in region III, it rises almost Arrheniusly with a relatively higher slope. The fall in the conductivity may be attributed to ordering (strengthening of lithium bonds) at the IL-LALZO interface. As ordered phase is less favorable for the electric transport. It is also likely that due to the irreversible nature of chemisorption, the desorbed products lead to a less conductive layer at the LALZO interface. Above the dip (T~238 °C) the conductivity rise is due to the electrical transport in LALZO via less conductive layer of grain-grain interface. The sample is then furnace cooled, and the second heating cycle is also performed. Conductivity again increases Arrheniusly with relatively higher slope (activation energy). No thermal events are observed in region-II, and the cycle almost matches the conductivity of the degraded LALZO-IL above T~ 250°C. The above results suggest irreversible nature of the conductivity above ~200°C. The behaviour of the conductivity is therefore aligned with the thermal events suggested by DSC and TGA.

To further investigate the effect of thermal events on electrical properties, another experiment was performed in which conductivity isotherms were obtained at T~ T_c (around ≥200 °C) i.e., at a temperature close to the onset of the exothermic peak observed in the DSC. The dynamic Nyquist plots were obtained as shown (in Fig. 6.7(b)) for the LALZO-6 EMIMBF₄ composite. The diameter of the semicircle observed with time gradually increases and almost saturates at later times. The conductivity (from semicircle diameter) at ≥200 °C is plotted with time (Fig. 6.7(c)). Apparently, it falls rapidly initially and stabilizes subsequently to a constant value. This fall in conductivity is more prominent in the case of the composite containing higher IL content. The conductivity $\Delta\sigma$ (ratio of conductivity at t=0 (σ_i) to the saturated value (σ_s)) obtained from Fig. 6.7(c) is plotted with the enthalpy content of the exothermic peak as shown in the inset of Fig. 6.7(c). Higher drop in the conductivity thus correlates well with corresponding higher enthalpy change.

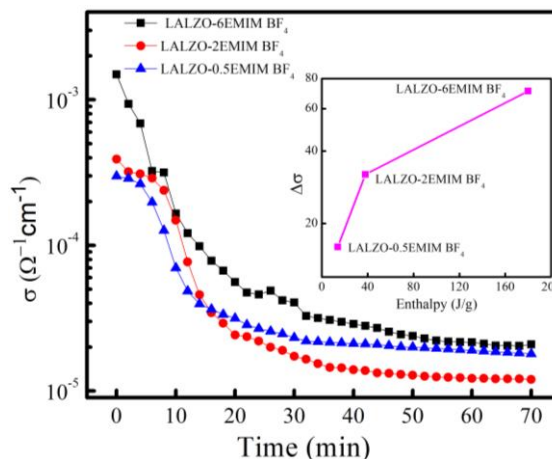


Fig 6.7 (c) Conductivity isotherm (at ~ 220 °C) for composites containing LALZO and different percent of EMIMBF₄. Inset: Enthalpy value obtained from DSC versus $\Delta\sigma$ (obtained from Fig. 6.7(c)) for composites containing LALZO and different percent of EMIMBF₄.

The electrical, structural, and thermal studies combined suggest the following qualitative mechanism for the electrical transport in these composites:

- (i) Ionic liquid essentially lies at the LALZO grain-grain interface. It does not react as such with the LALZO massively. This insertion, however, leads to IL's chemisorption on the surfaces. The adsorption also leads to localized amorphous regions between the grains, providing an electrical coupling and smooth long-range diffusive inter-grain transport. Consequent to the chemisorption, the weakening of bonds that bind the lithium ions to the solid happens thus enhancing the lithium ion mobility.
- (ii) During heating above a specific temperature, desorption occurs, and energy is released. The nature of this thermal event is irreversible (justified using the TGA and DSC results), where the desorbed ionic liquid (unlike the pristine one) does not lead to a sudden decomposition or weight loss.
- (iii) The desorption leads to either strengthening of mobile Li^+ ion bonding with the host matrix and/or may also lead to the possible formation of an undesired ionically insulating layer due to the formation of some unknown compound leading to poor conductivity at elevated temperatures. In any case, such a desorbed layer thus decouples the grain-grain interface. If the IL content is relatively high in the matrix, conductivity reaches a lower value

above T_c . This also suggests that desorbed compound/impure IL is less conductive in nature.

- (iv) The ions of the IL are not mobile. Their contribution to long-range diffusive motion is not likely due to dense structure and bigger ionic size. Still, their small ionic size provides better adsorption, possibly on the surface. This may be the reason for the high ionic conductivity observed in ILs with smaller ionic radii.

These results are starkly different from that of LTP-IL composites where possibly physisorption leads to relatively weak bonding, and the process of absorption–desorption of ionic liquid on the surface is reversible [1]. To validate the above hypothesis, we may need further sophisticated IL-LALZO interface studies.

6.5 Electrochemical characterization in battery configuration

The LALZO-6IL composite was tested as an electrolyte for batteries. Fig. 6.8 (a) shows the galvanostatic charge discharge (GCD) cycle for the lithium cell LFP//LALZO-6IL//Li at 0.1 C and 0.5 C discharge rates. The cell was charged using constant current-voltage mode, followed by discharge at constant current and ~ 30 minutes of rest time.

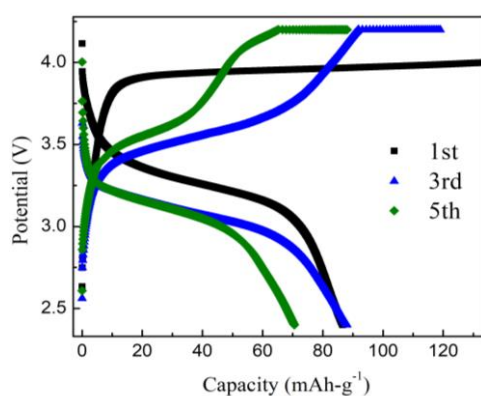


Fig 6.8 (a) GCD cycle for lithium cell at different discharge rate.

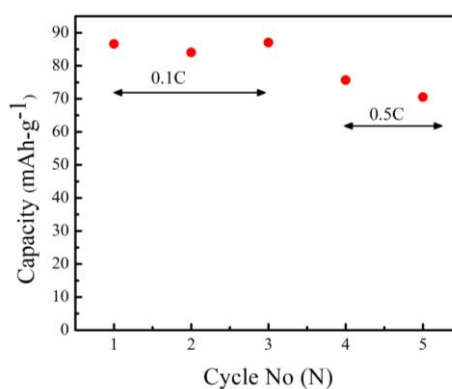


Fig 6.8 (b) Discharge capacity versus cycle number.

As evident in Fig 6.8(a), the cell shows IR overpotential of ~ 0.5 V at the first cycle. This could be due to the interfacial contact issues between cathode and LALZO-IL electrolyte. In all the discharge cycles a reasonably wide discharge-plateau is witnessed which is a typical characteristic of lithium cell. The very first charge-discharge cycle appears irreversible with low coulombic efficiency. Even though the LALZO conducts

only Li^+ ions, presence of IL ions, viz EMIM^+ and BF_4^- may lead to the formation of a complex SEI layer at the interface. During charging along with the Li^+ ions, the IL cations (EMIM^+) are directed towards Lithium anode may form complexes that are irreversible in nature. Such a formation may be responsible for low coulombic efficiency. Nevertheless, a coulombic efficiency of $\sim 100\%$ is witnessed in the later cycles. Such a behaviour also suggests that the SEI layers become stable at later times and Li^+ ions are the majority charge carriers. The cell shows an initial discharge capacity of $89 \text{ mAh}\cdot\text{g}^{-1}$ at 0.1C rate with a stable discharge plateau of 3.34V (Fig. 6.8(a)). Furthermore, as apparent in Fig. 6.8(b), the capacity is almost stable, and comparable to recent report on PEO-LLZTO based Li/LFP battery [9,10].

Based on the initial investigations, the LALZO-6IL electrolyte appears suitable at least for low-power devices. However, there is a scope for improvement by enhancing the mechanical stability of the composite, reducing the thickness of the electrolyte pellet, and improving the interface between the electrode and electrolyte by using suitable electrodes.

Finally, it is worth comparing the ionic liquid-garnet composite with the conductive ceramic filler (Bismuth doped LLZO particles) based polymer electrolyte (PEO-LiTFSI). In a study by Villa et al. [11], various experimental investigations were used to demonstrate that the ionic conductivity is primarily regulated by 'highly conductive transport channels' at the interface of the polymer-filler particles. As a result, at low temperatures where the interface resistance is high, the conductivity is also low. Conversely, the interface conductivity becomes significant for high temperatures close to the polymer's melting point. This leads to inter-grain ionic transport and enhanced ionic conductivity of the composite. In the present work, where ionic liquid occupies the matrix in place of polymer, the LALZO grains are well connected due to the presence of IL, and high ionic conductivity is witnessed in a reasonably wide range of temperatures. Compared to polymers, ionic liquids possess higher thermal stability. Therefore, the 'conductive channels' in this case have a different nature. However, there is still a similarity. Low ionic conductivity is witnessed when the IL-ceramic interface is degraded. Therefore, the ion conductive transport channels [11] at the interface possibly play an important role in controlling inter-grain ionic transport, similar to ceramic-polymer composites. In future work, to further tailor the ionic conductivity, it would also be interesting to study how the ionic liquid morphology and the interface

are affected by compositional alteration of the conductive LALZO ceramic, as demonstrated for the polymer-ceramic composites.

6.6 Electrochemical characterization in supercapacitor configuration

At the outset the electrical conductivity of the composite in a pellet geometry (diameter ~ 9 mm and thickness ~ 3 mm) was measured as a function of temperature in the 30 – 165 °C range (shown in the inset of Fig. 6.9). The LALZO with 6 wt% IL exhibits a high conductivity of $\sim 6 \times 10^{-4} \Omega^{-1} \text{cm}^{-1}$ at 35 °C, therefore found to be suitable as a SSC electrolyte. For the SSC electrode preparation, high surface area ($\sim 1500 \text{ m}^2/\text{g}$) activated charcoal was used. All the devices have been fabricated using electrodes having mass loading of $\sim 1.2 \text{ mg}/\text{cm}^2$. The SSCs in a coin cell geometry (2032 type) were studied at 0 °C, 35 °C, and 100 °C for testing their wide temperature applications. At the outset, Nyquist plots for SSCs at three different temperatures are displayed in Fig. 6.9 in a frequency range of 10 mHz to 0.1 MHz. Confirmation of supercapacitor formation at three different temperatures in a range of 0 °C to 100 °C is indicated by a tiny semicircle at higher frequencies followed by a steep vertical line at low frequencies. The semicircle, though with a small diameter, is most likely due to some charge transfer at the interface, suggestive of a weak faradic process.

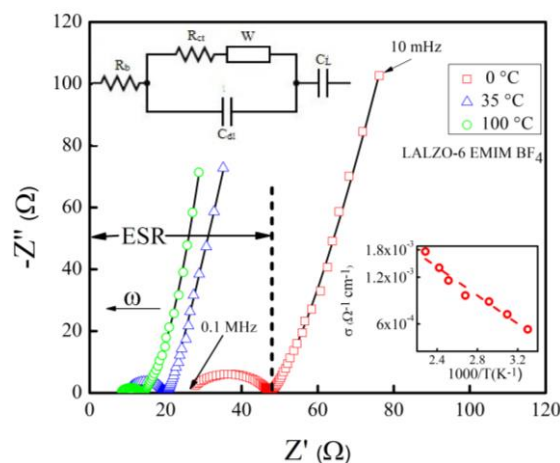


Fig. 6.9 The Nyquist plot and corresponding equivalent circuit for the SSC (2032 type) at different temperatures having LALZO-6 EMIMBF₄ composite as an electrolyte. Inset: Temperature dependence of total conductivity for composite LALZO-6 EMIMBF₄.

The equivalent series resistance (ESR) is obtained from the intersect of a vertical line with Z' axis as shown by the dotted line [2,12]. The ESR at 0 °C is about $\sim 80 \Omega \text{ cm}^2$ which reduces to a value of $\sim 34 \Omega \text{ cm}^2$ at 35 °C and $\sim 24 \Omega \text{ cm}^2$ at 100 °C. The impedance spectra depict SSC behaviour. A model shown in Fig. 6.9 inset fits well for all these Nyquist plots.

The CV patterns at 35 °C have been recorded for the device by gradually increasing the operating voltage range up to 3V as shown in Fig. 6.10(a). It has been observed that the shape of the CV curve remains intact and featureless up to 2 V, and above this, a deviation is seen. So, further studies were avoided above 2 V to remain in a pure electric-double layer type regime. Cyclic voltammetry scans (10 mV/s) were obtained at three temperatures as shown in Fig. 6.10(b). The charge storage ability at different temperatures can be depicted by observing the significant hysteresis in the CV. The CV scan (except at 35 °C) exhibit some peak-like features and deviations from the ideal box-like behaviour.

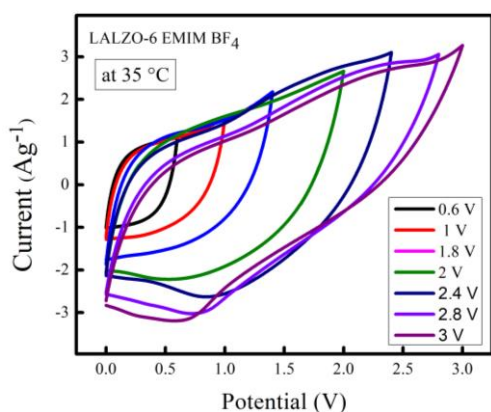


Fig. 6.10 (a) CV scans (at 10 mV/s) of SSC for different voltage ranges at 35 °C.

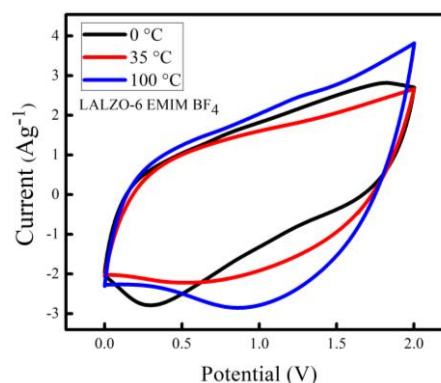


Fig. 6.10 (b) CV scans (at 10 mV/s) for the SSC for the 10th cycle at different temperatures.

Further, the galvanostatic charge-discharge (GCD) cycles were obtained to evaluate various performance parameters. The total device capacitance $C = \frac{I \Delta t}{\Delta V}$ (in F) is calculated using discharge current (I in A), discharge time (Δt in seconds), and voltage window of the discharge cycle (ΔV in volts). The specific capacitance (F/g) per electrode has been calculated as $C_s = \frac{4C}{m_{total}}$, where m_{total} is the activated carbon mass

in grams on the electrodes. Moreover, the specific energy ($E = \frac{1}{2} \cdot \frac{C(\Delta V)^2}{3.6 m_{total}}$) and specific power ($P = \frac{3600 \cdot E_s}{\Delta t}$) were obtained for the full device in the units of Wh/kg and W/kg, respectively. Furthermore, the equivalent series resistance ($ESR = \frac{\Delta V_{IR}}{2I}$) was calculated using the initial voltage drop during the discharge cycle. For comparison, the areal capacitance values with specific energy and power density were obtained and given in Table 6.1. The areal capacitance ($F \cdot cm^{-2}$) of the device has been obtained as $C = \frac{I \Delta t}{\Delta V A}$. Further, the energy density ($Wh \cdot cm^{-2}$) and power density ($W \cdot cm^{-2}$) have been calculated as $E_a = \frac{1}{2} \cdot \frac{C(\Delta V)^2}{3600}$ and $P_a = \frac{3600 \cdot E_a}{\Delta t}$ respectively.

The GCD curves were obtained for different cut-off voltages to evaluate the operating voltage limit as shown in Fig. 6.11(a). Evidently, beyond ~ 2 V the IR drop is quite significant with relatively poor coulombic efficiency (inset of Fig. 6.11(b)). The coulombic efficiency has a slow and gradual drop to ~ 2 V, beyond that it reduces sharply to almost 70 % at 2.5 V. Thus, the optimal operating voltage limit for these devices is considered close to 2 V. Importantly, for the voltages ≤ 1.5 V the GCD cycles are indeed of triangular shape suggestive of EDLC nature.

GCD cycles (2V) were further performed at 35 °C for various current densities ranging from 0.57 A/g (1 mA) - 6.8 A/g (12 mA) as shown in Fig. 6.11(b). Interestingly, a slight non-triangular nature is evident for all the discharge currents. Also, IR drop during the discharge cycle reduces gradually as discharge current density decreases. As expected, the discharge time increases as the discharge current decreases.

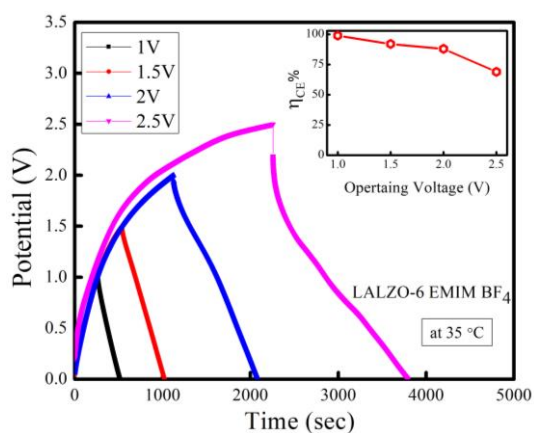


Fig. 6.11(a). GCD curves of SSCs for different voltage ranges at 0.57 A/g. Inset shows coulombic efficiency versus operating voltage.

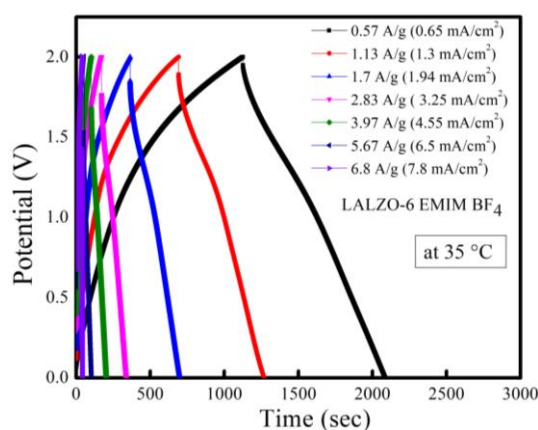


Fig. 6.11(b). GCD curves of SSCs for the 10th cycle at different discharge currents ranging from 0.57-6.8 A/g with areal current densities mentioned in brackets.

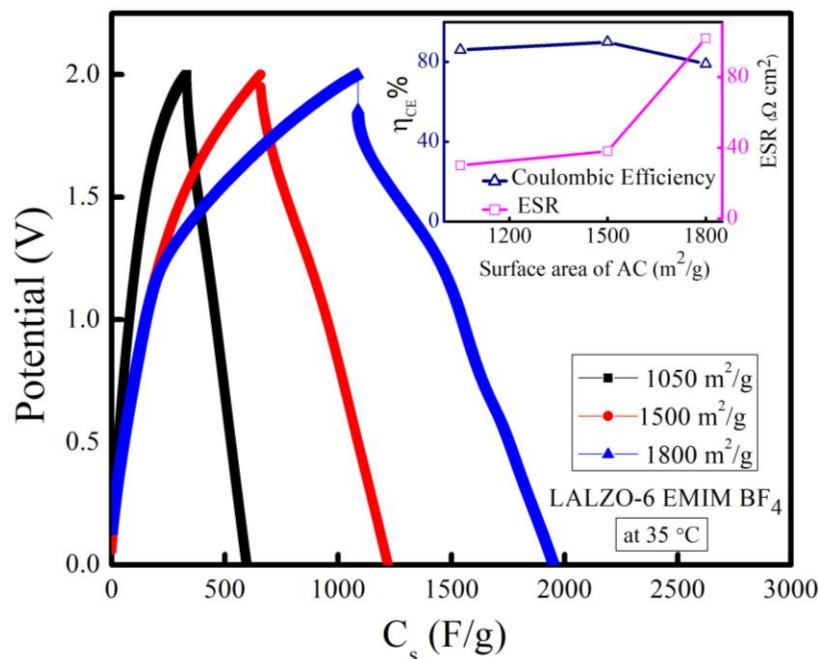


Fig. 6.11(c) GCD curves for SSCs at 0.57 A/g (1 mA) for different activated charcoal surface area electrodes.

GCD curves have also been obtained for the devices with same electrolyte LALZO-6 EMIM BF₄, but the activated carbon used for the electrode preparation is of different surface area (Fig. 6.11(c)). As the surface area increases, charge-discharge time also increases. The device with higher surface area appears to have more charge storage ability. However, the pseudo-type behaviour is also prominent with ~ 1800 m^2/g surface area. Further, as seen in inset, coulombic efficiency and ESR decreases. Thus, 1500 m^2/g is found to be a suitable surface area for these cells. Nevertheless, ionic liquid presence provides good wettability at the interface, and the surface area is effectively utilized by the mobile ions. The various performance parameters obtained for SSCs from Fig. 6.11(c) are shown in Table 6.1. The areal values are also provided for comparison.

Since a predominant EDLC behaviour is observed for operating voltages ≤ 1.5 , so long cycling was performed at 1 V. The potential versus specific capacitance for different charging-discharging cycles at 1 V and 1 mA (0.57 A/g) is shown in Fig. 6.11(d). The main characteristic features of discharge cycles remain the same even up to ~ 4000 cycles. The cycles remain symmetric and almost linear suggesting dominant EDLC behaviour.

Table 6.1: Specific Capacitance (C_s), specific energy (E), specific power (P), Equivalent series resistance (ESR), areal capacitance, energy density (E_a), and power density (P_a) for the SSCs of the composite LALZO-6 EMIM BF₄ as electrolyte having different surface area activated carbon for electrodes and operating current and voltage as 1 mA (0.57 A/g) and 2 V respectively. The range is specified for C_s and (*) represents values for a typical SSC used in the analysis that is close to the average performance of the SSC.

Surface area of activated charcoal (m ² /g)	C_s (F/g)	E (Wh·kg ⁻¹)	P (W·kg ⁻¹)	ESR (Ω cm ²)	Areal Capacitance (mF·cm ⁻²)	E_a (μ Wh·cm ⁻²)	P_a (μ W·cm ⁻²)
1050	255-265 262*	35*	277*	30*	145-155 150*	123*	979*
1500	560-570 562*	74*	276*	38*	315-325 322*	261*	974*
1800	850-860 855*	103*	264*	102*	486-494 490*	365*	932*

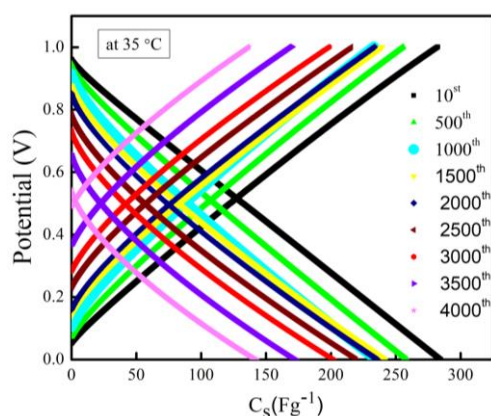


Fig. 6.11(d) Charge-discharge curves obtained at different cycles for SSC with LALZO-6 EMIM BF₄ composite as electrolyte at room temperature at 0.57 A/g (1 mA).

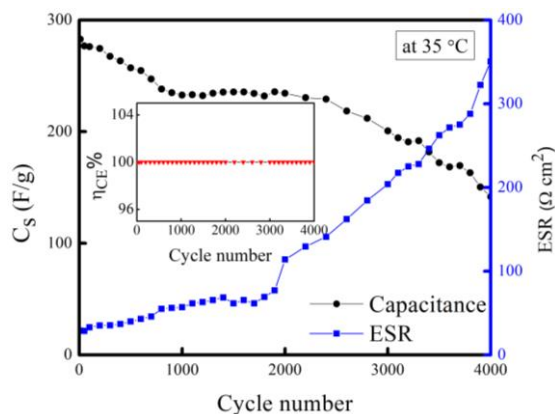


Fig. 6.11(e) Specific capacitance and ESR vs cycle number for SSC having electrolyte LALZO-6 EMIM BF₄. Inset shows coulombic efficiency vs cycle number up to 4000 cycles.

The C_s and ESR as a function of cycle number are shown in Fig. 6.11(e). As observed C_s falls slowly from 282 F/g to 235 F/g in first 1000 cycles and then stabilizes for the next 1500 cycles. Evidently, C_s value finally remains at a fairly high value of \sim 145 F/g even after \sim 4000 cycles with \sim 53 % capacity retention. The ESR is almost constant

initially and shows a gradual rise, but only after ~ 2000 cycles. As shown in the inset of Fig. 6.11(e), the cell exhibits a coulombic efficiency of $\geq 99\%$ throughout the ~ 4000 charging-discharging cycles which in turn suggests satisfactory electrochemical stability with a stable electrode-electrolyte interface. These results readily suggest there is no notable degradation of the device.

To further explore the SSC stability in adverse temperature conditions, GCD cycling was also performed at 0°C and 100°C . Fig. 6.11(f) shows the GCD curves up to ~ 200 cycles for SSC at 100°C with a current density of 1.13 A/g (2 mA). The cycles exhibit almost a continuous trend without any abruptness at such a high temperature. The C_s vs cycle number for 200 cycles at 100°C is shown in Fig. 6.11(g). As apparent, the C_s value remains almost constant to an appreciably high value around $\sim 300\text{ F/g}$. The ESR is quite low and remains almost constant, stabilizing to a value of $\sim 16\ \Omega\ \text{cm}^2$. The coulombic efficiency as shown in the inset of Fig. 6.11(g) increases gradually and then stabilizes to 97% . These results indicate excellent electrochemical stability of electrode-electrolyte interface.

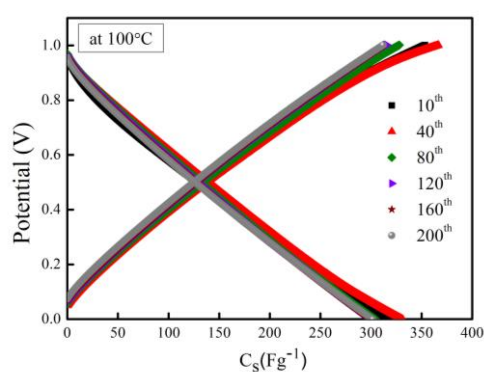


Fig. 6.11(f) GCD curves (at 1.13 A/g) for SSC up to 200 cycles at 100°C .

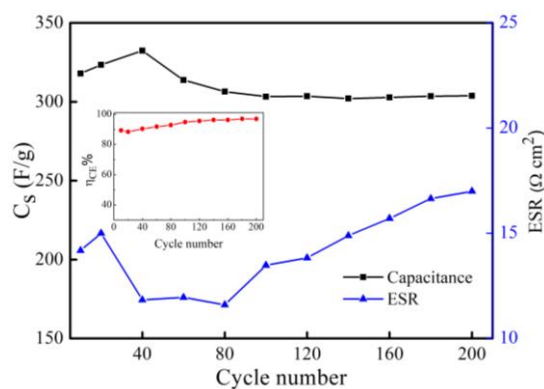


Fig. 6.11(g) C_s vs Cycle number for first 200 cycles at 100°C . Inset: coulombic efficiency versus cycle number.

Fig. 6.11(h) shows first 200 GCD cycles for the SSC at 0°C with a current density of 1.73 A/g (3 mA) at 2 V . These cycles also follow a constant pattern with a nominal drop in the C_s value. The C_s vs. cycle number for 200 cycles at 0°C is shown in Fig. 6.11(i). The C_s value gradually falls from 270 F/g to 220 F/g in the first 100 cycles and then almost stabilizes and remains at an appreciably high value of 206 F/g even after 200 cycles. The ESR accordingly shows a subtle but gradual rise depicting the stability

of the device. The coulombic efficiency is again appreciable throughout the cycling as shown in the inset of Fig. 6.11(i). These observations clearly demonstrate excellent electrochemical stability and a stable electrode-electrolyte interface even at such low temperatures.

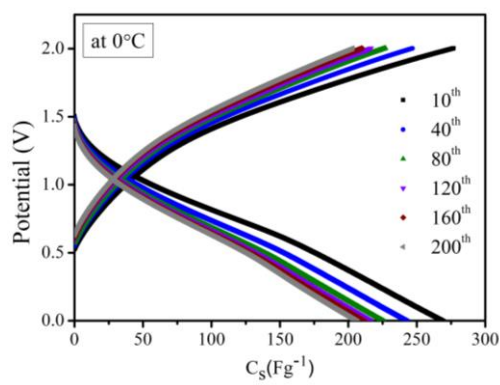


Fig. 6.11(h). GCD curves (at 1.73 A/g) for SSC up to 200 cycles at 0 °C.

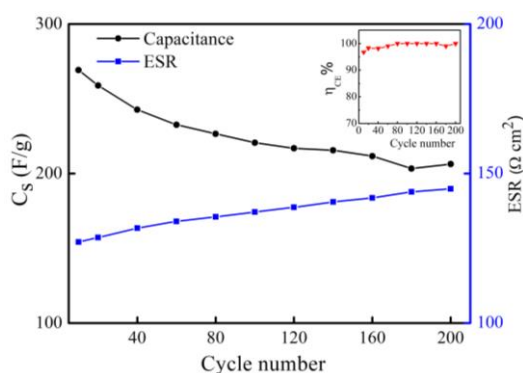


Fig. 6.11(i). C_s vs Cycle number for first 200 cycles at 0 °C. Inset: coulombic efficiency versus cycle number.

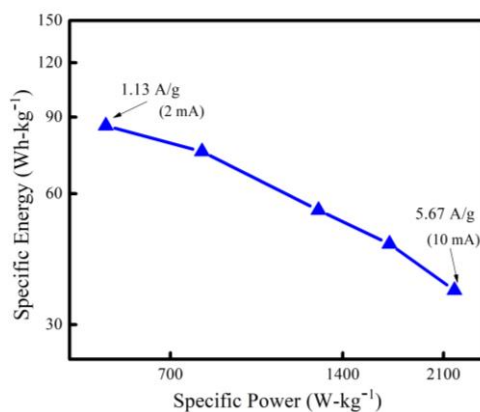


Fig. 6.11(j) Ragone plot for SSC in at 2 V.

Ragone plot for the supercapacitor at room temperature and 2 V operating voltage is shown in Fig. 6.11(j). The Specific energy (E) and specific power (P) values are appreciable at room temperature. At low specific power of 540 W/kg one observes a high value of specific energy of 86 Wh/kg. Further, with increasing power output, the

specific energy decreases. The highest specific energy and power are found to be 86 Wh/kg (at 1.13 A/g) and 2195 W/kg (at 5.67 A/g), respectively.

To demonstrate the applicability of the IL-garnet composites in other geometries, SSCs were developed in laminated geometry which is also suitable for creating ceramic supercapacitors. This fabrication technique is cost-effective and provides good contact between electrodes and electrolytes. Further investigations are planned in this direction.

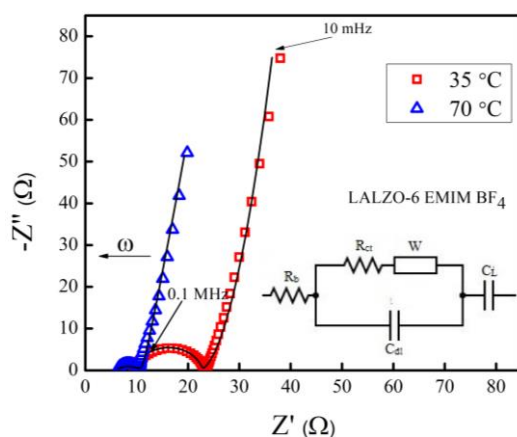


Fig. 6.12(a) Nyquist plot for laminated SSC with corresponding equivalent

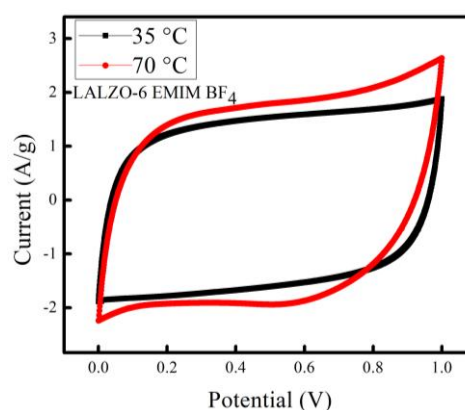


Fig. 6.12(b) CV (at 10 mV/s) scan for laminated SSC. In comparison to coin cells the feature is more 'box-like'.

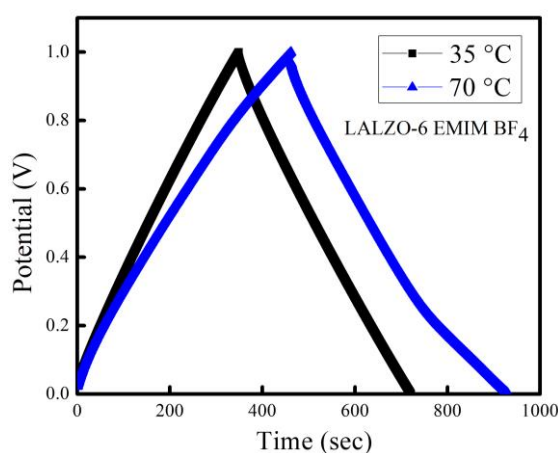


Fig. 6.12(c) GCD (at 0.57 A/g) cycles for laminated SSC. In comparison to coin cells apparently the ESR is less.

The Nyquist plot (frequency range of 10 mHz to 0.1 MHz) at two different temperatures with an equivalent circuit is shown in Fig. 6.12(a) for laminated SSCs. The

supercapacitor nature is clearly defined with very little resistance $\sim 34 \Omega \text{ cm}^2$ that decreases at high temperature to $\sim 17 \Omega \text{ cm}^2$. Apparently, the contact between electrodes and electrolyte remains intact in this geometry. Fig. 6.12(b) gives the CV scans of laminated SSCs at a scan rate of 10 mV/s which shows a featureless profile with a good charge storage ability.

The GCD cycles (at 0.56 A/g) for laminated SSCs at 35 °C and 70 °C are shown in Fig. 6.12(c). This depicts a substantial discharge time which further increases with temperature rise. The EDLC nature is quite evident from these cycles. It is appreciable to note that the ESR is very less in this geometry which shows a good interfacial contact between electrode and electrolyte.

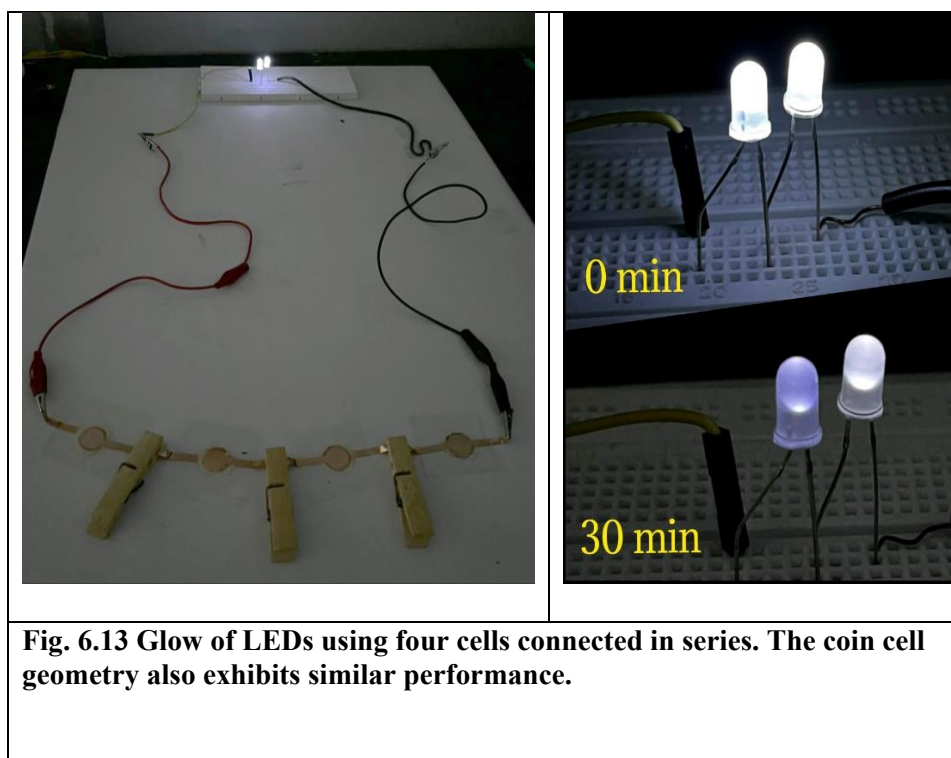


Fig. 6.13 Glow of LEDs using four cells connected in series. The coin cell geometry also exhibits similar performance.

To demonstrate the practical applicability of the SSCs, the series combination of four cells having LALZO-6 EMIM BF₄ composite as an electrolyte has been used to glow two LEDs of $\sim 6 \text{ V}$ as seen in Fig. 6.13. The LEDs during direct discharge could glow for ~ 30 minutes at a temperature of $\sim 25 \text{ }^\circ\text{C}$. In laminated as well as coin cell geometry the SSCs exhibit similar and reproducible performance.

The above discussion may be summarized as follows:

1. The SSCs discussed are predominantly of EDLC nature below 1.5 V operating voltage. However, above this voltage the pseudocapacitive effects appear; attributed to some unidentified redox process of the trace impurities or IL.
2. Room temperature operation of these cells is most effective and stable. The interface nevertheless is well maintained in a wide temperature range of 0 °C-100 °C. Thus, the IL possibly provides good coupling between electrodes and electrolytes.
3. As also observed in supercapacitors based on NASICON-IL composites [13] the predominantly EDLC behaviour is also observed up to 1 V. Apparently, Li⁺ ion garnet's presence in the electrolyte improves electrochemical stability window. Another advantage of the present system is that a lesser amount of IL (6 wt% against 13 wt% in NASICON-based systems) leads to similar performance and relatively higher operating voltages can be used for the operations.
4. The small amount of pseudo supercapacitance still needs investigation. However, one cannot deny a possibility that the presence of some functional groups in IL, or its hygroscopic nature, or some other trace impurities, may be responsible for this. These impurities, however, do not contribute significantly towards a chemical reaction at lower voltages. More systematic experiments are required to understand the partial pseudo nature of the capacitance.

6.7 Summary

- (i) By a simple synthetic procedure stable composite of LALZO and ILs has been produced which shows reproducible structural and electrical properties.
- (ii) The LALZO – IL composites show significant enhancement in electrical conductivity compared to pristine LALZO , attributed to the non-uniform and weak chemisorption of IL on the surface of LALZO and consequent weakening of bonds that bind the lithium ions to the solid. The electrical conductivity in the composites is assumed to be attributed to Li⁺ ions. Moreover, the amount and type of IL influence electrical conductivity.
- (iii) The synthesized composites have been found to be stable under battery conditions with good capacity value. The Preliminary investigations on Li|IL-LALZO|LFP button-type cells also suggest that IL-LALZO composite electrolytes have the potential for applications in lithium batteries. The

formation of the SEI layer at the interface, though, needs to be addressed with more experimental evidence. LALZO-IL composites can be directly applied to devices. They also offer a freedom of wide temperature applicability at least up to $\sim 200^{\circ}\text{C}$. Such composites in pellet form do not require high-temperature sintering prior to use in batteries.

- (iv) We have demonstrated that these composites can further be used to construct solid-state supercapacitors (SSCs) (only coin cell geometry has been considered); At low voltages (below 1.5 V) SSCs are predominantly EDLC in nature and pseudo capacitance effects appear at higher voltages;
- (v) The SSC cells that show good results are fabricated only by pressing the sandwich geometry, indicating that IL possibly provides a good coupling between the electrodes and electrolytes; The cells (interfaces) are stable in a wide range of temperature between 0°C - 100°C and the best operating condition happens to be that of room temperature.
- (vi) Compared to NASICON – IL composites, the LALZO – IL composites require lesser amounts (wt %) of IL for a similar performance. In both cases below 1 V predominant EDLC behavior is observed.
- (vii) Further systematic experiments are required to explain the pseudo capacitance appearing at high voltages; At this stage, we may only guess, that some redox process happens at higher voltage either due to the functional groups of IL or due to the impurities of various nature, such as the hygroscopic components, carbonates etc.

References

- [1] G. Kaur, M. D. Singh, S. C. Sivasubramanian, and A. Dalvi, “Investigations on enhanced ionic conduction in ionic liquid dispersed sol-gel derived $\text{LiTi}_2(\text{PO}_4)_3$,” *Materials Research Bulletin*, vol. 145, no. July 2021, p. 111555, 2022, doi: 10.1016/j.materresbull.2021.111555.
- [2] G. Kaur, S. C. Sivasubramanian, and A. Dalvi, “Solid-state supercapacitors using ionic liquid dispersed Li^+ -NASICONs as electrolytes,” *Electrochimica Acta*, vol. 434, no. May, p. 141311, 2022, doi: 10.1016/j.electacta.2022.141311.
- [3] J.B. Boyce, B.A. Huberman, Superionic conductors: Transitions, structures, dynamics, *Phys. Rep.* 51 (1979) 189–265. <https://doi.org/10.1016/0370->

1573(79)90067-X.

- [4] P. Bashiri, T.P. Rao, V.M. Naik, G.A. Nazri, R. Naik, AC conductivity studies of polyethylene oxide-garnet-type $\text{Li}_7\text{La}_3\text{Zr}_2\text{O}_{12}$ hybrid composite solid polymer electrolyte films, *Solid State Ionics*. 343 (2019) 115089. <https://doi.org/10.1016/j.ssi.2019.115089>.
- [5] Y. Tian, Y. Zhou, Y. Liu, C. Zhao, W. Wang, and Y. Zhou, “Formation mechanism of sol-gel synthesized $\text{Li}_{7-3x}\text{Al}_x\text{La}_3\text{Zr}_2\text{O}_{12}$ and the influence of abnormal grain growth on ionic conductivity,” *Solid State Ionics*, vol. 354, no. June, p. 115407, 2020, doi: 10.1016/j.ssi.2020.115407.
- [6] Y. Shimonishi *et al.*, “Synthesis of garnet-type $\text{Li}_{7-x}\text{La}_3\text{Zr}_2\text{O}_{12-1/2x}$ and its stability in aqueous solutions,” *Solid State Ionics*, vol. 183, no. 1, pp. 48–53, 2011, doi: 10.1016/j.ssi.2010.12.010.
- [7] Y. Meesala *et al.*, “An efficient multi-doping strategy to enhance Li-ion conductivity in the garnet-type solid electrolyte $\text{Li}_7\text{La}_3\text{Zr}_2\text{O}_{12}$,” *Journal of Materials Chemistry A*, vol. 7, no. 14, pp. 8589–8601, 2019, doi: 10.1039/c9ta00417c.
- [8] S. A. Pervez *et al.*, “Overcoming the Interfacial Limitations Imposed by the Solid–Solid Interface in Solid-State Batteries Using Ionic Liquid-Based Interlayers,” *Small*, vol. 16, no. 14, 2020, doi: 10.1002/smll.202000279.
- [9] L. Chen, Y. Li, S.P. Li, L.Z. Fan, C.W. Nan, J.B. Goodenough, PEO/garnet composite electrolytes for solid-state lithium batteries: From “ceramic-in-polymer” to “polymer-in-ceramic,” *Nano Energy*. 46 (2018) 176–184, doi.org/10.1016/j.nanoen.2017.12.037.
- [10] J. Lu, Y. Liu, P. Yao, Z. Ding, Q. Tang, J. Wu, Z. Ye, K. Huang, X. Liu, Hybridizing poly(vinylidene fluoride-co-hexafluoropropylene) with $\text{Li}_{6.5}\text{La}_3\text{Zr}_{1.5}\text{Ta}_{0.5}\text{O}_{12}$ as a lithium-ion electrolyte for solid state lithium metal batteries, *Chem. Eng. J.* 367 (2019) 230-238, doi.org/10.1016/j.cej.2019.02.148.
- [11] A. Villa, J.C. Verduzco, J.A. Libera, E.E. Marinero, Ionic conductivity optimization of composite polymer electrolytes through filler particle chemical modification, *Ionics (Kiel)*. 27 (2021) 2483–2493.

<https://doi.org/10.1007/s11581-021-04042-9>.

- [12] N. Yadav, N. Yadav, and S. A. Hashmi, “High-Energy-Density Carbon Supercapacitors Incorporating a Plastic-Crystal-Based Nonaqueous Redox-Active Gel Polymer Electrolyte,” *ACS Applied Energy Materials*, vol. 4, no. 7, pp. 6635–6649, 2021, doi: 10.1021/acsaem.1c00703.
- [13] C. Chen, Y. Sun, L. He, M. Kotobuki, E. Hanc, Y. Chen, K. Zeng, L. Lu, Microstructural and Electrochemical Properties of Al- And Ga-Doped $\text{Li}_7\text{La}_3\text{Zr}_2\text{O}_{12}$ Garnet Solid Electrolytes, *ACS Appl. Energy Mater.* 3 (2020) 4708–4719. <https://doi.org/10.1021/acsaem.0c00347>.

Chapter 7

Conclusions and future scope

7.1 CONCLUSION

This chapter provides a comprehensive overview of the thesis's findings and outline the potential directions for future research and development.

The current energy storage devices available in the market contain liquid or liquid slurry-based electrolytes, which have many issues related to safety, leakage, toxicity, operating temperature range, mechanical stability, etc. To overcome these issues, various new electrolytes in numerous forms e.g., gels, polymers, ionogels, etc., have been developed. Although these materials have been able to address some of the issues related to liquid electrolytes up to a certain limit, they are still lagging in terms of big commercial applications.

During the literature review, it is highlighted that there have been consistent efforts on the development of fast ionic ceramic solid electrolytes; despite high bulk conductivity comparable to liquid/aqueous electrolytes or gels, their direct application has been found to be far restricted. Among these fast ionic systems, Li^+ ion conductors such as NASICONs (LTP, LATP) and garnets (LLZO, LALZO) have shown immense potential for future solid ionic devices. In these, high grain boundary impedance and solid-solid (electrode-electrolyte interface) is the bottleneck. Various techniques have been applied to reduce the impedance at the interfaces, such as adding additives, forming glass ceramics, or making composites denser, but the intergrain transport still remains inadequate for device application. On the other hand, at the electrode-electrolyte interface, the ionic transport is slowed down which remains another major issue that needs to be resolved, before these ceramics can be utilized in all-solid-state devices.

Considering these issues on ion conducting ceramics, the present work was planned to tailor the grain-grain and electrode-electrolyte interfaces by developing novel composites of NASICONs (LTP, LATP) and garnets (LLZO, LALZO) with ionic liquids. There have been a few reports in the literature on ceramic-ionic liquid based

composites, particularly in the context of improving the interfacial contact between the electrode and solid electrolyte, but rarely applied to the solid electrolyte itself. Moreover, a detailed investigation of electrical transport and a mechanism for ceramic-IL composites' electrical conduction was missing. Further, in most of such composites reported earlier, the ionic liquid existed in a large amount (80-90%) which does not promote the cation transport from the host ceramic matrix. The present work was also focussed on ways to tailor the interface, i.e., improving electrode-electrolyte and grain-grain contacts, and to improve the performance of solid-state batteries and supercapacitors using the novel IL-ceramic composites.

Again, to emphasize that during the synthesis and in application, it has been ensured in this thesis that the basic 'solid-state' of the electrolyte is not compromised and the mobile (Li^+) ions from the ceramic matrix, mainly contribute to the electrical transport. Further, the concept of direct use of ceramics as supercapacitor electrolyte was novel, and as discussed there were truly no reports available on the use of Li^+ ion NASICONs or garnets in supercapacitors. Therefore, the present study was planned to explore these two potential battery materials for their usage in supercapacitors. While planning and consolidating the ideas for a systematic study on ceramic-ionic liquid-based composites, we pondered around the following areas having '*yet to be answered*' questions to define the proposed objectives (chapter 1) of the thesis.

- i. Ceramic Synthesis route: To explore an optimized synthesis route for preparing ceramics particularly Li^+ ion NASICON and garnet-type compounds that do not require high-temperature annealing conditions.
- ii. IL-ceramic composites: To explore if IL incorporation can enhance the conductivity in ceramics, finding an optimized amount of IL, and without compromising the 'solid state'.
- iii. Wide Compositions: A variety of novel compositions that can be prepared and explored using various ceramics and ILs.
- iv. Basic Characterization: The structural, thermal, and electrical properties of these composites and to set a correlation between IL amount and electrical properties.
- v. Electrical Transport: To explore the mechanism of conductivity enhancement. To understand the role of different ceramics in the composite's conductivity and other properties. Also, to comprehend the role

of IL ions in the process.

- vi. Role as Electrolyte: Due to the high ionic conductivity of these ceramic-IL based composites, to use them as electrolyte for solid-state batteries and solid-state supercapacitors.
- vii. Interfaces: To investigate if IL present in composites can be useful in improving the electrode-electrolyte and grain-grain interface.
- viii. IL-ceramics in Energy Storage: As ceramics-IL-based composites are expected to have better conductivity in both low and high temperatures, so to fabricate devices, particularly supercapacitors, using these composites for wide temperature applications.
- ix. Device and geometries: To explore possible geometries in which the supercapacitors can be fabricated considering flexibility, cost of fabrication, etc.

While a substantial amount of work was required on the above-defined challenging goals that can be consolidated and defined while preparing this thesis, most of these could finally be answered in the best possible way. The present work pays attention to novel synthesis routes for device fabrication and performance. Device point of view, it was decided to give more emphasis on less explored solid-state ceramic supercapacitors.

For developing these composites Li⁺ ion based NASICONs such as LiTi₂(PO₄)₃ (LTP), Li_{1.3}Al_{0.3}Ti_{1.7}(PO₄)₃ (LATP), and Li_{6.4}Al_{0.2}La₃Zr₂O₁₂ (LALZO) garnet were synthesized and various composites were prepared by carefully mixing them with three ILs, viz. EMIMBF₄, EMIMCF₃SO₃, and BMIMBF₄. To understand the role of ILs and ceramics in conductivity enhancement, the ionic transport mechanism was thoroughly explored while giving sufficient emphasis to comprehend structural and thermal properties. Further, to explore the potential of these electrolytes, solid-state batteries and supercapacitors were fabricated. The battery fabrication was essentially to test the potential of the composites under electrochemical conditions. The main emphasis was given to the supercapacitors. These were prepared in various geometries thoroughly characterized with temperature, operating voltage, and current variations. Importantly, these supercapacitors were tested for adverse temperature conditions i.e., operations in a wide range of -30 °C to 300 °C were carried out in this study.

The following points conclude the work done in the thesis:

1. NASICONs and garnet were synthesized by sol-gel route as this preparation method gives more homogeneous and fine powders with good crystallinity and purity. The work reveals that this technique requires low sintering temperature and hold time as compared to other conventional methods. The ceramic prepared through this method exhibited a porous structure that accommodates IL homogeneously to reach to inter-grain interfaces. The ceramic-IL composites were prepared by mixing them either in a simple mortar pestle or by using a ball milling process. Importantly, the IL content in the matrix was kept small (0.1-13 wt%), and the solid-state nature of the electrolyte was preserved. Different types of compositions were prepared to investigate various phenomena either by changing the ceramic, IL ions or by varying IL wt%.
2. The addition of IL in the ceramics exhibits a rapid enhancement in the conductivity. The conductivity saturates above a certain IL amount. Mostly between 7-10 wt% for LTP/LATP and 4-6 wt% for LALZO, the conductivity stabilizes to a higher value ~3 orders above the pristine conductivity of ceramics. Interestingly, the mechanism of this enhancement is found to be dependent on the nature of the ceramic.
3. The garnets and NASICONs exhibit different mechanisms for the conductivity rise. In the case of Li^+ -NASICONs, it is revealed that the IL occupies the inter-grain regions thus providing a coupling between the nearby grains. The added IL initially occupies the space between the grain boundaries. This leads to a substantial reduction in the grain boundary impedance and a steep rise in the conductivity. After filling the inter-grain regions, the remaining IL occupies the surface. Beyond a few monolayers, it is expected that the surface cannot hold IL and it spills out leading to saturation in the electrical conductivity. It has been observed that in LTP-IL and LATP-IL composites the IL occupies the surface and interfaces via predominant physisorption. This is complemented by TGA results that exhibit characteristics of pristine IL, suggesting no strong bonding of IL at the interface. On the other hand, LALZO-IL composites demonstrate stronger adsorption of the IL ions with a wide range of distributed bond strengths. During the composite formation, these new bonds between the IL and the garnet surface/interface may weaken the bonds of lithium with LALZO on its surface

which leads to an increase in Li^+ ion conductivity.

4. The present study, through various experimental evidence, reveals that these composites are essentially Li^+ ion conductors and the role of IL is to facilitate electrical transport by lowering the barriers for Li^+ ion movement or dissociating the Li^+ ions from the ceramic matrix. Ionic liquid cations and anions though exist in a molten state, the possibility of their contribution in providing mobile ions to the electrical transport is rather weak. In such dense and compact systems, it seems unlikely that ions with large ionic radii will undergo long-range diffusive motion. Further, the grain-grain interface is dense due to crowded IL ions. So, the possibility of electrical transport along the grain boundaries is also less. Thus, it has been brought out in the present investigation that IL occupying space in the matrix uniformly and facilitates inter-grain transport like a coupling agent.
5. Even though, IL does not provide its mobile ions for electrical conduction, both IL and ceramics play a vital role in conductivity enhancement. On the one hand, the bulk conductivity of ceramic plays a role, and on the other side, the addition of IL on the surface brings in further enhancement of conductivity. As seen, LATP-containing composites have better ionic conductivity as compared to LTP-based composites. Also, the size of IL ions affects the conductivity enhancement. Evidently, IL with a relatively smaller cation/anion size leads to better conductivity rise.
6. It is again revealed that the amount of IL that can be added to a ceramic has a strong dependence on its porosity and surface area. The Li^+ NASICON-based ceramics were found to be absorbing a relatively larger amount of IL than that of the LALZO garnet. The maximum weight percentage of IL that can be added to LTP/LATP is 13%, while for garnets it is 6%. Adding more IL beyond these specific weight percentages causes the excess IL to spill out, as the ceramic surface cannot hold it.
7. The potential of Li^+ -NASICON-IL and LALZO-IL composites has been explored under battery conditions. Preliminary findings with Li/LiCoO₂ electrode pair suggest that these composites are useful as electrolyte; however, some engineering of electrodes and the interface is required. Generally, in all solid-state batteries, the lithium metal-electrolyte contact is established by taking the cell a little above the melting point of lithium. This process could not be performed due to experimental limitations. Nevertheless, as evident, simple physical contacts also lead to mA of

current during discharge stable for 10-15 hours. More precisely, the use of LATP-13 EMIMBF₄ results in ~5 h of discharge with 10 μ A current. Further, as expected, the LALZO-6 EMIMBF₄ electrolyte based cell was able to deliver a higher current of ~50 μ A for the relatively higher time of ~ 16 h. Higher discharge currents could not be obtained, possibly also due to the substantial thickness of the electrolyte pellets (~ 1-0.5 mm). Literature reveals that generally ~ 30 μ m thick electrolyte should be used for battery operations. In the present study, such a small pellet thickness could not be obtained. Nevertheless, in this fundamental investigation it can be safely concluded that (i) the developed electrolyte composites are stable under battery conditions, and (ii) due to high conductivity with less intake of IL, LALZO-IL composites appear a better choice.

8. The performance of solid state supercapacitors based on these composites is promising. Li⁺-NASICON-IL as well as LALZO-IL composites could be successfully used as electrolytes. High and stable values of capacitance (C_s), coulombic efficiency (η_{CE}), energy density (E), and power density (P) were obtained and found to be better than those of gel based supercapacitors. The cyclic performance, studied up to ~ 10, 000 cycles, was also satisfactory. For example, Li⁺-NASICON based cells exhibit $C_s \sim 680$ F/g, $\eta_{CE} \sim 99\%$, $E \sim 87$ Wh-kg⁻¹, and $P \sim 275$ W-kg⁻¹ values. On the other hand, the garnet-IL supercapacitors display $C_s \sim 555$ F/g, $\eta_{CE} \sim 99\%$, $E \sim 74$ Wh-kg⁻¹, and $P \sim 271$ W-kg⁻¹ values. On comparing it appears that the Li⁺-NASICON-IL based composites exhibit better candidature, and their performance is more stable with time and cycling. However, such a comparison is not justifiable due to the different mechanisms by which the IL interacts with them. Since IL exhibits physisorption on Li⁺-NASICONs, it is therefore suggested that their use is appropriate in EDLC applications. Further, the garnet-IL composites exhibit chemisorption, they appear more useful in faradic processes i.e., pseudo supercapacitor applications.

Further, it is also interesting to see that both of these compounds are flexible for adopting different supercapacitor geometries, and in the pellet form with a substantial thickness of ~200 μ m useful for storing large amounts of energy.

9. The solid-state supercapacitors with the Li⁺-NASICON-IL containing composites can withstand a temperature from as low as -10 °C to as high as 300 °C. The composites are quite stable in this wide temperature range and do not show any features of degradation. The LALZO-IL composite-based supercapacitors can also

work within a temperature range of -10 °C to 150 °C. The thermal stability of garnet-based supercapacitors is less as compared to NASICON-based supercapacitors; while we have seen that the IL adsorption process is different in NASICONs (physisorption) and garnets (chemisorption), further fine sophisticated experiments may be required to explain the lower thermal stability of garnet composites compared to NASICON composites. These devices can be extremely useful in such cases where adverse temperature conditions exist like in industry applications or defence and space applications.

The conductivity and performance parameters related to devices for the optimized composites of Li⁺-NASICON and garnet with IL from the thesis work have been tabulated for comparison in Table 7.1.

Table 7.1 A comparison of electrical conductivity of the composites and device performance parameters obtained for the optimized composites of Li⁺-NASICON and garnet with IL

Composition	σ_{total} ($\Omega^{-1}\text{cm}^{-1}$) at 30 °C	Li cell performance with Li metal as anode and LiCoO ₂ as cathode	Supercapacitor performance at 1 mA, 2 V, and 35 °C with electrode having surface area $\sim 1500 \pm 100 \text{ m}^2/\text{g}$			
			C _s (F/g)	E (Wh-kg ⁻¹)	P (W-kg ⁻¹)	Cycling stability
LATP-13 EMIM BF ₄	1.72×10^{-3}	10 μA current withdrawn for 11-12 hours	675-685 680*	87*	275*	61 % capacity retention after 13000 cycles with ESR $12 \Omega \text{ cm}^2$
LALZO-6 EMIM BF ₄	6.9×10^{-4}	50 μA current withdrawn for 15-16 hours	550-560 555*	74*	271*	50 % capacity retention after 4000 cycles with ESR $350 \Omega \text{ cm}^2$

10. Different geometries for supercapacitors have been developed in the present investigations, such as coin cell fabrication, Swagelok assembly, and laminated supercapacitors. The study suggests that all these geometries have their features and advantages. Coin cell fabrication is one of the conventional geometry which gives intact packing with better contacts between the electrode and the electrolyte reducing resistance and keeping the cell moisture free. Swagelok assembly has been used mainly for high temperature characterization. Laminated supercapacitors have been developed for the first time in this work where direct

use of ceramics in the supercapacitors has been shown in a simple sandwich geometry cell prepared using a simple hot roll laminator. This method also proved to be economically very efficient.

7.2 FUTURE SCOPE

1. In this work, composites were developed using Li^+ -NASICON and garnet-based ceramics. However, various ceramics such as perovskites, LISICONs, Li_3N , etc. can be explored. Also, compositional variation in the LTP, LATP, and LALZO can be tried. For example, increasing the Li^+ ion content or elemental substitution can be explored as it can enhance the ionic transport, and, in turn, increase the device performance parameters.
2. Similar studies should be planned on Na^+ ion systems. The Na^+ ion solid electrolytes exhibit poor conductivity. The addition of IL can lead to much-improved values, suitable for applications to supercapacitors and batteries.
3. Varying Ionic liquid content and type can be explored, as the cation/ anion size can affect the electrical transport in the composites, hence device performance.
4. The ion transport mechanism proposed in the thesis should be examined for these composites using sophisticated techniques such as XANES, XPS, or solid-state NMR. These techniques can be used to find salt ion's interaction with ionic liquid. Investigations using these techniques can be done to do a judicial comparison between Li^+ ions and IL mobile ions. Also, impedance spectroscopy can further be explored in the GHz region for a better understanding of the electrical response.
5. The composites need to be explored through theoretical studies to have a better understanding of the morphological features, conduction pathways, etc.
6. New electrode materials, pseudo electrodes can be developed compatible with IL-ceramic composites. These can further enhance the capacity and can have better contact with these composites.
7. In the present work, solid-state supercapacitors have been developed. To further enhance their performance, novel electrode materials can be explored from different sources with a large surface area.
8. It is important to use a variety of sophisticated techniques to understand the mechanism of charge storage in the ceramic-IL based supercapacitors; Also further temperature variation studies of structure are required to elucidate the

comparatively lower thermal stability of garnet composites compared to the LATP composites.

9. Attempts are required to develop thin (< 50 microns, or so) and free-standing sheets of IL-ceramic composites. Solid ILs need to be explored for making composites with ceramics. Using solid ILs possibly mechanically stable ceramic sheets can be produced with large surface area.
10. More geometries for supercapacitors and batteries can be explored which can give better contacts between electrodes and electrolytes and are cost-effective. There is a need to develop a fabrication process that can work at high temperatures. Also, there is a need to develop thin films of ceramic electrolytes or to develop ways to make electrolytes as thin as possible as it leads to better results with less impedance and interfacial issues.
11. These composites as electrolytes can be explored for symmetric pseudo, asymmetric pseudo, and hybrid supercapacitors.

List of publications

International Journals

1. “Solid-state supercapacitors using ionic liquid dispersed Li⁺-NASICONs as electrolytes”, Gurpreet Kaur, S. C. Sivasubramanian, Anshuman Dalvi, **Electrochimica Acta (Elsevier)**, 434 (2022) 141311.
DOI: <https://doi.org/10.1016/j.electacta.2022.141311>
2. “Investigations on enhanced ionic conduction in ionic liquid dispersed sol-gel derived LiTi₂(PO₄)₃”, Gurpreet Kaur, M. Dinachandra Singh, S. C. Sivasubramanian, Anshuman Dalvi, **Materials Research Bulletin (Elsevier)**, 145 (2022) 111555.
DOI: <https://doi.org/10.1016/j.materresbull.2021.111555>
3. “All-solid-state Na⁺ ion supercapacitors using Na₃Zr₂Si₂PO₁₂-polymer hybrid films as electrolyte” M. Dinachandra Singh, Gurpreet Kaur, Shrishti Sharma, Anshuman Dalvi, **Journal of Energy Storage (Elsevier)**, 41 (2021) 102984.
DOI: <https://doi.org/10.1016/j.est.2021.102984>
4. “Improving interfaces in all-solid-state supercapacitors using polymer-added activated carbon electrodes” Shrishti Sharma, Gurpreet Kaur, Anshuman Dalvi, **Batteries (MDPI)**, 9 (2023) 81.
DOI: <https://doi.org/10.3390/batteries9020081>
5. “Ionic liquid composites with garnet-type Li_{6.75}Al_{0.25}La₃Zr₂O₁₂: Stability, electrical transport, and potential for energy storage applications” Gurpreet Kaur, Shrishti Sharma, M. D. Singh, K. S. Nalwa, S. C. Sivasubramanian, Anshuman Dalvi, **Materials Chemistry and Physics**.
6. “Solid state supercapacitors using garnet-type Li_{6.75}Al_{0.25}La₃Zr₂O₁₂-EMIMBF₄ composite electrolyte”, Gurpreet Kaur, Shrishti Sharma, Bhargab Sharma, S.

C. Sivasubramanian, Anshuman Dalvi, **Journal of Energy Storage**
(Communicated).

AIP Conference Proceedings

1. “Electrical Conductivity and Thermal Studies on [EMIM]BF₄, Li⁺ and Cu²⁺ Confined Silica Gel Composites”, Gurpreet Kaur, Rajinder Kaswan, S. C. Sivasubramanian, Anshuman Dalvi, 64th DAE Symposium on Solid State Physics, **AIP Conference Proceedings**, 2265, 030629-1-030629-4 (2020). DOI: <https://doi.org/10.1063/5.0016969>

Patent

1. Anshuman Dalvi, Gurpreet Kaur, S. C. Sivasubramanian, “Development of Li_{1.3}Al_{0.3}Ti_{1.7}(PO₄)₃-EMIM BF₄ nanocomposite electrolyte with wide thermal stability for all-solid-state supercapacitors”, No. 202211047554, August 2022 (Filed).

List of conferences/workshops

Conferences

1. “13th National Conference on Solid State Ionics” organized by Dept. of Physics, IIT-Roorkee from 16th to 18th December 2019.
2. “64th DAE symposium on Solid State Physics” organized by Bhabha Atomic Research Centre, Mumbai, India at IIT Jodhpur, from 18th to 22nd December 2019.
3. “14th National Conference on Solid State Ionics” organized by Dept. of Physics and Astrophysics, University of Delhi, from 16th to 18th December 2021.
4. “23rd International Conference on Solid State Ionics” organized by Massachusetts Institute of Technology, USA, from 17th to 22nd July 2022.

Workshops

1. “Workshop on Electron Microscope and Allied Analytical Techniques (EMAAT 2019)” on 5th June, 2019 at HPU Shimla.
2. “Workshop on EPR Spectroscopy and Its Applications” on 28th February, 2020 at IIT Bombay.

Brief biography of the supervisor

Prof. S. C. Sivasubramanian

He is an experienced professor with a demonstrated history of working in the higher education industry. Skilled in magnetic resonance spectroscopy, amorphous materials, and interested in curriculum development, e-learning, and data analysis. Strong education professional with a Ph.D. focused in Physical Chemistry from IIT Kanpur. He obtained his master's in chemistry from University of Hyderabad in 1982. Later, he received his doctoral degree in 1990 from IIT Kanpur in field of Physical Chemistry. Thereafter, he joined BITS Pilani, Pilani campus in academics in 1992.

His major interest was in physical chemistry, magnetic resonance spectroscopy (EPR and NMR) and in amorphous systems. He has also contributed in various administrative positions. He remained as a unit chief of CAHU (Computer Assisted Housekeeping Unit) from 2006-2018. He also handled the position of Dean Administration, BITS Pilani, Pilani Campus from 2014-2018 and was positioned as Acting Registrar from 2016-2018.

Prof. Anshuman Dalvi

Dr. Anshuman Dalvi is a Professor in the Department of Physics, BITS, Pilani. He did his M.Sc. from School of Physics, D. A. University, Indore in 1997 and PhD from Indian Institute of Technology, Kanpur under the supervisor of Prof. K. Shahi in the year 2003. He worked as a CSIR project scientist in Department of Physics, IIT Kanpur with Prof Satish Chandra Agarwal for a year. He joined the Department of Physics, BITS, Pilani in 2004 and working as a Professor in the Department of Physics, BITS, Pilani since 2018.

His area of expertise is predominantly experimental Solid State Ionics. He takes keen interest in exploring ionic and electronic properties of glasses, glass-ceramics, polymers and polymer-ceramic hybrids for applications in solid state ionic devices. He received the prestigious INSA fellowship under international bilateral exchange programme and worked in Warsaw university of Technology, Poland. He has a total of 70 referred indexed publications out of which 45 in journals of international repute. He has executed several DST, UGC-DAE collaboration scheme projects. He headed the Department of Physics, BITS, Pilani for one term during 2016-2018. He has guided five PhD students and is currently guiding five. He was also the convener of the 12th National conference on Solid State Ionics (NCSSI-12) held at BITS Pilani from 21st to 23rd December 2017.

Brief biography of the candidate

Ms. Gurpreet Kaur did her graduation in B.Sc. from M.C.M. DAV College Chandigarh, Panjab University in 2014. She then did her M.Sc. in Chemistry from DAV College Chandigarh, Panjab University in 2016. Thereafter, she joined the solid state ionics group for pursuing PhD under the supervision of Prof. S. C. Sivasubramanian and Prof. Anshuman Dalvi. In her PhD, she developed some novel composites based on Li⁺ NASICON and garnet with ionic liquids as solid electrolyte for solid-state battery and solid-state supercapacitor applications. She has developed solid-state supercapacitors in various geometries which can work in a wide temperature range of -10 °C to 300 °C which got recognition in DST news. She represented her work in various International and National conferences in the field of Solid State Ionics. She has filed one Indian patent and published six research papers in reputed international journal and one AIP conference proceedings.